ON THE POST-PRINTING HEAT TREATMENT OF WIRE ARC ADDITIVELY MANUFACTURED FERROUS ALLOYS

by

Alireza Vahedi Nemani

Submitted in partial fulfilment of the requirements
for the degree of Doctor of Philosophy

at

Dalhousie University
Halifax, Nova Scotia
April 2022

I dedicate my thesis to my beautiful wife, **Mahya**, for her endless love and support and my adorable parents who encouraged and guided me throughout my life.

TABLE OF CONTENTS

LIST OF TABLES

LIST OF FIGURES

ABSTRACT

Over the past decade, wire arc additive manufacturing has become a promising alternative to conventional manufacturing methods due to its great potential for fabrication of medium to large size components with high deposition rate, low raw material consumption, and flexibility in design. Despite the advantageous features of additive manufacturing technology, its complex thermal cycles result in microstructural heterogeneities and uncertainties in mechanical properties and corrosion performance of the additively manufactured components as compared to conventionally fabricated counterparts. Therefore, with the purpose of microstructural modifications and in-service performance improvements, this thesis aims to investigate the beneficiary effects of post-printing heat treatment on wire arc additively manufactured ferrous alloys, i.e., low-carbon low-alloy steel (ER70S), martensitic stainless steel (ER420) and a precipitation hardening martensitic stainless steel (PH 13-8Mo). The results of microstructural characterizations and mechanical properties evaluations showed that appropriate post-printing austenitizing heat treatments could eliminate the microstructural heterogeneities and minimize the anisotropic mechanical properties of the as-printed thin-wall component of low-carbon low-alloy steel (ER70S), which was characterized by periodic microstructural variations along the building direction with a much lower ductility in vertical direction (~ 12 % el.) as compared to the horizontal direction with around 35 % of elongation. In addition, post-printing austenitizing treatment at 1150 °C on the additively manufactured martensitic stainless steel (ER420) resulted in the removal of undesired δ-ferrite phase, which was formed in the as-printed material due to rapid cooling associated with manufacturing process and high chromium content (13 wt. %) of the feedstock material. Further tempering process led to the formation of chromium carbides with various sizes and distributions over different tempering temperatures, promoting secondary hardening during tempering with the maximum microhardness value of 550 ± 7 H V for the sample tempered at 400 °C. However, the microhardness reduced to the minimum value of 300 ± 1 H V at higher tempering temperatures ascribed to intergranular segregation and coarsening of carbides, leading to excessive softening of the martensitic matrix. Investigations on the effects of post-printing heat treatment on the corrosion properties of additively manufactured PH 13-8Mo stainless steel revealed that solution treatment could significantly improve the corrosion resistance of the material due to the removal of Cr-enriched δ-ferrite phases from the as-printed microstructure, which trigger the sensitization phenomena in Cr-depleted region at the boundaries of δ-ferrite and matrix. However, aging at a high temperature (600 °C) resulted in the formation of Cr-enriched $M_{23}C_6$ carbides that created micro-galvanic coupling sites throughout the microstructure, adversely affecting the corrosion performance of the alloy. Overall, it was concluded that microstructural features, mechanical properties, and corrosion performance of the additively manufactured ferrous alloys can be tailored based on the required in-service condition by implementation of proper post-printing heat treatment cycles.

LIST OF ABBREVIATIONS USED

AF	Acicular Ferrite
AM	Additive Manufacturing
APP	Anodic Potentiodynamic Polarization
B	Bainite
BM	Base Metal
C	Capacitance
CE	Counter Electrode
C_{eff}	Passive Film Capacitance
CMT	Cold Metal Transfer
CPE	Constant Phase Element
CPE_{cath}	Constant Phase Element of The Cathodic Phase
CPE_{dl}	Constant Phase Element of The Double Layer
CPE_{oxide}	Constant Phase Element of The Oxide Layer
CPE_{p}	Constant Phase Element of The Passive Layer
CPE_{pit}	Constant Phase Element of The Pitting
C_{SC}	Space Charge Capacitance
DED	Directed Energy Deposition
d	Grain Size
dl	Double Layer
DMLS	Direct Metal Laser Sintered
DP	Dual Phase
DRX	Dynamic Recrystallization
DSC	Differential Scanning Calorimetry
E	Applied Potential
e	Electron Charge
EBSD	Electron Backscattered Diffraction
$E_{corr.}$	Corrosion Potential
EDX	Energy Dispersive X-ray
EDS	Energy Dispersive Spectroscopy
E_{FB}	Flat Band Potential
EIS	Electrochemical Impedance Spectroscopy
E_{pit}	Pitting Potential
PF	Polygonal Ferrite
FESEM	Field Emission Scanning Electron Microscope
FIB	Focused Ion Beam
FSP	Friction Stir Processing
GB	Grain Boundary
GMA	Gas Metal Arc
GMAW	Gas Metal Arc Welding
GTA	Gas Tungsten Arc
HAGB	High Angle Grain Boundaries
HAZ	Heat Affected Zone
HIP	Hot Isostatic Pressing

ICHAZ	Inter-Critical Heat Affected Zone
$I_{Corr.}$	Corrosion Current Density
IPF	Inverse Pole Figure
k	Boltzmann's Constant
LAGB	Low Angle Grain Boundaries
LBM	Laser Beam Melting
LBZ	Localized Brittle Zones
LMD	Laser Metal Deposition
L-PBF	Laser-Powder Bed Fusion
MA	Martensite-Austenite
MP	Melt Pool
MSS	Martensitic Stainless Steel
n	Dispersion Coefficient
N_A	Acceptance Density
ND	Donor Density
NDT	Non-Destructive Testing
OCP	Open Circuit Potential
PBF	Powder Bed Fusion
PDM	Point Defect Model
PF	Pole Figure
PH	Precipitation Hardening
R_{ct}	Double Layer Resistance
RE	Reference Electrode
R_{el}	Electrolyte Resistance
R_{oxide}	Oxide Layer Resistance
Rp	Passive Layer Resistance
R_{pit}	Pitting Resistance
R_{pol}	Polarization Resistance
SEC	Simplified Equivalent Circuit
SEM	Scanning Electron Microscopy
SLM	Selective Laser Melting
STEM	Scanning Transmission Electron Microscopy
STEM-BF	STEM in Bright-Field Mode
STT	Surface Tension Transfer
TEM	Transmission Electron Microscopy
TMCP	Thermo-Mechanical Control Rolling
WAAM	Wire Arc Additive Manufacturing
WPF	Whole Pattern Fitting
XRD	X-Ray Diffraction
YS	Yield Strength
δ	Passive Layer Thickness
ε	Dielectric Constant
ω	Angular Frequency

ACKNOWLEDGEMENTS

First and for the most, I would like to express my sincere gratitude to my supervisor, Dr. Ali Nasiri, for his continual support, guidance, motivation and particularly his patience throughout my Ph.D. program.

I am also very grateful to the rest of my supervisory committee, Dr. Paul Bishop and Dr. Kyle Tousignant for their insightful comments and motivations.

My appreciation also goes to my colleagues in our research group who contributed to my research activities and without them this research would have been vastly more difficult.

Finally, I must express my special thanks to my adorable wife, Mahya, for her love, scientific support, and unwavering patience during this challenging journey.

CHAPTER 1 INTRODUCTION

1.1 WHAT IS ADDITIVE MANUFACTURING

Traditionally, different subtractive manufacturing methods were widely used for the fabrication of engineering components. Since the raw material in the conventional manufacturing techniques is commonly larger than the final product, the process starts with the removal of the extra material according to the intended design until the desired component is fabricated [1]. On the other hand, additive manufacturing (AM), also known as 3D-printing, is a rapidly emerging fabrication technology in which a fully functional part is produced through incremental depositing of the feedstock material in a layer-wise fashion resulting in a near-net-shape final product [2–4]. In this technology, 3D solid models are sliced into a large number of 2D thin cross-sections, which are uploaded into an AM machine to be combined in a layer-by-layer fashion and eventually translated into a physical object [5]. AM technology was primarily employed for rapid prototyping of the products, which were intended to be fabricated by other manufacturing methods. Although drawings are faster and simpler to generate, it is much more beneficial to fabricate and visualize a 3D model for better understanding the main intentions of the designer [5]. However, it is undervaluing to use AM only for prototyping purposes as this technology is able to offer a fair cost-saving capacity and also a substantial decrease in the production time, which make it an ideal substitute for the conventional subtractive fabrication methods [6][7]. Initially, AM technology was limited to softer materials such as polymers, waxes, and paper laminates, however, the developments in the technology expanded the applications of AM to a diverse range of other engineering materials such as concretes, ceramics, composites, and also a broad window of metallic materials to be fabricated by different techniques of 3D-printing [5][8][9][10].

1.2 CLASSIFICATIONS OF METAL AM PROCESSES

There are several approaches to categories metal AM technologies based on different criteria. This technology can be classified based on the feedstock material to two main categories of wire-based systems such as wire arc additive manufacturing (WAAM), or

powder-based systems like selective laser melting (SLM) [11]. Another well-known approach is to classify different AM techniques according to the feeding method of the feedstock material into two main classes of powder bed fusion (PBF) processes and directed energy deposition (DED) techniques in which the feedstock material (either wire or powder) is fused simultaneously as it is fed from a nozzle [12][13]. A wider classification can be implemented based on the employed heat source into two major groups of beam-based and arc-based systems [5]. Beam-based methods normally use laser or electron beams as the heat source, while arc-based systems, commonly known as WAAM, may employ gas metal arc (GMA), gas tungsten arc (GTA), or plasma arc (PA) welding power sources [14]. Fig. 1.1 classifies different AM methods under two categories of beam-based and arc-based systems.

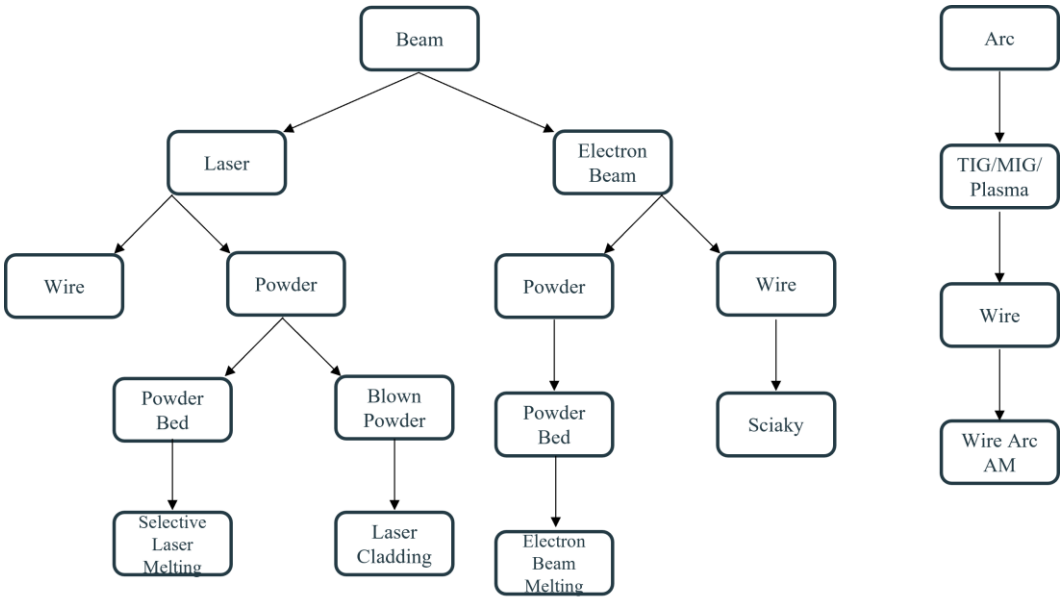

Figure 1.1 Classification of AM methods based on the employed heat source.

Laser-Powder Bed Fusion (L-PBF) is an AM method offering distinctive advantages, such as production of complex parts with intricate designs in a cost-effective manner with the possibility of fabricating the whole component in one step with minimal raw material's waste and shorter time to market. Not only academia, but also different industries such as aerospace, biomedical, automotive, oil and gas, and marine are showing significant interests in the parts fabricated by beam-based systems.

According to Fig. 1.2 [15], in a L-PBF system, a high energy laser is introduced to a powder bed and selectively melts a thin layer of the powder based on the intended design. The process continues with spreading another thin layer of the feedstock powder on previously deposited layer, followed by laser melting and metallurgical joining of the subsequent layers to the previous layers until the fully dense 3D-part is additively fabricated. It is notable that L-PBF method is called by different terminologies, such as Laser Beam Melting (LBM), Selective Laser Melting (SLM), or Direct Metal Laser Sintering (DMLS). Different grades of metals, such as ferrous alloys, Ni alloys, Al alloys, and Ti alloys have been successfully manufactured using different AM techniques. Electron beam melting (EBM) systems follows the same fabrication sequences as L-PBF except for using electron beam in an inert controlled- and vacuumed-atmosphere as the heat source instead of laser.

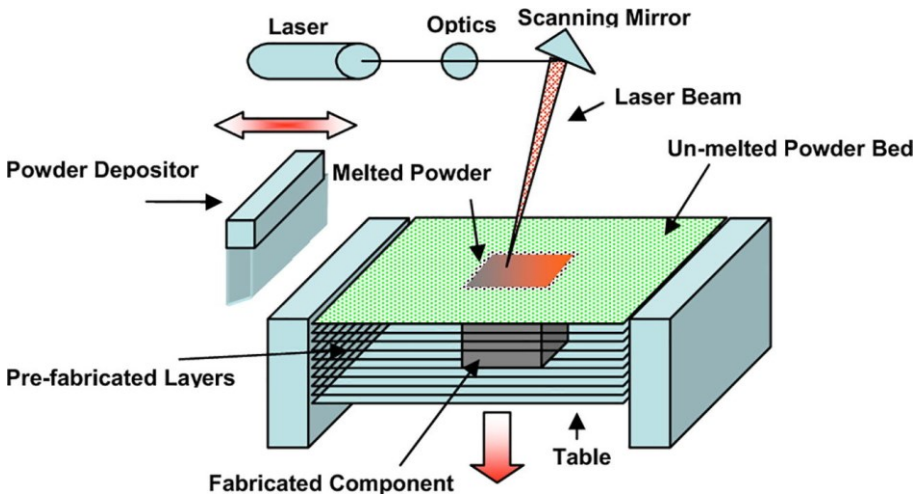

Figure 1.2 A schematic illustration showing a typical L-PBF system [15].

On the other hand, WAAM systems usually benefits from a robotic arm, carrying an arc welding torch as the energy source to fabricate metallic parts additively in the form of weld beads overlaid on previously deposited layers. In WAAM, all the consumable wire is continuously fed into the adopted electric arc or plasma and entirely melted, leading to extremely high deposition rate associated with this process, which is drastically higher than that in the powder-bed/feed AM systems. Fig. 1.3. is an schematic illustration showing a WAAM system using a GMA power source [16].

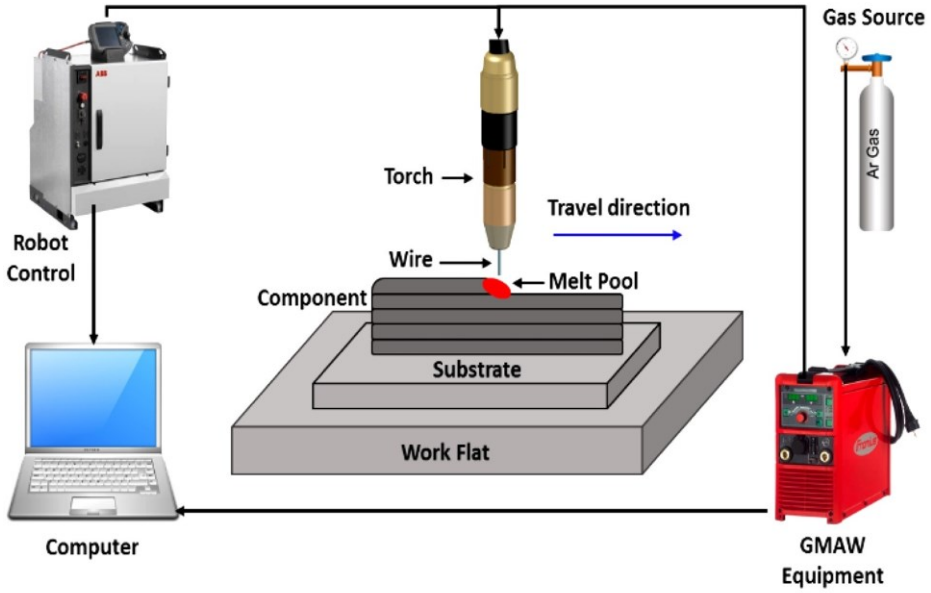

(a)

Figure 1.3 A schematic illustration showing a typical GMA-WAAM system [16].

In recent years, in multiple studies, the capabilities of the GMAWAAM in terms of technological issues and metallurgical properties for different alloys have been widely explored. For instance, the microstructure and tensile properties of 316 L austenitic stainless steel fabricated by GMA-AM [17], the feasibility of depositing steel parts by means of double electrode GMAW-based AM system [18], and the effect of the main deposition process parameters on the surface roughness of low-carbon steel parts fabricated using GMAW-based additive manufacturing [19] have been investigated. From the fabrication perspective, there are many similarities between conventional GMAW and wire arc additive manufacturing methods, leading to analogous challenges and difficulties associated with both processes. For instance, the strength–ductility combinations in steels can be affected adversely from the thermal cycles experienced during layer-by-layer deposition of WAAM, correlated to either the heat-affected zone (HAZ) softening and/or formation of localized brittle zones (LBZs) along the interpass regions, commonly observed in the multi-pass welding processes. Therefore, adopting an arc welding process with a low-heat input-transfer mode seems to be favorable for the purpose of WAAM.

Another complexity associated with the WAAM of ferrous alloys is that depending on the carbon content, alloying elements, and cooling rate of the steel, the manufactured component in the as-printed condition may possess a blend of different microstructures, e.g., ferrite, Widmanstätten ferrite, bainite, martensite, or acicular ferrite. Thus, to obtain a desired microstructure with adequate strength and toughness in a WAAM part, the GMAW process essential parameters should be carefully selected.

It is reported that the high cooling rate and temperature gradient experienced throughout the components during the AM fabrication process dictate the grain growth direction and morphology, yielding heterogeneous microstructures and anisotropic mechanical properties [20]. However, lower thermal input WAAM-based processes, such as WAAM–cold metal transfer (CMT) technique, can result in a more uniform microstructure and homogenous hardness profile. Wang *et al.* [21] also showed that in a 304-L austenitic stainless steel wall produced by directed energy deposition additive manufacturing, applying lower heat inputs resulted in a finer microstructure, and, therefore, higher yield and tensile strengths than those in the wall fabricated using a higher heat input. They also reported that at a specific heat input, the coarser microstructure at the top of the walls compared with the bottom of the components resulted in a lower yield and tensile strengths due to a lower cooling rate at the top areas of the wall [21].

Wilson-Heid *et al.* [20] studied the relationship between the microstructure and the anisotropy in ductility of an additively fabricated Ti-6Al-4V and concluded that the elongation percentage in the transverse direction is higher than that of the longitudinal direction. Wang *et al.* [22] also reported the anisotropic mechanical properties in a WAAM Ti-6Al-4V alloy, showing a higher strength and lower ductility in the horizontal direction compared with the building (vertical) direction. The authors correlated such properties to the existence of different crystallographic textures along the deposition direction versus the building direction developed from the directional columnar growth of Ti grains during solidification. On the other hand, Haden *et al.* [23] observed no obvious anisotropy in mechanical properties such as yield and tensile strength in a low-carbon low-alloy steel (ER70S-6) produced via WAAM. However, in their study, the reported

mechanical properties were not clearly correlated to the microstructure of the additively manufactured wall. In a recent study by Sridharan *et al.* [24], a GTA welding system was used to additively manufacture the low-carbon low-alloy steel ER70S-6 along the X-, Y-, and Z-directions followed by a detailed mechanical properties investigation. A significant scatter in the elongation with respect to the sample directions was reported and correlated to the differences in the level of porosities and discontinuities and the localized variations of the microstructural features in each sample.

In addition to all the experimental research on the advancement of the WAAM technology and its accelerated adoption in manufacturing of various engineering materials, the simulation and modeling of various aspects of the process have been also the focus of several studies. For example, the thermal history of the process [25], the deposition path [26], and the dynamics of metal transfer [27] during the fabrication process have been modeled in previous studies. In a study by Fachinotti *et al.* [25], a thermal-microstructural model capable of describing the thermal history of the WAAM process during the fabrication of Ti-6Al-4V alloy wall was developed. The proposed model was also capable of predicting important microstructural features in the fabricated part based on the predicted thermal history of the process [25]. In another study, the metal transfer dynamics of a wire feeding-based 3D printing process was extensively investigated, and a correlation model between the process parameters, such as heat input and scanning strategy, and the deposited bead geometry was developed [27].

It is well established that high-heat input-welding processes can lead to coarsening of the ferrite grains in steels due to recrystallization or abnormal phase transformation from Austenite [28]. The result can be a significant HAZ softening and a noticeable reduction in HAZ toughness. This issue is even more critical in the WAAM process due to the multi-pass nature of the process. Therefore, adopting a fast cooling version of the GMAW/GTAW process would plausibly favor the HAZ toughness of the WAAM-fabricated steels.

Surface tension transfer (STT) is an advanced current-controlled short-circuit metal transfer mode in the GMAW process developed by the Lincoln Electric Company [29]. The unique feature of the STT transfer mode is that it offers a combined reduction in energy and improved energy control through droplet by droplet control of the fusion zone, which can be beneficial in minimizing the extent of HAZ softening and can achieve a smooth bead profile and improved bead geometry. The heat input associated with the STT-GMAW process can be as low as 20% of that in conventional spray or pulsed-GMAW processes [29]. Hence, a fast cooling process, such as STT-GMAW, can dramatically enhance the HAZ toughness of high-strength low-alloy steels. The capabilities of this particular transfer mode for the WAAM of metallic components are hitherto unreported.

Most of the early-commercialized AM technologies were beam-based especially with a laser gun, which provides a collimated energy source with an elevated intensity being able to move precisely and quickly in a controlled fashion resulting in a high-resolution final product without too much heat accumulation [5]. However, there are some limitations associated with the beam-based systems such as low production rate, limited size of the product, high cost of equipment, and required vacuum chamber in the case of electron beam heat source [30]. Overall, beam-based systems are particularly suitable for the fabrication of low volume and geometrically complex components [30].

On the other hand, in the last decade, arc-based systems (WAAM) have increasingly drawn attention from different industries because of their potential to produce medium to large metallic parts with a relatively high deposition rate in addition to the competitive capital investments as compared to beam-based AM systems [31]. In addition, as opposed to powder-based systems, using wires as the feedstock material in WAAM technology results in avoiding the need for recycling the unused remaining powders, which improves the material deposition efficiency, and also significantly decrease the price per kilogram in different engineering alloys [31]. Interestingly, as compared with conventional subtractive fabrication methods, the production time can be reduced by ~50 % in WAAM [14]. In addition, the minimum required post-machining in WAAM leads to a great

saving opportunity in the raw material utilization [31][14]. As an industrial example, it has been reported that airplane landing gear ribs could be successfully fabricated through WAAM technology with around 78 % of saving in the raw material in comparison with the subtractive machining being traditionally used for the fabrication of the counterpart [14]. Complementary to this, specific tooling is not required in WAAM process, which is one the main challenges in the conventional manufacturing methods such as casting and forging resulting in higher production costs and more cycle time [31].

1.3 METALLURGICAL DRAWBACKS OF AM PARTS

Despite the advantages of the AM processes, there are some metallurgical drawbacks associated with this manufacturing technology, which are mostly related to its layer-by-layer deposition strategy being comparable to multi-pass welding process [5].
The repetitive melting and solidification of the deposited material, making the process prone to the formation of solidification defects including discontinuities, such as hot cracks, pores, and lack of fusions. Some common defects in WAAM, laser AM, and Arc welding processes are shown in Fig. 1.4 [16].

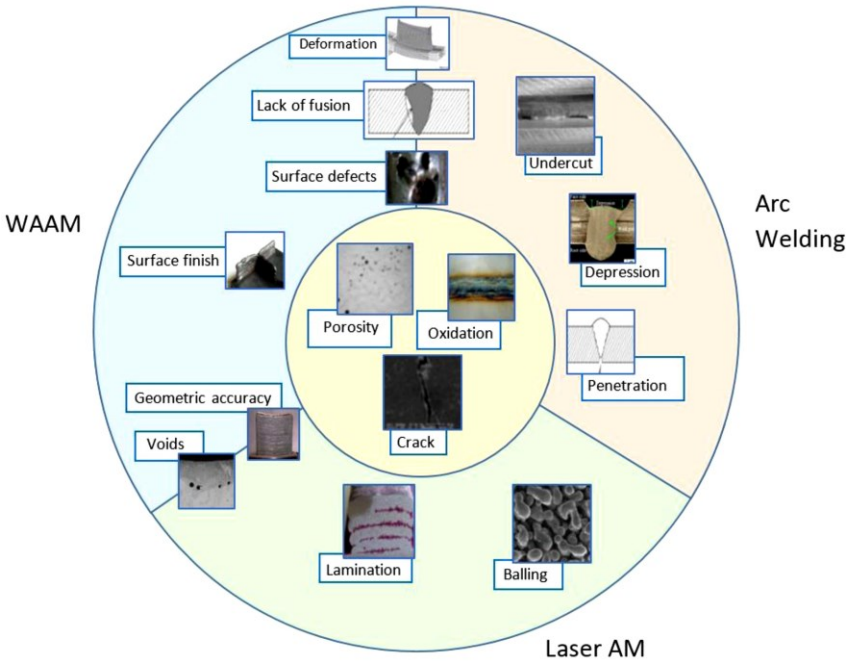

Figure 1.4 Different types of defects in WAAM, Laser AM, and Arc welding [16].

Such a high susceptibility of the fabricated parts to manufacturing defects highlights the importance of establishing quality assurance procedures to guarantee the reliability of the additively manufactured components. Different qualification procedures have been suggested to control the quality of both the AM fabrication process and the printed components, including (1) accurate logging and investigation of AM process parameters using fast Fourier transform data analysis techniques, and/or (2) in situ monitoring of individual deposited layers through thermal and optical imaging [32][33]. Additionally, simulation and modeling of various aspects of metal AM, i.e., in-situ process control and ex-situ process simulation, have been developed and could potentially be adopted by manufacturers to envisage any possibility of discontinuity formation. The presence of defects in a component can lead to the premature failure or a drastic reduction in the ductility/toughness of the part. Furthermore, solidification-induced defects could potentially contribute to anisotropic mechanical properties along the deposition and building directions of an AM part, ascribed to the higher density of interpass regions in the vertical direction, containing heat-affected zones and possibly a higher density of discontinuities in the melt pool boundaries. Such anisotropy in the microstructure and mechanical properties can be diminished or even eliminated by either optimizing the process parameters or adopting appropriate postfabrication heat treatment processes. In a recent study, Xu *et al.* [34] reported that the microstructural heterogeneity and anisotropic mechanical properties in a WAAM-fabricated maraging steel component could be minimized by applying a solutionizing heat treatment followed by aging, which eliminated the microstructural inhomogeneity from the bottom to top of the component. Therefore, comprehensive investigation of the formation of discontinuities and microstructural defects in WAAM-fabricated components and implementation of post fabrication processes, such as heat treatment or hot isostatic pressing (HIP) cycles, to alleviate these defects by transforming the microstructures to those fit for service conditions, are extremely crucial.

The sequential heating and cooling cycles experienced by the material normally affects the microstructure and consequently in-service performance of the fabricated parts [35]. For example, the heat generated during the deposition of each track may reheat the

previous layers and adversely affect the microstructure by potential solid-state phase transformations [5]. As a result of that, in most cases, additively manufactured parts are characterized by a heterogeneous and location-dependant microstructure [5]. These microstructural transitions could be observed from the melt pool centers to melt pool boundaries and heat affected zones (HAZs) [36], or it may happen in a larger scale resulting in different microstructural characteristics from bottom to middle or top sections of the component due to heat buildup during part construction resulting in different cooling rates along the building direction [2]. The thermal history at each point of the part includes the maximum experienced temperature, the soaking time at the maximum temperature, number of reheating cycle and the subsequent cooling rate, which may vary at different points of the component, leading to a final product with a non-uniform microstructure [5]. Ge *et al.* [35] reported variations in the cooling rate at different locations of a WAAM-fabricated 2Cr13 MSS. They recorded 7–11 times faster cooling at the bottom regions of the part as compared to the top areas, which affected the relative volume fraction of martensite and ferrite along the building direction [35]. In addition, the significant directional heat dissipation from the substrate usually leads to a directional solidification from bottom to top of the part resulting in a textured structure along the building direction [37]. For example, ferrous alloys are highly prone to the formation of a strong fibre texture in <001> direction aligned with the building direction [38,39], attributed to the fact that <001> is the preferential growth orientation in cubic metals [40]. Moreover, additively manufactured parts are typically exposed to higher cooling rates as compared to other manufacturing processes resulting a rapid solidification and consequently formation of non-equilibrium phases inducing residual stress, which may lead to cracking during the deposition process or after part construction [41]. The formation of undesirable δ-ferrite as a non-equilibrium phase at room temperature was frequently reported in WAAM-fabricated martensitic stainless steel (MSS) as a result of rapid solidification [42,43] [44,45]. It has been reported that the presence of δ-ferrite in the microstructure of MSS parts deteriorates both corrosion and mechanical properties of the alloy [46][47][48].

From a metallurgical point of view, these kinds of microstructural inhomogeneities could potentially result in anisotropic mechanical properties [37,49,50]. For instance, Wang *et al.* [21] reported anisotropic ductility in the transverse and longitudinal directions in an additively manufactured 304L stainless steel due to the formation of columnar δ-ferrite dendrites grown preferentially along the building direction. Anisotropic mechanical properties were also observed in a WAAM-fabricated Ti-6Al-4V part due to a strong crystallographic texture developed as a result of directional columnar growth of primary β grains along the building direction [22].

Over and above that, some feedstock alloys are not intended to be used in the as-solidified condition as they might require post-process heat treatment to deliver the desired microstructure. In particular, age-hardenable alloys are relatively soft in the as-printed state due to the rapid solidification and subsequent fast cooling, which hinders the formation of precipitates [51]. For example, AM-fabricated precipitation hardening stainless steels need to be solution treated followed by aging process to form precipitates as a reinforcement agent in the matrix in order to improve the mechanical properties of the component [52].

In conclusion, majority of additively manufactured parts are highly prone to varieties of microstructural defects and heterogeneities, which need to be modified through appropriate post-printing heat treatments prior to implementation in their intended service condition.

1.4 Post-Printing Heat Treatment of Additively Manufactured Parts

Post-printing heat treatment is generally applied to additively manufactured parts to homogenize the microstructure, decrease the residual stress, minimize the anisotropic properties, improve the mechanical properties, and even enhance the corrosion performance of the material [53][14]. In some cases, traditional heat treatment recipes of the conventionally fabricated materials are applicable for additively manufactured parts [54], while the intended times and temperatures might vary due to potential differences

between the initial microstructure of the 3D-printed and conventionally fabricated parts [55]. For example, it has been reported that secondary hardening occurs at higher tempering temperature in AM-fabricated H13 tool steel as compared to the conventionally fabricated alloy due to the difference in the content of retained austenite in their initial microstructures [56].

Selection of a proper heat treatment could significantly boost the in-service performance of the part, while employing an incorrect cycle could potentially result in extra residual stress, high probability of crack formation/propagation, and possibly catastrophic failures [14]. Hadadzadeh *et al.* [57] studied the effect of post-printing heat treatment on an AM-fabricated Fe–Cr–Ni–Al maraging stainless steel and reported that conventional austenitization-aging treatment detrimentally influenced the strength of material due to martensite laths coarsening and hindrance of precipitate formation during subsequent aging. However, they concluded that direct aging of the as-built material (skipping the conventional austenitization) led to strength improvement due to martensite lath size refinement in addition to precipitation of nanometric and coherent β-NiAl spherical phases [57]. Saeidi *et al.* [58] also reported that selection of an extremely high annealing temperatures (above 1150 °C) results in partial formation of δ-ferrite needles, which causes a reduction in the strength of the additively manufactured 316L austenite stainless steel.

On the other hand, beneficial effects of post-printing heat treatment on the additively manufactured parts were also frequently reported by different researchers in the literature. For example, Wang *et al.* [59] reported the elimination of anisotropic mechanical properties in a WAAM-fabricated H13 steel as a result of annealing heat treatment for 4 h at 830 °C due to obtaining a homogeneous microstructure in the heat-treated condition. Li *et al.* [60] investigated the post-printing heat treatment optimization of WAAM-fabricated Grade 91 steel and showed that the as-printed part is much more brittle than the wrought counterpart due to a heterogeneous microstructure consisting of segregated MX precipitates, high density of dislocations, and ultra-fine martensite laths along with residual δ-ferrite. However, post-printing homogenizing and aging treatment resulted in

an excellent combination of strength and ductility due to dissolution of pre-existing MX phases in the matrix, which facilitates the formation of dispersive $M_{23}C_6$ and MX phases in the matrix [60].

1.5 Additive Manufacturing of Ferrous Alloys

Ferrous alloys are known as the most common engineering materials with a wide range of applications in different industries due to their excellent characteristics such as great combination of mechanical properties (strength, hardness, toughness, ductility, and wear resistance), decent corrosion resistance specially in the case of stainless steels, and more importantly their lower price compared to most of other engineering materials [53][61][62]. Interestingly, ferrous alloys are incredibly versatile as their properties can be tailored due to their wide range of achievable microstructural features and phases (ferrite, pearlite, bainite, martensite, etc.) with distinct properties [53]. For example, high-strength low-alloy steels are called when a material is needed to be employed under mechanical loading in a non-corrosive environment. However, stainless steels (ferritic, austenitic, martensitic) are the best choice when a part is intended to be in contact with a corrosive environment at moderate temperature [53]. On the other hand, precipitation-hardened stainless steels are employed when a part is required to serve in a harsh corrosive media under severe mechanical stresses [63]. Tool steels also provide an excellent combination of wear resistance, hardness, and yield strength required for specific applications such as tool and die making industry [53].

Another important feature of ferrous alloys which make them a good candidate for AM technology is their great fusion weldability since during the AM process the feedstock material undergoes sequential melting and solidification, which is very similar to multi-pass welding [62]. Wire arc additive manufacturing of ferrous alloys has increasingly drawn attention of different research institutions, and various aspects of WAAM-fabricated ferrous alloys such as process parameters, residual stress and distortion, correlation between microstructure and mechanical properties, corrosion properties, etc. For example, Liberini *et al.* [2] studied the microstructural features of thin wall components fabricated by wire arc additive manufacturing using a low-carbon low-alloy

steel (ER70S) feedstock material. They reported microstructural variations along the building direction characterized by a ferritic-pearlitic microstructure at the bottom zone, equiaxed ferrite grains at the middle, and a bainitic structure at the top regions of the component [2]. They correlated the observed heterogeneities to the different thermal history experienced by different regions of the wall during the fabrication process [2]. Although mechanical testing in their work was limited to microhardness measurements, it is so important to the evaluate the potential anisotropic performance when dealing with inhomogeneous microstructure specially in additively manufactured components that are naturally prone to have orientation-dependant properties [35].

One of the most common microstructural imperfections in additively manufactured stainless steels is the formation of a higher content of δ-ferrite as compared to conventionally fabricated counterparts [64]. For instance, in the case of 17-4 PH stainless steel with a Cr_{eq}/Ni_{eq}>1.55 and a ferrite solidification mode, the phase transformation sequence under equilibrium cooling is as follows: Liquid → δ-ferrite → γ-austenite + δ-ferrite → martensite + δ-ferrite [65]. However, the diffusional transformation of δ-ferrite → γ-austenite is decelerated during AM due to high cooling rate associated with nature of the process [64]. Therefore, the content of δ-ferrite in AM-fabricated 17-4 PH stainless steel is much higher than that of the conventionally fabricated counterpart [64]. It has been reported that the presence of δ-ferrite in the microstructure of stainless steel parts deteriorates both corrosion and mechanical properties of the alloy [46][47][48]. As an example, Tarasov *et al.* [66] studied the stability of the oxide passivation layer formed on the surface of an AM-fabricated AISI 304 SS. It was indicated that the heat input as the most important process parameter affects the δ-ferrite content in the as-printed condition [66]. Their investigations revealed that corrosion resistance of the material highly depends on the volume fraction of Cr-enriched δ-ferrite as the maximum corrosion mass loss coincided with the sample containing of the highest content of δ-ferrite [66]. They reported that the local corrosion attack occurred in the austenite phases at austenite/ferrite boundaries, which were depleted in chromium [66].

Although successful AM-fabrication of different ferrous alloys have been reported in the literature [62], it has been frequently declared that microstructural characteristics, corrosion performance and mechanical properties of the WAAM-fabricated ferrous alloys are different from the conventionally fabricated parts [53][62]. Therefore, there is still an essential need to further investigate different aspects of the process and also the effect of post-printing heat treatment on the microstructure and properties of the additively manufactured parts [62]. Accordingly, in this research, three different ferrous alloys, including a low-carbon low-alloy steel (ER70S), a martensitic stainless steel (ER420), and a precipitation hardening martensitic stainless steel (PH 13-8Mo) were selected as the feedstock material for wire arc additive manufacturing. Following the fabrication process, the effect of post-printing heat treatment on different aspects of the additively manufactured parts were comprehensively studied. In particular, in the first phase of the research, the effect of quenching media after austenitizing was investigated on the microstructure and anisotropic mechanical properties of the WAAM ER70S thin-wall component. In the second phase, the effect of tempering process on the microstructure and secondary hardening was investigated in the WAAM 420 martensitic stainless steel part. In the third phase of the research, effect of post-printing solution and aging treatment on the secondary phase formation and the resultant corrosion performance of an additively manufactured precipitation hardening martensitic stainless steel (WAAM PH 13-8Mo) were investigated.

1.6 Organization of The Thesis

This thesis is prepared in a paper-based format in three main phases. Overall, as a result of the research activities during this Ph.D. program, 16 articles were published in/submitted to peer-reviewed journals (six articles as the first author, and 10 articles as the co-author). Moreover, the thesis's outcomes were presented in different conferences (two papers as the first author and three papers as the co-author).

The papers written as the first author are included in three main chapters (two papers in each chapter), and the co-authored articles are also listed for further information.

List of publications:

Journal Papers:

1) **Alireza Vahedi Nemani,** Mahya Ghaffari, Ali Nasiri. "Comparison of Microstructural Characteristics and Mechanical Properties of Shipbuilding Steel Plates Fabricated by Conventional Rolling versus Wire Arc Additive Manufacturing.", *Journal of Additive Manufacturing* **(IF= 10.998)**, Volume 32, Page 101086, (2020).

2) **Alireza Vahedi Nemani,** Mahya Ghaffari, Ali Nasiri. "On the Post-printing Heat Treatment of a Wire Arc Additively Manufactured ER70S Part.", *Journal of Materials* **(IF= 3.623)**, Volume 13, Page 2795, (2020).

3) **Alireza Vahedi Nemani,** Mahya Ghaffari, Salar Salahi, and Ali Nasiri. "Effects of post-printing heat treatment on the microstructure and mechanical properties of a wire arc additive manufactured 420 martensitic stainless steel part." *Journal of Materials Science and Engineering: A* **(IF= 5.234)**, Volume 813, Page 141167, (2021).

4) **Alireza Vahedi Nemani,** Mahya Ghaffari, Salar Salahi, Jonas Lunde, and Ali Nasiri. "Effect of interpass temperature on the formation of retained austenite in a wire arc additive manufactured ER420 martensitic stainless steel." *Journal of Materials Chemistry and Physics* **(IF= 4.094)**, Volume 266, Page 124555, (2021).

5) **Alireza Vahedi Nemani,** Mahya Ghaffari, Salar Salahi, and Ali Nasiri. "On the microstructural characteristics and corrosion performance of as-printed and heat-treated PH 13-8Mo martensitic stainless steel fabricated by wire arc additive manufacturing." Submitted to the *Journal of Electrochimica Acta* **(IF= 6.901)**.

6) **Alireza Vahedi Nemani,** Mahya Ghaffari, Salar Salahi, and Ali Nasiri. "On the nucleation site and formation sequence of secondary phases during isothermal high-temperature aging of wire arc additively manufactured PH13-8Mo stainless steel." Submitted to the *Journal of Vacuum* **(IF= 3.627)**.

7) Mahya Ghaffari, **Alireza Vahedi Nemani,** Mehran Rafieazad, Ali Nasiri. "Effect of solidification defects and HAZ softening on the anisotropic mechanical properties of a wire arc additive-manufactured low-carbon low-alloy steel part.", *Journal of the Minerals, Metals & Materials Society (JOM)* **(IF= 2.989)**, Volume 71, Pages 4215–4224, (2019).

8) Mehran Rafieazad, Mahya Ghaffari, **Alireza Vahedi Nemani,** Ali Nasiri. "Microstructural evolution and mechanical properties of a low-carbon low-alloy steel produced by wire arc additive manufacturing.", *The International Journal of Advanced Manufacturing Technology* **(IF= 3.320)**, Volume 105, Pages 2121–2134, (2019).

9) Mehran Rafieazad, **Alireza Vahedi Nemani,** Mahya Ghaffari, Ali Nasiri. "On Microstructure and Mechanical Properties of a Low-Carbon Low-Alloy Steel Block Fabricated by Wire Arc Additive Manufacturing.", *Journal of Materials Engineering and Performance* **(IF= 1.895)**, Volume 30, Pages 4937–4945, (2021).

10) Mahya Ghaffari, **Alireza Vahedi Nemani,** Ali Nasiri. "Interfacial bonding between a wire arc additive manufactured 420 martensitic stainless steel part and its wrought base plate.", *Journal of Materials Chemistry and Physics* **(IF= 4.094)**, Volume 251, Page 123199, (2020).

11) Salar Salahi, Mahya Ghaffari, **Alireza Vahedi Nemani,** and Ali Nasiri. "Effects of Secondary-Phase Formation on the Electrochemical Performance of a Wire Arc Additive Manufactured 420 Martensitic Stainless Steel under Different Heat Treatment Conditions." *Journal of Materials Engineering and Performance* **(IF= 1.895)**, Volume 30, Pages 6618–6629, (2021).

12) Salar Salahi, **Alireza Vahedi Nemani,** Mahya Ghaffari, Jonas Lunde, and Ali Nasiri. "On microstructure, crystallographic orientation, and corrosion properties of wire arc additive manufactured 420 martensitic stainless steel: Effect of the inter-layer temperature." *Journal of Additive Manufacturing* **(IF= 10.998)**, Volume 46, Page 102157, (2021).

13) Salar Salahi, **Alireza Vahedi Nemani,** Mahya Ghaffari, and Ali Nasiri. "Microstructural evolution, Crystallographic Orientation, and Electrochemical Performance of the Interfacial Region between a Wrought and a Wire Arc Additive Manufactured 420 Martensitic Stainless Steel." Submitted to the *Journal of Materials Characterization* **(IF= 4.342)**.

14) Mahya Ghaffari, **Alireza Vahedi Nemani,** Ali Nasiri. "Microstructure and mechanical behavior of PH 13–8Mo martensitic stainless steel fabricated by wire arc additive manufacturing.", *Journal of Additive Manufacturing* **(IF= 10.998)**, Volume 49, Page 102374, (2022).

15) Mahya Ghaffari, **Alireza Vahedi Nemani,** Ali Nasiri. "Effects of post-printing heat treatment on the microstructure and mechanical properties PH 13-8Mo Martensitic Stainless Steel Fabricated by Wire Arc Additive Manufacturing.", Submitted to the *Journal of Materials Science and Engineering: A* **(IF= 5.234)**.

16) Salar Salahi, **Alireza Vahedi Nemani,** Mahya Ghaffari, and Ali Nasiri. "Electrochemical Performance of the Interfacial Region between an AISI 420 and a Wire Arc Additive Manufactured PH 13–8Mo Martensitic Stainless Steel." Submitted to the *Journal of Additive Manufacturing* **(IF= 10.998)**.

Conference Papers:

1) **Alireza Vahedi Nemani,** Mahya Ghaffari, Mehran Rafieazad, Ali Nasiri. "Post-Printing Heat Treatment of a Wire Arc Additively Manufactured Low Carbon Low Alloy Steel.", *CSME conference, London,* June 2019.

2) **Alireza Vahedi Nemani,** Mahya Ghaffari, Mehran Rafieazad, Ali Nasiri. "On the Hardening and Subsequent Tempering of a Wire Arc Additively Manufactured 420 martensitic stainless steel.", *60th Conference of Metallurgists, Halifax*, August 2021.

3) Mahya Ghaffari, **Alireza Vahedi Nemani,** Mehran Rafieazad, Ali Nasiri. "Anisotropy in Mechanical Properties of a Wire Arc Additive Manufactured Low Carbon Low Alloy Steel.", *CSME conference*, *London,* June 2019.

4) Mahya Ghaffari, **Alireza Vahedi Nemani,** Mehran Rafieazad, Ali Nasiri. "Effect of Columnar Grain Growth and Inhomogeneous Microstructure on the Anisotropic Mechanical Properties of a Wire Arc Additive Manufactured PH 13-8Mo Martensitic Stainless Steel.", *60th Conference of Metallurgists, Halifax*, August 2021.

5) Salar Salahi, **Alireza Vahedi Nemani,** Mahya Ghaffari, and Ali Nasiri. "Microstructural Evolution and Electrochemical Performance of the Interfacial Region between a Wrought and a Wire Arc Additive Manufactured 420 Martensitic Stainless Steel." *60th Conference of Metallurgists, Halifax*, August 2021.

CHAPTER 2 Effect of Post-printing Heat Treatment on the Microstructure and Anisotropic Mechanical Properties of Low-carbon Low-alloys Steel (ER70S) Fabricated by Wire Arc Additive Manufacturing

2.1 Comparison of Microstructural Characteristics and Mechanical Properties of Shipbuilding Steel Plates Fabricated by Conventional Rolling versus Wire Arc Additive Manufacturing

Alireza Vahedi Nemani[1], Mahya Ghaffari[1], Ali Nasiri[2]

1- Graduate Student, Dalhousie University, Halifax, Nova Scotia, Canada

2- Assistant Professor, Dalhousie University, Halifax, Nova Scotia, Canada

Status: Published Journal Paper, Journal of Additive Manufacturing (IF= 10.998), Volume 32, Pages 101086

Authors' Contribution

Alireza Vahedi Nemani: Conceptualization, Investigation, Writing - original draft, Visualization.

Mahya Ghaffari: Methodology, Fabrication Process, Validation, Investigation, Review & Editing.

Ali Nasiri: Supervision, Writing - review & editing, Funding acquisition.

2.1.1. Abstract

This study aims to investigate the fabrication feasibility of a conventionally rolled low-carbon low-alloy shipbuilding steel plate (EH36) by emerging wire arc additive manufacturing (WAAM) technology using ER70S feedstock wire. Following the fabrication process, different heat treatment cycles, including air-cooling and water-quenching from the intercritical austenitizing temperature of 800 °C, were applied to both conventionally rolled and WAAM samples. Microstructural features and mechanical properties of both rolled and WAAM fabricated ship plates were comprehensively characterized and compared before and after different heat treatment cycles. Both air-cooling and water-quenching heat treatments resulted in the formation of hard martensite-austenite (MA) constituents in the microstructure of the rolled ship plate, leading to the increased hardness and tensile strength and reduced ductility of the component. On the

other hand, air-cooling heat treatment was found to homogenize the microstructure of the WAAM ship plate, causing a slight decrease in the hardness and tensile strength, while the water-quenching cycle led to the formation of acicular ferrite and intergranular pearlite, contributing to the improved mechanical properties of the part. Therefore, the enhanced mechanical integrity of the water-quenched WAAM component as compared to its rolled counterpart verified the fabrication feasibility of the ship plates by the WAAM.

2.1.2. INTRODUCTION

ASTM A131 EH36 alloy is a low-carbon low-alloy steel characterized by a great combination of strength and ductility, high toughness, and excellent weldability, suitable for structural applications, and widely used in the marine and shipbuilding industry [67]. Some applications of this grade of steel include cabin structures, ship hull components, and some structural parts, such as bow plates of ships and cruisers [68]. EH36 ship plates are commonly manufactured through the conventional hot rolling process or thermo-mechanical control rolling (TMCP) with an accelerated cooling process [69]. The conventional hot rolling technique yields a relatively coarse banded microstructure [70], which reduces the strength and ductility of the component due to the entrapment of hydrogen at the band interfaces [69]. On the other hand, the equiaxed grain structure of TMCP-EH36 steel leads to the improved mechanical and corrosion properties of the component [71]. Such rolling processes are mostly suited for the fabrication of simple geometry parts, such as ship hulls, but incapable of fabricating more complex geometries, such as bow structures in a one-step manufacturing process.

Newly developed additive manufacturing (AM) techniques, also known as 3D-printing, are able to fabricate complex geometry components at a relatively high deposition rate, the lowest possible number of production cycles, minimum materials waste and energy expenditures in contrast with the conventional subtractive fabrication techniques [14,26,72–74]. By drastic reduction in the fabrication time and production steps, minimizing the on-hold inventory, reducing the number of distinct parts needed for an assembly, and almost no design boundary, additive manufacturing technologies have the potential to revolutionize the industrial manufacturing sectors [14,75].

Wire arc additive manufacturing (WAAM) is a large-scale metal AM technology utilizing an arc welding torch as a heat source and a consumable wire as the feedstock material to fabricate a near-net-shape component layer by layer additively [14]. In this manufacturing method, typically, the welding torch is mounted on a robotic arm connected to a computer controller capable of producing low to medium complexity and medium to large scale metallic parts [75,76]. In recent years, WAAM has been known as an evolving manufacturing method for several industrial materials, such as nickel, aluminum, steel, and titanium alloys [14]. Weldability is the most important factor controlling the fabrication feasibility of a material by WAAM since the process is based on depositing successive layers of weld beads on top of each other until the near-net-shape part is completely built. Therefore, the low-carbon low-alloy nature of the steel raw material used in shipbuilding not only facilitates the weldability of the alloy [70], but also ensures its fabrication feasibility using the wire arc additive manufacturing. Although 3D-printing of ship plates have previously been carried out successfully through powder-based additive manufacturing systems, such as selective laser melting (SLM) [77,78], WAAM of ship plates has never been reported in the literature. The main drawback of the powder-based additive manufacturing systems is the limited size of the 3D-printed parts due to the small size of the build envelop [76], and also the low deposition rate of the process (0.1-0.6 kg/h) [79]. Differently, in WAAM, not only the component size is independent of a confined build chamber, but also the entire feedstock material (consumable wire) is continuously fed into the electric arc, resulting in a considerably higher deposition rate (3-8 kg/h) as compared to the powder-based systems [6,74,79]. Consequently, adopting wire-based systems for manufacturing of large-scale shipbuilding plates with medium complexity in design are more operational.

Considering the recent developments in the shipbuilding industry, superior mechanical properties of ship structures are highly demanded to ensure a prolonged and reliable service life of the ship in harsh marine environments [80]. On the other hand, reducing the overall weight/thickness of the components without any compromise in the strength is a principal objective for all transportation industries for reducing fuel consumption and energy-saving purposes, and also reducing the environmental pollutants [81]. Therefore,

developing and implementing appropriate heat treatment cycles capable of modifying the microstructure of shipbuilding steels and consequently improving the mechanical properties, such as strength, ductility, and toughness of ship structures, are highly important and of great interest of the marine sector [82].

Heat treatment of low-alloy steels can be classified based on the austenitizing temperature into two main categories, *i.e.*, upper-critical (above Ac_3 line of Fe-Fe_3C binary phase diagram) and intercritical (between Ac_1 and Ac_3 lines) temperatures [83]. It has been reported that as a result of water-quenching from upper-critical temperature, the microstructure transforms to almost full martensite, leading to an increase in hardness, but a significant drop in ductility and toughness [83]. However, water-quenching from intercritical temperatures results in a dual-phase microstructure, including ferrite and martensite, which exhibits a better combination of strength and ductility [83,84]. Hayat *et al.* [81] studied the water-quenching heat treatment of Grade A (GA) ship plate steels from different austenitizing temperatures, *i.e.,* the upper-critical temperature of 900 °C and intercritical temperatures of 730 °C, 760 °C, and 800 °C. The results from Hayat's study [81] showed that although the water-quenching from upper-critical temperature (900 °C) considerably increased the hardness and strength, this heat treatment deteriorated the ductility of the component due to the formation of a fully martensitic microstructure. However, in dual-phase (DP) steels, the presence of 70-90% soft ferrite grains as the matrix provides a great ductility, while the hard martensite as the reinforcement improves the hardness and strength of the component [85–87].

This study is intended to investigate the fabrication feasibility of bow plates in the ship hull structure implementing the wire arc additive manufacturing technology using ER70S feedstock wire through in-depth microstructural and mechanical properties analyses. The results were compared with the properties of an as-received conventionally rolled EH36 shipbuilding steel plate. Furthermore, two different heat treatment cycles, including air-cooling and water-quenching from the intercritical austenitizing temperature of 800 °C were applied to both as-received and as-printed components in order to study the effect of

heat treatment on the microstructural features and the resultant mechanical properties of the parts.

2.1.3. EXPERIMENTAL PROCEDURE

2.1.3.1 Materials and Fabrication Process

In this study, two different materials, including as-received conventionally rolled and WAAM fabricated ship plates, were compared in terms of microstructural characteristics and mechanical properties. The raw material used for the rolled shipbuilding plate was EH36 steel, and the feedstock material utilized for WAAM was ER70S wire with 0.9 mm (0.035 inches) diameter. The chemical composition of the raw materials are listed in Table 2.1.1. It is notable that the ER70S is the commercial available wire with the closest chemical composition to its shipbuilding plate counterpart, which is also the most commonly used wire for welding of EH36 shipbuilding plates [88,89]. An S-350 Power Wave Lincoln Electric MIG welding machine equipped with an advanced surface tension transfer (STT) mode with processing parameters listed in Table 2.1.2 was employed as the heat source for wire arc additive manufacturing of the part. It has been reported that the advanced STT mode is capable of depositing high-quality beads at a low heat input and a minimum amount of spattering and lack of fusions [8,90]. To further reduce the heat accumulation during WAAM in the previously deposited layers, 10-min dwell time was implemented between deposition of consecutive layers, ensuring a less than 165 °C interpass temperature as recommended by AWS A28/A5 standard [91].

Table 2.1.1 The nominal chemical composition of the raw materials, including EH36 and ER70S (all data in wt. %).

Material	C	Mn	Si	Cr	Ni	Mo	S	Al	V	Nb	Cu	P	Fe
EH36	0.14	1.47	0.28	0.05	0.30	0.01	0.002	0.04	0.03	0.03	0.20	0.02	Bal.
ER70S	0.08	1.45	0.98	0.05	0.07	0.05	0.01	-	0.04	-	0.25	0.01	Bal.

Table 2.1.2 The WAAM processing parameters for fabrication of the ship plate using ER70S wire as the feedstock material.

Arc Current	Arc Voltage	Wire Feeding Rate	Scanning Rate	Argon Flow Rate
320 A	28 V	0.104 m/s	0.005 m/s	45 L/min

2.1.3.2 Heat treatment processes

Following the fabrication process, two types of heat treatment processes, including air-cooling and water-quenching, were conducted on both rolled and WAAM fabricated components to modify the microstructure and the resultant mechanical properties of the ship plates. Fig. 2.1.1a depicts a graphical illustration of different heat treatment cycles used in this study. Prior to performing the heat treatment cycles, all samples were annealed by heating up to 1000 °C (above Ac_3 line) for 30 min and then furnace-cooled to ensure providing a homogenous microstructure before applying the main heat treatment cycles. Following this annealing step, the samples were held at the intercritical austenitizing temperature of 800 °C (between Ac_1 and Ac_3) for 1 h, and then subjected to different cooling rates, *i.e.*, air cooling and water quenching.

It should be mentioned that the effect of alloying elements on the Ac_1 and Ac_3 lines can be calculated according to equations (2.1.1) and (2.1.2), suggested by Andrews [92].

$$Ac_1(°C) = 723 - 10.7Mn - 3.9Ni + 29Si + 16.7Cr + 290As + 6.38W. \quad (2.1.1)$$

$$Ac_3(°C) = 910 - 230(C)^{0.5} - 15.2Ni + 44.7Si + 104V + 31.5Mo + 13.1W. \quad (2.1.2)$$

Using equations (2.1.1) and (2.1.2) and also the chemical composition of the alloys (Table 2.1.1), Ac_1 and Ac_3 lines were determined to be 715 °C and 835 °C for EH36 steel, and 736 °C and 893 °C for ER70S alloy, respectively. Accordingly, the austenitizing temperature was selected at 800 °C, which falls between Ac_1 and Ac_3 lines for both rolled (EH36) and WAAM manufactured (ER70S) ship plates.

2.1.3.3 Microstructural Characterizations

Metallographic samples were prepared from the rolled, as-printed, and heat treated samples using a Tegramin-30 Struers auto-grinder/polisher with a final polishing of 0.25 μm using Colloidal Silica suspension, followed by 15 s etching using 5% Nital reagent. The microstructural features were characterized by a Nikon Eclipse 50i optical microscope and an FEI MLA 650F field emission scanning electron microscope equipped with an energy dispersive spectroscopy (EDS) detector. The volume fractions of the microstructural phases were calculated through image analysis of at least five different spots using the ImageJ software. In addition, Nordlys II HKL electron backscatter diffraction (EBSD) analysis was employed to further investigate the texture, the grains size distribution, grains shape aspect ratio, and the grains misorientation angle distribution in both as-received rolled and as-printed ship plates. The EBSD analysis was performed with a tilt angle of 70° and a step size of 1.4 μm. The HKL Inc. software (Channel 5) was also used to perform post-processing analysis on the collected EBSD raw data. A Rigaku Ultimate IV X-ray diffraction (XRD) device equipped with Cu-K_α source at 44 mA and 40 kV with a step size of 0.02° covering a diffraction angle range of 40°-85° (2θ) was employed for phase detection and further characterization. Moreover, MDI JADE 2010 software and ICDD databases were used to quantify the volume fraction of different phases based on the method of Whole Pattern Fitting (WPF).

2.1.3.4 Mechanical Properties Measurements

Vickers microhardness was measured at least ten times on different locations of each sample utilizing a Buehler Micromet hardness test machine with a load of 300 g and a dwell-time of 45 s. The uniaxial tensile testing was also conducted using a 5585H Instron load frame with a maximum load capacity of 250 kN and a strain rate of 8 mm/min. In order to prepare the tensile samples, the as-build wall was initially milled to remove 1.2 mm from each side of the part and eliminate the as-printed surface roughness, providing a flat surface suitable for the subsequent cutting process. The tensile test samples were then prepared by water jet cutting machine with a total length of 100 mm, a gauge length of 25 mm, and a thickness of 5 mm as recommended by ASTM E8m-04 [93]. In order to study possible existing anisotropy in mechanical properties, the tensile testing was performed

along the deposition and building directions in the WAAM part (see Fig. 2.1.1b), and also the rolling and transverse directions in the rolled sample. To avoid considering outliers and achieve meaningful average values, at least five samples were subjected to uniaxial tensile testing for each tested direction.

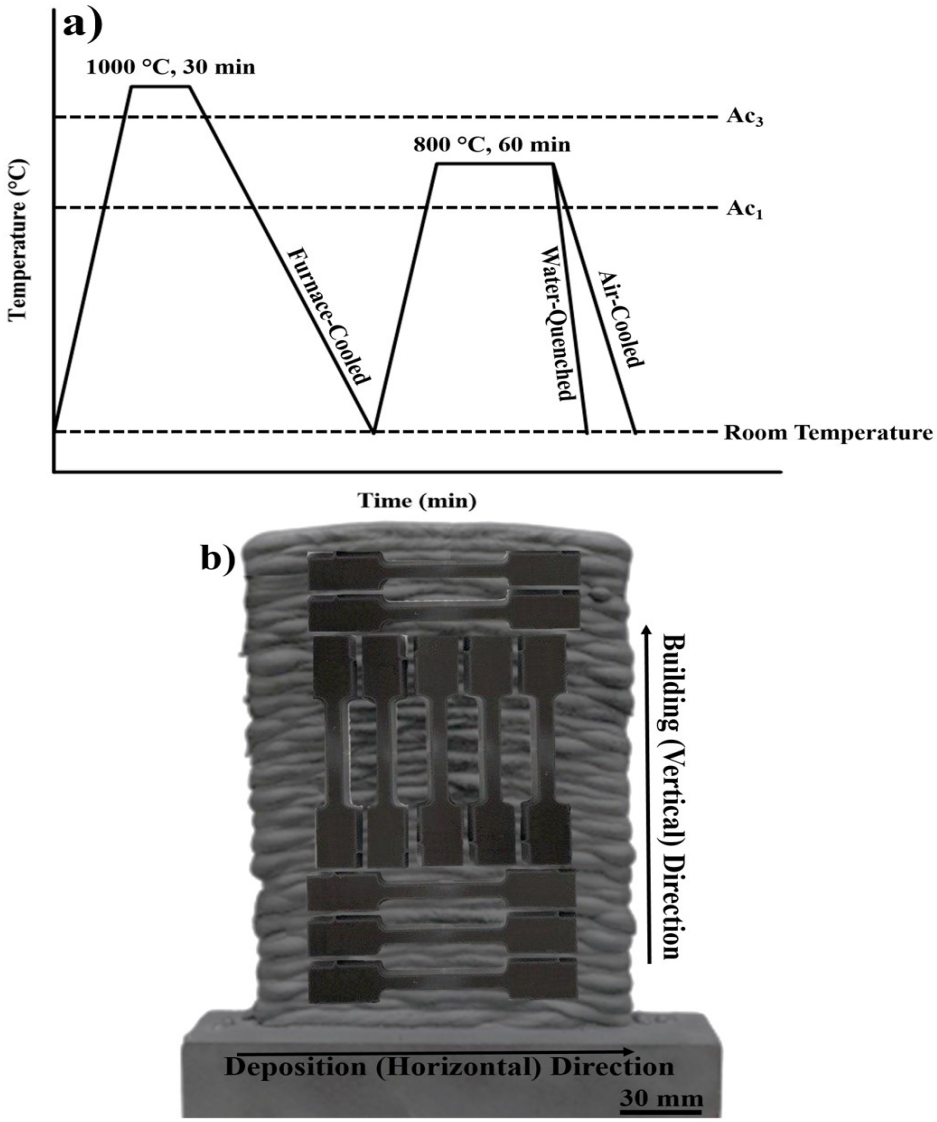

Figure 2.1.1 (a) The adopted heat treatment cycles in this study, including initial annealing, intercritical reheating, followed by different cooling cycles, (b) the WAAM fabricated part indicating the locations of tensile samples.

2.1.4. RESULTS

2.1.4.1 Microstructural Characterizations

2.1.4.1.1 As-received rolled and WAAM fabricated shipbuilding plates

Fig. 2.1.2a shows a three-dimensional optical microscopy image of the as-received rolled ship plate (EH36) containing a banded microstructure with an interval of ~ 40 μm, which is elongated along the rolling direction. According to the SEM micrographs shown in Fig. 2.1.2b and c, the microstructure of the as-received ship plate consists of ferrite grains (F) beside pearlite regions (P) with a fine lamellar morphology. On the other hand, as shown by the schematic illustration and the low magnification optical microscope image in Fig. 2.1.3a, the microstructure of the WAAM fabricated ship plate (ER70S) contains three distinguishable regions in each deposited layer, including melt pool center, melt pool boundary, and heat affected zone (HAZ). This pattern is repeated throughout the building direction of the component with ~ 3 mm interval, which is the thickness of each deposited layer. As depicted in Fig. 2.1.3b, the melt pool center comprises of polygonal ferrite (PF) along with a small volume fraction of intergranular lamellar pearlite, whereas the melt pool boundaries (Fig. 2.1.3c) include a mixture of acicular ferrite (AF), bainite (B), and martensite-austenite (MA) phases.

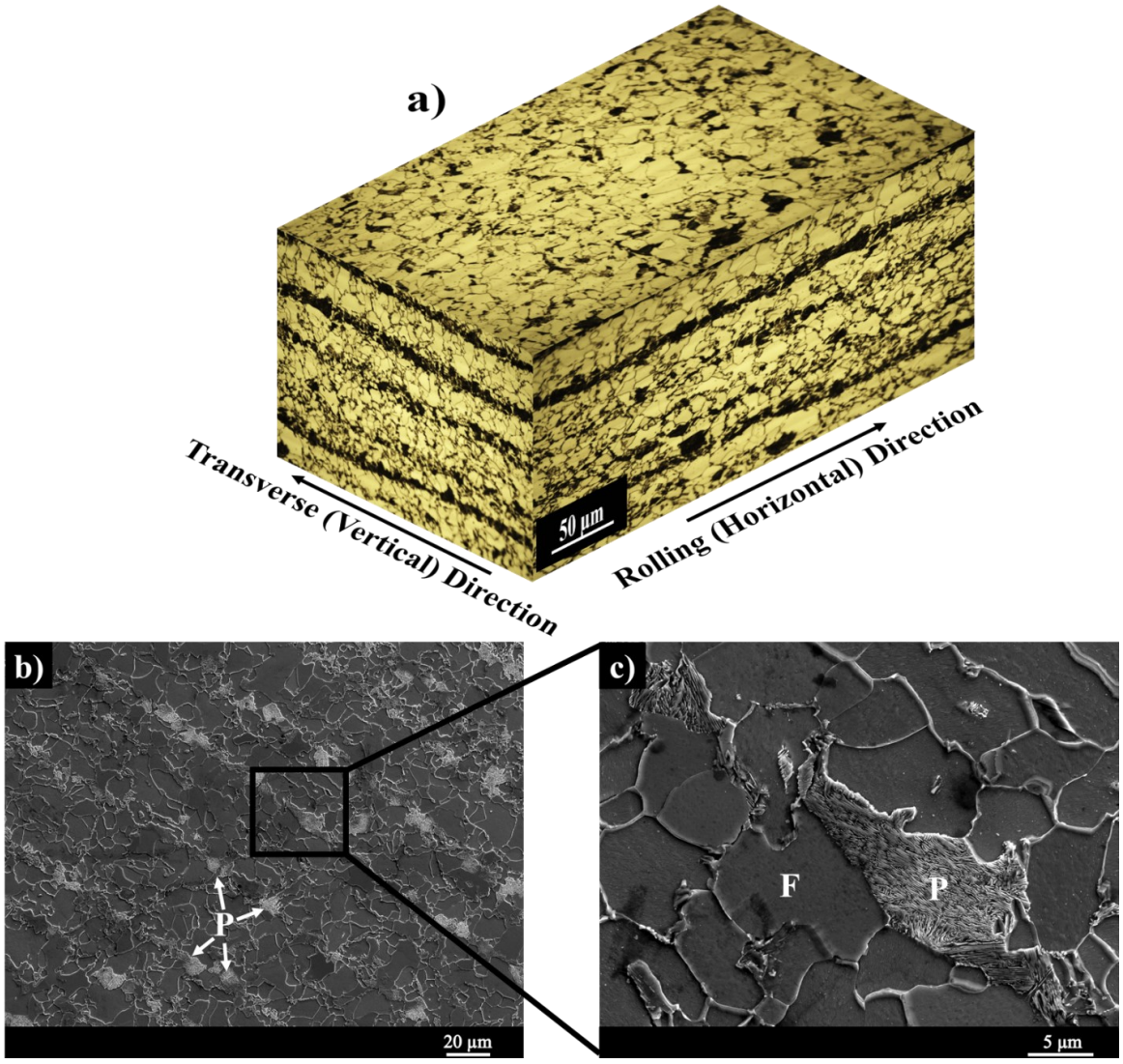

Figure 2.1.2 (a) Three-dimensional optical micrograph of the as-received conventionally rolled EH36 shipbuilding steel, (b) SEM micrograph from the side view of the rolled ship plate, and (c) higher magnification of the enclosed area in (b).

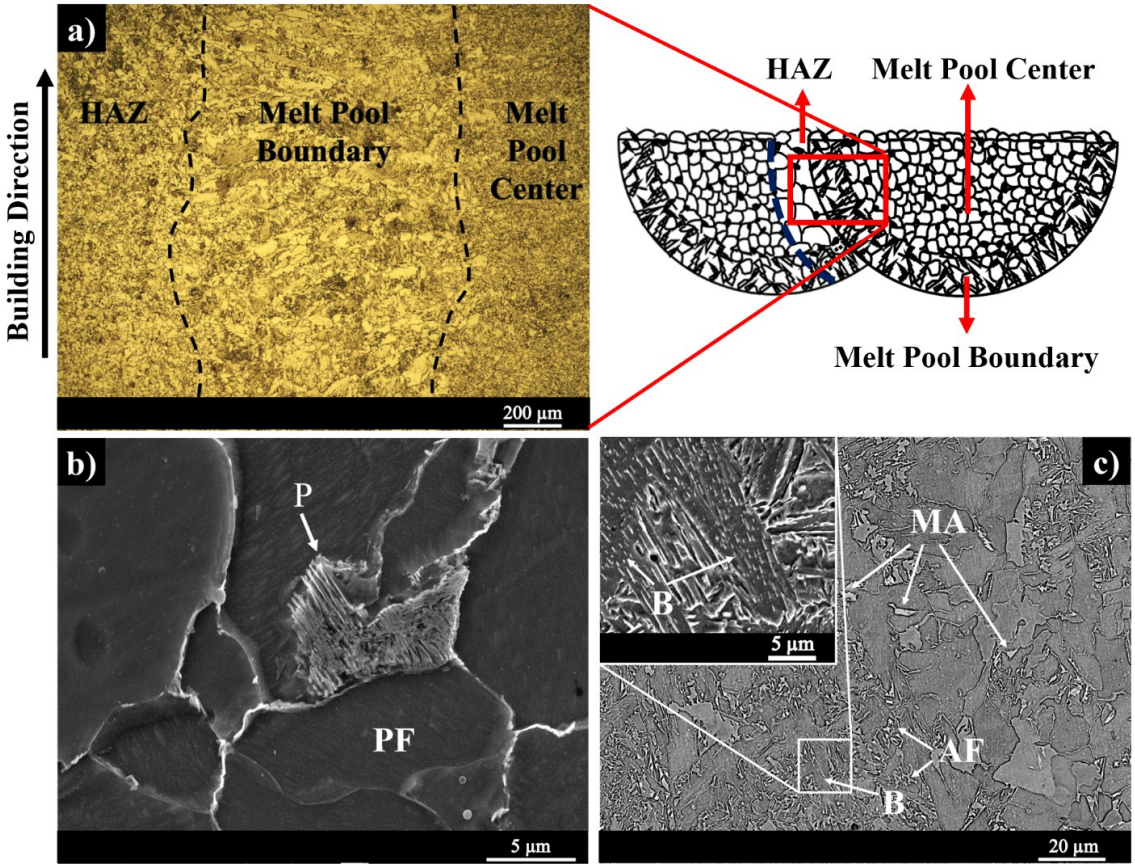

Figure 2.1.3 (a) Schematic illustration of two successive deposited layers along with a low magnification optical micrograph of the WAAM fabricated ship plate (ER70S) containing three distinguishable regions including melt pool center, melt pool boundary, and HAZ, (b) high magnification SEM micrograph of the melt pool center, and (c) the melt pool boundary.

To compare the volume fraction of the pearlite phase in the conventionally rolled (EH36) and additively manufactured (ER70S) ship plates, a comprehensive microstructural image analysis from several spots of both samples were carried out using the ImageJ software (a representative of each sample is shown in Fig. 2.1.4). The pearlite volume fractions were measured to be 20.32 ± 0.81% and 12.54 ± 0.56% of the total microstructure (highlighted by the red color in Fig. 2.1.4) for the conventionally rolled and the melt pool center of the WAAM fabricated ship plates, respectively. Overall, the microstructural analysis of the as-received and as-printed ship plates revealed that both samples contained an inhomogeneous microstructure, which can potentially be modified by applying appropriate heat treatment cycles.

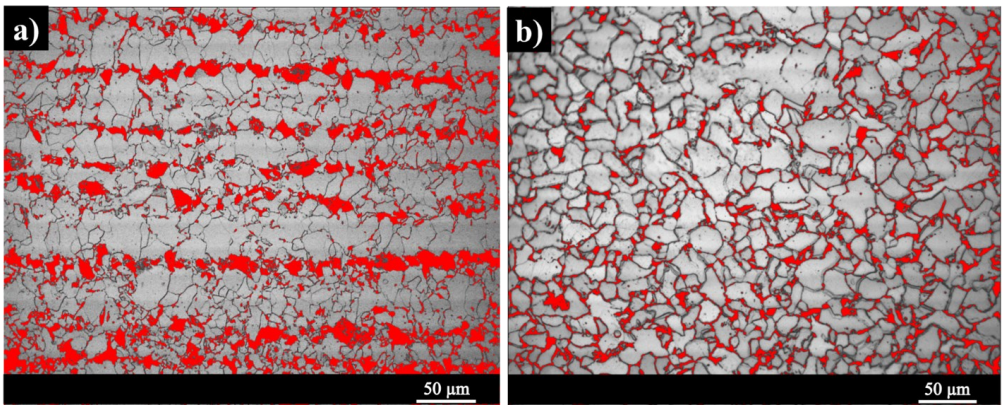

Figure 2.1.4 Phase fraction analysis of the (a) as-received rolled and (b) WAAM fabricated ship plates showing the pearlite phase in red and the ferrite grains in gray.

Fig. 2.1.5 demonstrates the inverse pole figure (IPF) maps of the as-received rolled steel and the as-printed ship plate covering the transition from the melt pool center to the heat affected zone in addition to the statistical graphs obtained from the EBSD raw data. According to the bar charts of the grains size distribution (Fig. 2.1.5c), the average grain size of the as-printed sample was found to be 7.30 ± 5.51 µm, confirming the presence of a bimodal grain size distribution as evidenced by the relatively high standard deviation of the grain size. To be precise, 45% of the grains were finer than 5 µm, 21% of the grains had a dimension between 5 µm and 10 µm, while 34% of the grains reached a range of 10 µm to 40 µm. The small grains (less than 5 µm) can be attributed to the fine grain structure in the melt pool center, while the large grains (10-40 µm) can be associated with the coarse HAZ, and the grains with a dimension between 5 µm and 10 µm are related to the transition zone from the melt pool center to the HAZ. The grain coarsening in HAZ can also be clearly observed on the IPF map of the as-printed sample (Fig. 2.1.5b). Considering the impact of the grain size on the mechanical properties of the material according to the Hall-Petch equation [94], the grain size variations through the building (vertical) direction, where a higher density of interpass regions and HAZs has formed, can potentially deteriorate the mechanical properties of the as-printed ship plate in the building direction. On the other hand, in the as-received rolled ship plate, 91% of the grains were finer than 5 µm, confirming a fine and uniform grain size structure with an average size of 1.95 ± 0.23 µm. According to the grains misorientation angle distribution graph (Fig. 2.1.5d), 93% of the grains in the as-received rolled ship plate showed a

misorientation angle less than 1 degree, which can potentially be ascribed to the applied plastic deformation during the rolling process. However, the grain boundaries misorientation angles were more disordered in the as-printed sample showing a random misorientation mostly in a range of 1 to 5 degrees. The formation of grains with disordered misorientation angles was previously observed in additively manufactured steel components, and was attributed to the high energy of the heat source and fast scanning rate during the deposition process [95]. Regrading the aspect ratio, it is well-known that the grains with the aspect ratio less than 3 are considered as equiaxed grains, while the columnar grains have an aspect ratio of higher than 3 [96,97]. According to Fig. 2.1.5e, both the as-received rolled and as-printed ship plates are dominantly (~ 95%) composed of equiaxed grains, confirming no preferential distortion direction for the grains.

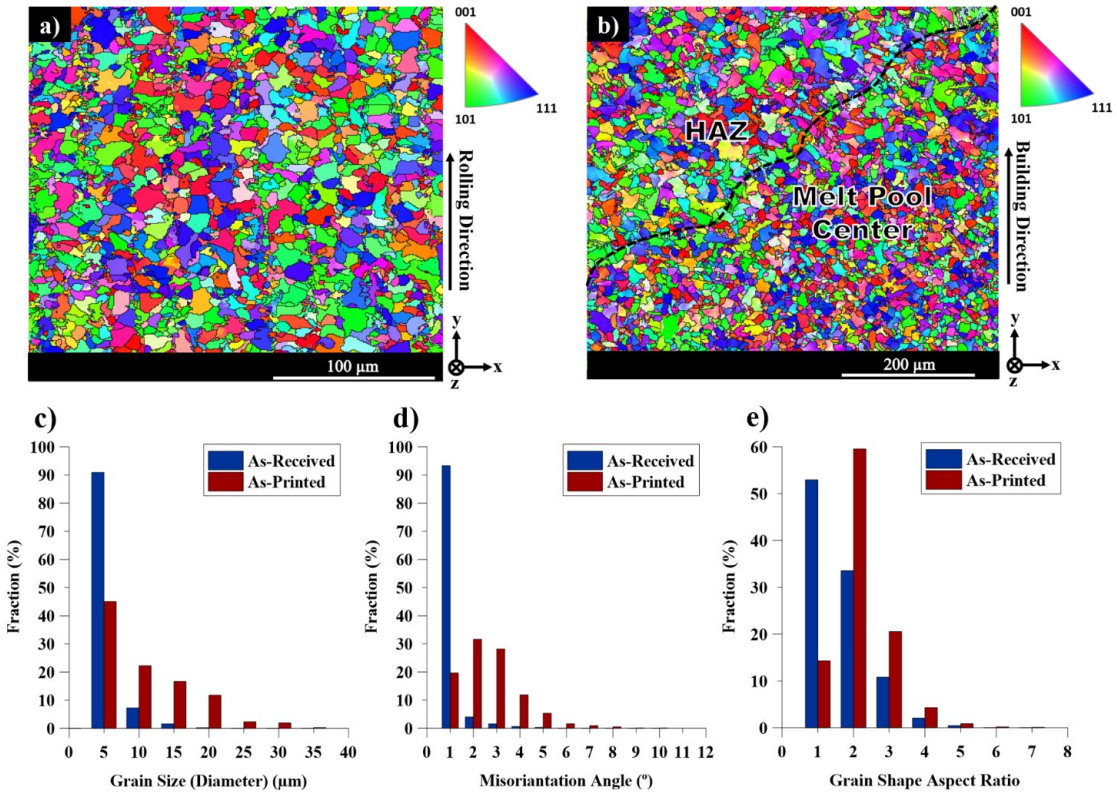

Figure 2.1.5 The EBSD-IPF maps of the (a) as-received rolled ship plate, (b) as-printed ship plate. The plots of (c) grains size distributions, (d) grains misorientation angle distributions, and (e) grains shape aspect ratio distributions.

Although the IPF maps for both samples did not reveal a specific dominant grain orientation, more detailed and quantitative information on the texture can be obtained from the pole figure (PF) maps. Fig. 2.1.6a and b also show the pole figures (PFs) derived from the IPF maps of the as-received rolled and as-printed ship plates, respectively. The comparison between the pole figures revealed that albeit both structures are not strongly textured, the as-printed structure of the WAAM sample possesses a stronger texture component with a maximum intensity of 3.08, particularly for the {111} crystal planes approximately 45° from the Y-axis. The position of the poles with the highest intensity on the {111} pole figure refers to the {111}[$10\bar{1}$] texture component, which is known as one of the main texture components in a material with BCC crystal structure (*e.g.*, ferrite), transformed from the FCC crystal structure (*e.g.*, austenite) [98]. Such phase transformation occurs during solidification of each deposited layer and also during cooling of the previously solidified layer(s) that have been re-austenitized when a new layer is deposited.

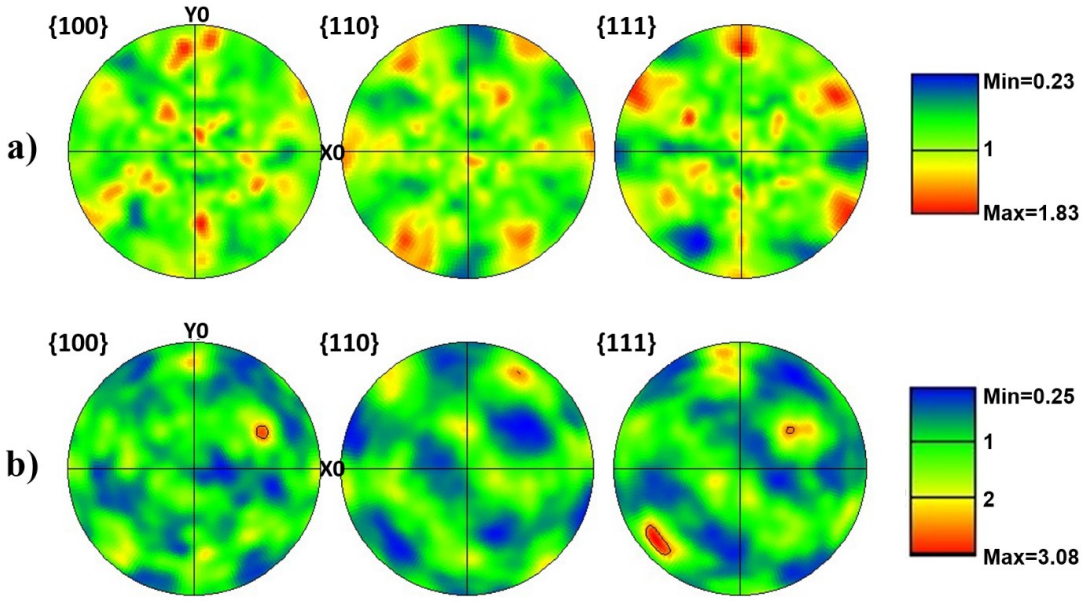

Figure 2.1.6 Pole figures of the (a) as-received rolled and (b) WAAM ship plates.

2.1.4.1.2 Heat treated rolled and WAAM fabricated shipbuilding plates

Figs. 2.1.7 and 2.1.8 demonstrate the microstructure of the conventionally rolled and additively manufactured samples, respectively, after applying different heat treatment cycles, including air-cooling and water-quenching from the austenitizing temperature of 800 °C. According to Fig. 2.1.7a and b, the air-cooling heat treatment on the rolled ship plate resulted in the formation of mostly slender MA phases located at the grain boundaries of the ferrite grains in addition to some coarse lamellar pearlite regions. On the other hand, the rapid cooling rate due to the water-quenching from the austenitizing temperature of 800 °C caused the formation of mostly blocky MA phases at the matrix of polygonal ferrite (see Fig. 2.1.7c and d).

The X-ray diffraction spectra of the rolled ship plate before and after air-cooling and water-quenching heat treatments are shown in Fig. 2.1.9. It can be deduced from the X-ray diffraction patterns that the as-received rolled ship plate does not contain any retained austenite phase due to owning an entirely ferritic-pearlitic microstructure, whereas the heat treated samples accommodate retained austenite in the MA phases. A quantitative comparison between the volume fraction of the retained austenite in the air-cooled and water-quenched rolled ship plates is presented in the discussion section.

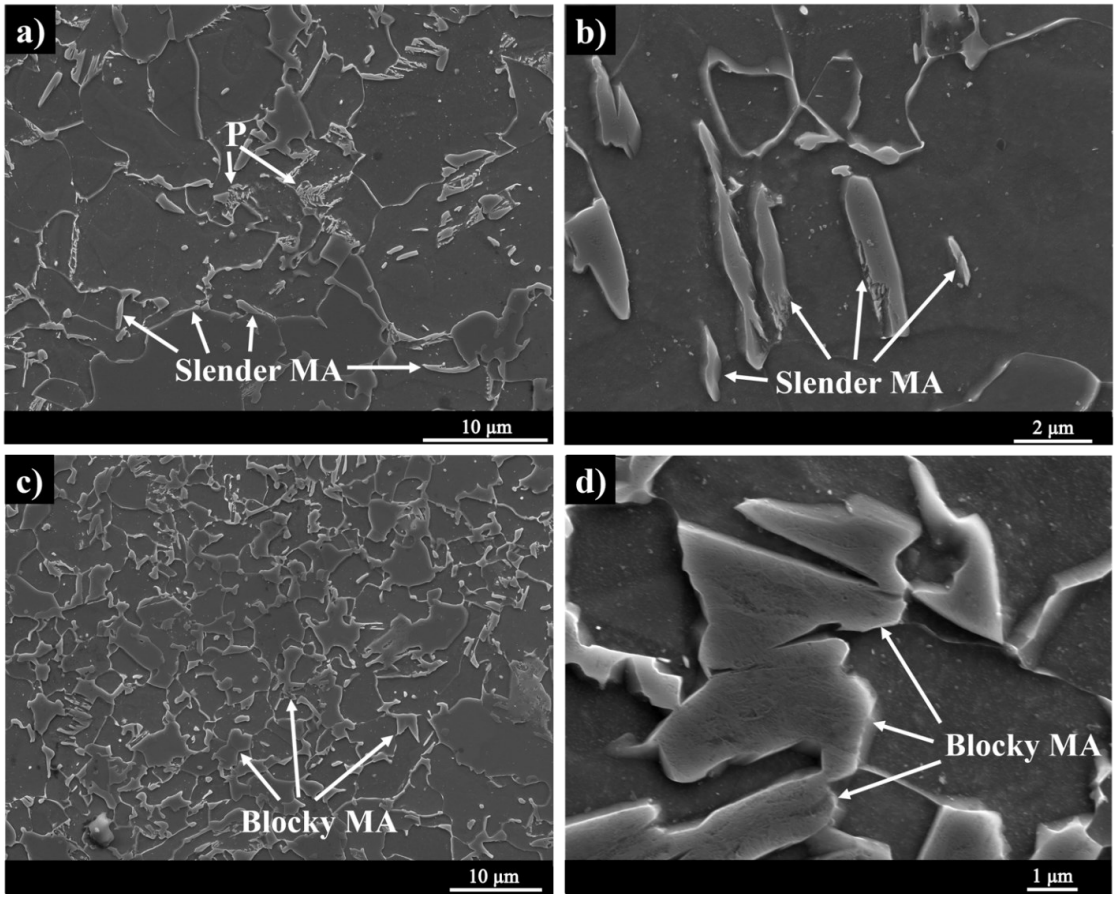

Figure 2.1.7 SEM micrographs taken from the rolled ship plate after applying different heat treatments including: (a) & (b) air-cooling cycle, and (c) & (d) water-quenching cycle.

Applying the air-cooling heat treatment on the as-printed WAAM ship plate (ER70S) resulted in the formation of a ferritic-pearlitic microstructure, homogenously developed over the entire sample (see Fig. 2.1.8a and b). It is worth mentioning that the homogeneity and uniformity of the microstructure after air-cooling were promoted both in terms of the formed micro-constituents and the grain size distribution. Differently, the water-quenching cycle led to the formation of tiny (approximately 1 µm long) and sharp acicular ferrite at the grain boundaries of the polygonal ferrite grains plus a low volume fraction of intergranular lamellar pearlite (see Fig. 2.1.8c and d). The microstructure of each sample before and after heat treatments will be thoroughly deliberated in the discussion section.

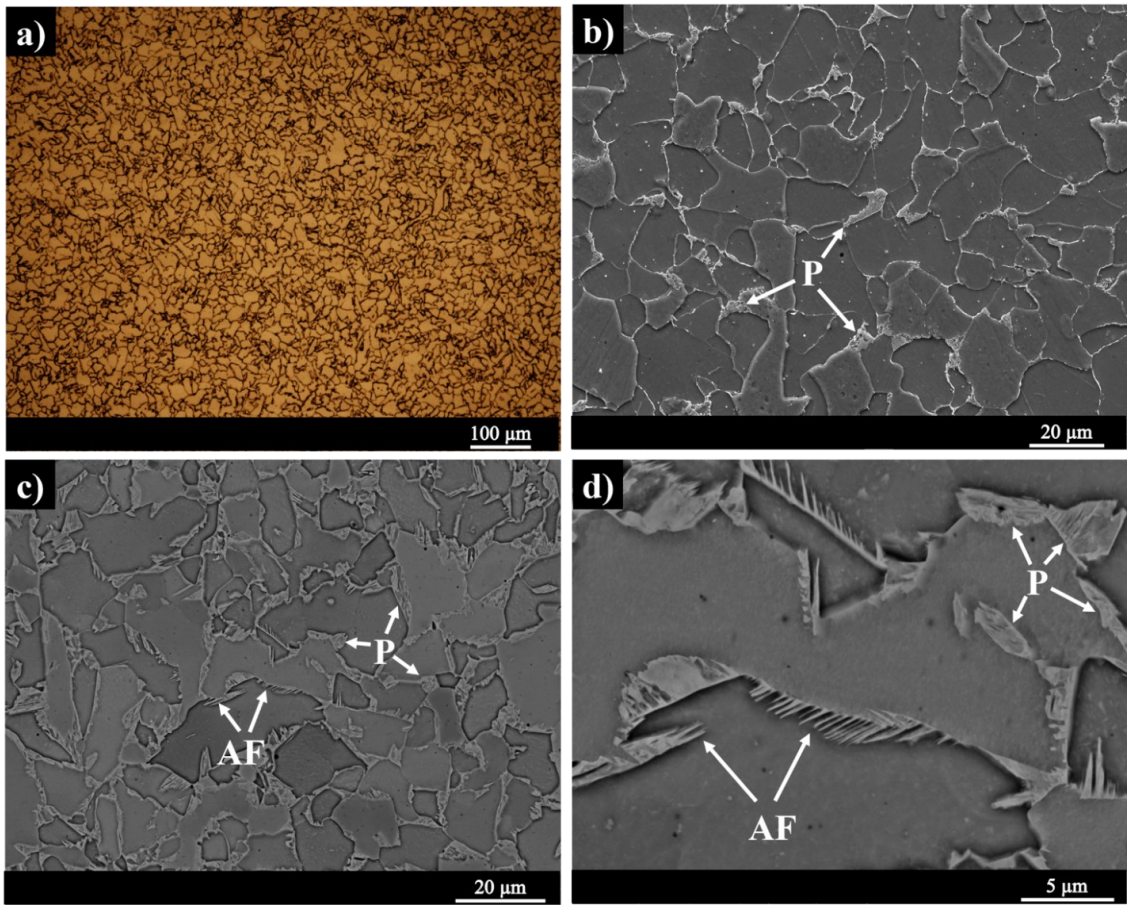

Figure 2.1.8 Optical and SEM micrographs taken from the WAAM sample after different heat treatments including: (a) & (b) air-cooling cycle, and (c) & (d) water-quenching cycle.

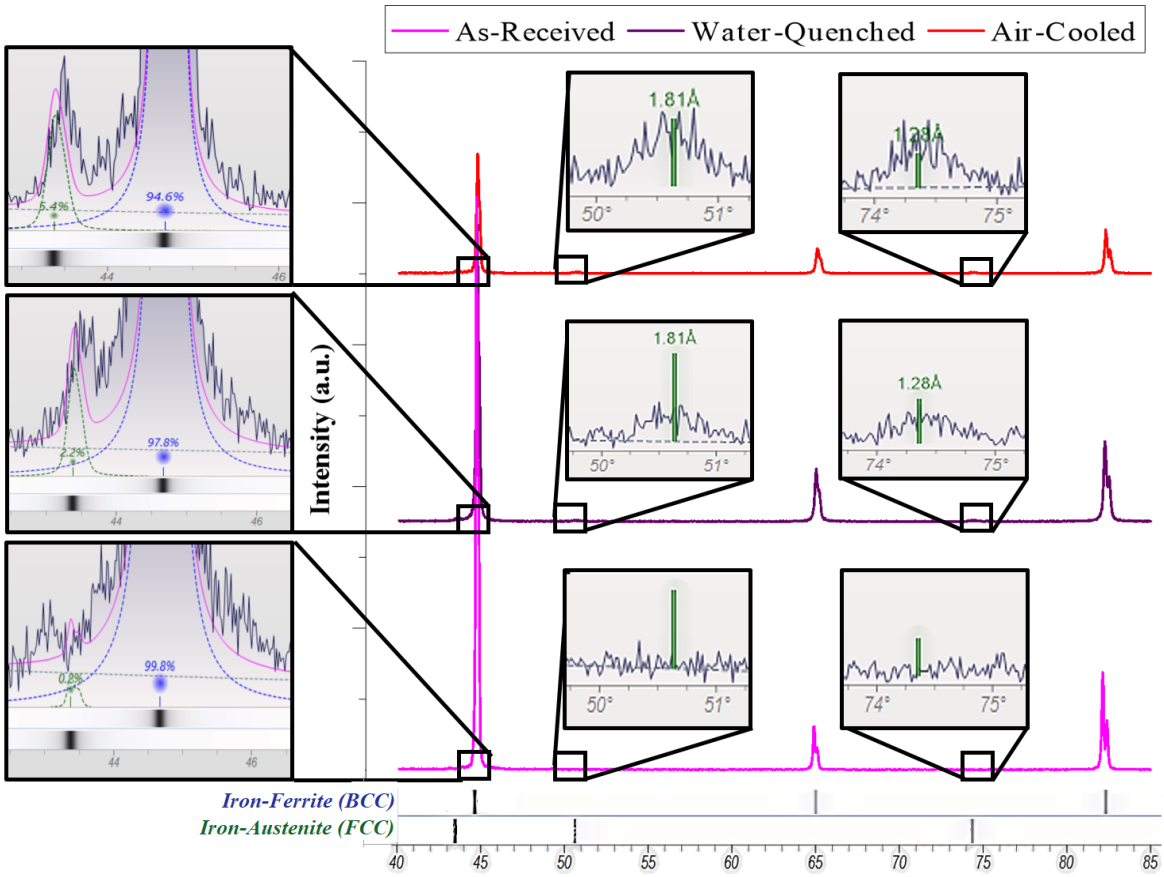

Figure 2.1.9 X-ray diffraction patterns of the as-received rolled ship plate before and after different heat treatments, including air-cooling and water-quenching.

2.1.4.2 Mechanical Properties

The results of microhardness testing on both rolled and WAAM ship plates before and after applying different heat treatments (air-cooling (AC) and water-quenching (WQ)) are presented as a box plot in Fig. 2.1.10. The average microhardness of the rolled and WAAM ship plates were measured at 170 ± 1 HV and 160 ± 7 HV, respectively. The water-quenching heat treatment was found to increase the hardness of both rolled and WAAM samples by ~ 128 HV and ~ 41 HV, respectively. However, the air-cooling thermal cycle led to a slight drop of microhardness value of the WAAM sample to 145 ± 1 HV and a moderate increase in the microhardness of the rolled ship plate to 216 ± 2 HV.

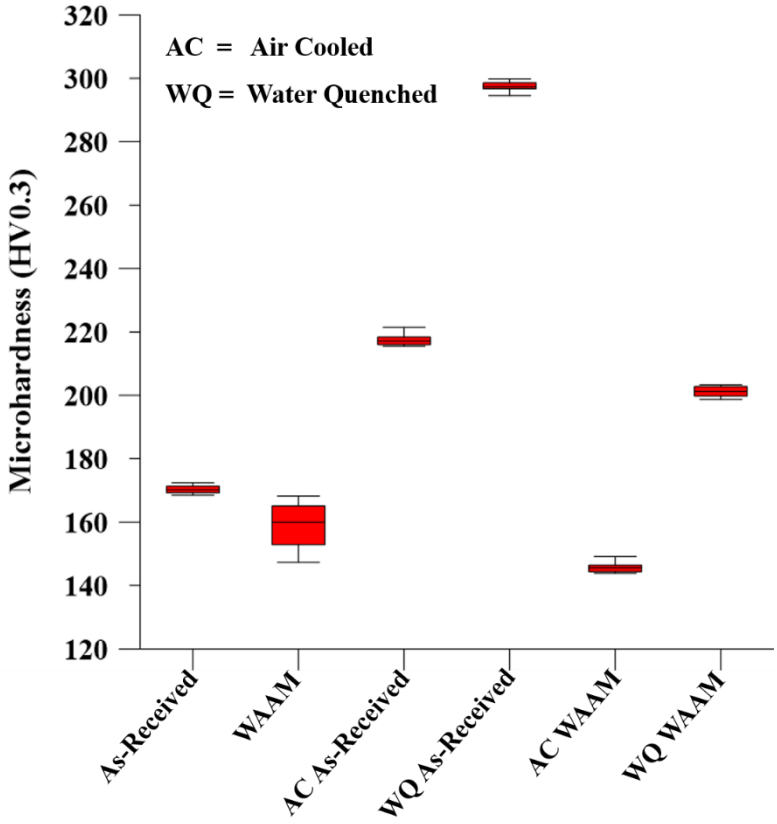

Figure 2.1.10 Vickers microhardness of the as-received rolled and WAAM ship plates before and after different heat treatments, i.e., air-cooling (AC) and water-quenching (WQ).

The stress-strain curves of the as-received rolled ship plate in the rolling (horizontal) and transverse (vertical) directions along with the heat treated samples just in rolling direction are all plotted in Fig. 2.1.11a. It should be noted that since the as-received samples in both rolling and transverse directions showed a similar mechanical performance with no anisotropy, the heat treated samples were tested only in the rolling direction. Fig. 2.1.11b also shows the results of uniaxial tensile testing on both as-printed and heat treated additively manufactured ship plates along the deposition (horizontal) and building (vertical) directions. According to Fig. 2.1.11a and b, the ultimate tensile strength (UTS) of the as-printed sample (~ 500 MPa) is comparable to the UTS of the as-received rolled ship plate (~ 550 MPa), confirming the fabrication feasibility of the ship plates using wire arc additive manufacturing. However, the as-printed sample showed an anisotropic ductility in the horizontal direction (with 35 ± 2% of elongation) versus the vertical

direction (with 12 ± 3% of elongation), as compared to ~ 35% of elongation for the rolled ship plate in both horizontal and vertical directions. As a result of air-cooling heat treatment, the UTS of the WAAM sample slightly dropped by around 50 MPa, and the anisotropy was decreased from 23% difference between the horizontal and vertical directions to a negligible amount of 4% difference in the elongation percentage. In contrast, the UTS of the air-cooled rolled ship plate increased by nearly 85 MPa at the expense of roughly 8% reduction in the elongation. On the other hand, the water-quenching thermal cycle increased the UTS of the rolled ship plate up to 885 ± 17 MPa and reduced the ductility by ~ 15%, which is consistent with the results of microhardness measurements (see Fig. 2.1.10). Interestingly, in the case of the WAAM sample, the water-quenching heat treatment increased the UTS of the component up to ~ 550 MPa and also considerably decreased the anisotropy in ductility from 23% difference between the horizontal and vertical directions to an insignificant amount of 2%. All results of the mechanical testing, including microhardness measurement and tensile testing of both rolled and WAAM ship plates before and after heat treatment are summarized in Table 2.1.3. Moreover, a detailed discussion on the correlation between the obtained mechanical properties and the microstructural characteristics, before and after heat treatments, are included in the discussion section.

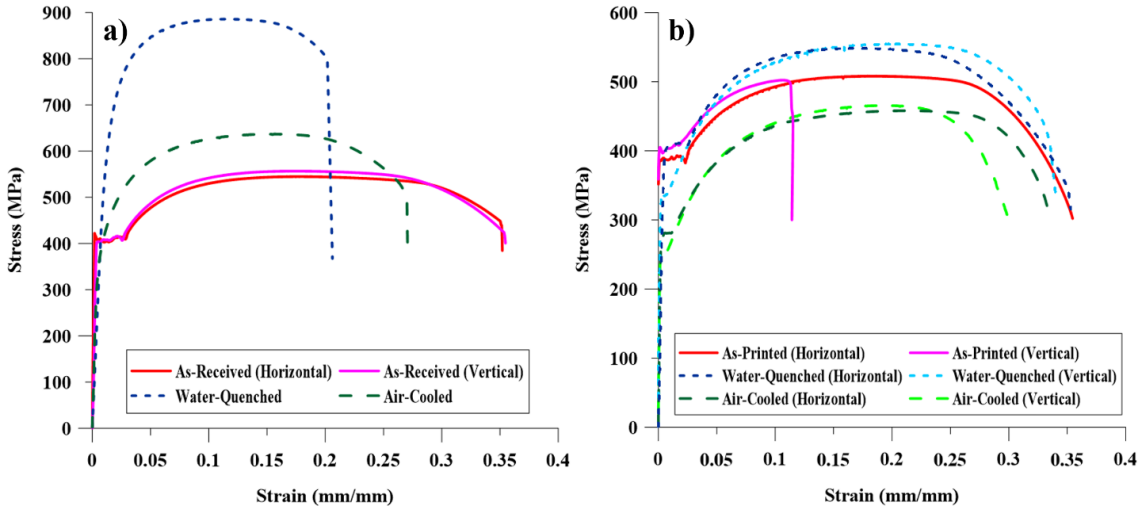

Figure 2.1.11 Stress-Strain curves of the as-received rolled and WAAM ship plates before and after different heat treatments, *i.e.*, air-cooling and water-quenching.

Table 2.1.3 A summary of mechanical properties of the rolled and WAAM fabricated ship plates before and after different heat treatments.

Material	UTS (MPa)	Elongation (%)	Microhardness (HV)
As-Received (Horizontal)	548 ± 14	35 ± 1	170 ± 1
As-Received (Vertical)	554 ± 12	35 ± 1	170 ± 1
As-Received (AC)	635 ± 12	27 ± 1	216 ± 2
As-Received (WQ)	885 ± 17	20 ± 1	298 ± 2
WAAM (Horizontal)	497 ± 18	35 ± 2	160 ± 7
WAAM (Vertical)	504 ± 21	12 ± 3	160 ± 7
WAAM (Horizontal AC)	447 ± 11	34 ± 1	145 ± 1
WAAM (Vertical AC)	455 ± 13	30 ± 2	145 ± 1
WAAM (Horizontal WQ)	551 ± 16	35 ± 1	201 ± 1
WAAM (Vertical WQ)	555 ± 17	33 ± 1	201 ± 1

2.1.5. Discussion

2.1.5.1 Microstructural Characterizations

2.1.5.1.1 As-received rolled and WAAM fabricated shipbuilding plates

According to Figs. 2.1.2 and 2.1.3b, the dominant microstructure of the WAAM sample (presented in the melt pool centers) is the same as the ferritic-pearlitic microstructure of the as-received rolled ship plate. However, an obvious microstructural difference is the banded morphology of the pearlite phase in the rolled ship plate (Fig. 2.1.2) versus the even distribution of the pearlite phase at the grain boundaries of polygonal ferrite in the melt pool centers of the WAAM component (Fig. 2.1.3b). The banded structure is the typical microstructure of EH36 steel produced by the conventional rolling process, while the EH36 steel fabricated using TMCP contains an equiaxed grain structure, which is a more desirable microstructure due to its better weldability, higher strength, toughness, and corrosion resistance [69]. Furthermore, higher magnification SEM image (Fig. 2.1.3c) taken from the melt pool boundaries of the as-printed sample revealed that the faster cooling rate in the boundaries of each melt pool as compared to its center, resulted in the formation of some meta-stable phases, such as acicular ferrite (AF), bainite (B), and localized small martensite-austenite (MA) islands that embrittle the melt pool

boundaries. It is also previously reported [99–101] that the presence of the MA phase in the steel's structure deteriorates the ductility and toughness of the component by debonding from the matrix and forming crack initiation sites during tensile or impact loadings. The formation mechanism and adverse effects of MA phases are comprehensively discussed in previous studies by the authors [7,8]. Moreover, according to Fig. 2.1.3a, an obvious grain coarsening in the HAZ occurred as a result of the thermal effect of each successive deposited bead on the previous track. It is notable that these microstructural transitions are inevitable in an additive manufactured component due to the complex thermal histories as a result of overlapping scanning lines and thereby various heating and cooling rates in different zones, including the melt pool center, melt pool boundary and heat affected zone [102]. As shown in Fig. 2.1.4, another microstructural difference is the relatively higher volume fraction of pearlite phase in the rolled ship plate (20.32 ± 0.81%) compared to the WAAM sample (12.54 ± 0.56%), which is attributed to the higher carbon content of the rolled ship plate (0.14 wt.% C) versus the WAAM sample (0.08 wt.% C). The higher volume fraction of pearlite can potentially lead to better mechanical properties, particularly hardness and tensile strength.

2.1.5.1.2 Heat treated rolled and WAAM fabricated shipbuilding plates

2.1.5.1.2.1 Air-cooled rolled ship plate

As shown in Fig. 2.1.7a and b, the microstructure of the air-cooled rolled EH36 alloy contains polygonal ferrite as the matrix in addition to mostly slender MA islands and a low volume fraction of coarse lamellar pearlite phases. Regarding the dispersion of the phases, both the MA and pearlite phases are distributed primarily at the grain boundaries and scarcely inside the ferrite grains. According to the equations (2.1.1) and (2.1.2), the Ac_1 and Ac_3 temperatures of the EH36 alloy are 715 °C and 835 °C, respectively. Hence, during the heating cycle to the intercritical temperature of 800 °C, once passing the eutectoid transformation line (Ac_1 = 715 °C), the austenite grains start to nucleate and grow preferably from the pearlite regions containing an elevated carbon content, and consequently, the austenite phase becomes rich of carbon [103]. Subsequently, during the cooling cycle, the small carbon-rich austenite grains were subjected to the air-cooling.

Although the air-cooling is not considered as a fast cooling cycle, a low volume fraction of tiny MA phases were formed due to the high carbon content of the primary austenite grains. Theoretically, two complementary factors, including high cooling rate and high carbon content, lead to the military-diffusionless phase transformation of austenite to martensite. In the case of air-cooling cycle, the carbon content of the primary austenite was high enough to form the MA phases even at a moderate cooling rate. It is important to note that the formation of some pearlite regions confirms that the air-cooling process was not fast enough to transform all the primary austenite phases to the brittle MA constituent, and consequently some pearlite regions have been also formed.

Fig. 2.1.12 depicts the EDS elemental maps of the alloying elements distribution inside and around the MA phase. Fig. 2.1.12b confirms the higher carbon content of the MA phase as compared to its surrounding area. The higher carbon content of the MA regions than that of the polygonal ferrite phase is also reported in previous studies [104]. Moreover, the higher concentration of austenite stabilizer elements, *i.e.*, Ni and Mn, in the MA phase confirms the presence of retained austenite in the MA islands (see Fig. 2.1.12d and e). The slightly higher concentration of Si and Nb observed in the MA phase mapping is consistent with other studies [105–107], suggesting that the presence of these two elements facilitates the formation of MA phases (see Fig. 2.1.12f and g).

Regarding the impact of the MA phase on the mechanical properties of various ferrous alloys, the review of the existing literature reveals some inconsistencies in the reported results. Some studies [100,101] have stated that the formation of the MA phase deteriorates the toughness of the component, while others [106,108–110] have shown that the presence of the MA phase leads to the improved toughness and ductility of the material. Overall, the reported variations in the MA phase characteristics, such as its distribution, volume fraction, and morphology, dictate its final impact on the mechanical properties of the alloy [99,111].

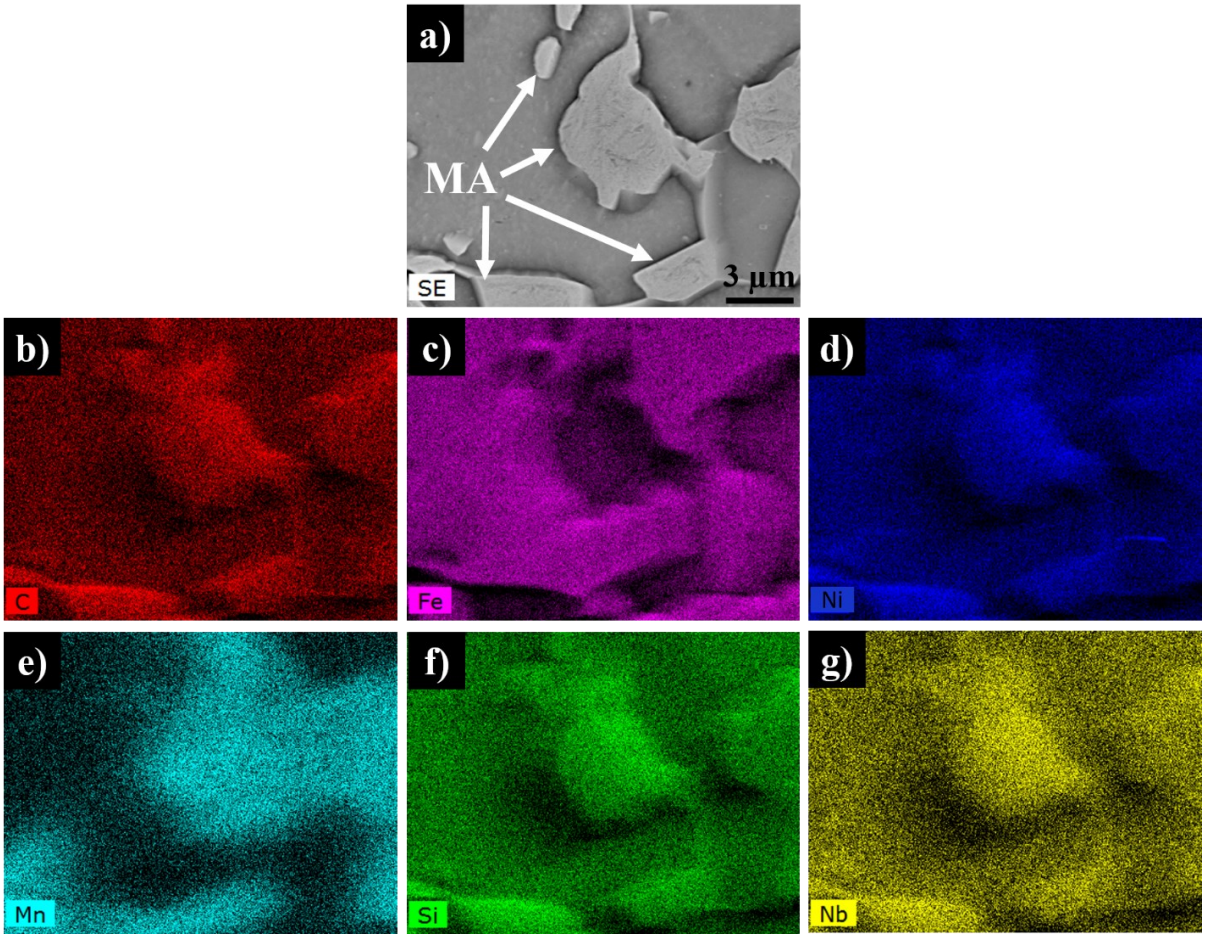

Figure 2.1.12 EDS elemental mapping analysis of the MA micro-constituent in a matrix of the ferrite phase.

2.1.5.1.2.2 Water-quenched rolled ship plate

In the case of water-quenching of the EH36 rolled ship plate (Fig. 2.1.7c and d), the microstructure only contains MA phases in the matrix of polygonal ferrite, and no pearlite region has been formed, confirming that water-quenching was fast enough to transform all the primary austenite phase to the hard and brittle MA micro-constituent. In terms of the morphology, the MA islands are formed mostly in a blocky shape in the water-quenched sample, in contrast to the slender shape of MA islands in the air-cooled sample. Huda *et al.* [99] also observed that the slender MA micro-constituents typically form at the slower cooling rates, such as air-cooling, while the blocky morphology of the MA phases mostly forms due to higher cooling rates, such as water-quenching. Higher

magnification SEM micrographs of both slender and blocky MA phases (Fig. 2.1.13a and b) show that the MA islands are composed of two co-existing phases, including martensite (bright) and retained austenite (dark). Formation of negligible but different volume fractions of retained austenite in the MA phase has been reported in different studies [99,112,113].

Quantitatively, the volume fraction of the retained austenite, calculated from the X-ray spectra using WPF method (see Fig. 2.1.9), in the air-cooled sample was ~ 5.4%, which is higher than that of the water-quenched sample (~ 2.2%). It has been reported that an increase in the cooling rate leads to the formation of a lower volume fraction of retained austenite due to the variations in the M_s (martensite start) and M_f (martensite finish) temperatures arising from slower carbon migration and diffusion rates [114,115]. It is worth mentioning that the retained austenite is a primary crack initiation and propagation site since impurities and inclusions prefer to gather around the austenite phase [116]. Moreover, the dislocation density in the retained austenite is much lower as compared to other phases, such as ferrite, pearlite, and martensite [99]. Therefore, the relative volume fraction of austenite and martensite inside the MA phases could potentially play an important role in the resultant mechanical properties of the alloy.

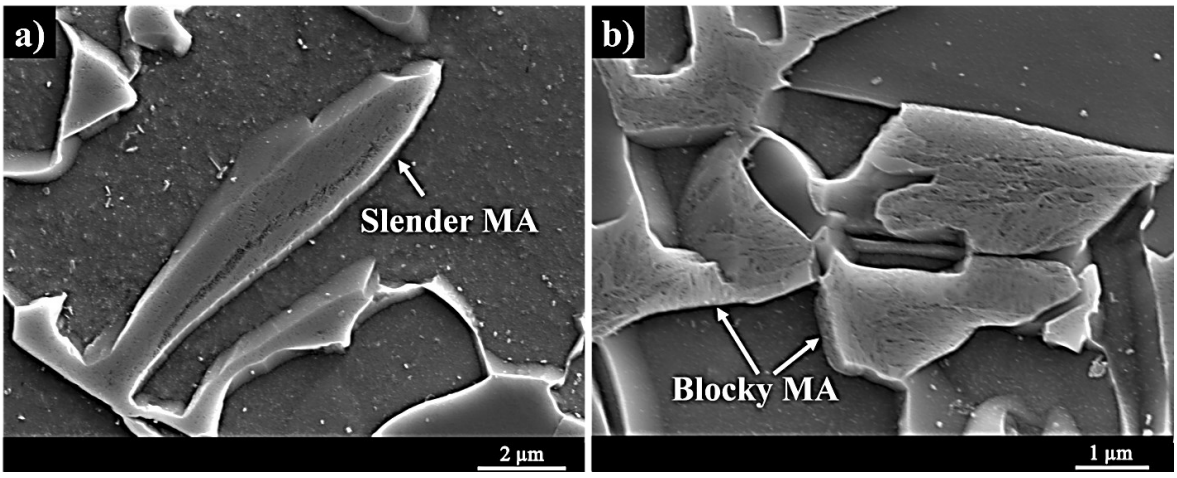

Figure 2.1.13 High magnification SEM micrographs of the (a) slender MA and (b) blocky MA phases, showing the co-existence of both martensite (bright) and retained austenite (dark) phases inside the MA islands.

2.1.5.1.2.3 Air-cooled WAAM fabricated shipbuilding plate

As depicted in Fig. 2.1.8a and b, the resultant microstructure after air-cooling heat treatment of the WAAM ship plate was a uniform ferritic-pearlitic microstructure in which the pearlite phase is formed along the grain boundaries and triple junctions of the polygonal ferrite grains. It is notable that no meta-stable phases, such as martensite, acicular ferrite, or MA phases were formed in the case of air-cooling of ER70S alloy with a carbon content of 0.08 wt. %. Neither the rapid cooling nor the high carbon content requirement was addressed in this treatment, causing the phase transformations to follow the equilibrium binary phase diagram of Fe-Fe_3C. Therefore, primary austenite grains, which are formed at the intercritical temperature (800 °C), experienced a eutectoid transformation during the cooling cycle and transformed into the lamellar pearlite with an even distribution throughout the component. Consequently, the air-cooling heat treatment of the WAAM ship plate not only developed a homogenized microstructure, but also eliminated the formation of brittle melt pool boundaries and the soft heat affected zones. Formation of a more uniform and homogenous grain structure after air-cooling heat treatment of Grade X70 pipeline steel (with a close chemical composition to ER70S) has been also reported by Natividad *et al.* [117]. It is interesting to note that homogeneity and uniformity of microstructure resulted from the air-cooling heat treatment can potentially eliminate or diminish the anisotropy in the ductility of the WAAM sample.

2.1.5.1.2.4 Water-quenched WAAM fabricated shipbuilding plate

According to Fig. 2.1.8c and d, water-quenching heat treatment of the WAAM sample resulted in a microstructure including polygonal ferrite along with intergranular pearlite beside acicular ferrite constituents. In terms of the phase distribution, the acicular ferrite nucleated along the grain boundaries of polygonal ferrite and scantly grew through the grains (see Fig. 2.1.8d). During water-quenching of the WAAM ship plate, although the sample experienced a fast cooling, the carbon content of the ER70S alloy (0.08 wt. % compared to 0.14 wt. % for EH36 alloy) was not sufficient to form a martensitic microstructure. In addition, the lower content of Ni (as a strong austenite stabilizing element) and the higher content of Mo and Si (both as ferrite stabilizer) have retarded the austenitization of the alloy, ultimately leading to a lower volume fraction of austenite

possessing a lower carbon content in ER70S sample at 800 °C as compared to that of the EH36 alloy. Thus, the primary austenite grains in ER70S alloy transformed into pearlite and acicular ferrite during the cooling cycle. It is worth noting that the formation of acicular ferrite needs a higher cooling rate as compared to pearlite, and the water-quenching has provided a sufficiently high cooling rate adequate for the formation of acicular ferrite in addition to the pearlite phase. Yang *et al*. [118] also studied the heat treatment of API X70 steel by heating to an intercritical temperature (between Ac_1 and Ac_3) and reported the formation of acicular ferrite beside pearlite as a result of water-quenching heat treatment. Regarding the formation mechanism, the acicular ferrite formation starts with the nucleation of its primary plates from the non-metallic inclusions or grain boundaries by a shear transformation without any change of compositions and then at the next stage grows by establishing a second generation of ferrite plates nucleated at the interface of austenite and pre-existing acicular ferrite plates [119]. The presence of acicular ferrite in the microstructure can increase the hardness and strength, and also reduce the stress-corrosion-cracking and hydrogen-induced-cracking susceptibility of the material [120,121]. It has been also reported [122,123] that acicular ferrite is identified as the optimum micro-constituent in steels, which can provide a supreme combination of strength and ductility due to its fine grain size, high-angle boundaries, and comparatively high dislocations density hindering the easy movement of dislocations. Thereby, the formation of an adequate volume fraction of acicular ferrite in the microstructure can result in balanced properties suitable for service conditions that require high strength and high ductility simultaneously.

The impact of existing compositional variations between EH36 and ER70S alloys on the martensite start (M_s) and finish (M_f) temperatures should not be overlooked. The higher content of carbon and other austenite stabilizing elements, *i.e*. Ni, and the lower content of ferrite stabilizers, *i.e*. Mo and Si, in EH36 alloy reduce both M_s and M_f temperatures of the alloy, rendering a delayed transformation of austenite to martensite. However, the formation of martensite islands in the form of MA phase was only detected in the EH36 alloy, suggesting that the M_s and M_f temperatures of the alloys are not the dominating factors that control the formation of the martensite phase. But rather, the higher content

of C and Ni in EH36 alloy has retarded the eutectoid transformation reaction (the formation of pearlite and bainite), causing the improved hardenability of the EH36 alloy resulted from shifting the nose of its CCT diagram to longer times.

2.1.5.2 Mechanical properties

2.1.5.2.1 As-received rolled and WAAM fabricated shipbuilding plates

A comparison between the microhardness values of the as-received rolled ship plate (EH36) and the WAAM part (ER70S) revealed a slightly higher hardness of the rolled component (see Fig. 2.1.10). The measured ~ 10 HV difference between the average microhardness values can be ascribed to the higher carbon content of the raw material used for the rolled ship plate (EH36), leading to its higher pearlite volume fraction as previously described with reference to Fig. 2.1.4. Moreover, the microhardness data of the WAAM sample showed a large standard deviation (±7 HV) due to its microstructural variation from the melt pool center towards melt pool boundaries and HAZ. The melt pool center with a fine ferritic-pearlitic microstructure possessed the microhardness of 160 ± 2 HV, while the HAZ with coarser grains revealed a slightly reduced microhardness of 150 ± 1 HV, and the melt pool boundaries containing brittle MA phases showed a microhardness of 175 ± 2 HV.

As shown in Fig. 2.1.11a and b, the ultimate tensile strength of the as-received rolled sample both in horizontal and vertical directions was ~ 550 MPa, and the WAAM ship plate showed a UTS value of ~ 500 MPa in both horizontal and vertical directions. The higher strength of the as-received rolled ship plate also confirms that the higher volume fraction of pearlite in the rolled ship plate has resulted in improving the mechanical properties, *i.e.,* microhardness and tensile strength. Therefore, the insignificant difference in the UTS of two components is associated with the richer carbon content of the raw material used for the rolled sample (EH36) as compared to the WAAM feedstock material (ER70S), and should not be correlated to the manufacturing process. Differently, the measured ductilities revealed a more significant difference between the rolled ship plate with ~ 35 % of elongation in both vertical and horizontal directions and the WAAM component, which was more ductile in the horizontal direction (35 ± 2 % of elongation)

than the vertical direction (12 ± 3% of elongation), confirming the anisotropic behavior in ductility as a result of additive manufacturing process.

A comparison between the engineering stress-strain curves (Fig. 2.1.11a and b) revealed that tensile properties of the WAAM component in the horizontal direction meet the mechanical properties requirements of the as-received conventionally rolled ship plate. However, the detected anisotropic response in ductility of the WAAM fabricated sample needs to be addressed prior to its implementation in service. There are three main factors that potentially contribute to the decreased ductility of the WAAM sample in the vertical direction, *i.e.*, (*i*) the presence of discontinuities, such as interpass lack of fusion, (*ii*) grain coarsening in the heat affected zone, and (*iii*) the formation of brittle MA phases in the regions adjacent to the melt pool boundaries, which all are comprehensively discussed in a previous study by the authors [7]. Among these factors, factors (*ii*) and (*iii*) correspond to the microstructural inhomogeneity in the as-printed sample, which can be plausibly modified through adopting appropriate heat treatment cycles. Therefore, it is essential to identify the optimum cycle that can potentially improve the mechanical properties of the WAAM ship plate, to reach or even surpass the properties of the conventionally manufactured ship plate.

2.1.5.2.2 Heat treated rolled and WAAM fabricated shipbuilding plates

2.1.5.2.2.1 Air-cooled rolled ship plate

According to the results of microhardness measurements (Fig. 2.1.10), the air-cooling heat treatment slightly increased the microhardness of the as-received rolled ship plate from 170 ± 1 HV to 216 ± 2 HV due to the formation of tiny and slender brittle MA phases. Although the MA constituent is identified as a super hard phase [124,125], its presence did not significantly affect the microhardness of the component due to its slender morphology and much lower volume fraction compared to the polygonal ferrite as the matrix phase. The stress-strain curves of the as-received and heat treated rolled ship plates (Fig. 2.1.11a) showed a moderate raise in the UTS of the air-cooled rolled ship plate from ~ 550 MPa to ~ 635 MPa along with 8% reduction in the ductility, which

is in agreement with the results of microstructural characterizations and microhardness measurements.

2.1.5.2.2.2 Water-quenched ship plate

According to Fig. 2.1.10, the microhardness of the rolled ship plate was boosted from 170 ± 1 HV to 298 ± 2 HV as a result of water-quenching heat treatment. This drastic increase in microhardness can be attributed to the microstructural changes due to the applied rapid cooling from the austenitizing temperature (800 °C) to room temperature. As previously described, water-quenching heat treatment led to the formation of hard and brittle blocky MA phases with a higher volume fraction compared to the slender MA phases formed in the air-cooled sample. As shown in Fig. 2.1.11a, although the formation of blocky MA phases increased the UTS of the water-quenched sample from ~ 550 MPa up to ~ 880 MPa, this process dramatically reduced the elongation percentage of the component from ~ 35% to ~ 20%. Since the ductility is of great importance in the marine applications, particularly in arctic and sub-arctic regions, this heat treatment cycle is not recommended for the ship plates in order to avoid brittle catastrophic failures. On the other hand, comparing the ductility of the water-quenched (20 ± 1%) and air-cooled (27 ± 1%) rolled ship plates revealed that the higher volume fraction of the MA phase in addition to its blocky morphology in the water-quenched sample led to a lower ductility. It has been also reported [126,127] that the blocky MA phase requires less energy for crack initiation as compared to the slender MA phase. It should be also noted that the average grain size of the water-quenched sample (~ 4 μm) was finer than that of the air-cooled one (~ 11 μm), confirming that the presence of the large and blocky MA phase is much more detrimental to the mechanical properties as compared to the side effect of the coarse grains in the microstructure of an alloy.

2.1.5.2.2.3 Air-cooled WAAM fabricated shipbuilding plate

The results of microhardness measurements on the WAAM ship plate before and after air cooling heat treatment (Fig. 2.1.10) showed a slight drop (~ 15 HV) in the microhardness value from 160 ± 7 HV to 145 ± 1 HV. Interestingly, the standard deviation of the

microhardness data was also decreased due to the homogenous microstructure developed throughout the component. As previously explained, the as-printed ship plate had a large variation in the microhardness values from ~ 150 HV to ~ 175 HV as a result of its microstructural inhomogeneity. Another deteriorative consequence of microstructural inhomogeneity of the as-printed component was the detected anisotropic ductility. According to Fig. 2.1.11b, the air-cooling heat treatment was found to abate the anisotropic ductility of the WAAM ship plate, causing the reduction of the elongation difference between the vertical and horizontal directions of the as-printed sample from 23% to a negligible amount of 4%. Therefore, the small variation in the microhardness values and the isotropic ductility of the air-cooled WAAM component can be associated with its homogenous ferritic-pearlitic microstructure in which the brittle melt pool boundaries (including MA phase) and the soft HAZ (including coarse grains) have been entirely eliminated. However, the UTS of the sample has been reduced from ~ 500 MPa to ~ 450 MPa after air-cooling heat treatment, consistent with the results of microhardness measurements (~ 15 HV drop). It can be concluded that even by applying the air-cooling cycle, the WAAM ship plate cannot meet the mechanical properties requirement of the as-received rolled ship plate due to ~ 100 MPa difference in their UTS values.

2.1.5.2.2.4 Water-quenched WAAM fabricated shipbuilding plate

In contrast to the air-cooling thermal cycle, water-quenching heat treatment fairly increased the microhardness from 160 ± 7 HV to 201 ± 1 HV, resulted from the formation of acicular ferrite. Accordingly, the UTS of the WAAM component is moderately enhanced from ~ 500 MPa to ~ 550 MPa due to the formation of the sharp acicular ferrite apart from intergranular pearlite in the matrix of polygonal ferrite. The water-quenching cycle not only increased the microhardness and UTS of the WAAM sample but also dramatically improved the ductility of the vertical sample and considerably minimized the anisotropic ductility of the WAAM component. It is well-known that the acicular ferrite is an exceptional phase capable of increasing both the strength and ductility of the component simultaneously [122]. Therefore, the water-

quenched WAAM sample can reach the mechanical properties of the as-received rolled ship plate in terms of strength, ductility, and hardness.

Overall, the comprehensive analysis of the microstructural features and mechanical properties achieved by different heat treatment cycles on both rolled and WAAM ship plates revealed that the conventional fabrication process (rolling) of the ship plates can be well replaced by the state-of-the-art wire arc additive manufacturing process followed by applying the post-printing heat treatment cycle of austenitizing to the intercritical temperature of 800 °C and then water-quenching to the room temperature.

2.1.6. CONCLUSIONS

In this study, the fabrication feasibility of low-carbon low-alloy steel (EH36) ship plates through the emerging wire arc additive manufacturing (WAAM) method was investigated. Microstructural characteristics and mechanical properties of the conventionally rolled and WAAM fabricated ship plates were compared before and after applying different heat treatment cycles. The following conclusions can be drawn from this study:

1. Both rolled and WAAM ship plates contained a dominant ferritic-pearlitic microstructure. However, the rolled sample showed a banded morphology of pearlite phase while the WAAM fabricated ship plate contained intergranular pearlite in the melt pool centers, meta-stable micro-constitutes, such as bainite, acicular ferrite, and localized tiny martensite-austenite phases in the melt pool boundaries, and a coarse grain structure in the heat affected zones (HAZ).
2. The formation of meta-stable micro-constitutes along the melt pool boundaries was found to locally increase the hardness and brittleness of the alloy, whereas the grain coarsening in the HAZ resulted in a slight localized softening. Such inhomogeneous microstructure led to an anisotropic ductility in the WAAM ship plate.
3. The rolled ship plate showed a higher microhardness (170 ± 1 HV) and UTS (~ 550 MPa) compared to the WAAM sample with the average hardness of 160 ± 7 HV and UTS of ~ 500 MPa. The slight higher mechanical properties of the rolled ship plate as

compared to those in the as-printed sample were attributed to its richer carbon content (0.14 wt.% in EH36 versus 0.08 wt.% in ER70S).

4. As a result of applying either air-cooling or water-quenching heat treatments on the austenitized rolled samples, hard and brittle martensite-austenite (MA) phases were formed in a matrix of polygonal ferrite. The formed MA phases were mostly slender and elongated in the air-cooled sample, while the water-quenched sample contained mostly blocky MA constituents. The formation of the MA phases in the microstructure increased the hardness and UTS of both air-cooled and water-quenched rolled ship plates. However, the brittle nature of this phase reduced the ductility of the component by ~ 8% and ~ 15%, respectively.
5. Although applying the air-cooling heat treatment on the WAAM sample homogenized the microstructure, eliminated the formation of brittle fusion boundaries and coarse heat affected zones, and minimized the anisotropic ductility, it slightly decreased the microhardness and UTS by ~ 15 HV and ~ 50 MPa, respectively.
6. The water-quenching heat treatment on the WAAM ship plate formed an ideal microstructure, including acicular ferrite and intergranular pearlite in a matrix of polygonal ferrite, leading to a great combination of strength and ductility in the fabricated part due to (i) increasing the ductility of the WAAM ship plate in the vertical direction by ~ 22%, (ii) nearly eliminating the anisotropic ductility, and (iii) improving the UTS by ~ 50 MPa. This WAAM fabricated product with improved properties is ideal for replacing conventionally manufactured ship plates.

ACKNOWLEDGMENT

The authors would like to thank the support of Natural Sciences and Engineering Research Council of Canada (NSERC) [grant number RGPIN-2017-04368] and the Memorial University of Newfoundland for sponsoring this work. The authors are also grateful to Irving Shipbuilding Inc., Halifax, NS, for providing the EH36 steel samples.

2.2. On the Post-printing Heat Treatment of a Wire Arc Additively Manufactured ER70S Part

Alireza Vahedi Nemani[1], Mahya Ghaffari[1], Ali Nasiri[2]

1- Graduate Student, Dalhousie University, Halifax, Nova Scotia, Canada

2- Assistant Professor, Dalhousie University, Halifax, Nova Scotia, Canada

Status: Published Journal Paper, Journal of Materials (IF= 3.623), Volume 13, Issue 12, Pages 2795

Authors' Contribution

Alireza Vahedi Nemani: Conceptualization, Investigation, Writing - original draft, Visualization.

Mahya Ghaffari: Methodology, Fabrication Process, Validation, Investigation, Review & Editing.

Ali Nasiri: Supervision, Writing - review & editing, Funding acquisition.

2.2.1. Abstract

Wire arc additive manufacturing (WAAM) is known to induce a considerable microstructural inhomogeneity and anisotropy in mechanical properties, which can potentially be minimized by adopting appropriate post-printing heat treatment. In this paper, the effects of two heat treatment cycles, including hardening and normalizing on the microstructure and mechanical properties of a WAAM fabricated low-carbon low-alloy steel (ER70S-6) are studied. The microstructure in the melt pools of the as-printed sample was found to contain a low volume fraction of lamellar pearlite formed along the grain boundaries of polygonal ferrite as the predominant micro-constituents. The grain coarsening in the heat affected zone (HAZ) was also detected at the periphery of each melt pool boundary, leading to a noticeable microstructural inhomogeneity in the as-fabricated sample. In order to modify the nonuniformity of the microstructure, a normalizing treatment was employed to promote a homogenous microstructure with uniform grain size throughout the melt pools and HAZs. Differently, the hardening treatment contributed to the formation of two non-equilibrium micro-constituents, i.e., acicular ferrite and bainite, primarily adjacent to the lamellar pearlite phase. The results of microhardness testing revealed that the normalizing treatment slightly decreases the microhardness of the sample; however, the formation of non-equilibrium phases during hardening process significantly increased the microhardness of the component. Tensile

testing of the as-printed part in the building and deposition directions revealed an anisotropic ductility. Although normalizing treatment did not contribute to the tensile strength improvement of the component, it suppressed the observed anisotropy in ductility. On the contrary, the hardening treatment raised the tensile strength, but further intensified the anisotropic behaviour of the component.

2.2.2. INTRODUCTION

Wire arc additive manufacturing (WAAM) is a novel technology capable of producing metallic components utilizing an arc welding process to additively fabricate engineering parts [128], with various applications such as impeller blades [129], bridge structures [130], shipbuilding plates [131], and wing ribs in the aerospace industry [132]. Different from the metal powder-based additive manufacturing processes, such as direct metal laser sintering (DMLS) and selective laser melting (SLM), wire arc additive manufacturing uses a consumable metallic wire as the feedstock material [74]. In WAAM, the entire consumable wire is continuously fed into an adopted electric arc or plasma, leading to an extremely high deposition rate as compared to that of the powder-based AM systems [6]. Therefore, wire-based systems are generally suitable for producing large-scale components with less complexity in geometry and design, in contrast to the powder-bed systems, which typically fabricate small and high-definition parts [72]. From another perspective, powder-bed additive manufacturing techniques are limited to a build envelope, but in wire-based systems, the torch is usually mounted on a robotic arm having more freedom of movement, implying that the component's size is not confined by a chamber.

During wire arc additive manufacturing process, the feedstock material is melted and deposited in the form of weld beads layer by layer on the previously solidified tracks. As the consecutive layers fuse into the previous ones, the material is built up until the near-net-shape component is completed [43]. Since the process is involved with sequential melting and solidification, each region of the component is subjected to periodic fast heating and cooling cycles by the deposition of upper layers. Such complex localized thermal cycles lead to heterogeneous microstructure and anisotropic mechanical

properties in the AM fabricated components [128,133,134]. This is one of the main drawbacks of the WAAM technique as compared to the conventional methods of manufacturing. Sridharan et al. [135] studied the microstructure and mechanical properties of low-carbon low-alloy steel (ER70S) built through additive manufacturing and reported anisotropic elongation percentage in different directions. They concluded that the anisotropy in mechanical properties is related to the inhomogeneous and localized microstructure [135]. Haden et al. [136] also investigated wire arc additive manufacturing of 304 stainless steel and reported graded wear and hardness properties in both deposition and building directions. Their findings showed that this anisotropy is due to the fluctuation in localized thermal histories, consequently leading to the formation of a variety of microstructures, from austenitic to solidification structures owning mixed ferrite morphology with abrupt texture changes at different regions of the sample [136].

In addition to the microstructural inhomogeneity, the formation of internal defects between the deposited layers as a result of high heat removal capacity from the inter-pass regions may deteriorate the mechanical properties of the additively manufactured components [8,74,135,137]. The inter-pass defects being formed in the fusion boundaries commonly include entrapped gas, porosities, and lack of fusion [138,139]. The presence of the mentioned discontinuities acting as a stress riser in the structure can potentially make crack initiation sites leading to premature brittle fracture under tension, which has been extensively investigated in a previous authors' publication [137].

Interestingly, the heterogeneous microstructure and anisotropic mechanical properties in a WAAM fabricated part can be minimized by applying a tailored post-printing heat treatment cycles [131]. For instance, Wang *et al.* [59] studied the effect of heat treatment on the anisotropic mechanical properties of a WAAM fabricated H13 steel. They reported that the homogeneous microstructure achieved by annealing heat treatment for four hours at 830 °C led to diminishing the anisotropic mechanical properties of the part. Xu *et al.* [140] also successfully minimized the microstructural inhomogeneity of a wire arc additive manufactured maraging steel part by performing a post-process heat treatment *i.e.,* solutionizing and aging, which resulted in a significant improvement in mechanical

properties of the WAAM fabricated component. Although applying a post-fabrication heat treatment has been previously reported by different studies [59,140,141], to the best of the authors' knowledge, heat treatment of WAAM ER70S-6 has not been investigated heretofore, except for one of the authors' previous studies [131], in which the impacts of a different heat treatment cycle (inter-critical austenitizing temperature) on the WAAM ER70S-6 microstructure and mechanical properties were investigated.

In this study, with the aim of homogenizing the microstructure and diminishing the induced anisotropy in an as-printed WAAM-ER70S-6 low-carbon low-alloy steel part, two heat treatment cycles, including normalizing (austenitizing followed by still-air cooling) and hardening (austenitizing followed by water quenching) from an upper-critical austenitizing temperature, were conducted on the as-printed samples. Microstructural and mechanical properties characterizations were carried out on both as-printed and heat-treated samples in different orientations, including deposition (horizontal) and building (vertical) directions.

2.2.3. EXPERIMENTAL PROCEDURE

2.2.3.1 Material, Fabrication Process, and Post-Fabrication Heat Treatment

In the present study, a wall of low-carbon low-alloy steel (ER70S-6) was fabricated using the wire arc additive manufacturing method utilizing a Lincoln Electric GMA machine with a torch mounted on a 6-axis Fanuc robot as the power source. To minimize the heat input of the WAAM process and be able to adjust the heat independent of the wire feed speed, an advanced current controlled surface tension transfer (STT) process was employed for fabrication. Utilizing the STT can further contribute to reducing the surface irregularities and spattering during the building process [142]. In order to smoothly feed the wire to the melt pool, the stand-off distance was held constant at 3 mm between the tip of the filler wire and the surface of the previous layer. Figure 2.2.1 schematically represents the set-up of the WAAM process.

Table 2.2.1 shows the nominal chemical composition of the ER70S-6 feedstock solid wire with 0.9 mm diameter manufactured by Lincoln Electric. The selected WAAM process parameters yielding the optimum bead quality and appearance with minimum spattering are listed in Table 2.2.2. ASTM A36 mild steel with a thickness of 12 mm was used as the substrate, which was attentively wire brushed and then cleaned by acetone to prevent contamination of the melt pools and the formation of gas pores during the solidification process. The whole part contained 50 consecutive layers, and each layer was comprised of six beads with a length of 135 mm and a 3 mm center-to-center overlap, resulting in a wall with a total width of 22 mm and a height of 150 mm. Employing a Thermo-Scientific Lindberg furnace, two heat treatment cycles were applied to the as-printed component, including (i) normalizing (austenitizing followed by still-air cooling), and (ii) hardening (austenitizing followed by water quenching). For initial austenitizing in both cycles, the samples were heated up to 900 °C for 1 hour. The purpose of the normalizing process was to homogenize the microstructure by producing a uniform grain size along the melt pools, fusion boundaries, and heat affected zones. The intention of the hardening heat treatment was also to increase the hardness and tensile strength of the component.

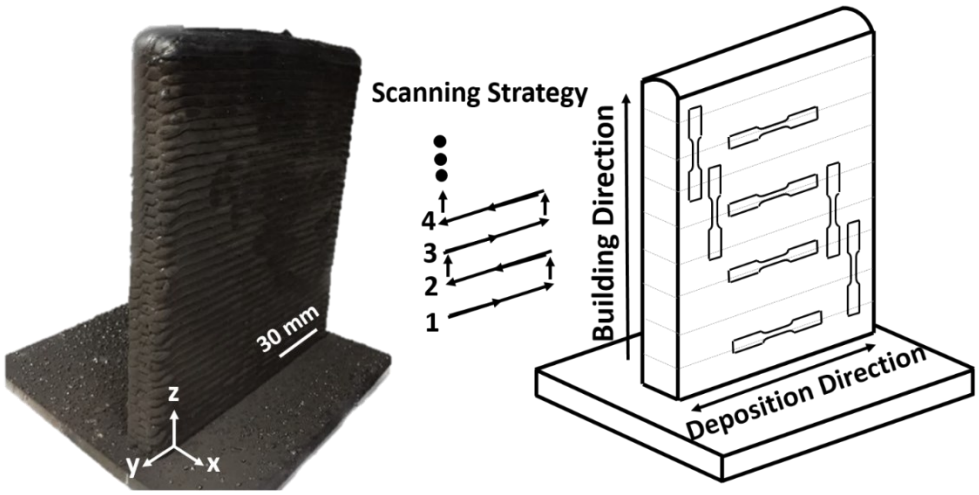

Figure 2.2.1 (a) Three-dimensional optical micrograph of the as-received conventionally rolled EH36 shipbuilding steel, (b) SEM micrograph from the side view of the rolled ship plate, and (c) higher magnification of the enclosed area in (b).

Table 2.2.1 The nominal chemical composition of the ER70S-6 feedstock wire (wt. %).

C	Mn	Si	S	P	Cr	Ni	Mo	V	Cu	Fe
0.06-0.15	1.40-1.85	0.80-1.15	0.04 max	0.03 max	0.15 max	0.15 max	0.15 max	0.03 max	0.5 max	Bal.

Table 2.2.2 The processing parameters used for the wire arc additive manufacturing of the low-carbon low-alloy steel (ER70S-6).

Average Arc Current	Arc Voltage	Wire Feeding Rate	Scanning Rate	Argon Flow Rate	Heat Input
135 A	28 V	104 mm/s	5 mm/s	20 L/min	7.56 kJ/cm

2.2.3.2 Microstructural Characterization

To prepare the samples for microstructural characterizations, a Tegramin-30 Struers auto-grinder/polisher was employed, then the samples were etched chemically using a 5 vol. % Nital reagent for 15-20 s [143]. The microstructure of the fabricated component was characterized at different regions from the bottom to the top of the wall to detect any microstructural changes throughout the whole part. To perform the microstructural characterization at different magnifications, an optical microscope (Nikon Eclipse 50i) and a field emission scanning electron microscope (FEI MLA 650F) were employed.

2.2.3.3 Mechanical Properties Evaluation

Microhardness distribution was measured and plotted along a line covering five successive layers through the building (vertical) direction on different zones including the center of the melt pools, fusion boundaries, and heat affected zones (HAZs), using a Buehler Micromet hardness test machine with the applied load of 300 g and an indentation time of 45 s. It should be noted that the reported data of microhardness are the average of five different measurements. The indentations were done on the polished and etched surfaces in order to distinguish the position of each indentation relative to the melt pool's geometry. Moreover, microhardness profiles were produced by subsequent

indentations with 300 µm intervals (approximately five times more than the diagonal of each indent) to avoid the work hardening effect.

Tensile test specimens from the as-printed and heat-treated samples were machined parallel and perpendicular to the building directions based on the ASTM E8m-04 standard sub-size specimen [144] with dimensions of 100 mm × 25 mm × 5 mm. The room temperature uniaxial tensile tests were carried out using an Instron load frame equipped with an extensometer at the crosshead speed of 8 mm/min. Each tensile test was repeated five times under the same conditions to obtain a reliable average value.

2.2.4. Results and Discussion

2.2.4.1 Microstructural Characterization

Figure 2.2.2a illustrates a low magnification OM micrograph of the as-printed sample showing the transition from the center of the melt pool to the melt pool boundary and then the heat affected zone. The dominant microstructure in the center of the melt pool consists of a low volume fraction of lamellar pearlite (P) primarily formed at the grain boundaries of polygonal ferrite (PF) (Figure 2.2.2b). Figure 2.2.2c depicts the SEM micrograph taken from the melt pool boundary region (denoted as the fusion boundary shown in Figure 2.2.2a) at higher magnification, revealing the formation of acicular ferrite (AF) and bainite (B) due to the faster cooling rate along the boundaries of each deposited bead as compared to its center. The aforementioned transition in the microstructure during 3D-printing of ER70S wire is also reported by Haselhuhn et al. [145]. In another investigation, Lee et al. [146] also studied the microstructure of the welded low-carbon low-alloy AH36 steel and similarly reported the formation of acicular ferrite and bainite near the fusion line.

It is well established that the presence of acicular ferrite and bainite constituents in the microstructure of steels can promote the mechanical properties of the component. This is primarily resulted from the finer structure of both phases, a more uniform distribution of carbide and higher dislocation density and internal stresses in the bainite phase, contributing to a higher hardness/strength and ductility in the alloy [118,147,148].

However, it should be noted that since the volume fraction of acicular ferrite and bainite constituents are negligible as compared to the dominant ferritic and pearlitic microstructure of the alloy, the presence of acicular ferrite and bainite cannot have a significant contribution to the mechanical properties of the WAAM-ER70S sample. On the other hand, according to Figure 2.2.2a, the microstructure of the HAZ consists of coarser grains of polygonal ferrite in comparison with the interior of the melt pool, as the thermal cycle associated with each depositing track facilitates the grain growth in the previous bead. The grain coarsening in the HAZ can potentially lead to a remarkable softening in this area, consequently resulting in a reduced localized strength and hardness in a sample that accommodates this region [149]. The formation of such microstructural inhomogeneity from the center of the melt pool to its boundaries and to HAZ is attributed to the overlapping scanning strategy associated with the multi-layer deposition nature of the WAAM process. Consequently, this process evokes various thermal cycles in different regions of the sample [150].

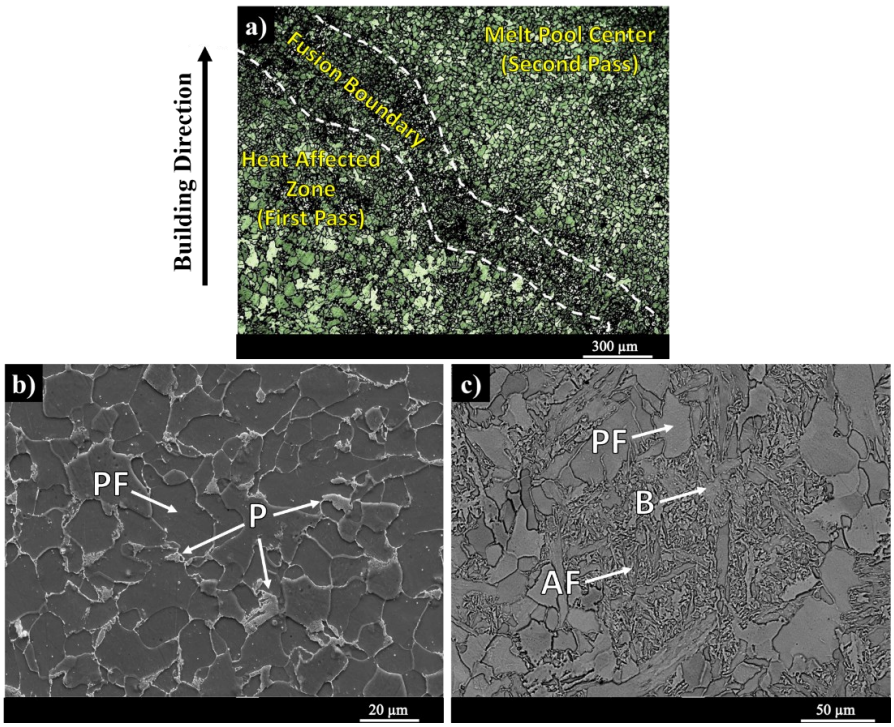

Figure 2.2.2 (a) Low magnification optical micrograph of the as-printed sample, (b) higher magnification SEM micrograph of the melt pool center, and (c) fusion boundary (PF: polygonal ferrite, P: lamellar pearlite, B: bainite, AF: acicular ferrite).

Post printing heat treatment is commonly used to modify the microstructure and, consequently the mechanical properties of an additively manufactured component [131,141]. Figure 2.2.3a-d depict the microstructure of the WAAM-ER70S-6 wall after applying different heat treatment cycles, including normalizing (Figure 2.2.3a, b) and hardening (Figure 2.2.3c-d) at different magnifications. According to the thermodynamically simulated continuous cooling transformation (CCT) diagram for the ER70S-6 wire [151], moderate cooling rates in the range of 10 - 100 °C/s results in a ferritic-pearlitic microstructure, while severe cooling rates in the range of 0.1 - 1 °C/s leads to the formation of non-equilibrium phases such as bainite. As indicated in Figure 2.2.3a, b, the normalizing heat treatment with moderate cooling rate from the austenitizing temperature of 900 °C, has not altered the pre-existing constituents of the microstructure of the as-printed sample. However, the grain size became more uniform and homogenous from the center of each melt pool toward the heat affected zone in the adjacent track. In other words, the grain coarsening in the heat affected zone was eliminated after normalizing heat treatment.

For the initial austenitizing step, the sample was heated up to 900 °C, where γ is the only stable phase since the Ac_3 temperature of the alloy was calculated to be at ~ 883 °C, using a reported empirical equation that predicts austenite formation temperatures, *i.e.*, Ac_1 and Ac_3, for the low-alloy steels with less than 0.6 wt. % C [152]. Subsequently, uniformly distributed austenite grains nucleate and grow evenly in any region of the material during austenitization. Following the full austenitization of the microstructure, the sample is subjected to a relatively slow cooling by exposing the sample to room temperature. The slow cooling rate associated with the normalizing heat treatment hinders the formation of unstable or metastable phases, such as bainite or martensite, during the normalizing heat treatment. Therefore, the microstructure of the sample in terms of the formed constituents was analogous to the dominant microstructure of the as-printed sample containing polygonal ferrite, pearlite and precipitation of tertiary cementite, whilst the grains obtained a more homogeneous and uniform distribution after the normalizing heat treatment. The precipitation of the tertiary cementite in the ferrite grain boundaries, as a high energy site for nucleation of a new phase, has been also reported in other grades of

low-carbon steels family [153,154]. Natividad *et al.* [117] also performed the normalizing heat treatment on Grade X70 pipeline steel and reported the formation of polygonal ferrite and pearlite areas with more homogenous and uniform microstructure in comparison with the as-received material. Figure 2.2.3c-d illustrate the microstructure after hardening heat treatment, which is a mixture of pearlite, bainite and acicular ferrite.

In the case of hardening heat treatment cycle, the sample was exposed to an extremely high cooling rate (water quenching), resulting in the formation of the meta-stable bainite and acicular ferrite phases besides the lamellar pearlite phase. It should be mentioned that similar to the scenario of the normalizing heat treatment, the hardening heat treatment also resulted in the formation of a homogeneous microstructure with a uniform grain size throughout the sample from the bottom to the top of the WAAM fabricated wall. The formation of the acicular ferrite and bainite phases by quenching of the sample at higher cooling rates from the austenite stability region has also been reported in other low-carbon low-alloy steels, such as API X70 and X80 [117,118,147].

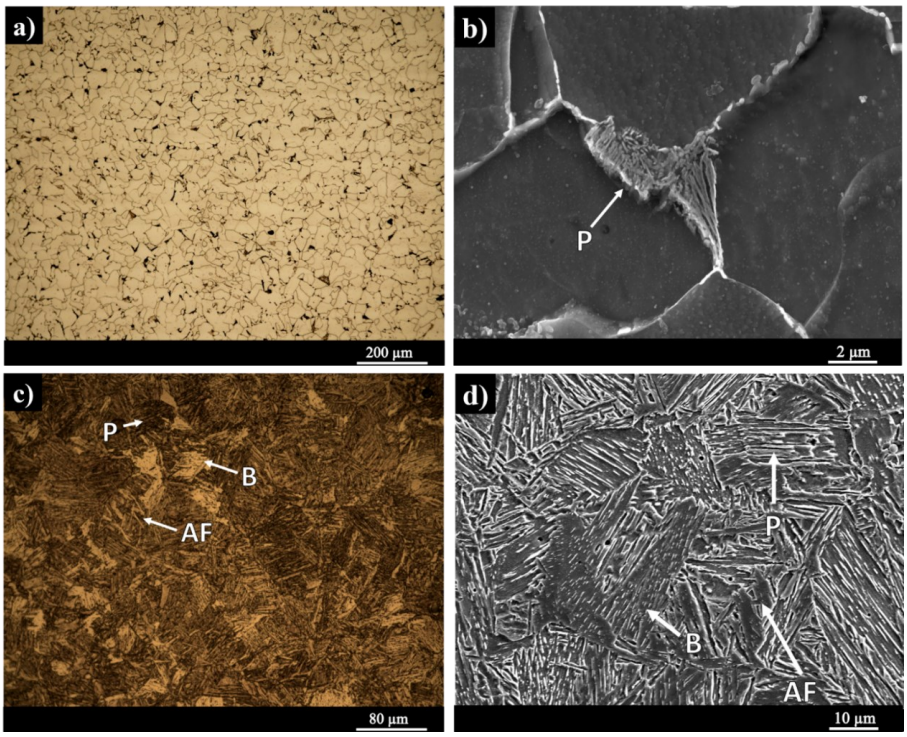

Figure 2.2.3 The microstructure of the normalized sample (a and b), and hardened (water-quenched) sample (c and d) at different magnifications.

2.2.4.2 Mechanical Properties Evaluation

Figure 2.2.4 shows the microhardness profile of the as-printed and heat-treated samples along a line covering five consecutive layers through the building (vertical) direction on different zones, including the center of the melt pools, fusion boundaries, and heat affected zones (HAZs). The overall microhardness of the as-printed sample was 160 ± 7 HV, which showed a relatively significant fluctuation from a minimum of 150 ± 1 HV to 160 ± 2 HV, and then to the maximum of 175 ± 2 HV. The observed fluctuation was ascribed to the presence of different phases along the melt pool center, the fusion boundary, and the heat affected zone. In particular, the lowest amount of microhardness (150 ± 1 HV) corresponded to the HAZ containing coarser polygonal ferrite grains than the rest of the fusion zone, and the maximum microhardness (175 ± 2 HV) was correlated to the fusion boundaries, where acicular ferrite and bainite constituents exist. The center of the melt pool, owning the dominant microstructure of the component (lamellar pearlite and polygonal ferrite), revealed the microhardness of 160 ± 2 HV. The fluctuations in the microhardness values were considerably lower in both hardened (water-quenched) and normalized samples as compared to the as-printed component due to the homogeneity of the microstructure in the heat-treated samples.

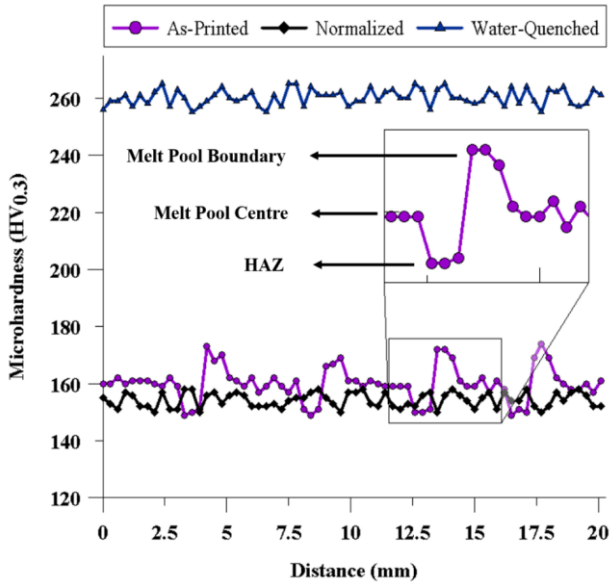

Figure 2.2.4 Vickers microhardness profile of the as-printed and heat-treated samples along a line covering five successive layers through the building (vertical) direction.

The normalized sample with a microstructure analogous to the dominant microstructure of the as-printed sample showed the microhardness of 154 ± 1 HV, comparable to that of the center of the melt pools in the as-printed sample. It is also worth noting that the microhardness of the normalized sample was slightly decreased after the heat treatment, primarily due to (i) the stress relieving occurred during heating to austenitizing temperature, (ii) diminishing of lattice defects formed during the rapid solidification associated with the WAAM, (iii) potential growth of primary austenite grains [155], and (iv) omitting the acicular ferrite and bainite phases from the microstructure of the fusion boundaries. Contrarily, the microhardness of the hardened (water-quenched) sample was 260 ± 3 HV, drastically higher than the other samples, ascribing to its microstructure, including pearlite, bainite, and acicular ferrite as the predominant micro-constituents in its structure. It has been reported that the presence of bainite, along with a finer microstructure, can increase the microhardness of low-carbon steels [155]. However, it should also be noted that a higher microhardness is not always beneficial to the overall mechanical performance of the material since the ductility and toughness of the alloy could potentially be degraded. The adverse effect of existing hard micro-constituents can be more crucial particularly in the case of samples manufactured by a welding process, which are usually prone to the presence of welding defects, discontinuities, and residual stresses. Such discontinuities can readily propagate into a brittle microstructure and form internal micro-cracks during the tensile loading of the sample.

Figure 2.2.5 shows the engineering tensile stress-strain curves for the as-printed and heat-treated WAAM-ER70S-6 samples in the building (vertical) and deposition (horizontal) directions. In the as-printed component, the vertical and horizontal tensile strengths were approximately similar (~500 MPa). However, the ductility (elongation percentage) of the vertical sample only reached to 12 ± 3 %, whereas the horizontal sample showed a significantly higher ductility at 35 ± 2 %, indicating a large plastic deformation prior to the fracture with an obvious necking phenomenon. Therefore, the results of tensile testing of the as-printed part revealed anisotropy in ductility. Wang *et al.* [21] investigated the anisotropy in the mechanical properties of the additively manufactured 304L stainless steel parts, and reported that the elongation percentage in the transverse direction was

higher compared to the longitudinal direction, while the tensile strength was fairly isotropic. The substantial lower ductility of the vertical samples as compared to the horizontal ones herein can be justified by (i) the existence of solidification imperfections and flaws, such as inter-pass lack of fusion (LOF) and (ii) the HAZ softening as a result of grain coarsening. Since the long axis of the inter-pass lack of fusions is perpendicular to the loading direction in the vertical samples, the sharp edges of these defects can serve as stress concentration sites, causing the propagation of the discontinuity in the vertical samples during uniaxial tensile loading, but not in the horizontal ones [137]. A similar observation was also reported by Wang *et al.* [156]. In another study, Lopez *et al.* [138] demonstrated the formation of manufacturing defects in the wire arc additive manufacturing of ER70S-6 using different nondestructive examination methods including radiographic testing (X-ray), liquid penetrant inspection (LPI), and ultrasonic testing (UT), and reported the presence of the LOF defect between the deposited layers.

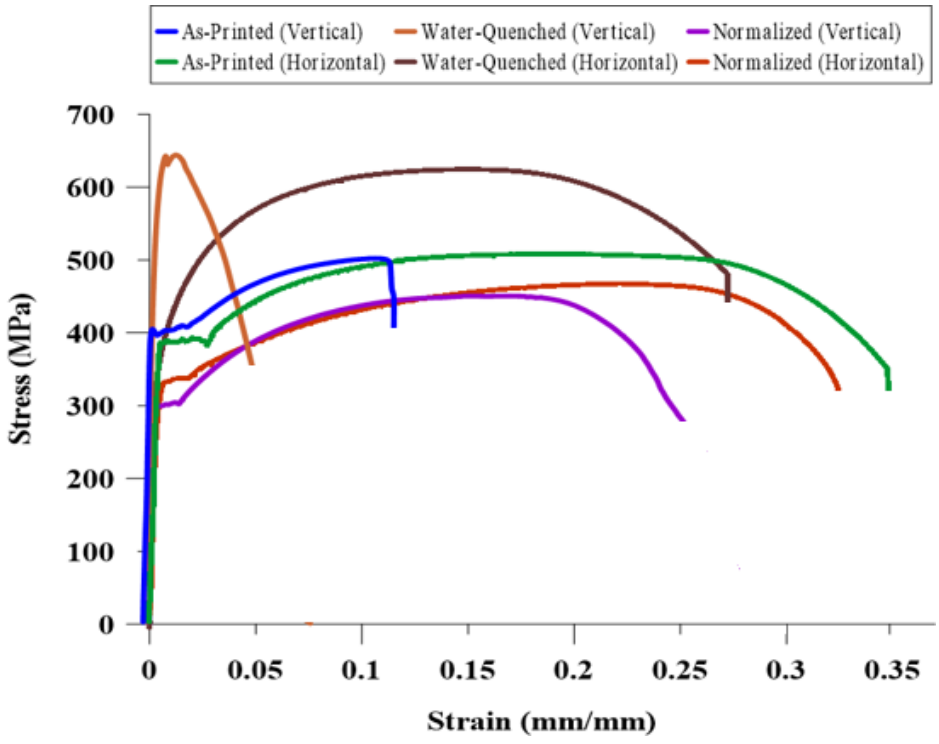

Figure 2.2.5 The stress-strain curves for the as-printed and heat-treated samples in the building (vertical) and deposition (horizontal) directions.

The anisotropy in the mechanical properties has been reported as a common issue in various metals and alloys produced by additive manufacturing processes [37,157,158], which can be minimized by applying proper post-printing heat treatment cycles [131,141]. Hardening treatment could increase the tensile strength of the WAAM-ER70S steel from ~ 500 MPa for the as-printed sample to 640 ± 14 MPa and 624 ± 13 MPa in vertical and horizontal heat-treated samples, respectively. This improvement in the tensile strength of the hardened alloy is attributed to its bainitic, acicular ferritic, and pearlitic microstructure with ~ 62 % higher microhardness compared to the as-printed sample. However, the ductility of the hardened samples was reduced by 4 % and 7 % for the vertical and horizontal samples, respectively. Although, the horizontal sample with the UTS value of 624 ± 13 MPa and elongation of 28 ± 2 % plausibly satisfies the mechanical integrity requirement for the service conditions of this alloy, the anisotropic mechanical behaviour of the component cannot be diminished since the sample revealed a severe brittle fracture in the vertical direction with only 8 ± 1 % elongation. It should be mentioned that in the case of the as-printed vertical sample, the formation of some defects, flaws, and also possible weak metallurgical bonding between the layers (lack of fusion) can potentially reduce the degree of plastic deformation that the material can accommodate before its failure. This scenario can be intensified when the microhardness increases from 160 ± 7 HV for the as-printed sample to 260 ± 3 HV for the hardened sample. Consequently, as a result of the hardening cycle, the ultimate tensile strength increased at the expense of a reduction in ductility. Overall, it can be inferred that the hardening heat treatment exhibited a positive effect on the mechanical properties in the horizontal direction but was not found beneficial to the vertical sample, leading to its brittle fracture during the uniaxial tensile loading.

On the other hand, the normalizing process that contributed to the formation of a homogenized microstructure, characterized by a uniform grain size along the center of the melt pool, fusion boundary, and the heat affected zone could increase the tensile strength neither in horizontal nor in the vertical samples. Similar to the slight reduction in the microhardness of the normalized sample, its tensile strength was expected to be slightly lower (~465 MPa) than the as-printed sample (~500 MPa). Moreover, a closer

look at the stress-strain curves of the normalized samples revealed that there is not a huge difference between the elongation of the component in the vertical (29 ± 2 %) and horizontal (34 ± 3 %) directions. It should be mentioned that the purpose of the normalizing cycle was to eliminate the inhomogeneous microstructure resulted from the complex thermal cycles associated with the layer-by-layer deposition nature of the wire arc additive manufacturing process. As a consequence of heating the sample up to a temperature above the upper critical temperature (Ac3), and formation of new austenite grains, the inhomogeneous microstructure including coarse grains of HAZ was totally eliminated. Accordingly, during the cooling process in still-air, the whole part experiences a similar cooling rate leading to a uniform microstructure at different zones of the sample. Therefore, the anisotropy in the elongation can be eliminated or weaken through modifying the microstructure from an inhomogeneous one to a homogenized microstructure with a uniform grain size.

Figure 2.2.6 demonstrates the reduction of area (RA) for the as-printed and heat-treated samples in both vertical and horizontal directions. The stereomicroscope images of the fractured surfaces are also attached to each point of the plot in order to clarify the brittle or ductile nature of the fracture in different samples. The results of fractography investigations revealed that horizontal samples experienced an entire ductile fracture, while the vertical specimens showed a mixed mode of ductile-brittle fracture, which is consistent with the results obtained from the uniaxial tensile testing (see Figure 2.2.5). As clearly shown in Figure 2.2.6, there is a considerable difference between the RA values of the horizontal and vertical tensile samples in both as-printed and hardened conditions, implying a significant anisotropy in ductility of the component. However, the RA values of the normalized sample in the vertical and horizontal directions are relatively close to each other, indicating a negligible anisotropy in ductility. Therefore, normalizing treatment can be utilized as a post-printing cycle to minimize the anisotropic behaviour of the wire arc additively manufactured low-carbon low-alloy steel (ER70S-6) by homogenizing the grain size and eliminating the inhomogeneous microstructure through the melt pool center, fusion boundary, and the heat affected zone.

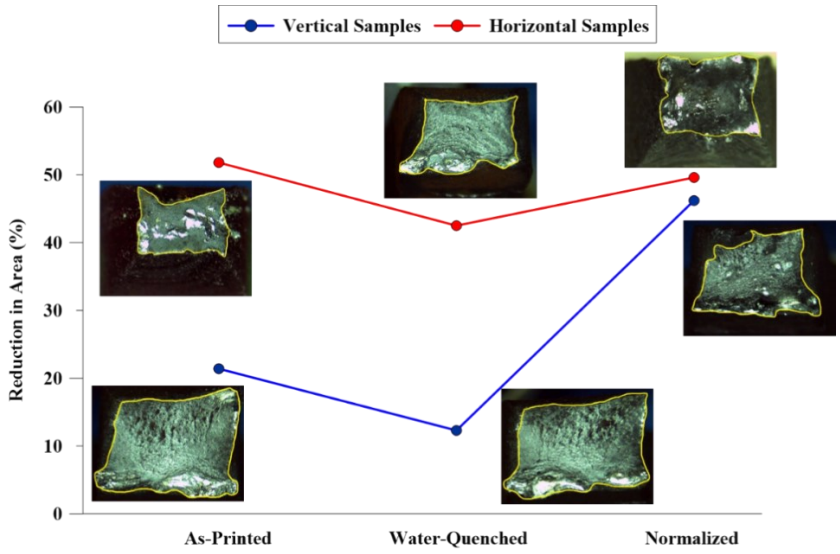

Figure 2.2.6 The reduction in area (RA) for the as-printed and heat-treated samples in both vertical and horizontal directions.

2.2.5. CONCLUSIONS

This study aimed to investigate the effect of two post-printing heat treatment cycles, including normalizing and hardening, on the microstructure and mechanical properties of a wire arc additively manufactured low-carbon low-alloy steel (ER70S-6). The following are the key conclusions of the study:

1. The dominant microstructure of the as-printed WAAM-ER70S-6 component consisted of polygonal ferrite grains along with a small volume fraction of lamellar pearlite formed at the ferrite grain boundaries. In addition, the formation of acicular ferrite and bainite constituents were detected as the primary phases along the melt pool boundaries. Furthermore, a heat affected zone comprised of coarser polygonal ferrite grains adjacent to each deposited track in the previously solidified bead also formed, associated with the layer-by-layer deposition nature of the process, inducing multiple heating cycles on each deposited track.
2. Normalizing heat treatment eliminated the meta-stable constituents, i.e., acicular ferrite and bainite, from the as-printed microstructure, leading to a more uniform and homogeneous ferritic/pearlitic microstructure within the melt pool center, fusion boundaries, and the heat affected zone. On the contrary, the hardening heat

treatment altered the microstructure of the as-printed part to a combination of pearlite, bainite, and acicular ferrite.

3. Microhardness of the as-printed sample slightly decreased from 160 ± 7 HV to 154 ± 1 HV after the normalizing heat treatment, while the hardening treatment could increase the microhardness to 260 ± 3 HV.
4. Uniaxial tensile testing of the as-printed samples indicated a comparable tensile strength in horizontal and vertical samples, while a considerable anisotropy in the ductility with 35 ± 2% and 12 ± 3% of elongation, in horizontal and vertical directions, respectively, was apparent.
5. Although the hardening heat treatment could increase the tensile strength of the component by around 20%, it intensified the anisotropy in the ductility of vertical and horizontal samples.
6. The anisotropy in ductility was minimized by normalizing heat treatment due to the removal of the coarse grain regions in the HAZ and the resultant uniformity and homogeneity of the microstructure.

ACKNOWLEDGMENT

The authors gratefully acknowledge the support of the Natural Sciences and Engineering Research Council of Canada (NSERC) [grant number RGPIN-2017-04368] and Memorial University of Newfoundland for sponsoring this work.

CHAPTER 3 Effect of Interpass Temperature and Post-printing Austenitizing-Tempering Heat Treatment on the Microstructural Features and Mechanical Properties (Secondary Hardening) of a Wire Arc Additive Manufactured Martensitic Stainless Steel (ER420)

3.1 Effects of Post-Printing Heat Treatment on the Microstructure and Mechanical Properties of a Wire Arc Additive Manufactured 420 Martensitic Stainless Steel Part

Alireza Vahedi Nemani[1], Mahya Ghaffari[1], Salar Salahi[2], Ali Nasiri[3]

1- Graduate Student, Dalhousie University, Halifax, Nova Scotia, Canada

2- Graduate Student, Memorial University, St. John's, Newfoundland, Canada

3- Assistant Professor, Dalhousie University, Halifax, Nova Scotia, Canada

Status: Published Journal Paper, Journal of Materials Science and Engineering: A (IF= 5.234), Volume 813, Issue 12, Pages 141167

Authors' Contribution

Alireza Vahedi Nemani: Conceptualization, Investigation, Writing - original draft, Visualization.

Mahya Ghaffari: Methodology, Fabrication Process, Validation, Investigation, Review & Editing.

Salar Salahi: EBSD Analysis, Review & Editing.

Ali Nasiri: Supervision, Writing - review & editing, Funding acquisition.

3.1.1. Abstract

In this study, microstructural features and mechanical properties of a wire arc additively manufactured 420 martensitic stainless steel were investigated in as-printed and heat-treated conditions. Initial microstructural investigations on the as-printed part revealed the formation of residual δ-ferrite during the solidification process, which is known as a deleterious phase to both mechanical and corrosion performance of stainless steels. To remove the residual δ-ferrite and obtain a fully martensitic microstructure, the as-printed samples were subjected to different austenitizing temperatures of 950, 1050, 1150, and 1300 °C. Austenitizing at 1150 °C was selected as the optimum cycle due to removal of undesirable phases, such as δ-ferrite and carbides, resulting in a fully martensitic microstructure. Following the austenitizing heat treatment, the samples were tempered at

different temperatures including 200, 300, 400, 500, and 600 °C. Increasing the tempering temperature was found to vary the size, morphology, and distribution of chromium carbides precipitated during the tempering process. Although, tempering at lower temperatures (200 and 300 °C) decreased the hardness due to the formation of tempered martensite and stress relieving of the structure, the intermediate temperature of 400 °C increased the hardness value by virtue of the formation of carbides at optimum size and distribution. However, tempering at 500 and 600 °C decreased the hardness as compared to 400 °C due to intergranular accumulation and coarsening of carbides. The results of uniaxial tensile testing were consistent with the hardness measurements and confirmed that the tempering temperature of 400 °C led to the optimal combination of strength and ductility ascribed to the formation of fine and homogenously distributed chromium carbides embedded in a moderately tempered martensitic matrix.

3.1.2. INTRODUCTION

Martensitic stainless steels (MSS) are one of the most common industrial materials being widely used for fabrication of die-casting molds, mixer blades, steam generators, surgical tools, offshore platforms, and pressure vessels due to their superior mechanical performance and acceptable corrosion resistance [159–162]. Martensitic stainless steels are not generally categorized as easily formable metals due to their high hardness and low ductility. This constraint stimulates the need for advanced fabrication methods, such as 3D-printing, capable of producing the whole component in one fabrication step.

Wire arc additive manufacturing (WAAM) is a newly developed and fast-evolving fabrication method of large-scale metallic materials that yields a near-net-shape part with a high production rate and low environmental contaminants [8,163]. This method employs an electric arc as the heat source, and is based on incremental layer-by-layer deposition using a continuous wire as the feedstock material [14,74]. In contrast to powder-based additive manufacturing techniques, WAAM does not require an enclosed and protected building envelope, leading to the enhanced cost-efficiency of the process, and also eliminates the geometry and size restrictions of the fabricated parts [164,165]. In the past decade, WAAM has been considered as a promising manufacturing technique for

producing a large number of industrial materials, such as nickel [166], titanium [167], aluminium alloys [168], and steels [18].

However, the complex thermal history associated with the WAAM process, in particular rapid solidification and frequent heating and cooling cycles, results in the formation of a non-homogeneous microstructure containing non-equilibrium micro-constituents, which could potentially impact the final mechanical performance and corrosion properties of the end-product [7,128,169,170]. Ge *et al.* [35] studied the effect of local thermal history on the microstructure and mechanical characteristics of a WAAM 2Cr13 MSS fabricated using a gas metal arc welding (GMAW) power source equipped with cold metal transfer mode. They found that the cooling rate of the initial layers of the wall was 7–11 times higher than that of the middle and top regions, and also reported that the relative fraction of martensite to ferrite gradually increased from the 5^{th} to the 25^{th} layer of the WAAM wall, which can be related to the thermally-induced solid state transformation of martensite to ferrite [35]. In another similar study by Ge *et al.* [171], a periodic microhardness profile was reported due to the variation in the martensite lath size as a result of the location-related thermal history experienced by the material during wire additive manufacturing process.

The rapid solidification nature of WAAM for the 420 MSS in particular leads to the formation of non-equilibrium residual δ-ferrite phase at room temperature [42,43], which is considered as a detrimental phase in MSSs family [44,45]. The presence of δ-ferrite not only deteriorates the mechanical properties of the fabricated part [46], but also adversely affect the corrosion performance of the material [47]. It has been reported that both toughness and hardness of steels can be reduced by the formation of δ-ferrite at room temperature [48]. Wang *et al.* [172] studied the influence of δ-ferrite on the impact toughness of 13Cr–4Ni MSS and reported that the presence of δ-ferrite decreased the energy required for nucleation and growth of cracks, and also changed the fracture mode from dimple to quasi-cleavage, resulted from the increased ductile-to-brittle transition temperature of the alloy. Moreover, Cr-rich δ-ferrite triggers the sensitization phenomena in its adjacent area and causes selective corrosion attack in the Cr-depleted zones [173–

175]. Therefore, a proper post-fabrication heat treatment process is usually needed to modify the microstructure of the additively manufactured components and improve the in-service performance of the material [14,131].

In contrast to other types of stainless steels, MSSs are highly responsive to heat treatment and accordingly a wide range of mechanical properties can be obtained under different heat treatment conditions [160]. Depending on the implemented heat treatment cycle and the chemical composition of the alloy, MSSs may consist of a broad range of micro-constituents including martensite, retained austenite, α-ferrite, residual δ-ferrite, and undissolved carbides [176]. Therefore, it is critical to select an ideal post-fabrication heat treatment cycle to avoid the formation of undesirable phases, such as untempered martensite or residual δ-ferrite, and also obtain an optimal combination of strength and ductility. The heat treatment cycle of MSSs is essentially similar to the hardening treatment of low-alloy and plain-carbon steels, which includes austenitizing, quenching, followed by tempering treatments [162,176]. However, MSSs are more sensitive to the heat treatment variables stemmed from their higher content of alloying elements. For example, the formation of carbides in the microstructure during the heating cycle postpones the austenitizing process and results in an inhomogeneous distribution of alloying elements in the primary austenite grains since the maximum solubility of austenite strongly varies by temperature. Barlow *et al.* [176] studied the influence of austenitizing temperature on the microstructure of AISI 420 alloy, and reported that higher austenitizing temperatures lead to further dissolution of carbides and decrease the martensite start and finish temperatures, resulting in a higher risk of retained austenite formation. Moreover, during the tempering process, further formation of alloy carbides, such as M_7C_3 and $M_{27}C_6$ at a specific temperature range can provide precipitation hardening [160]. Bonagani *et al.* [177,178] reported that tempering of 13 wt. % Cr MSS at 550 °C can deteriorate the performance of the alloy by facilitating the hydrogen embrittlement and the pitting tendency of the material. Therefore, to be able to tailor the desired microstructure possessing an excellent combination of mechanical and corrosion properties in the alloy, an optimum heat treatment cycle should be carefully developed for the as-printed alloy.

The details of such optimized heat treatment cycle, *i.e*. austenitizing and tempering cycles, primarily depend on the starting chemical composition and the initial microstructure of the alloy and these can vary drastically by changing the implemented fabrication process or the feedstock material. This study aims to develop an optimal heat treatment cycle that leads to enhanced mechanical properties for a wire arc additive manufactured 420 MSS through a comprehensive microstructural and mechanical properties investigation of the heat-treated samples at different austenitizing and tempering temperatures.

3.1.3. EXPERIMENTAL PROCEDURE

3.1.3.1 Materials and Fabrication Process

In this study, 420 martensitic stainless steel thin-wall components were fabricated by gas metal WAAM employing an S-350 Power Wave Lincoln Electric GMAW power source equipped with an advanced surface tension transfer (STT) arc mode. Fig. 3.1.1a illustrates the set-up and different equipment used for the fabrication process. The electric arc between the wire and the sample was also shielded using a 99.9% pure argon gas to prevent exposure of the melt pool to environmental contaminations, oxide inclusions, porosities, and spattering. A 6-axis Fanuc robot was employed in order to provide the required degrees of freedom for the heat source to follow the deposition pattern. It is well-established that the STT mode provides a more controlled heat input and smooth deposited beads with minor defects, such as interpass lack of fusion or spattering, during the fabrication process [29]. Table 3.1.1 shows the optimum WAAM process parameters selected based on the minimal spattering and the highest bead quality with the lowest surface irregularities. AWS A5.9-17 Class ER-420 solid wire manufactured by United States Welding Corporation, with a diameter of 1.14 mm and nominal chemical composition (wt. %) listed in Table 3.1.2, was used as the feedstock material. The standoff distance between the feedstock wire and previously deposited track was kept around 3 mm during the whole deposition process. An interpass dwell time of 10 min was applied in order to prevent the accumulation of heat during the deposition of consecutive beads. It is notable that the sample was fabricated on a 25 mm thick AISI 420 stainless

steel substrate, which was thoroughly degreased and cleaned by acetone before the fabrication process to prevent the formation of gas porosities in the printed structure. It should be noted that the metallurgical bonding between the WAAM fabricated 420 stainless steel and the AISI 420 stainless steel substrate has been studied in a previous publication by the authors [43].

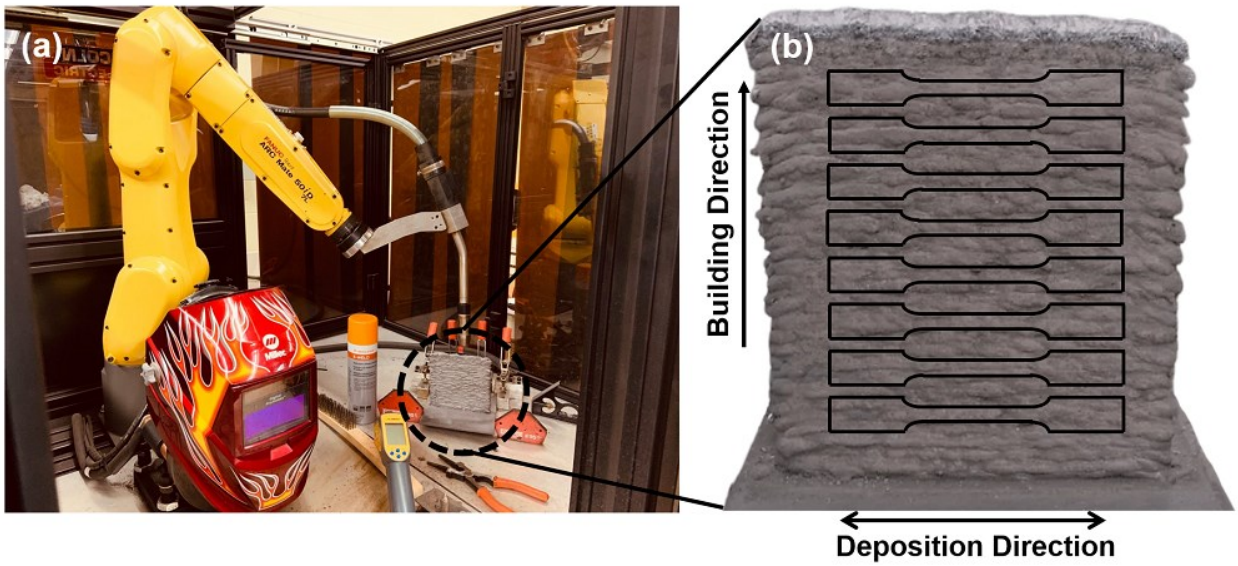

Figure 3.1.1 (a) The fabrication set-up and different equipment used for wire arc additive manufacturing of 420 MSS wall, and (b) the WAAM fabricated 420 MSS wall showing the tensile samples' orientation.

Table 3.1.1 The optimum WAAM processing parameters used for fabrication of the 420 MSS wall.

Arc Current	Arc Voltage	Wire Feeding Rate	Scanning Rate	Argon Flow Rate
135 A	29 V	67.7 mm/s	3.6 mm/s	20 L/min

Table 3.1.2 Nominal chemical composition (wt.%) of the ER-420 feedstock solid wire.

Cr	C	Si	Mn	Ni	Mo	P	S	Cu	Al	Fe
12-14	0.3-0.4	0-1	0-1	0-0.5	0-0.5	0-0.04	0-0.03	0-0.5	0-0.05	Bal.

3.1.3.2 Post-fabrication Heat Treatment Process

Employing a Thermo-Scientific Lindberg furnace, the as-printed WAAM fabricated 420 MSS samples were subjected to post-fabrication heat treatment in order to eliminate microstructural inhomogeneities, undesirable phases, and ultimately improve the mechanical properties. It is important to note that since the initial microstructure of a WAAM 420 MSS sample is different from commercially available AISI 420 plates, the optimum temperatures of different stages of heat treatment cycles might vary from those recommended in the literature for the conventionally fabricated AISI 420 alloy. Therefore, to optimize the post-fabrication heat treatment process, a variety of austenitization and tempering temperatures were selected, and the effect of different heat treatments on the microstructure and resultant mechanical properties of a WAAM fabricated 420 MSS component were comprehensively characterized. Accordingly, the samples were first austenitized for 30 min at different temperatures of 950, 1050, 1150, and 1300 °C, then quenched in still air to room temperature. As the second stage of the heat treatment, the as-quenched samples were subjected to a two-hour tempering process at different temperatures including 200, 300, 400, 500, and 600 °C, followed by air cooling. The austenitized and quenched samples were denoted by A950, A1050, A1150, A1300, and the tempered samples were named as T200, T300, T400, T500, and T600. To prevent surface oxidation and decarburization during the heating process, 99.9% pure argon gas was purged into the furnace during the heat-treating process.

3.1.3.3 Microstructural Characterizations

Metallographic specimens with the dimensions of 5 mm × 10 mm × 10 mm from both as-printed and heat-treated samples were sectioned using a water jet cutting machine. Then, the samples were hot mounted, ground, and polished to a surface roughness of ~0.25 μm using an automatic Tegramin-30 Struers auto-grinder/polisher. To reveal the microstructural features, the samples were immersed for ~20 s in Vilella's reagent composed of 1 g picric acid, 5 ml hydrochloric acid, and 100 ml ethanol. All samples were then characterized using an optical microscope (OM) (Nikon Eclipse 50i), field emission scanning electron microscope (SEM) (FEI MLA 650F), and Cu-K_α X-ray

diffraction (Rigaku Ultima IV) at 40 kV and 44 mA with a step size of 0.02° in an angle range of 40°-100°. For quantitative comparison of the size and volume fraction of the micro-constituents, SEM images taken from five different locations of each sample were analyzed using ImageJ software. Moreover, electron backscattered diffraction (EBSD) analysis was also carried out to acquire additional information about crystallographic orientation and texture of the fabricated samples. The EBSD analysis was performed using a Nordlys II HKL EBSD detector (Oxford Instrument) with a step size of 0.7 μm and a tilt angle of 70°, covering an area of 500 × 500 μm^2. The acquired raw EBSD data was post-processed using HKL Inc. software, also commercially known as Channel 5.

3.1.3.4 Mechanical Properties Measurements

In order to study the effect of applied heat treatments on the mechanical properties of WAAM-420 MSS components, hardness and uniaxial tensile testing were conducted on both as-printed and heat-treated samples. Hardness values were measured on the as-polished samples using a Buehler Micromet microhardness testing machine under the load of 3 N and a dwell time of 45 s. The room-temperature tensile performance of the samples was also evaluated utilizing a 5585H Instron load frame with 1 mm/min strain rate. A 25 mm-gauge extensometer was connected to the tensile samples to accurately measure the strain values during the uniaxial tensile testing. According to the ASTM E8m-04 standard [179], the dimensions of the tensile test specimens were selected as 25 mm gauge length, 4 mm width, and 5 mm thickness. As shown in Fig. 3.1.1b, the tensile specimens were prepared along the deposition (horizontal) direction of the fabricated wall. In order to obtain accurate results and avoid outliers during the mechanical testing, hardness values were measured ten times and tensile tests were repeated at least three times in each condition.

3.1.4. RESULTS AND DISCUSSION

3.1.4.1 Microstructural Evaluations

3.1.4.1.1 As-printed Sample

Fig. 3.1.2 shows the OM and SEM images taken from the microstructure of the as-printed WAAM 420 MSS sample at different magnifications in addition to the corresponding EDS elemental maps of Cr and Fe. According to the 13%Cr pseudo-binary phase diagram of AISI 420 alloy [180], the microstructure of the sample under the equilibrium cooling condition is expected to include chromium carbides embedded in a ferritic matrix. However, the relatively high cooling rate associated with the WAAM process along with the high hardenability of the alloy resulted in the formation of a martensitic matrix in the as-printed condition [43]. The absence of carbides can also be ascribed to the rapid solidification and high cooling rates, which could hinder the diffusion process and formation of carbides in the as-printed sample. In addition, residual δ-ferrite (δF) patches, with an approximate volume fraction of 20 %, were also distributed in the inter-dendritic regions of the martensitic (M) matrix as indicated by white arrows in Fig. 3.1.2. The higher magnification image (Fig. 3.1.2b) also confirms that the lath morphology entirely disappears in the δ-ferrite region. The stabilization of δ-ferrite at room temperature is related to the presence of high Cr content as a ferrite stabilizing element and also the rapid solidification process, which decelerated the diffusion-controlled transformation of δ-ferrite to austenite at around 1400 °C [48,172]. The EDS elemental maps (Fig. 3.1.2c and d) also confirm the higher content of Cr as a ferrite promoter in the Fe-depleted δ-ferrite regions. It is worth mentioning that the δ-ferrite phase is reported to be a potential crack nucleation site [172,181], and should be eliminated from the structure through applying a proper post-fabrication heat treatment cycle [48,172,182].

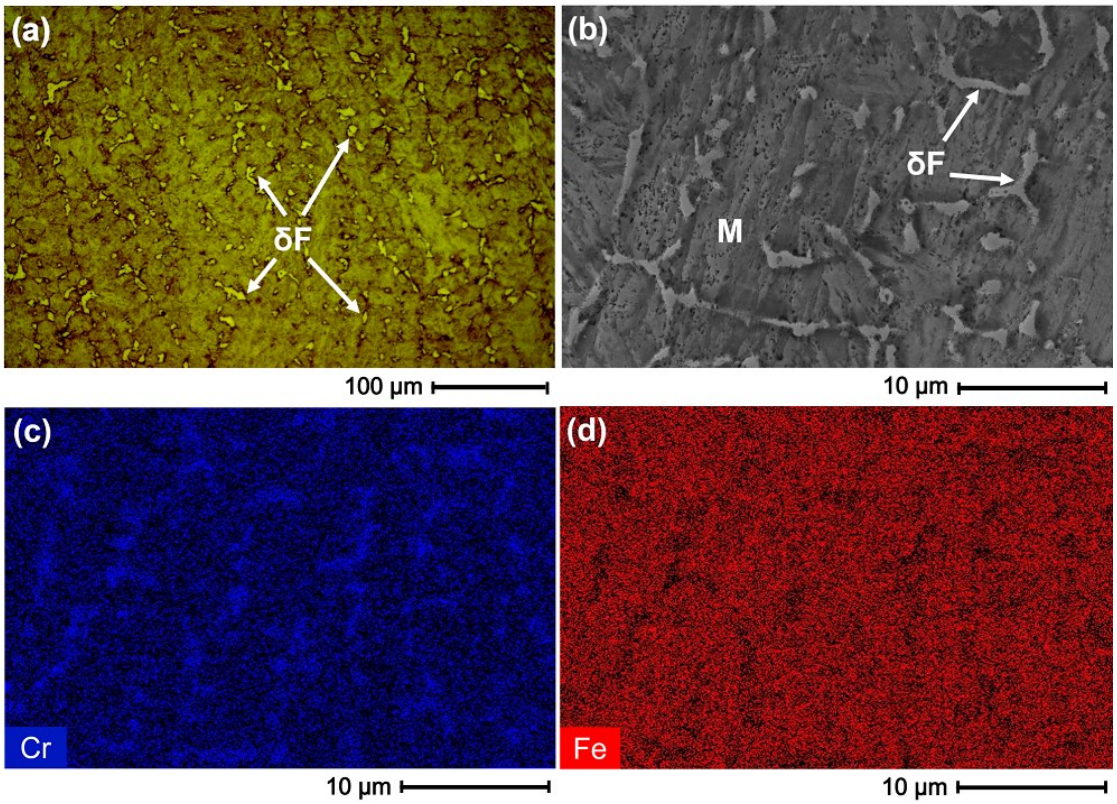

Figure 3.1.2 (a) OM, (b) SEM images, (c) & (d) EDS elemental maps of Cr and Fe taken from the microstructure of the as-printed WAAM MSS 420 sample.

3.1.4.1.2 Heat-treated Samples

3.1.4.1.2.1 Austenitized Samples

Since austenitizing is usually the first step of most heat treatment cycles for ferrous alloys, selecting the austenitizing temperature is of great importance due to its further considerable impact on the resultant microstructure upon the cooling cycle. In order to optimize the austenitization cycle, the as-printed samples were austenitized at four different temperatures, *i.e.*, 950, 1050, 1150, and 1300 °C, followed by air-quenching. Fig. 3.1.3a and b illustrates the SEM micrographs and EDS elemental maps of A950 and A1050 samples, which consist of small carbides distributed in a martensitic matrix indicating that the peak temperature was not high enough to reach to austenite single phase stability region. It is important to note that carbide networks are mostly nucleated from the Cr-rich δ-ferrite regions as shown in the microstructure of the A950 sample (see

Fig. 3.1.3a). However, as depicted in Fig. 3.1.3b, the carbide networks are slightly collapsed in the sample austenitized at 1050 °C. Moreover, the density and volume fraction of carbides decreased as compared to A950 sample. The EDS elemental maps of chromium and carbon also show that the carbides are rich in chromium, confirming the formation of Cr-carbides in the martensitic matrix.

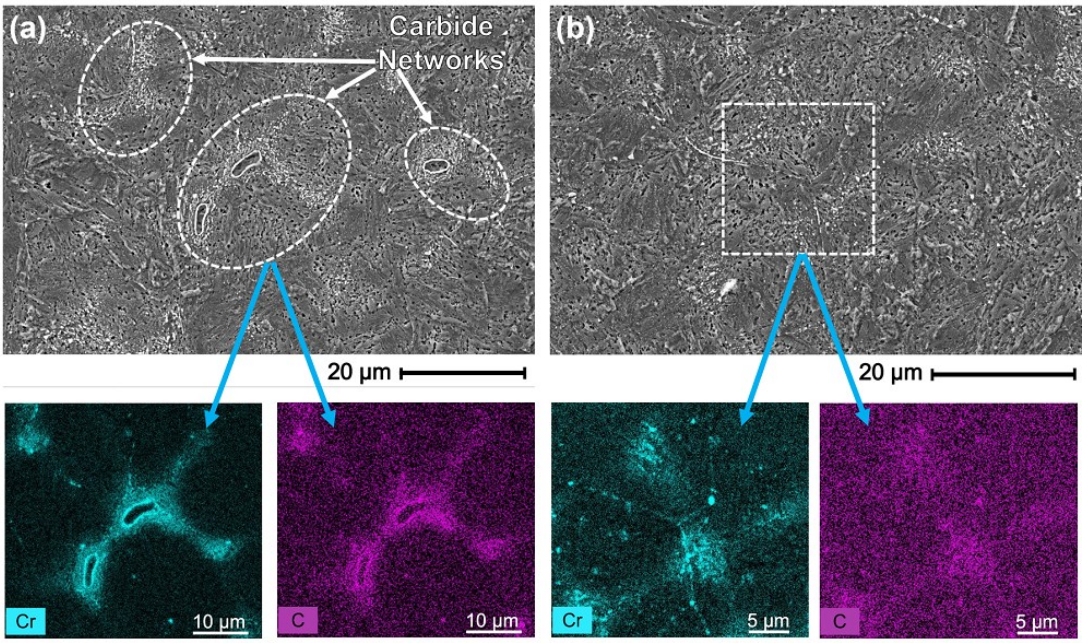

Figure 3.1.3 SEM micrographs and EDS elemental maps of Cr and C taken from the microstructure of (a) A950 and (b) A1050 samples.

On the other hand, the absence of the carbides in the sample austenitized at 1150 °C with a fully martensitic microstructure (shown in Fig. 3.1.4a and b) confirms the full dissolution of delta ferrite without any carbide precipitation as a result of austenitizing process. Heating up to 1300 °C, however, resulted in the coarsening of prior austenite grains and also re-formation of residual δ-ferrite, with an approximate volume fraction of 17 %, in a martensitic matrix as shown in Fig. 3.1.4c and d.

It is important to note that the initial microstructure of the material profoundly affects the kinetic of the austenitizing process by controlling the distance over which the diffusion of solute atoms occurs during the heating cycle [183]. In the current study, the presence

of Cr-enriched δ-ferrite phase decelerates the kinetics of austenitizing process since the compositional homogenization requires the dissolution of coarse δ-ferrite phases and diffusion of alloying elements to other solute-depleted areas. In the case of insufficient austenitizing temperature, the formation of an inhomogeneous austenite leads to a variation of martensite starts and finish temperatures (M_s and M_f) throughout the microstructure, and consequently an inhomogeneous microstructure forms during subsequent quenching. On the other hand, too high austenitizing temperature results in excessive growth of austenite grains [176], and also the re-formation of undesirable δ-ferrite (as seen in Fig. 3.1.4c and d for A1300 sample), which can potentially lessen both hardness and toughness of the component [172].

Considering the above discussion, 1150 °C was selected as the optimum austenitizing temperature due to its fully homogenized martensitic microstructure containing neither carbides nor residual δ-ferrite. Therefore, the following tempering cycles were only applied to the samples quenched from 1150 °C austenitizing temperature. It is interesting to note that the optimum austenitizing temperature of the conventionally fabricated AISI 420 MSS has been reported to be in the range of 1000-1050 °C [160,184]. This inconsistency can be correlated to the differences between the initial microstructure of the conventionally and additively fabricated samples. The microstructure of a conventional 420 MSS alloy is commonly comprised of a low volume fraction of micron or sub-micron carbides embedded in a ferritic matrix, while the as-printed WAAM samples contain a martensitic matrix along with a high-volume fraction of residual δ-ferrite. This high content of δ-ferrite phase in the as-printed WAAM 420 MSS alloy further postpones the austenitizing process as a complete dissolution of δ-ferrite phase is required prior to the full austenitization.

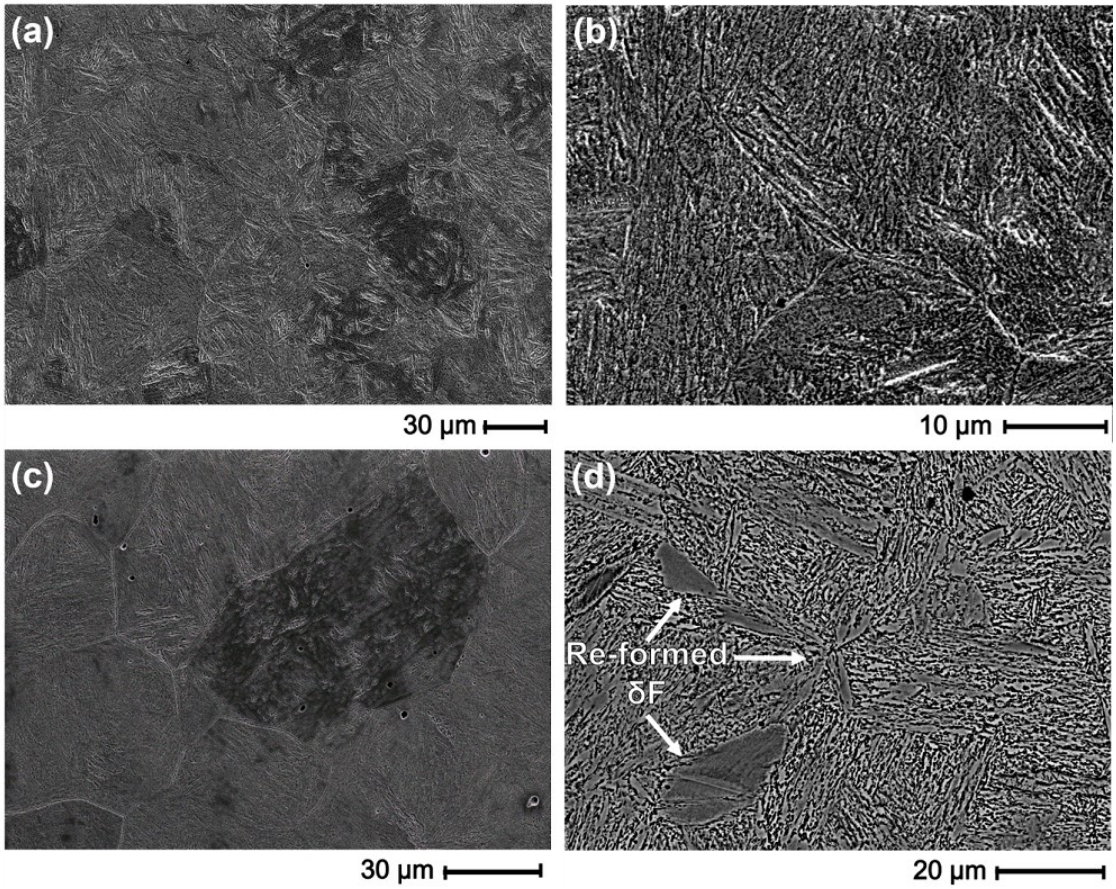

Figure 3.1.4 SEM micrographs of (a) & (b) A1150, and (c) & (d) A1300 samples.

3.1.4.1.2.2 Tempered Samples

The sample quenched from 1150 °C was subjected to five different tempering temperatures, including 200, 300, 400, 500, and 600 °C for 2 h. Generally, tempering treatment of martensitic stainless steels substantially facilitates the nucleation, growth, and finally coarsening of secondary phases, which are mostly alloy carbides [44]. The nature, morphology, size, and distribution of these precipitates play a crucial role in the performance of the component during in-service conditions [185]. Fig. 3.1.5a-d illustrates SEM micrographs of the samples tempered at 200 and 300 °C at different magnifications. As shown in Fig. 3.1.5a and b, no significant changes were observed as a result of tempering at 200 °C and a fully martensitic microstructure identical to the microstructure of as-quenched sample (A1150) was obtained (see Fig. 3.1.4a and b). On the other hand, tempering at 300 °C has triggered the nucleation of sub-micron inter/intra-lath carbide

particles with a fine needle-like morphology, homogenously distributed in the martensitic matrix (Fig. 3.1.5c and d).

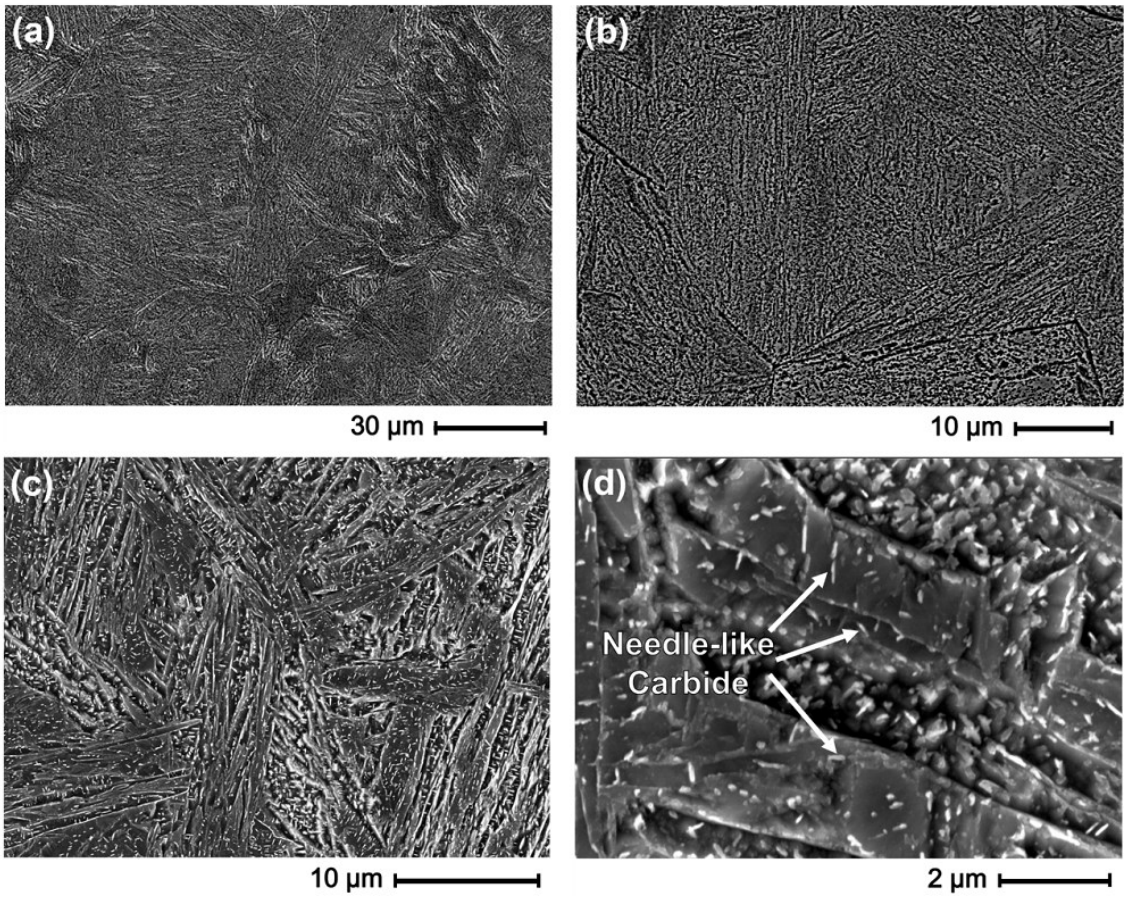

Figure 3.1.5 SEM micrographs taken from (a) & (b) T200, and (c) & (d) T300 samples.

According to Fig. 3.1.6a and b, increasing the tempering temperature to 400 °C resulted in a slight growth of carbide particles, which mostly appeared with a round morphology rather than needle-shaped. Differently, tempering at higher temperatures caused the accumulationof carbides at the grain boundaries of prior austenite grains in the case of 500 °C (see Fig. 3.1.7a) and further coarsening of carbide particles when the sample was tempered at 600 °C (see Fig. 3.1.7b).

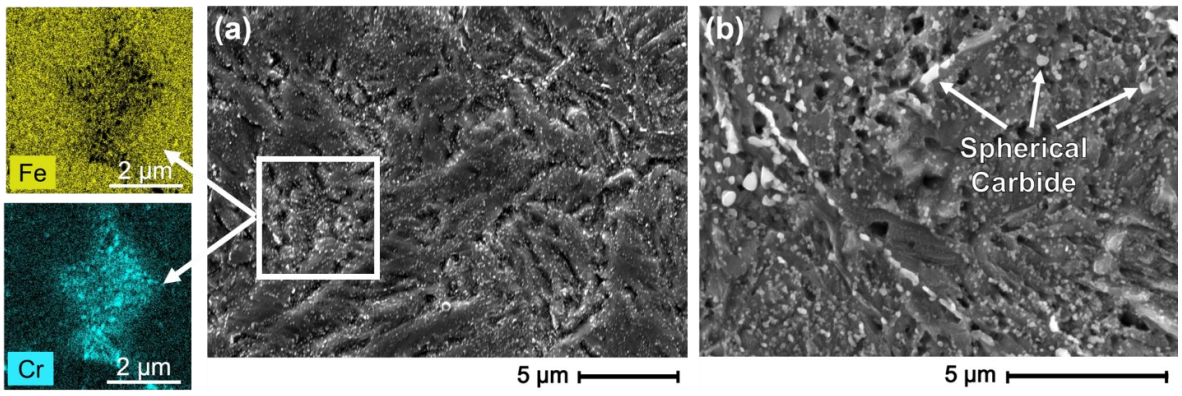

Figure 3.1.6 (a) & (b) SEM images taken from the microstructure of T400 sample at different magnifications along with the EDS elemental maps of Fe and Cr from the enclosed area shown in (a).

Theoretically, the tempering process provides the conditions for diffusion of carbon atoms entrapped in the octahedral interstitial sites of iron lattice and redistribution to the sites with lower energy level, such as dislocations. Then, the released carbon atoms undergo a series of reactions that eventually lead to the formation of Fe_3C or alloy carbides coinciding with a gradual decrease in residual stress level [186]. The tempering treatment primarily causes a reduction in the hardness and tensile strength, but an increase in ductility and toughness of the material [187]. However, under particular conditions, such as precipitation of alloy carbides, hardness may stay unaffected or even rise during tempering [187]. This hardness enhancement is called secondary hardening, which happens mostly due to the presence of strong carbide formers, such as molybdenum, vanadium, chromium, and tungsten [176]. It is also important to note that the shape, size, composition, and distribution of these carbides play a substantial role in the corrosion and mechanical properties of the tempered samples. Interestingly, stainless steels having chromium as the main alloying element are usually subjected to secondary hardening during tempering process in a specific range of temperatures that provide the optimum size and distribution of chromium carbide particles [177], However, by increasing the tempering temperature to above the optimum range, the carbide particles start to accumulate at the grain boundaries and become coarser, which are the case of tempering at 500 and 600 °C (see Fig. 3.1.7). According to the literature [44,188–190], as tempering temperature of martensitic stainless steels increases from 300 to 600 °C, the

sequence of carbide precipitation would be $(Cr,Fe)_3C$, $(Cr,Fe)_7C_3$, and finally $(Cr,Fe)_{23}C_6$. Although EDS results cannot be used to accurately identify the carbides' type, the EDS elemental maps taken from highly accumulated carbides' areas in the T400 sample (see Fig. 3.1.6), suggest that the alloy carbides formed during the tempering of WAAM-420 MSS were mostly enriched in chromium than iron. Fig. 3.1.8a and b provide a quantitative comparison of the size and volume fraction of carbides formed as a result of different heat treatments estimated based on the image processing using ImageJ software (see Fig. 3.1.7c and d as representatives of the processed microstructural images). It can be seen that the size and volume fraction of carbides decreased from $4.67\pm3.40 \times 10^{-1}$ µm and 7.91±0.54 % for A950 sample to $2.35\pm0.98 \times 10^{-1}$ µm and 5.12±0.50 % for A1050 sample, respectively, while no carbides were formed during austenitizing at 1150 and 1300 °C. Moreover, it can be observed that the size and volume fraction of carbides continuously increased by increasing the tempering temperature.

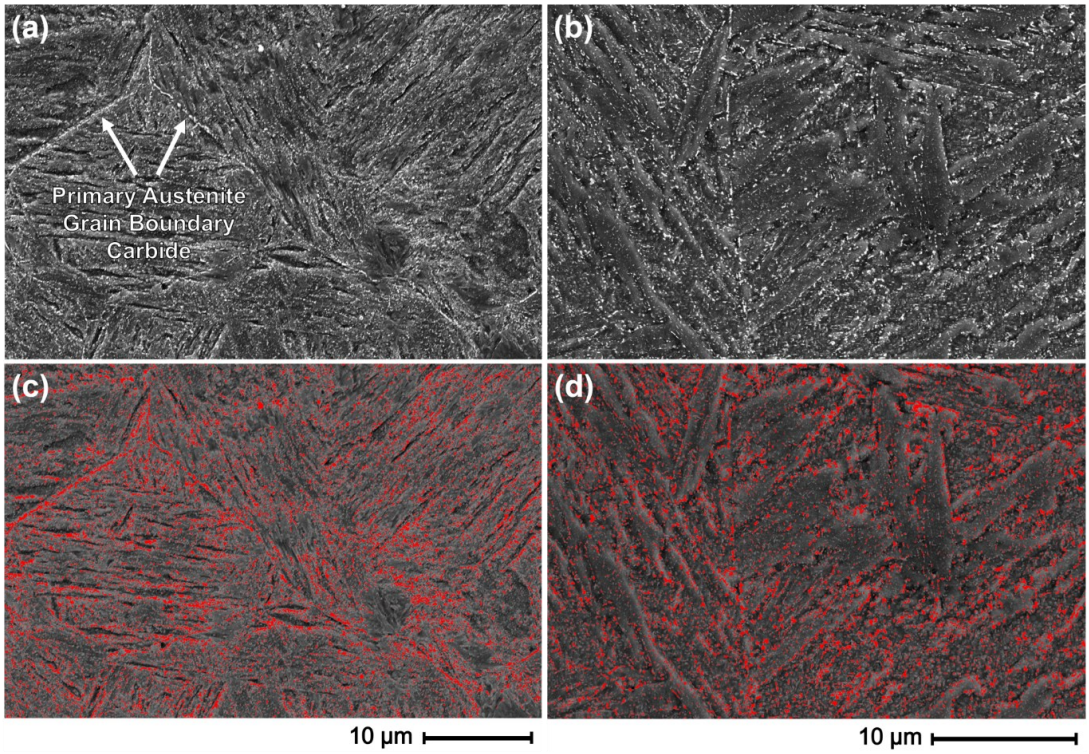

Figure 3.1.7 SEM micrographs and the corresponding processed images using ImageJ software of (a) & (c) T500 and (b) & (d) T600 samples.

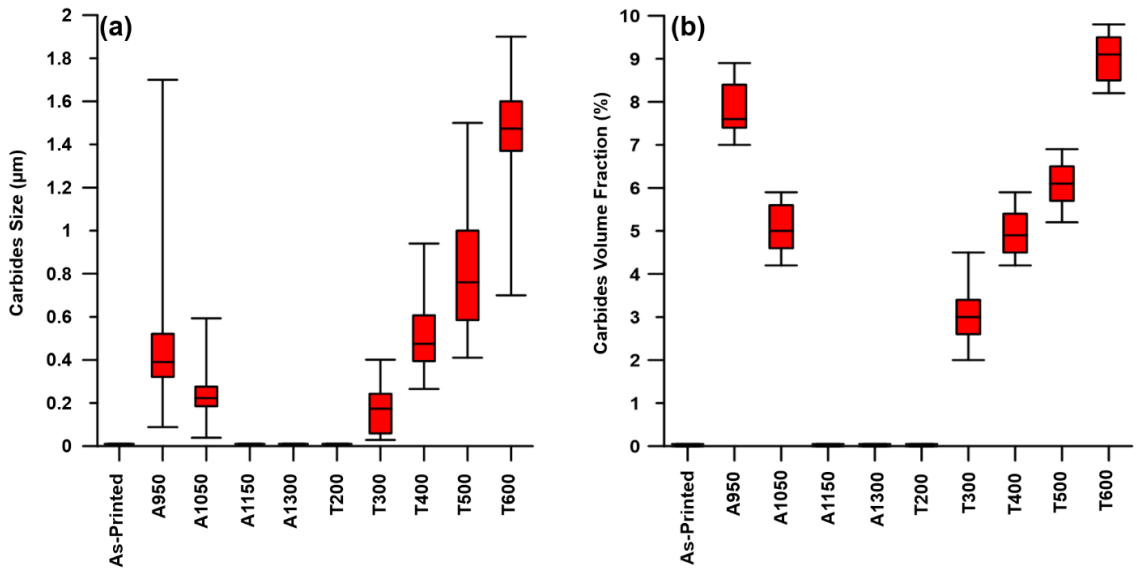

Figure 3.1.8 Quantitative analysis of the (a) size, and (b) volume fraction of carbides formed in the as-printed and heat-treated samples.

The XRD patterns of the as-printed, A1150, and T400 samples are shown in Fig. 3.1.9. In contrast to the heat-treated samples, a few weak peaks representing the FCC-iron (austenite) were detected in the as-printed sample, which is formed due to the sequential heating and cooling cycles associated with the WAAM process. According to the literature [92,176], the martensite start (M_s) and finish (M_f) temperatures of 420 MSS alloy can be roughly approximated as ~210 °C and ~30 °C, respectively. During the fabrication process, deposition of each track increases the temperature of the previously deposited layer to a temperature just above M_s, providing sufficient energy to facilitate the diffusion of carbon atoms from the supersaturated martensite to its adjacent austenite. Referred to martensitic transformation temperature equations [92,176], carbon acts as an austenite stabilizing element and decreases M_f to temperatures below the room temperature. Consequently, the high-carbon austenite can be retained at room temperature during the final cooling process. Such an in-situ heat treatment has been previously reported during selective laser melting of AISI 420 martensitic stainless steels [191]. On the other hand, during the post-printing heat treatment process, the sample does not experience a sequential heating and cooling cycles. Therefore, an almost fully martensitic microstructure will form during the single cooling process from the

austenitizing temperature of 1150 °C. Moreover, the tempering temperature was not high enough to form reversed austenite. It is also important to note that the peaks of alloy carbides can not be observed in the T400 sample, plausibly ascribed to their much lower volume fraction as compared to martensite [35].

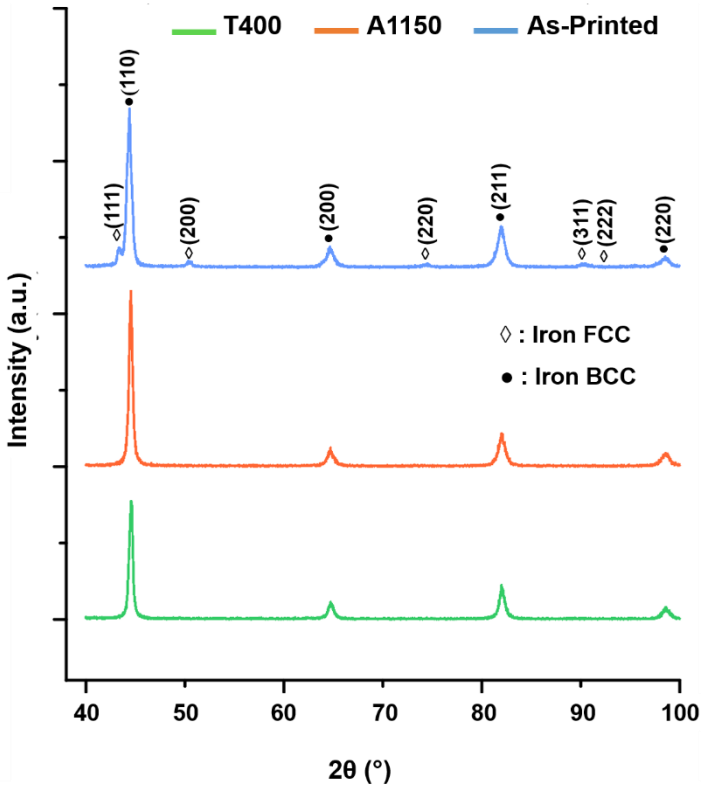

Figure 3.1.9 X-ray diffraction patterns of the as-printed, A1150, and T400 samples.

Fig. 3.1.10 illustrates the inverse pole figures (IPFs) along the building direction (BD) and the corresponding phase maps in the as-printed, T400, and T600 samples. As shown in the IPF maps of the as-printed and heat-treated samples (Fig. 3.1.10a, b and c), martensitic structure was revealed within the prior-austenite grain boundaries (PAGB) with a combination of various crystallographic orientations normal to {001}, {101}, and {111} planes. Unlike the as-printed sample that contains mostly individual and randomly distributed martensite blocks with a more equiaxed shape, both tempered samples (T400 and T600) revealed the hierarchical nature of the martensitic structure consisting of uniaxial and elongated martensite blocks orderly embedded in different packets, which

are confined by the prior austenite grains (PAGs) [192]. As an example, some blocks and packets are shown by dash-lines in the inverse pole figure maps of the T400 and T600 sample (see Fig. 3.1.10b and c). This difference can be correlated to the size of the PAGs in the heat-treated and as-printed samples due to the theoretical limit for the growth of martensite phase across the parent austenite boundaries [193]. Therefore, coarser PAGs lead to elongated blocks and packets, while fine PAGs result in the formation of martensite phase in a more equiaxed shape [193]. It is worth noting that the prior austenite grains are coarser in the heat-treated samples due to their longer holding time (30 min) at the austenitizing temperature as compared to the as-printed sample's PAGs that formed during the continues cooling after the solidification process. Ge *et al.* [171] also observed refined martensite morphology in the WAAM 2Cr13 part in the as-printed condition and correlated it to the breakage of grains as a result of successive deposition process inducing intensive thermal shocks to the previously deposited layers. Previous studies [194] on the dislocation-interface interactions revealed that the resistance to dislocation gliding across individual lath boundaries is negligible as compared to the dislocation gliding across block and packet boundaries. This can be one of the controlling factors affecting the tensile strength of the tempered samples with hierarchical martensitic structure containing martensite lath, block, and packets, in contrast to the as-printed sample with a randomly distributed individual equiaxed martensitic structure.

According to the phase maps of the as-printed and heat-treated samples (Fig. 3.1.10d, e, and f), the BCC structure in red standing represents both the residual δ-ferrite phase and the martensite laths for the as-printed sample, while the BCC structure in the tempered samples (T400 and T600) solely represents the tempered martensite structure since δ-ferrite phase was entirely eliminated during the austenitizing cycle as shown in Fig. 3.1.4a and b. Moreover, nearly 3 % of retained austenite with FCC crystal structure is observed in blue color on the as-printed phase map distribution (Fig. 3.1.10d). However, phase maps of the tempered samples (T400 and T600), shown in Fig. 3.1.10e and f, revealed insignificant volume fraction of FCC phase (≤ 0.2 %) due to dissolution of the retained austenite phase during the austenitization and subsequent quenching, resulting in the formation of a fully martensitic microstructure in the as-quenched condition. It is

notable that the results of the EBSD phase maps were consistent with the XRD patterns showing the presence of retained austenite in the as-printed sample and its dissolution in the heat-treated conditions. It has been reported that the stabilization of the retained austenite at room temperature during solidification of martensitic stainless steels can be related to the localized high concentration of carbon, which can locally decrease the martensite finish temperature (M_f) to below ambient temperature [195]. On the other hand, re-transformation of the austenite phase to chromium carbides can also occur dictated by active diffusion of carbon element during tempering process [196,197].

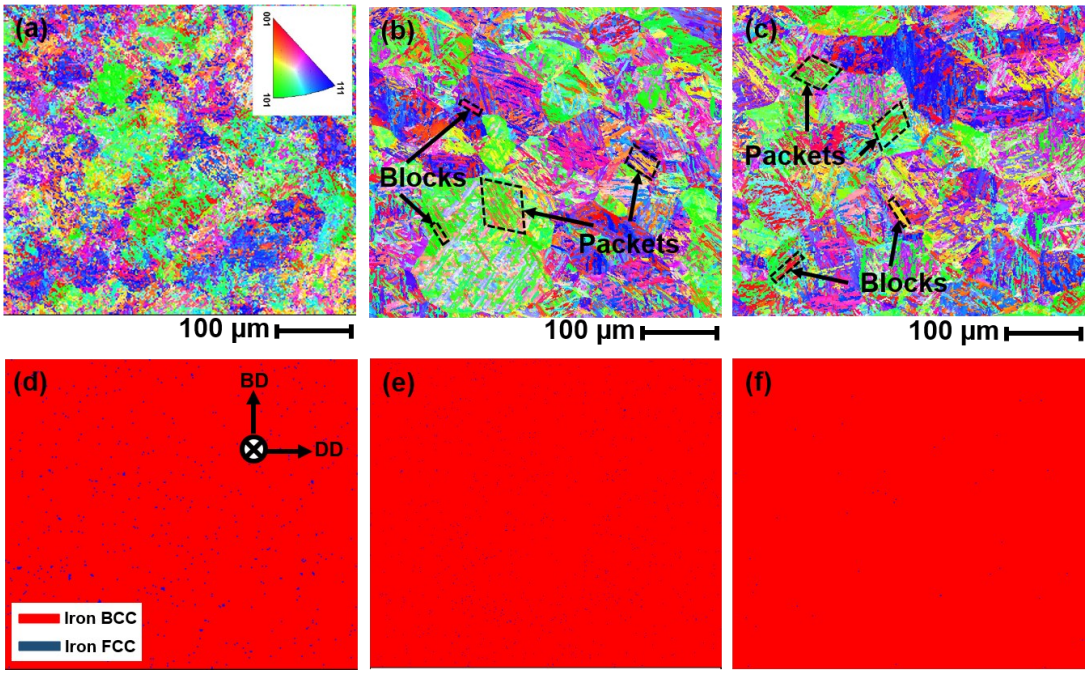

Figure 3.1.10 (a-c) The inverse pole figure maps and (d-f) the corresponding phase maps of the as-printed, T400, and T600 samples, respectively.

3.1.4.2 Mechanical Properties

3.1.4.2.1 Microhardness Measurements

Fig. 3.1.11a compares the microhardness of the as-printed part with the quenched samples including, A950, A1050, A1150, and A1300 °C. Although the quenching medium of all samples was identical (air cooling), the measured microhardness values

were found to be different, which can be attributed to the maximum temperatures experienced by the samples during the heating cycle. The as-printed sample with the minimum microhardness value (550 ± 12 HV) experienced the maximum heating temperature higher than the melting point temperature of the alloy during the fabrication process. Therefore, this sample contains an as-solidified microstructure composed of inter-dendritic δ-ferrite in a martensitic matrix with a negligible amount of retained austenite. The minimum microhardness of the as-printed sample can be associated with the presence of a high volume fraction of δ-ferrite as compared to the quenched samples [198]. However, austenitizing at 950 °C improved the microhardness of the sample to 590 ± 6 HV as a result of dissolution of the inter-dendritic δ-ferrite during the heating cycle. Increasing the austenitizing temperature to 1050 °C further improved the microhardness value to 640 ± 4 HV, correlated to their slightly different microstructural features. The higher austenitizing temperature of 1050 °C was found to disrupt the carbide network that was detected in A950 sample (see Fig. 3.1.3), stimulating further dissolution of δ-ferrite and causing the formation of a lower fraction of carbides with smaller size in the A1050 sample (Fig. 3.1.3b). Essentially, the presence of any carbides in the prior austenite phase lowers the dissolved carbon content in the austenite phase, and ultimately leads to reduced microhardness of the resultant as-quenched martensite. On the other hand, the more dissolution of carbides raises the carbon concentration of martensite and increases the hardness of the as-quenched sample [176].

The austenitizing temperature of 1150 °C yielded the maximum microhardness value (670 ± 4 HV) as a consequence of the full dissolution of all existing micro-constituents and secondary phases, including the δ-ferrite phase, in the austenite phase, resulting in a fully martensitic microstructure with a high carbon content after quenching (see Fig. 3.1.4a and b). Calliari *et al.* [199] also studied the effect of austenitizing temperature on the hardness of the as-quenched modified AISI 420 alloy and reported that the maximum hardness is obtained when complete carbide removal occurred during austenitizing process. Contrarily, further increase in the austenitizing temperature up to 1300 °C caused a significant drop in the microhardness value to 555 ± 7 HV. This microhardness reduction can be attributed to the excessive growth of austenite grains (see Fig. 3.1.4c),

re-formation of undesirable δ-ferrite (see Fig. 3.1.4d), and potential oxidation and decarburization as a result of ultra-high austenitizing temperature. Based on the above discussions, austenitizing temperature of 1150 °C with the maximum microhardness (~670 HV) was selected as the optimum temperature and the further tempering cycles were applied to A1150 samples.

Fig. 3.1.11b compares the microhardness values of the as-printed and A1150 samples with those tempered at different temperatures, including T200, T300, T400, T500, and T600. Tempering at 200 °C caused a significant drop in the microhardness value from 670 ± 4 HV for the A1150 sample to 460 ± 3 HV for the T200 sample, potentially as a result of stress relieving of the martensitic matrix at the initial stage of the tempering process. Although increased tempering temperature to 300 °C led to the nucleation of sub-micron carbides (see Fig. 3.1.5c and d), the sample experienced further microhardness reduction to 440 ± 4 HV. The observed microhardness reduction in T300 sample can be ascribed to further softening of martensite during tempering, while the carbides were not large enough to provide secondary hardening. On the contrary, tempering at 400 °C improved the microhardness value up to 550 ± 7 HV as a result of the growth of alloy carbides to an optimum size (see Fig. 3.1.6), providing precipitation hardening also known as secondary hardening in the tempering process of stainless steels [176]. On the other hand, increasing the tempering temperature up to 500 °C resulted in the accumulation of carbides at the primary austenite grain boundaries (see Fig. 3.1.7a), which decreased the microhardness value to 490 ± 7 HV. Interestingly, tempering at 600 °C caused a dramatic drop in the microhardness value to 300 ± 1 HV, which can be related to the significant coarsening of carbides particles embedded in an extremely tempered martensite matrix (see Fig. 3.1.7b). Isfahany *et al.* [160] also reported that the secondary hardening was observed during the heat treatment of AISI 420 martensitic stainless steel at the tempering temperature range of 400–500 °C as a result of nucleation of M_7C_3, while higher tempering temperatures led to softening of the material due to coarsening of M_7C_3 and its partial transformation to $M_{23}C_6$ carbides.

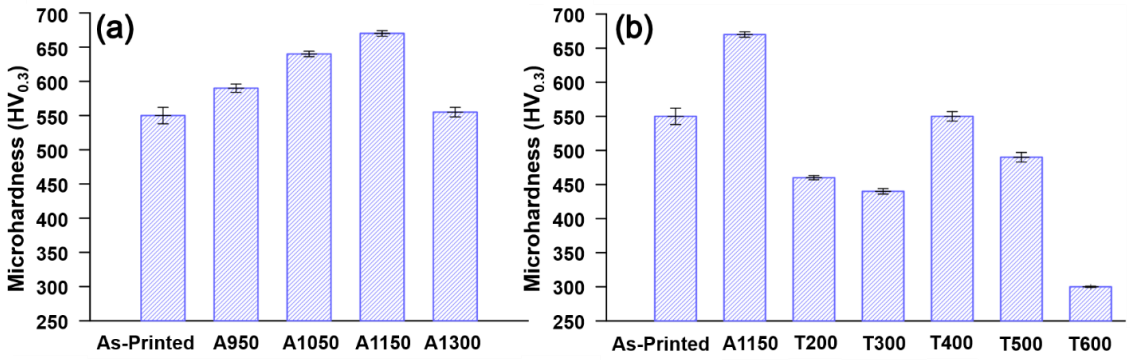

Figure 3.1.11 (a) & (b) Vickers microhardness values of the as-printed and heat-treated samples, including A950, A1050, A1150, A1300, T200, T300, T400, T500, and T600.

3.1.4.2.2 Uniaxial Tensile Testing

The engineering stress-strain curves of the as-printed and heat-treated samples are plotted in Fig. 3.1.12a, and the ultimate tensile strength (UTS) and elongation percentage values are summarized in Fig. 3.1.12b. The maximum tensile strength was measured for the A1150 sample with the UTS of 1903 ± 12 MPa as compared to 1151 ± 9 MPa for the as-printed sample. Expectedly, the drastic increase of tensile strength in the as-quenched sample co-occurs with the loss of the material's ductility (only ~1.7 % elongation) due to the formation of a fully untempered martensitic microstructure, which is super-saturated with carbon solute atoms and contains a high density of dislocations [200]. Consistent with the results of microhardness measurements (see Fig. 3.1.11b), tempering at both 200 and 300 °C reduced the tensile strength from 1903 ± 12 MPa for the as-quenched sample (A1150) to 1729 ± 11 and 1573 ± 8 MPa for T200 and T300 samples, respectively, while improved the ductility of the material as a result of the decreased martensite tetragonality and stress relieving during tempering. Although the tensile strengths of T200 and T300 samples are higher than the as-printed part, 200 and 300 °C cannot be considered as the optimum heat treatment cycles due to their lower ductility as compared to the as-printed sample (see Fig. 3.1.12b for the details). Differently, tempering at 400 °C improved both tensile strength and ductility of the material to 1442 ± 5 MPa and 11.8 ± 1 %, respectively, as compared to the as-printed part with UTS of 1151 ± 9 MPa and elongation of 9.9 ± 0.5 %.

It is interesting to note that although the microhardness of the as-printed material and T400 sample are almost the same (~550 HV), a significant difference can be observed in their performance under uniaxial tensile loading, ascribed to their different microstructural features. The as-printed material consists of untempered martensite as the matrix and residual δ-ferrite as the secondary phase, while the sample tempered at 400 °C has a moderately tempered martensitic matrix and owes its hardness to the precipitation strengthening effect from the embedded carbide particles in the matrix. The presence of optimum-sized carbide particles homogeneously distributed in the matrix of the T400 sample not only improved the hardness but also enhanced the ductility of the material.

On the contrary, further tempering at 500 °C decreased the tensile strength to 1313 ± 10 MPa by virtue of a slight coarsening of carbide particles precipitated at the grain boundaries and divergence from the optimal size and distribution of precipitates. This cycle not only decreases the strength but also reduces the ductility of the materials, which is commonly termed as temper embrittlement [201]. Consistent with the microhardness values (see Fig. 3.1.11b), the minimum tensile strength (935 ± 9 MPa) and maximum ductility (13.5 ± 1.5 %) were obtained for the 600 °C tempered sample due to its severely tempered martensitic matrix containing coarse carbide particles. Similarly, Bonagani *et al.* [177] reported that the formation of coarse carbides during high-temperature tempering of 13 wt.% Cr martensitic stainless steel resulted in an increased ductility at the expense of decreased tensile strength.

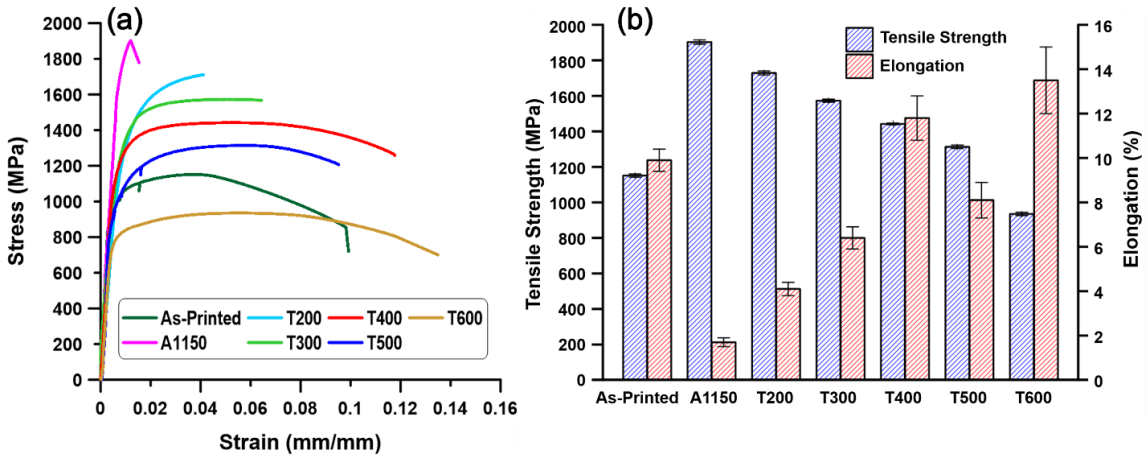

Figure 3.1.12 (a) Stress-Strain curves of the as-printed and heat-treated samples, including A1150, T200, T300, T400, T500, and T600, (b) summary of the measured UTS and percent elongations at different conditions.

3.1.4.2.3 Fractography analysis

The fractography analysis of the heat-treated samples revealed two distinguishable regions including a narrow band in the lateral zones and a wider region with different characteristics at the center of the fractured surfaces, shown in Fig. 3.1.13a for the T400 sample as an example. Higher magnification SEM image (Fig. 3.1.13b) taken from the interface of these two regions revealed that the lateral part contains characteristics of plastic deformation, such as conical dimples, while the central regions showed indications of brittle fracture like intergranular cracks, cleavage facets, and tear ridges. Therefore, the area fraction of these two regions corresponds well to the fraction of ductile to brittle fractures during uniaxial tensile loading for each sample.

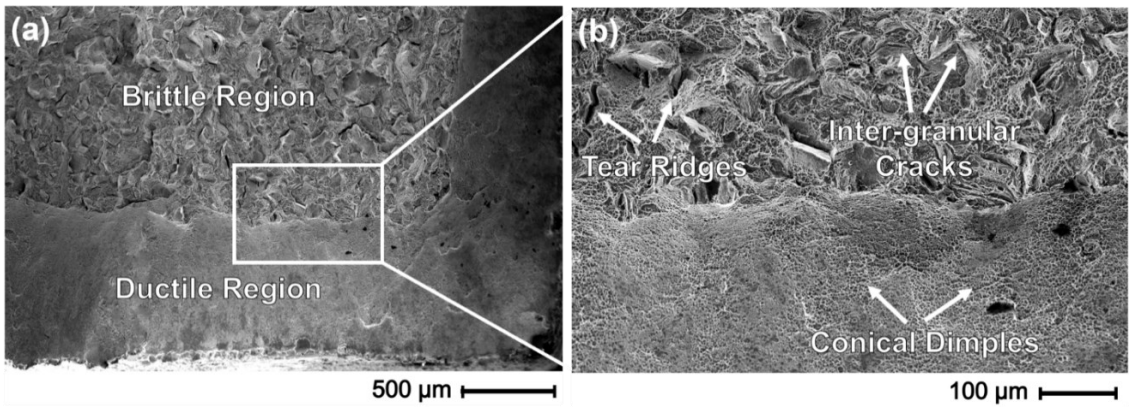

Figure 3.1.13 (a) & (b) Multi-scale SEM fractography images taken from T400 sample after uniaxial tensile testing.

The low-magnification fractography images (Fig. 3.1.14a-f) taken from different heat-treated samples reveal the impact of applied tempering process on the fracture mechanism of the samples, causing the variation of the fraction of ductile to brittle areas, which is shown quantitatively using a bar chart in Fig. 3.1.14g. As expected, the quenched sample (A1150) with a fully martensitic microstructure (see Fig. 3.1.4a and b) showed a predominantly brittle fracture (~ 95%), while tempering at 200 °C resulted in the formation of an obvious ductile band around the fracture surface (compare Fig. 3.1.14a and b). In addition, higher tempering temperatures increased the fraction of ductile region from ~ 21% for the T200 to ~ 33% and ~ 54% for T300 and T400 samples, respectively. The larger portion of the ductile region in the tempered samples can be attributed to the more stress relieved-nature of the martensite phase in these samples, possessing a lower tetragonality and decreased dislocation density as a result of tempering process [44]. In contrast, tempering at 500 °C interestingly decreased the area fraction of ductile region to ~ 39%, and promoted the intergranular fracture in the central areas of the sample. From the microstructural perspective, the higher intergranular fracture region of the T500 sample can be related to the accumulationof carbides at the grain boundaries of prior austenite grains, provoking brittle fracture of the intergranular regions. Previous studies [177,201,202] on the heat treatment of martensitic stainless steels also reported that the samples tempered at around 500 °C are highly prone to temper embrittlement and their fracture surfaces were characterized by a brittle intergranular fracture. Contrarily, tempering at 600 °C significantly enhanced the fraction

of ductile fracture to ~ 65%, attributed to its fully tempered martensitic microstructure consisting of homogeneously distributed coarse carbides.

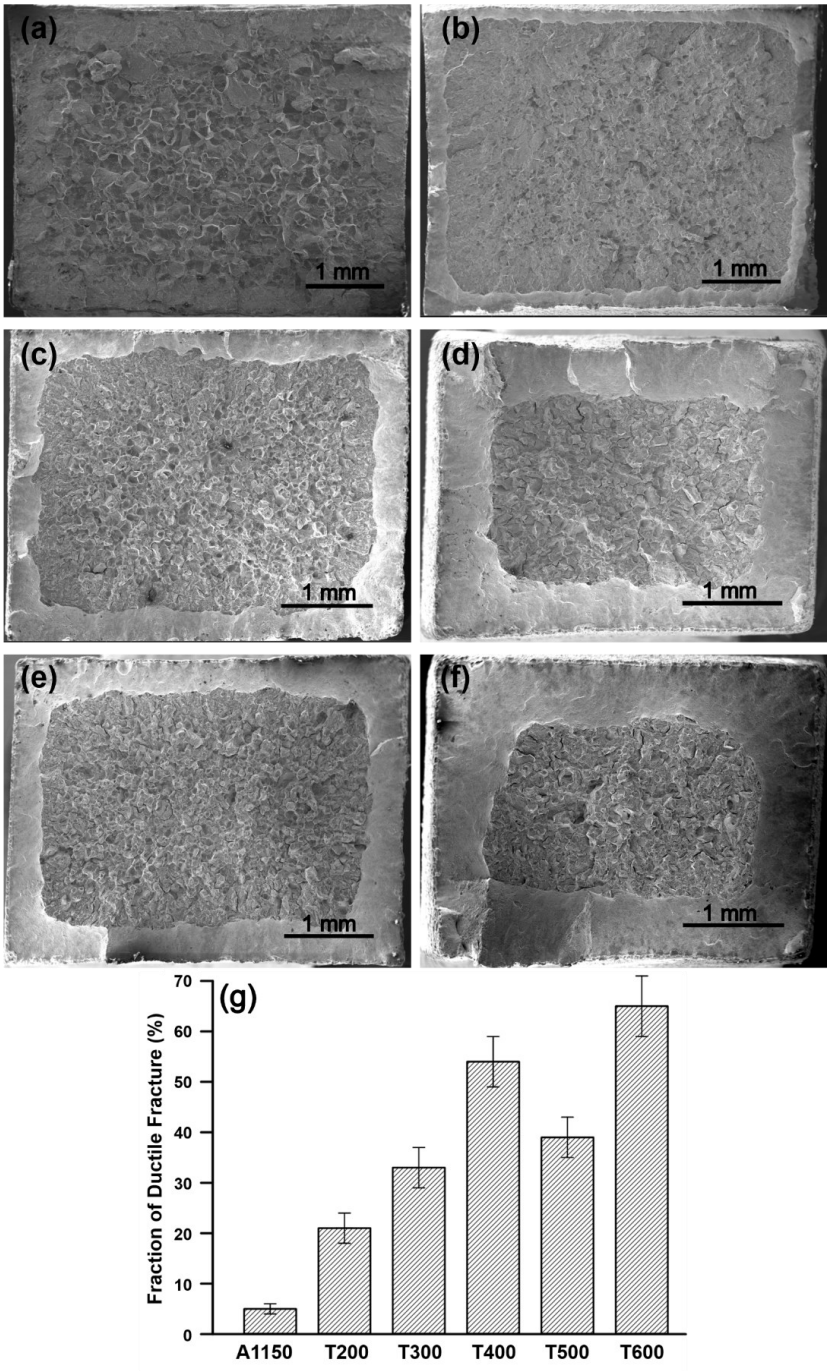

Figure 3.1.14 Low magnification SEM fractographs taken from (a) A1150, (b) T200, (c) T300, (d) T400, (e) T500, (f) T600 samples, and (g) relative area fraction of ductile regions in the fracture surfaces shown in a-f.

Detailed features of the fractured surfaces were also studied at higher magnifications by SEM (Fig. 3.1.15). Although ductile regions of all samples revealed identical features comprised of numerous conical dimples, the characteristics of the central brittle regions varied for different samples with different tempering temperatures. Although traces of brittle fracture like cleavage facets, river patterns, and tear ridges can be observed in the central region of the samples with extremely low ductility (as-quenched and T200 samples), intergranular fracture was the predominant fracture mechanism in these samples (see Fig. 3.1.15a and b). However, increasing the tempering temperature to 300, 400, and 500 °C resulted in the formation of conical ductile micro-dimples even at the central regions of the fracture surfaces, suggesting a mix ductile-brittle fracture behaviour (see Fig. 3.1.15c, d, and e). In the case of the highest tempering temperature (600 °C), although the central region still consists of intergranular cracks, there is no sign of cleavage facets, and instead large and deep cuplike depressions and conical dimples with relatively uniform size were formed, confirming the severe shear plastic deformation prior to the fracture. This observation is consistent with the results of uniaxial tensile testing showing the highest ductility for the 600 °C tempered sample.

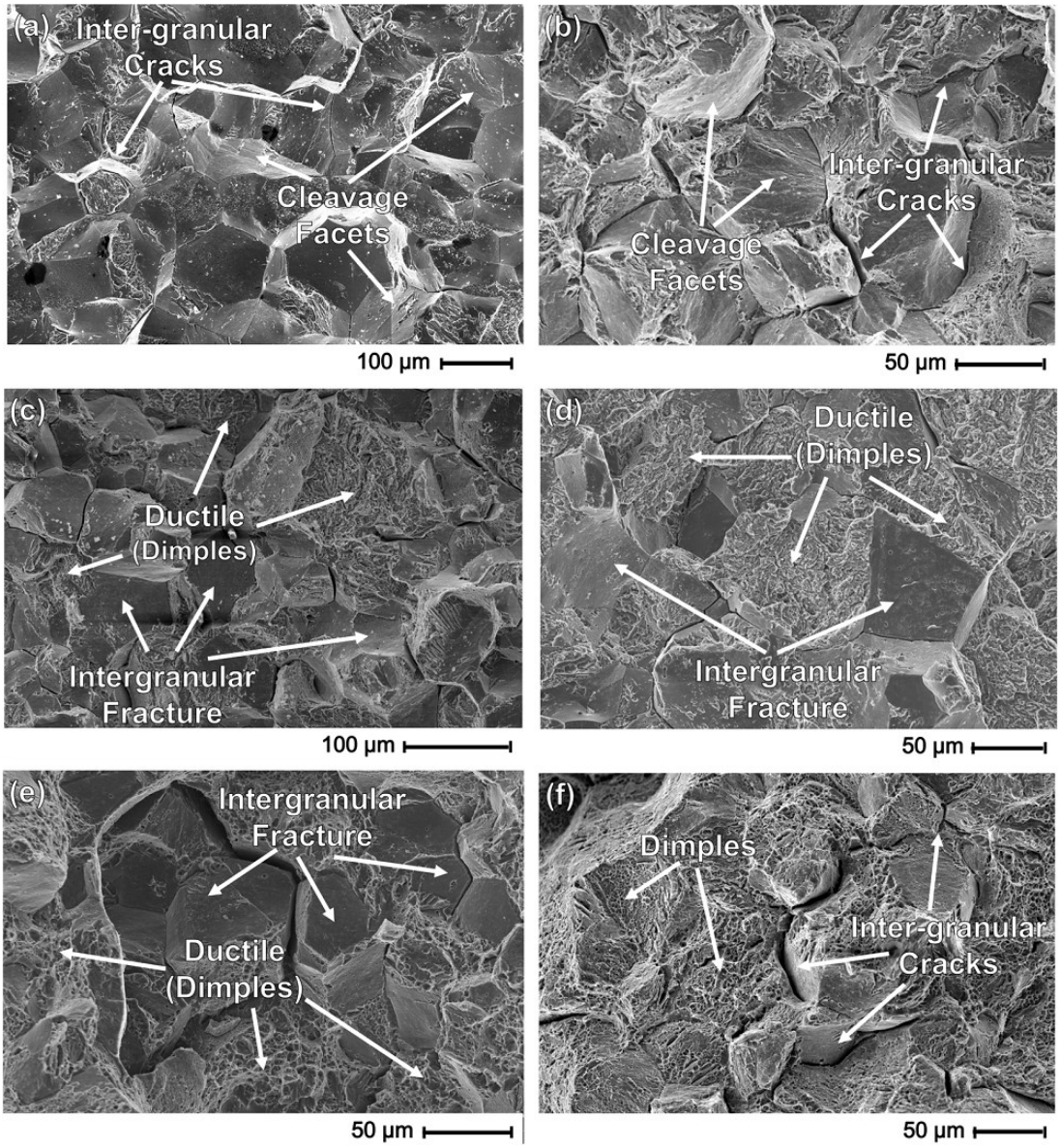

Figure 3.1.15 High magnification SEM fractography images taken from (a) A1150, (b) T200, (c) T300, (d) T400, (e) T500, and (f) T600 samples.

3.1.5. CONCLUSIONS

This study reports the successful fabrication of 420 MSS parts implementing state-of-the-art wire arc additive manufacturing method utilizing surface tension transfer arc mode. For the first time, the impacts of post-printing heat treatment cycles, *i.e.,* austenitizing and tempering at different temperatures on the microstructural features and mechanical

performance of the WAAM fabricated 420 MSS were comprehensively studied and the following conclusions were drawn:

1. Microstructure of the as-printed WAAM 420 sample included residual inter-dendritic δ-ferrite surrounded by an untempered martensitic matrix in addition to a small volume fraction of retained austenite.
2. 1150 °C was selected as the optimum austenitizing temperature due to the formation of a fully martensitic microstructure in the as-quenched condition with the maximum hardness of 670 ± 4 HV. The austenitizing temperatures either lower (950 and 1050 °C) or higher (1300 °C) than this optimum temperature resulted in the formation of undesirable phases, such as Cr-rich carbides and residual δ-ferrite, and led to reduction of their as-quenched microhardness compared with the 1150 °C austenitized sample.
3. The obtained optimum austenitizing temperature (1150 °C) for the WAAM-420 MSS was found to be 100-150 °C higher than the recommended austenitizing temperature for conventionally fabricated 420 MSS due to their different initial microstructures, *i.e.* δ-ferrite in a martensitic matrix for the WAAM-420 MSS as compared to carbides in ferritic matrix for the conventionally fabricated 420 MSS.
4. Microstructural characterization of the tempered samples revealed the nucleation of sub-micron needle-like chromium carbides at 300 °C and their further growth at higher temperatures. The morphology of carbides turned to spherical shape at 400 °C, followed by their noticeable accumulationalong the primary austenite grain boundaries at 500 °C, while further carbides' coarsening was observed in the microstructure of 600 °C tempered sample.
5. The microhardness measurements confirmed the occurrence of secondary hardening during tempering of WAAM-420 MSS, attributed to the precipitation of Cr-carbides. The maximum microhardness value (550 ± 7 HV) was recorded for the 400 °C tempered sample, associated with the formation of homogeneously distributed spherical carbides in a moderately tempered martensitic matrix. The observed microhardness reduction in the samples tempered at higher temperatures (500 and 600 °C) can be ascribed to over accumulationand coarsening of carbides, leading to excessive softening of the martensitic matrix.

6. Consistent with the results of microhardness measurements, tempering at 400 °C was found to be the optimum tempering temperature due to yielding the optimum combination of ultimate tensile strength (1442 ± 5 MPa) and elongation (11.8 ± 1 %), while other tempering temperatures resulted in either brittleness of the material or insufficient strength.

7. Finally, the current study affirmed the necessity of applying post-printing heat treatment on as-printed WAAM-420 MSS parts for applications where an excellent combination of high hardness, strength, and ductility is required.

Acknowledgements

The authors gratefully acknowledge the supports of Natural Sciences and Engineering Research Council of Canada (NSERC) through Canada Research Chair (Tier II) program in ocean engineering and Discovery Grant, Ocean Frontier Institute (OFI), Dalhousie University, and Memorial University of Newfoundland for sponsoring this work.

3.2 Effect of Interpass Temperature on the Formation of Retained Austenite in a Wire Arc Additive Manufactured ER420 Martensitic Stainless Steel

Alireza Vahedi Nemani[1], Mahya Ghaffari[1], Salar Salahi[2], Jonas Lunde[2], Ali Nasiri[3]

1- Graduate Student, Dalhousie University, Halifax, Nova Scotia, Canada
2- Graduate Student, Memorial University, St. John's, Newfoundland, Canada
3- Assistant Professor, Dalhousie University, Halifax, Nova Scotia, Canada

Status: Published Journal Paper, Journal of Materials Chemistry and Physics (IF= 4.094), Volume 266, Pages 124555

Authors' Contribution

Alireza Vahedi Nemani: Conceptualization, Investigation, Writing - original draft, Visualization.

Mahya Ghaffari: Methodology, Fabrication Process, Validation, Investigation, Review & Editing.

Salar Salahi: EBSD Analysis, Review & Editing.

Jonas Lunde: Fabrication Process, EBSD Analysis, Review & Editing.

Ali Nasiri: Supervision, Writing - review & editing, Funding acquisition.

3.2.1. Abstract

In this study, thin-wall components of ER420 martensitic stainless steel were fabricated through wire arc additive manufacturing (WAAM) at two different interpass temperatures of 25 °C and 200 °C. The effects of thermal history on the formation, volume fraction, and distribution of retained austenite were characterized by scanning electron microscopy, electron backscattered diffraction, and X-ray diffraction analyses. It was concluded that the higher interpass temperature of 200 °C leads to the formation of a higher content of retained austenite resulted from in-situ quenching and partitioning heat treatment during the fabrication process.

3.2.2. Introduction

The chemical compositions of martensitic stainless steels (MSS) are designed to provide an adequate hardenability by forming a supersaturated martensitic microstructure when air cooled from the austenite stability region [187]. Although MSSs are generally designed for high-strength applications, their toughness and corrosion behaviour should

also be contemplated for harsher environment applications, such as mixer blades, pressure vessels, etc [160]. The fraction of retained austenite in this family of stainless steels can play a crucial role in both mechanical and corrosion properties [203–205]. Lu *et al.* [204] was able to increase the volume fraction of retained austenite in a 0.3C–13Cr MSS by quenching and partitioning heat treatment and reported an improved pitting corrosion resistance as compared to the conventionally quenched and tempered alloy with a fully martensitic microstructure. The superior corrosion resistance of the austenite phase as compared to the martensite can be ascribed to its less internal stresses and lower lattice defects [206,207]. The presence of retained austenite can also improve the mechanical performance of the part by increasing the strain hardening during plastic deformation [51,203].

The layer-by-layer fabrication nature of additive manufacturing processes imposes sequential heating and cooling cycles to the previously solidified tracks during printing, leading to in-situ and localized heat treatment of the component during the fabrication process. A deep understanding of these in-situ heat treatment cycles enables the manufacturer to manipulate the microstructure based on the desired mechanical and corrosion properties.

This study, for the first time, investigates the in-situ heat treatment in a wire arc additively manufactured 420 MSS applied using different interpass temperatures during the fabrication process. In addition, the effects of the resultant thermal history on the formation, volume fraction, and distribution of retained austenite in the fabricated 420 MSS part are comprehensively characterized.

3.2.3. EXPERIMENTAL PROCEDURE

In this experiment, two interpass temperatures of 25 °C (below martensite finish temperature of the alloy, M_f) and 200 °C (between martensite start (M_s) and M_f temperatures) were implemented for WAAM of thin-wall ER420 MSS components. The fabricated samples were denoted by IT25 and IT200, respectively. The nominal chemical composition of the used feedstock wire is listed in Table 3.2.1. A robotic gas metal arc

welding platform utilizing an advanced surface tension transfer (STT) mode was used as the power source of the WAAM process. The process parameters were set as follows: a wire feed speed of 67.7 mm/s, an arc current of 135 A, a traveling speed of 3.6 mm/s, an arc voltage of 29 V and pure argon as the shielding gas with the flow rate of 20 L/min. The microstructural features of the fabricated walls were characterized through scanning electron microscopy (SEM), energy dispersive spectroscopy (EDS), electron backscatter diffraction (EBSD), and X-ray diffraction (XRD) analyses. The volume fraction of different micro-constituents were also calculated by applying the method of whole pattern fitting to the raw XRD data.

Table 3.2.1 Nominal chemical composition of the feedstock material (wt. %).

Material	C	Cr	Mn	Si	S	P	Ni	Mo	Cu	Al	Sn	Fe
ER420	0.3-0.4	12-14	0-1	0-1	0-0.03	0-0.04	0-0.5	0-0.5	0-0.5	0-0.05	0-0.05	Bal.

3.2.4. RESULTS AND DISCUSSION

The low magnification SEM micrographs of IT25 and IT200 samples (Fig. 3.2.1a and c, respectively) revealed that the dominant microstructure of both samples consists of a martensitic matrix containing inter-dendritic delta-ferrite phase. According to the phase diagram of 420 MSS [180], the alpha ferrite phase is the room-temperature stable phase in this alloy, however, the fast cooling rate associated with the WAAM process provokes the martensitic transformation in the matrix of the material [43]. Furthermore, the concentration of chromium as a ferrite-stabilizer alloying element in the inter-dendritic regions has resulted in the stabilization of delta-ferrite (shown in Fig. 3.2.1e and f). The higher magnification SEM images (Fig. 3.2.1b and d) revealed the formation of retained austenite in IT200 as opposed to IT25. Ge *et al.* [171] also reported that a shorter inter-layer dwelling time (higher interpass temperature) leads to a higher fraction of retained austenite in additively manufactured 2Cr13 MSS. It is well-known that the presence of retained austenite could potentially affect both mechanical and corrosion properties of a material [203–205]. For instance, the presence of high fractions of retained austenite can

lead to an excellent combination of strength and ductility as a result of stress-driven austenite-to-martensite transformation during plastic deformation [208].

Fig. 3.2.2a and b illustrate the XRD patterns of the bottom, middle and top areas of both samples and also Fig. 3.2.2c shows the variations of retained austenite volume fraction at different regions for each sample. It is obvious that the retained austenite volume fraction of IT200 is considerably higher than that of the IT25 throughout the part (see Fig. 3.2.2c). Since all the WAAM process parameters except for the interpass temperature were kept constant between the IT25 and IT200 samples, the difference between the austenite content should be related to the thermal history experienced by the deposited tracks as a result of different interpass temperatures. According to the theoretical methods and empirical equations suggested in the literature [92,176], the martensite start and finish temperatures (M_s and M_f) for the ER420 alloy were estimated to be ~210 °C and ~30 °C, respectively. Therefore, the interpass temperature of IT25 (25 °C) is just below the M_f, resulting in a fully martensitic microstructure with a negligible amount of retained austenite surrounded by martensite lathes. In contrast, the higher interpass temperature in IT200 (200 °C) is between M_s and M_f temperatures, leading to the formation of martensitic microstructure containing higher content of untransformed retained austenite.

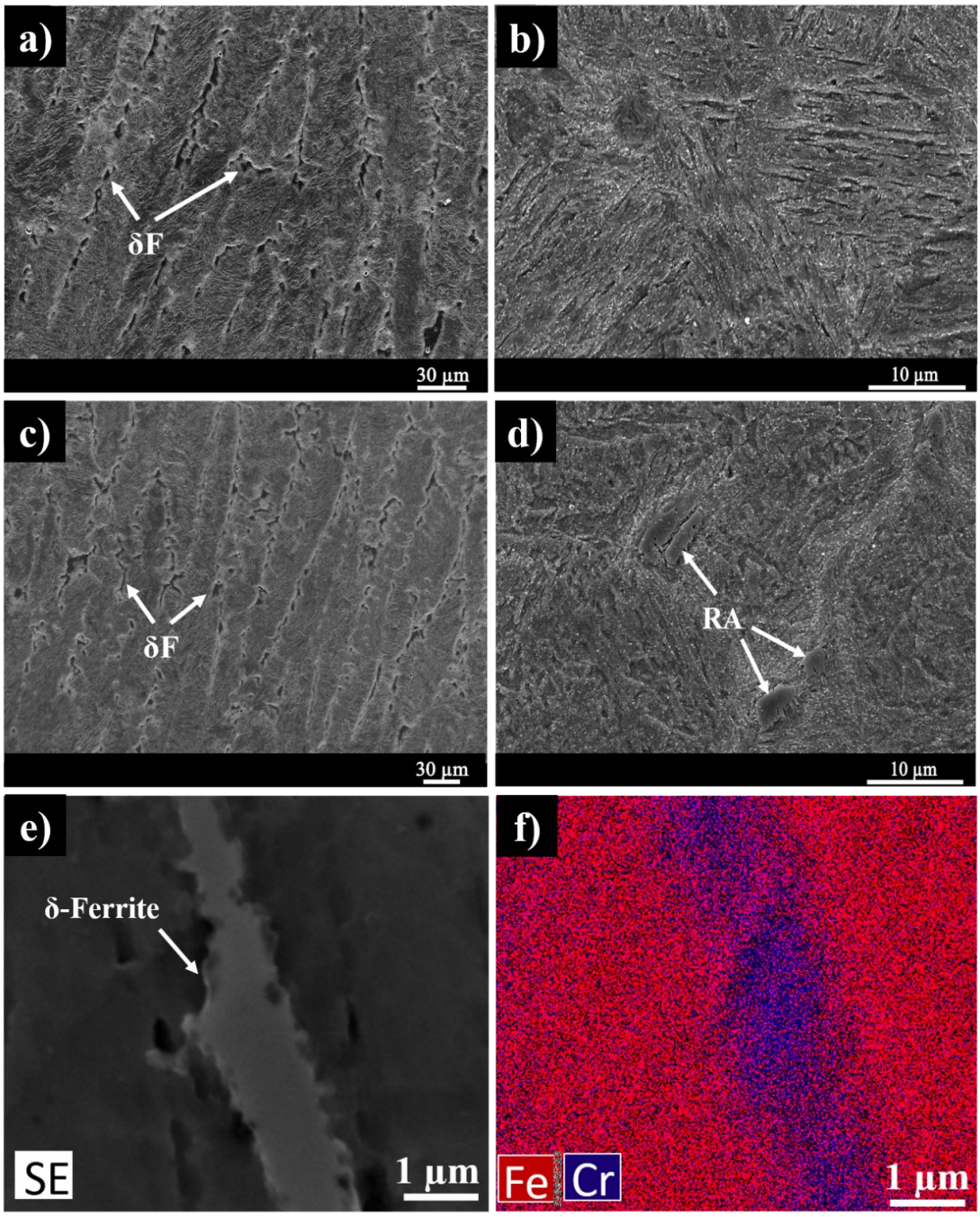

Figure 3.2.1 SEM micrographs of (a) and (b) IT25, (c) and (d) IT200, (e) the delta-ferrite phase, and (f) EDS elemental map taken from (e).

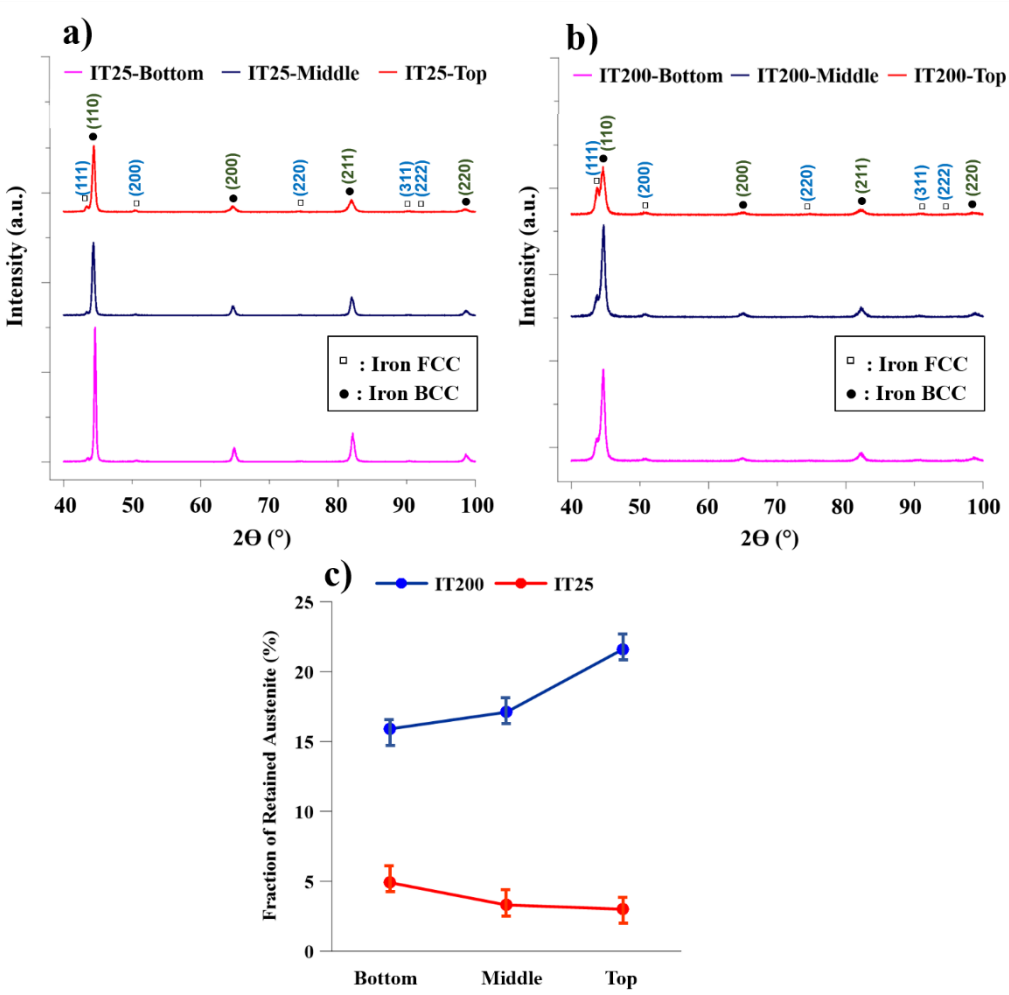

Figure 3.2.2 XRD spectra taken from various locations of (a) IT25 and (b) IT200 samples, (c) variations of retained austenite content along the building direction of the fabricated samples.

It should be also noted that the 420 MSS is a fairly hardenable alloy containing a relatively high carbon concentration (0.3-0.4 wt. %). Therefore, the formed martensite phase has a high level of tetragonality with a great tendency of rejecting the super-dissolved carbon atoms into the surrounding austenite. During the WAAM fabrication process, deposition of subsequent tracks frequently increases the temperature of previously solidified layers to temperatures above the M_s. This provides enough energy to trigger the diffusion of carbon atoms from the supersaturated martensite to the retained austenite with a face-centered cubic (fcc) structure with much higher solid solubility for carbon as compared to the martensite phase with a body-centered tetragonal (bct)

structure. Considering the martensitic transformation temperature equations [92,176], the higher carbon content decreases both M_s and M_f, causing further stabilization of the austenite phase. Accordingly, the formed carbon-rich austenite phase with an M_f below the room-temperature will be stabilized at room temperature during the final cooling cycle associated with the fabrication process. Fig. 3.2.3 shows the typical thermal history experienced by each deposited track as a result of two interpass temperatures of 25 °C and 200 °C along with a schematic illustration of the resultant microstructures. Such in-situ thermal history experienced by IT200 sample is analogous to the commonly known quenching and partitioning heat treatment cycle, which is intended to increase the content of retained austenite in martensitic steels [203,204]. In this heat treatment cycle, the sample is quenched to a temperature between M_s and M_f to form a mixture of martensite and untransformed austenite, followed by subjecting the material to a reheating cycle slightly above M_s to redistribute carbon atoms from martensite to austenite leading to a higher fraction of retained austenite [203,204,209]. It is worth mentioning that quenching and partitioning heat treatment does not normally result in nucleation of new austenite grains, but this heat treatment cycle can potentially lead to retaining of the pre-existing austenite phase at the partitioning temperature.

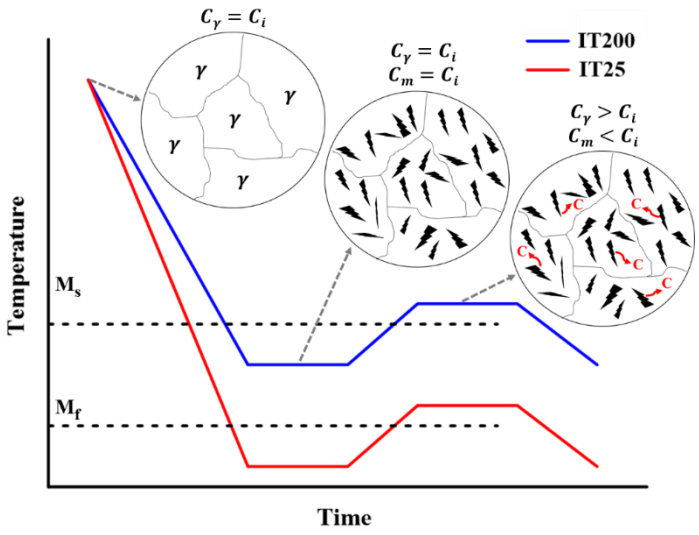

Figure 3.2.3 Schematic illustration of the thermal histories experienced by each deposited track as a result of two interpass temperatures of 25 °C and 200 °C.

The EBSD phase maps results also confirmed the higher fraction of retained austenite in IT200 (the blue phase in Fig. 3.2.4a) as compared to IT25 (Fig. 3.2.4d). The primary austenite grain boundaries can be roughly traced based on the martensite lath orientations in the inverse pole figure (IPF) maps of both samples (Fig. 3.2.4b and e), showing three and four primary austenite grains for IT200 and IT25 samples, respectively. The obtained IPF of the fcc phase in IT200 sample (Fig. 3.2.4c) indicates that all the retained austenite phases inside each primary austenite grain have the same crystal orientation. For instance, all the retained austenite phases in the right primary grain are closely oriented along the [111] crystal orientation, while the retained austenite phases in the middle grain are primarily aligned with the [101] crystal orientation (see the IPF legend in Fig. 3.2.4). This observation confirms that the detected retained austenite micro-constituents are formed due to carbon partitioning mechanism, and are not resulted from the formation of new austenite grains during reheating process.

According to Fig. 3.2.2c, the fraction of retained austenite in IT200 rises from the bottom to the top regions of the wall, which can be attributed to different thermal histories experienced by various regions along the building direction of the component during the fabrication process. The part experiences a higher cooling rate in the bottom regions as a result of the higher heat sink of the substrate. Therefore, only a limited time is provided for diffusion of carbon from martensite to austenite grains, which diminishes the partitioning process. On the other hand, the top regions of the component is subjected to a slower cooling rate due to the slight heat sink provided by heat-accumulated previous tracks. Therefore, in contrast to the bottom regions, the part stays longer at partitioning temperature (above M_s) in top regions during the deposition of each subsequent track. Consequently, the carbon content of austenite in the top regions will be higher, leading to a lower M_f and consequently formation of a higher fraction of retained austenite. It is worth mentioning that the effects of retained austenite volume fraction on the corrosion resistance and mechanical performance of the WAAM fabricated 420 MSS part will be comprehensively investigated in another study by the authors.

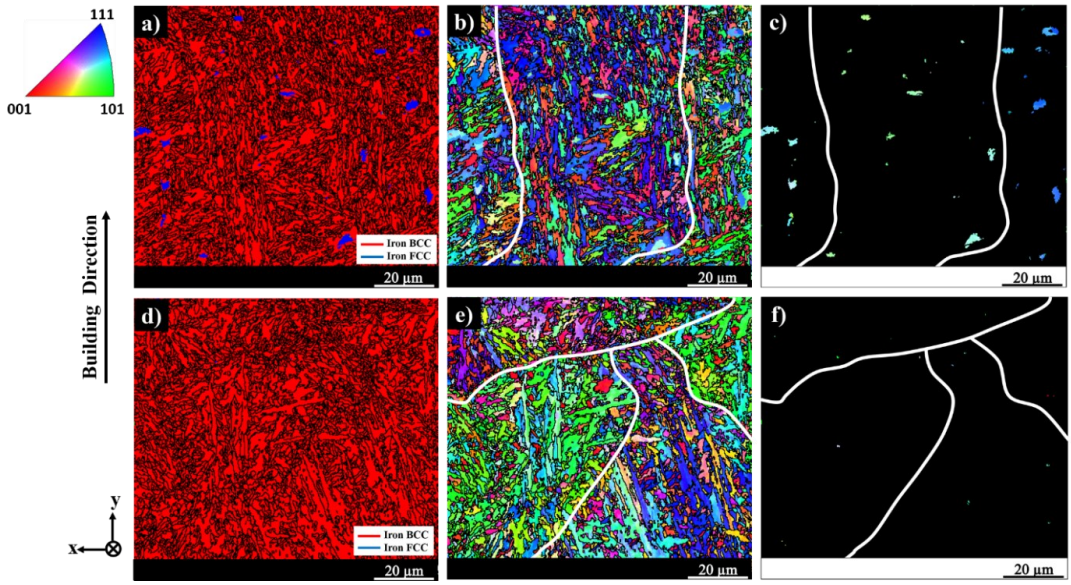

Figure 3.2.4 Schematic illustration of the thermal histories experienced by each deposited track as a result of two interpass temperatures of 25 °C and 200 °C.

3.2.5. CONCLUSION

The WAAM of ER420 MSS with different interpass temperatures, *i.e.* 25 °C (denoted by IT25) and 200 °C (denoted by IT200), revealed that the obtained as-printed microstructure highly depends on the thermal cycles experienced by the material during the fabrication process. Microstructure of IT25 was found to be composed of interdendritic delta-ferrite phase embedded in a martensitic matrix with a negligible amount of retained austenite. On the other hand, as a result of frequent in-situ quenching and partitioning heat treatment during the fabrication of IT200, a higher fraction of retained austenite was stabilized among the martensite lathes. Therefore, by proper adjustment of the interpass temperature during WAAM, a desired microstructure can be tailored in the as-printed 420 MSS component.

Acknowledgments

The authors would like to thank the support of Natural Sciences and Engineering Research Council of Canada (NSERC) [grant number RGPIN-2017-04368] and Memorial University of Newfoundland for sponsoring this work.

CHAPTER 4 Effect of Time and Temperature of Post-printing Aging Process on the Formation Sequence of Secondary Phases and Electrochemical Behaviour of Precipitation Hardening Martensitic Stainless Steel (PH 13-8MO) Fabricated by Wire Arc Additive Manufacturing

4.1 On the Microstructural Characteristics and Corrosion Performance of As-Printed and Heat-Treated PH 13-8Mo Martensitic Stainless Steel Fabricated by Wire Arc Additive Manufacturing

Alireza Vahedi Nemani[1], Mahya Ghaffari[1], Salar Salahi[2], Ali Nasiri[3]

1- Graduate Student, Dalhousie University, Halifax, Nova Scotia, Canada
2- Graduate Student, Memorial University, St. John's, Newfoundland, Canada
3- Assistant Professor, Dalhousie University, Halifax, Nova Scotia, Canada

Status: Submitted to the Journal of Electrochimica Acta (IF= 6.901)

Authors' Contribution

Alireza Vahedi Nemani: Conceptualization, Investigation, Writing - original draft, Visualization.

Mahya Ghaffari: Methodology, Fabrication Process, Validation, Investigation, Review & Editing.

Salar Salahi: EBSD Analysis, Corrosion Analysis, Review & Editing.

Ali Nasiri: Supervision, Writing - review & editing, Funding acquisition.

4.1.1. Abstract

In this study, the effect of post-printing solution and aging treatments on the microstructure and corrosion properties of a wire arc additive manufactured PH 13-8Mo martensitic stainless steel were investigated. The heat treatment cycles included solution treatment for 1 h at different temperatures (950, 1050, and 1200 °C), followed by aging process for 4 h at 400, 500, and 600 °C. The microstructural studies revealed that the solution treatment at 1050 °C could eliminate the columnar structure and also removed the undesired residual delta ferrite. Further aging process resulted in a coarser martensite lath structure at 400 °C, precipitation of β-NiAl phases at 500 °C, and formation of reverted austenite and M23C6 carbides at 600 °C. The effects of different microstructural features on the corrosion response of the as-printed (AP) and heat-treated samples were investigated by different electrochemical measurements, including open circuit potential

(OCP), potentiodynamic polarization (PD), electrochemical impedance spectroscopy (EIS), and Mott-Schottky (MS) tests. The electrochemical responses obtained from different samples showed that the elimination of Cr-enriched delta ferrite from the as-printed sample significantly improved the corrosion performance of the heat-treated samples, while the formation of M23C6 carbides at the highest aging temperature (600 °C) derived the sensitization phenomena and consequently impaired the corrosion resistance of the material.

4.1.2. INTRODUCTION

Additive manufacturing (AM), also known as 3D-printing, is an evolving technology for fabricating 3D near-net-shaped metal components with great cost-saving potential and significant reduction in the fabrication time, making this technology an ideal alternative to conventional subtractive manufacturing techniques [6][7]. A broad window of different materials including polymers, ceramics, composites, concretes and also a wide range of different metals and alloys can be 3D-printed employing different AM techniques [8][9][10]. Based upon the feeding method of the raw material, metal AM can be categorized into two major families of powder bed fusion (PBF) processes and directed energy deposition (DED) techniques [12][13]. In addition, a variety of energy sources, including laser, arc, plasma, and electron beam may be adopted to melt or sinter the feedstock material in each major process category [74][210]. Wire arc additive manufacturing (WAAM) is the most efficient DED process, which combines a consumable wire with an arc heating source to deposit low to medium complexity parts in a layer-by-layer manner [211][14]. WAAM offers a high material efficiency and deposition rate (as high as ~160 g/min) through continuous feeding of the entire feedstock material into the melt pool. Such deposition capability is suited for manufacturing large-scale metallic components in short time spans with a good structural integrity [212][76][14][8].

Despite the beneficial features of AM, most of the additively manufactured components are highly prone to form a non-uniform microstructure containing undesired non-equilibrium phases dictated by the complex thermal history associated with deposition of

sequential layers on top of each other during the manufacturing process [213][214][31][169]. In addition, a large number of alloys are not primarily used in the as-solidified condition as they are intended to be strengthened by different post-fabrication processes. For example, additively manufactured precipitation hardening martensitic stainless steels (PHMSS) not only are highly prone to form a textured microstructure along the building direction, but also encompass undesired residual delta ferrite phase in the as-printed condition, known as a detrimental phase to both corrosion and mechanical properties [47][46][215][64]. In addition, as reflected in their family name, precipitation hardening alloys need to be solution-treated and aged to attain the desired in-service performance through the formation of secondary phases, reiterating the necessity of implementing a post-printing operation on the additively manufactured parts. In particular, PH 13-8Mo MSS with a wide range of industrial applications are normally aged at different temperatures in the range of 400 to 700 °C to form β-NiAl precipitates to improve the mechanical properties of the alloy [52]. However, some other secondary phases, such as carbides and reverted austenite, may form during the aging treatment of PH 13-8Mo MSS especially at higher aging temperatures [216]. There is a controversary in terms of the recommended optimum aging temperature for this alloy in the literature derived by the differences in the intended in-service conditions. For applications in mild and non-corrosive environments, aging at 500-550 °C is recommended. In this temperature range, the formation of coherent β-NiAl phases can lead to significantly improved mechanical performance of the material, while the presence of carbides and reverted austenite in the over-aged condition deteriorates the mechanical properties [217][218][219][52][220]. On the contrary, for harsh environment applications, such as hydrogen or saturated H_2S solution, the use of this alloy in the over-aged condition is recommended in which the presence of reverted austenite improves the toughness and the resistance of the material to stress corrosion cracking [221][222][223]. This discrepancy implies the cruciality of investigating the effect of aging temperature on the microstructure and the influence of different microstructural features on the performance of the material based on the actual in-service condition.

To the authors' best knowledge, there is no study in the literature investigating the effect of different secondary phases formed during the aging process on the passive layer stability and electrochemical performance of a wire arc additively manufactured PH13-8Mo MSS under simulated sea-water condition (naturally-aerated 3.5 wt.% NaCl solution). Therefore, for the first time, the current study investigates the effect of post-printing heat treatment, including solution treatment (at 900, 1050, and 1200 °C) followed by an aging treatment (at 400, 500, 600 °C) on the microstructural features and electrochemical performance of a WAAM fabricated PH 13-8Mo MSS.

4.1.3. MATERIALS AND METHODS

In this study, a thin wall-shaped PH 13-8Mo MSS part was additively manufactured using a S-350 Lincoln Electric GMAW machine with a torch integrated with a six-axis Fanuc robotic arm. The process parameters were optimized to attain minimum splashing and the highest arc stability during deposition, leading to the lowest possible interpass defects and lack of fusions. The optimum process parameters and the nominal chemical composition of the feedstock wire are listed in Table 1 and 2, respectively. More details about the fabrication process can be found in the authors' previous publication [215].

Table 4.1.1 The optimum process parameters used for WAAM of PH 13-8Mo stainless steel.

Arc Current	Arc Voltage	Wire Feeding Speed	Scanning Rate	Shielding Gas	Argon Flow Rate
135 A	28 V	67 mm/s	4 mm/s	90% He, 7.5% Ar, and 2.5% O_2	20 L/min

Table 4.1.2 The nominal chemical composition (wt. %) of the feedstock wire (PH 13-8Mo).

Cr	Ni	Mo	Al	Mn	Si	C	S	N	Fe
12.25-13.25	7.5-8.5	2-2.5	0.9-1.35	0.1	0.1	0.05	0.01	0.01	Bal.

To investigate the effects of post-printing heat treatment on the microstructure and corrosion properties, the as-printed samples were subjected to different solution and aging treatments using a Thermo-Scientific Lindberg furnace. With the aim of optimizing the post-printing heat treatment parameters, the samples were initially subjected to 1 h solution treatment at 900, 1050, and 1200 °C (denoted as S900, S1050, S1200 samples, respectively), followed by 4 h aging process at 400, 500, and 600 °C (denoted as A400, A500, and A600, respectively). It is notable that both solution and aging treatments were followed by still-air cooling.

Both as-printed and heat-treated samples were then subjected to multi-scale characterization methods. To do so, the samples were ground and polished followed by etching for around 20 s with Fry's reagent. Initially, microstructural characterizations at low magnifications were carried out employing a stereo microscope (AmScope), and an optical microscope (OM) (Nikon Eclipse 50i). To further characterize the microstructural features, a scanning electron microscope (SEM) (FEI MLA 650FEG) equipped with electron back-scattered diffraction (EBSD) and energy-dispersive X-ray spectroscopy (EDS) detectors was employed. To identify the potentially formed nano-scale precipitates during the aging process, high magnification images were obtained using a Talos 200X scanning transmission electron microscope (STEM) equipped with an extreme field emission gun (X-FEG) source operating at 200 kV. X-ray diffraction (XRD) technique was also used to calculate the dislocation density of the samples using a Cu-Kα source and a Rigaku Ultima IV X-ray machine.

To analyze the corrosion performance and electrochemical stability of the passive layers formed on the as-printed and heat-treated samples, an IVIUM Potentiostat device was used to perform different electrochemical measurements, including potentiodynamic polarization (PDP), electrochemical impedance spectroscopy (EIS), and Mott-Schottky (MS) analysis in a naturally aerated 3.5 wt.% NaCl electrolyte maintained at 25±0.5 °C using a temperature-controlled water bath. To set up the corrosion cell, three electrodes, including an Ag/AgCl reference electrode, a graphite rod as the counter electrode, and the working electrode (sample) were utilized. It is notable that prior to performing each

measurement, the open circuit potential (OCP) was run for 1 h on the mirror-like polished surfaces to ensure the potential stability between the reference and working electrodes. The PDP test was conducted at the scanning rate of 0.1 mV/s in a potential range of -0.5 to +1.0 $V_{Ag/AgCl}$ versus the OCP. In addition, the EIS measurement was run in a range of frequency between 100 kHz and 10 mHz with a sinusoidal perturbation voltage of 10 mV following 1 h, 3 days, and 5 days of immersion time. The MS tests were conducted at a frequency of 1000 Hz with a 10 mV AC potential in a range between –1000 and 1000 $mV_{Ag/AgCl}$ with a rate of 50 mV/step. To analyze the morphology, density, and depth of the pits formed during the corrosion tests, a scanning laser confocal microscope (Keyence VK-X1000) was used.

4.1.4. RESULTS AND DISCUSSION

4.1.4.1 Microstructural Characterization

4.1.4.1.1 As-printed Sample

The macrostructure of as-printed WAAM PH 13-8Mo stainless steel sample, as depicted in the stereo microscopy images in Fig. 4.1.1, was characterized by coarse uniaxial columnar grains nucleated from the substrate and elongated parallel to the building direction up to the top of the wall. It is noticeable that as each layer was deposited upon the previous one, the grains epitaxially grew on the columnar grains of the previously solidified track, which eventually resulted in an orientation-dependent directional growth along the building direction.

According to the SEM image shown in Fig. 4.1.1, the microstructure of the as-printed sample primarily consists of ~11% of residual delta (δ) ferrite (indicated by white arrows in Fig. 4.1.1) embedded in a fine and low-carbon (less than 0.05 wt.%) martensitic matrix. Hochanadel *et al.* [220] also reported the formation of residual delta ferrite in the microstructure of the as-solidified investment cast PH 13-8Mo stainless steel. The presence of residual delta ferrite at room temperature can be attributed to the high chromium content (13%) of the alloy as a ferrite stabilizing alloying element in addition to the rapid cooling rate associated to the nature of the additive manufacturing process,

restricting the diffusional solid-state transformation of delta ferrite to austenite [215]. EDS elemental maps of Cr and Ni (see Fig. 4.1.1) also confirm that the delta ferrite phases were depleted in Ni (an austenite promoting element) and enriched in Cr as a ferrite stabilizing element. Similar observations in terms of the compositional content of delta ferrite was also reported by Hochanadel *et al.* [220]. It is notable that Cr-enriched delta ferrite acts similar to chromium carbides in stainless steels, provoking the sensitization phenomena leading to weakened corrosion performance of the material [224][225]. Considering the martensite finish temperature of the PH 13-8Mo alloy being above room temperature ($M_f \approx 30$ °C) [226], no retained austenite (RA) was expected to form in the as-printed sample. However, the TEM analysis, including the bright-field image and its associated selected area electron diffraction (SAED) pattern, confirmed the formation of retained austenite in the as-printed sample (see Fig. 4.1.1). The formation of retained austenite in the as-printed sample can be attributed to the implementation of the interpass temperature of ~100 °C (between $M_s \approx 120$ °C [226][227], and $M_f \approx 30$ °C of the alloy), resulting in an in-situ quenching and partitioning heat treatment, which promoted the formation of retained austenite in the as-printed part. A more detailed elaboration on this in-situ heat treatment along with a comprehensive discussion on the microstructural evolution of the as-printed sample and its effect on the mechanical properties of the fabricated wall can be found in the authors' previous publications [215].

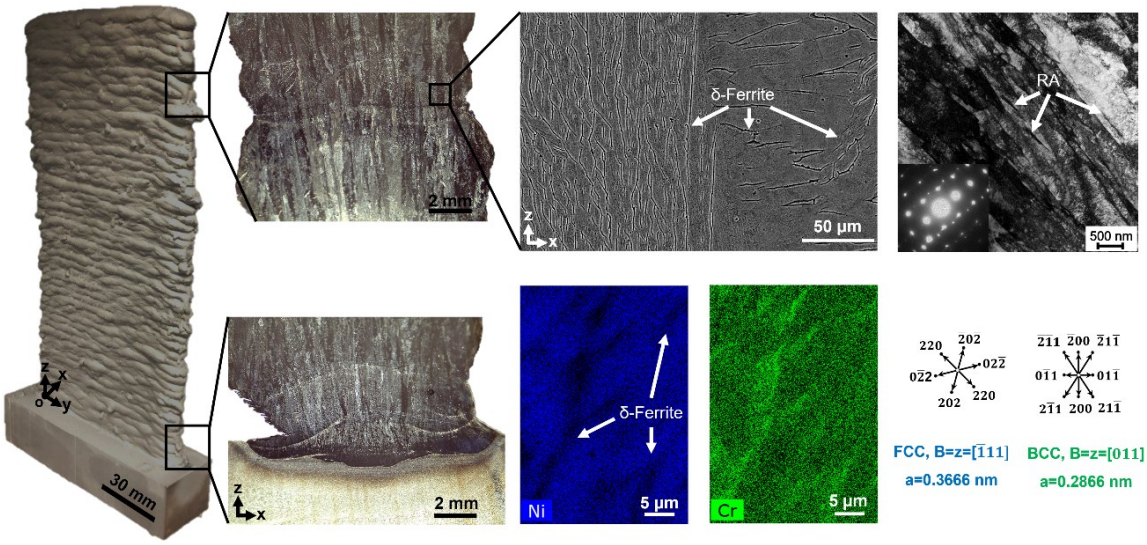

Figure 4.1.1 The as-printed WAAM 13-8Mo MSS wall along with its macro/microstructural analysis results including stereo microscope images, SEM, EDS elemental maps, the bright field TEM image and its associated SAED pattern analysis.

4.1.4.1.2 Heat-treated samples

4.1.4.1.2.1 Solution treatment

To reduce the process-induced residual stress, eliminate the large columnar grain structure, and remove the deleterious residual delta ferrite from the structure of the as-printed material, post-fabrication heat treatment including a solution treatment followed by an aging process was applied to the WAAM PH13-8Mo MSS wall. The solution treatment was performed for 1 h at three different temperatures, *i.e.,* 900, 1050, and 1200 °C, to obtain the optimal solutionizing temperature. Fig. 4.1.2 compares the microstructure of different solution-treated samples. According to Fig. 4.1.2a, the solution treatment at the lowest temperature (900 °C) was not successful in eliminating the columnar structure of the material, affirming that 900 °C was not high enough to reach the single-phase austenite stability region. In addition, as revealed by the SEM image (see Fig. 4.1.2b), the delta ferrite phase was stable and detectable in the S900 sample, which is not aligned with the primary intention of performing solution treatment. On the other hand, although solution treatment at the highest temperature of 1200 °C

eliminated the columnar grains from the structure (see Fig. 4.1.2f), it resulted in the partial re-formation of delta-ferrite phase at the boundaries of primary austenite grains as shown in Fig. 4.1.2g. The presence of undesired delta ferrite in the microstructure of this sample also disqualifies 1200 °C from being an optimum solutionizing temperature. However, as shown in Fig. 4.1.2c, the solutionizing temperature of 1050 °C completely removed the columnar structure from the as-printed sample, resulting in the nucleation and growth of newly formed equiaxed austenite grains. Furthermore, high-magnification SEM images taken from S1050 sample confirmed the elimination of residual delta ferrite phase, leading to the formation of a fully martensitic microstructure at room temperature (see Fig. 4.1.2d).

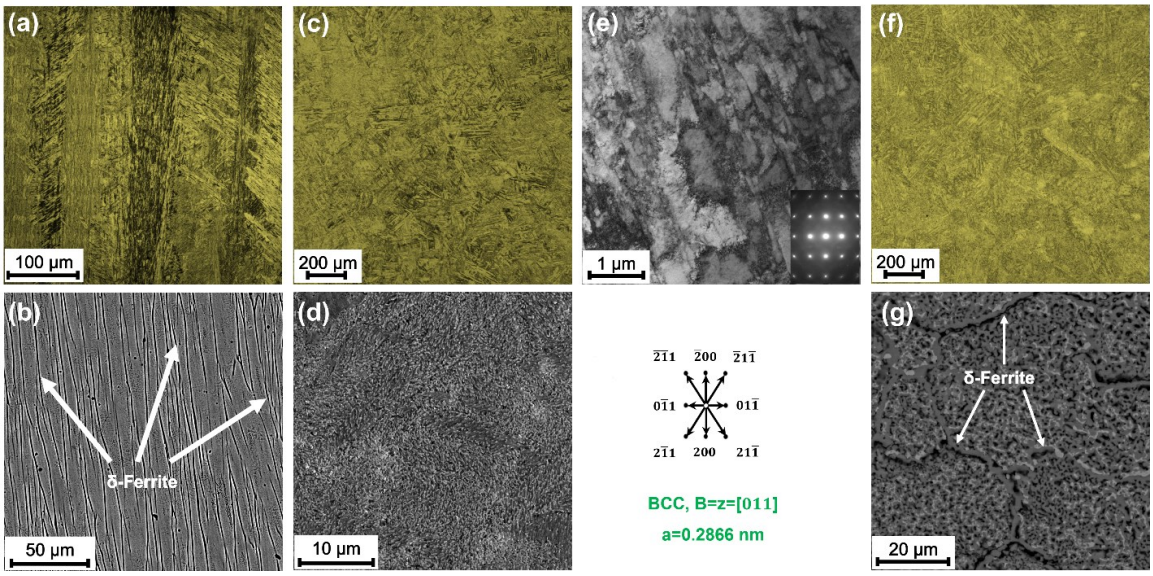

Figure 4.1.2 Microstructural analysis of different solution treatment conditions, including (a and b) S900, (c-e) S1050, and (f and g) S1200 samples.

The TEM bright-field image and the corresponding SAED pattern taken from the S1050 sample illustrated a fully martensitic microstructure with no evidence of retained austenite (see Fig. 4.1.2e). The elimination of retained austenite in S1050 sample can be related to its single heating cycle to single-phase austenitic stability region followed by air-quenching to below M_f temperature. Seetharaman *et al.* [228] also studied the precipitation hardening process in PH 13-8Mo stainless steel and reported the absence of

any secondary phases, such as residual delta ferrite, retained austenite or different types of carbides, in the solution-treated condition. Fig. 4.1.3 illustrates the 2D and 3D orientation distribution function (ODF) maps and the corresponding crystallographic directions and planes of the AP and S1050 samples, confirming the elimination of the columnar structure from the as-printed sample during solution treatment. According to the obtained ODFs at φ_2=45°, AP sample showed a strong dominancy of preferential {001}<100> solidification texture with a maximum intensity of 16.24 (Fig. 4.1.3a), while a weaker texture components of {011}<111> and {001}<100> were observed for the S1050 sample (Figs. 4.1.3b) with a maximum intensity of 2.51. The stronger texture of the as-printed sample can be attributed to the texture formation during solidification and multi-reheating cycles associated with the WAAM process [229–231]. However, as a result of the solution treatment, the preferred texture of the as-printed sample was disrupted due to recrystallization and growth of new austenite grains, which led to the formation of a more homogeneous microstructure with a weakened texture.

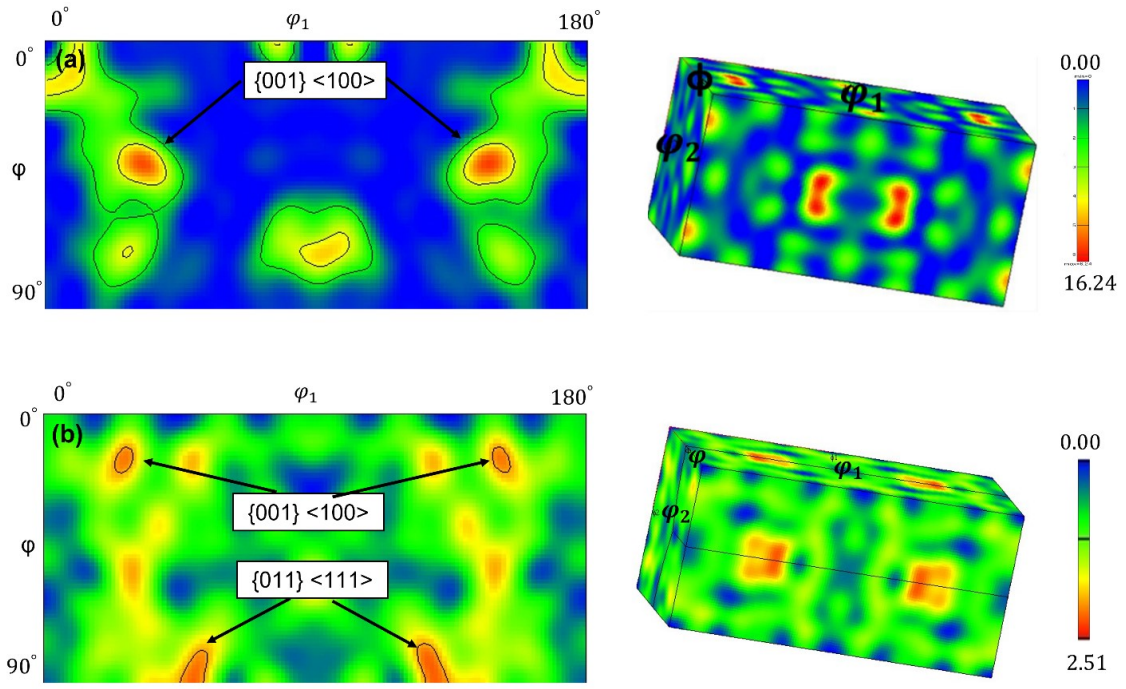

Figure 4.1.3 Angular textural cross-sections of orientation distribution function at φ_2=45° for the (a) AP and (b) S1050 samples.

Overall, according to the aforementioned microstructural features in each sample, 1050 °C was selected as the optimum solutionizing temperature due to the complete elimination of grains directionality and residual delta ferrite from the microstructure. Therefore, further aging process was only applied to the sample being solution-treated at 1050 °C.

4.1.4.1.2.2 Aging Process

In order to investigate the effect of aging process on the microstructure and corrosion performance, three aging temperatures of 400, 500, and 600 °C were applied to the 1050 °C solution-treated sample. According to the TEM images taken from the aged samples at different temperatures (Figs. 4.1.4-6), the predominant microstructure of all aged samples was characterized by a lath martensite structure regardless of their aging temperature. However, the microstructure of different aged samples can be differentiated in terms of various secondary phases and precipitates that were formed at different aging temperatures, which will be comprehensively discussed in the following sections.

As depicted in Fig. 4.1.4a and b, aging at 400 °C did not significantly alter the microstructure except for partial shrinkage of the laths, promoted by the lath boundaries migration [228]. The migration of lath boundaries during the aging process decreased the lath size aspect ratio ($\frac{\text{major axis (c)}}{\text{minor axis (a)}}$) resulting in a less-elongated lath structure as compared to more uniaxial/elongated shaped martensite laths with sharp tips in the as-printed and solution-treated samples. It is notable that the formation of secondary phases or precipitates were not evident in the A400 sample even at very high magnifications (see Fig. 4.1.4b).

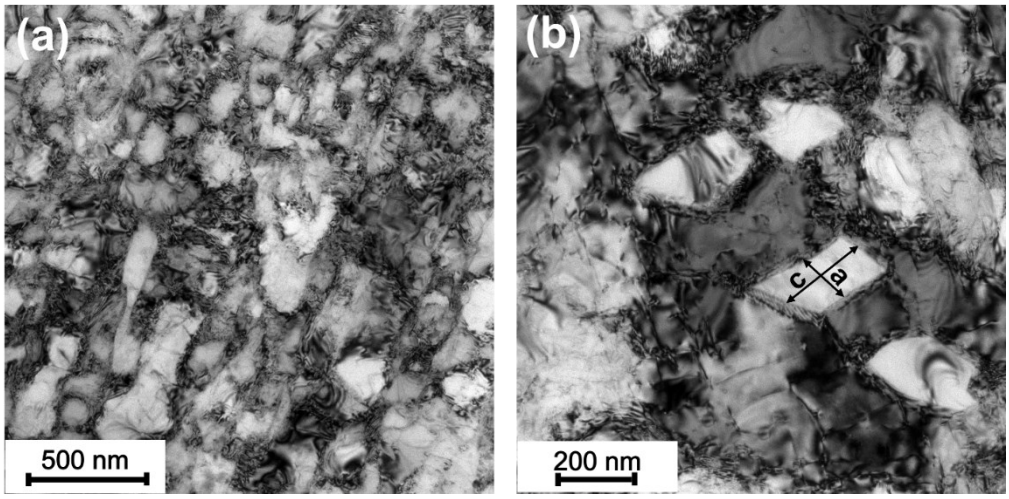

Figure 4.1.4 Bright field TEM images taken from the microstructure of A400 sample at (a) low and (b) high magnifications.

However, aging at 500 °C led to the formation of a considerable volume fraction of spherical precipitates with a size in the range of 10-15 nm diameter and an inter-spacing of around 15-20 nm (see Fig. 4.1.5a). One can claim that the precipitates experienced a homogeneous nucleation since they were formed in a spherical morphology mostly within martensite laths rather than being formed on lath boundaries [52]. The precipitates were just observed in some random laths, which can be attributed to the dependency and sensitivity of phase detection to the relative orientation of the matrix resulting in some precipitates to be out of contrast in some neighboring laths [220]. According to the indexed SAED pattern (enclosed in Fig. 4.1.5a), the nanoscale spherical phases were characterized as β-NiAl precipitates. The associated STEM-EDS elemental maps taken from β-NiAl also show the enrichment of the precipitates in Al and their depletion in Cr and Fe (see Fig. 4.1.5b-d). It is notable that β-NiAl precipitates have a B2 (CsCl) structure with a lattice parameter of 0.2887 nm being very close to the lattice constant of BCC-Fe (0.2866 nm) [232]. The close lattice parameter of β-NiAl and the matrix results in the formation of highly coherent precipitates with minimal lattice mismatch along their interface with the matrix [232], as confirmed by the high-resolution TEM image shown in Fig. 4.1.5e

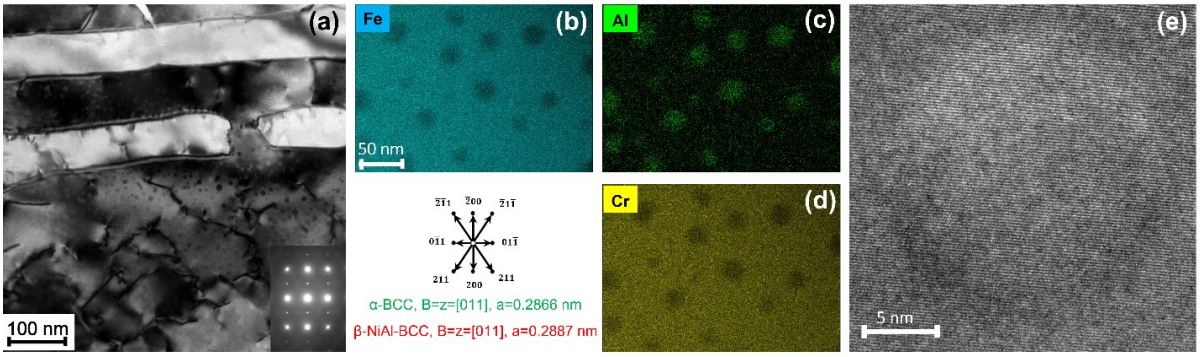

Figure 4.1.5 (a) Bright field TEM image along with its enclosed SAED pattern, (b-d) EDS elemental maps (Fe, Al, and Cr) and (e) high-resolution TEM image taken from an AlNi precipitate in A500 sample.

The low magnification bright-field TEM image of A600 sample (Fig. 4.1.6a) along with the diffraction pattern taken from a selected area (Fig. 4.1.6b) indicated the formation of reverted austenite (γ-Fe, FCC, a = 0.366 nm [52]) in this sample, consistent with previous observations during high temperature aging of PH 13-8Mo alloy in the literature [216][222][220][228]. The formation of reverted austenite can be attributed to the micro-segregation of austenite stabilizing alloying elements, such as Ni, at the lath boundaries or around the high-energy spots in the matrix, such as lattice defects and dislocations, resulted from martensitic transformation. The STEM-EDS line scan taken from the reverted austenite (Fig. 4.1.6b) also confirms the higher concentration of Ni in the reverted austenite herein. Schnitzer *et al.* [216] also measured the Ni content of austenite phase formed in 13-8Mo PH stainless steel using atom probe tomography (APT) technique and reported ~14 at.% Ni in austenite as compared to ~4 at.% Ni in the matrix, while Al content remained relatively unchanged. The stabilization of reverted austenite during the subsequent cooling cycle can be attributed to the higher local concentration of austenite stabilizing alloying elements in the reverted austenite, which results in the reduction of martensite finish temperature (M_f) to below room temperature [220].

Higher magnification TEM image of A600 sample (Fig. 4.1.6c) illustrated the formation of another secondary phase with an oval morphology at the vicinity of the reverted austenite with a size in the range of 10-30 nm. Further higher magnification bright-field TEM image along with its associated SAED pattern shown in Fig. 4.1.6d, confirmed the

formation of $M_{23}C_6$ carbides, with FCC crystal structure and a lattice parameter of a = 1.0666 nm, embedded in a martensitic matrix including homogenously distributed pre-existing spherical β-NiAl precipitates, which is consistent with previous observations in the literature [220][52][222][217][233]. It has been reported that the formation of carbides promotes the nucleation of reverted austenite since $M_{23}C_6$ has very limited solid solubility for Ni, leaving the matrix with an enriched Ni content, which ultimately stimulates the nucleation and stability of reverted austenite [233]. The STEM-EDS line scan taken from a carbide particle presented in Fig. 4.1.6 shows that the carbides are enriched in Cr, while its adjacent area is enriched in Ni.

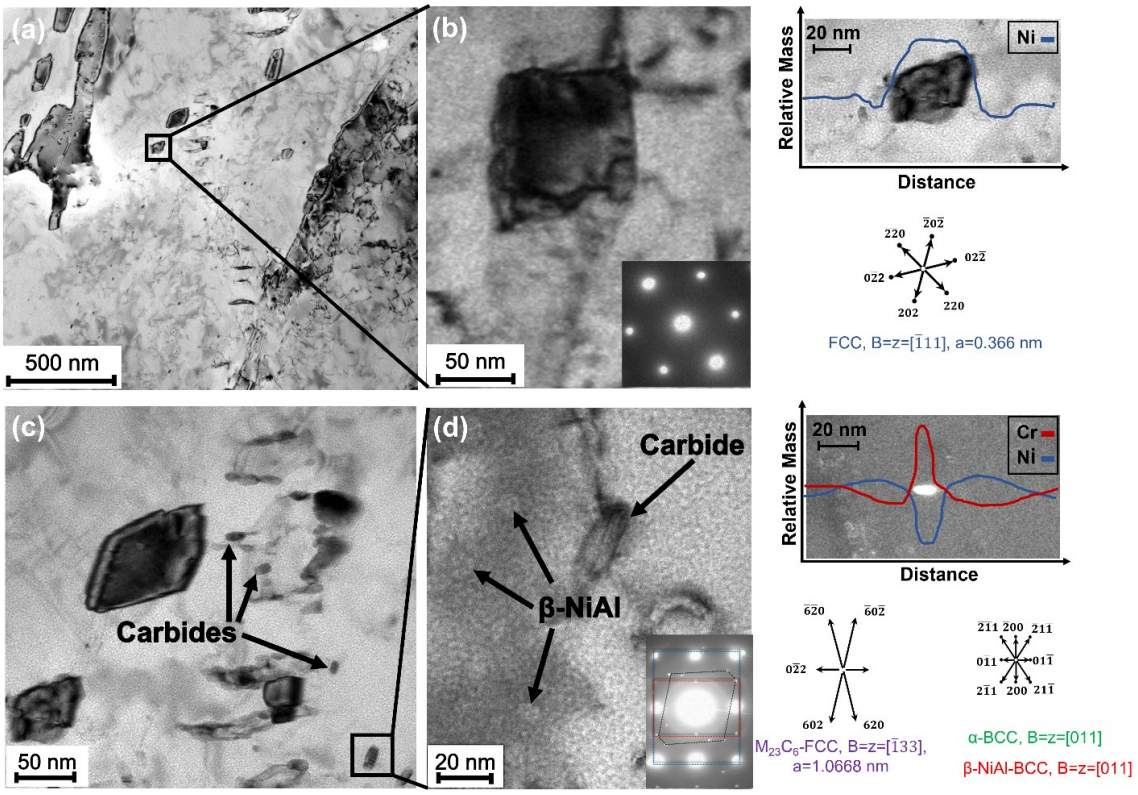

Figure 4.1.6 TEM analysis of A600 sample including (a) low magnification bright field image, (b) selected area from reverted austenite along with its diffraction pattern and EDS line scan of Ni, (c) high magnification TEM image showing the formation of carbides around the revered austenite, (d) selected area from carbides along with its diffraction pattern and EDS line scan of Ni and Cr.

4.1.4.2 Electrochemical analysis

4.1.4.2.1 Open circuit potential (OCP)

In order to stabilize the potential between the reference and working electrodes and also obtain an initial understanding from the electrochemical response of the as-printed and different heat-treated samples, open circuit potential (OCP) tests were monitored for 1 h in naturally-aerated 3.5 wt. % NaCl solution at room temperature. The OCP curves shown in Fig. 4.1.7 reveals that the as-printed sample exhibited the lowest average OCP value (-0.071 ± 0.015 V) relative to the heat-treated samples, indicating a lower corrosion resistance and more instability in its electrochemical response. Among the heat-treated samples, A500 had the noblest OCP value with an average of 0.443 ± 0.013 V as compared to A400 with 0.201 ± 0.011 V and A600 with the average OCP value of 0.064 ± 0.007 V. The observed fluctuations in the OCP curves of AP and A600 samples is also another indication of their more active-like surfaces potentially as a result of some localized attacks and metastable pitting corrosion [224], while the more stable OCP curves of A400 and A500 samples suggest a more passive-like behavior of the material over the immersion period. A deeper electrochemical analysis will be carried out in the following sections by PDP, Mott-Schottky, and EIS measurements.

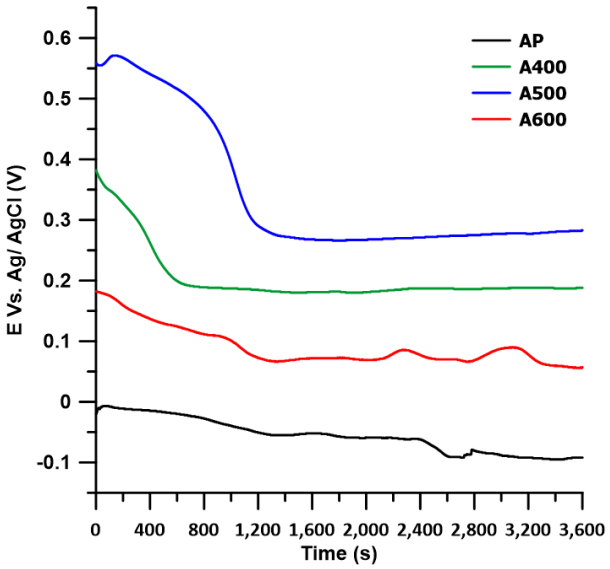

Figure 4.1.7 The OCP curves over 1 h immersion in an aerated 3.5 wt. % NaCl electrolyte for AP, A400, A500, and A600 samples.

4.1.4.2.2 Potentiodynamic polarization (PDP) measurements

Fig. 4.1.8 shows the results of the potentiodynamic polarization measurements of the as-printed and heat-treated samples. Different electrochemical parameters detected from the PDP test, including pitting and corrosion potentials (E_{pit} and E_{corr}), and pitting and corrosion current densities (i_{pit} and i_{corr}), are given in Table 4.1.3. Expectedly, a relatively extensive passive section was identified in the anodic branch of all samples since stainless steels normally form a passive film on their surfaces while immersed in a chloride solution with a cathodic reaction of oxygen reduction in aerated, near neutral pH solutions [234]. Interestingly, the corrosion and pitting potentials of all heat-treated samples were higher than that of the as-printed sample showing a better corrosion resistance as a result of post fabrication heat treatment. Among the heat-treated samples, the highest pitting potential (1.306 ± 0.010 $V_{Ag/AgCl}$) was related to A500 sample showing its higher resistance to pitting corrosion, while A600 exhibited the lowest pitting potential (0.767 ± 0.024 $V_{Ag/AgCl}$) indicating more susceptibility to pitting corrosion [234]. Additionally, another indication of a better corrosion resistance is the smaller corrosion current density (i_{corr}) [170]. According to Table 4.1.3, the lowest i_{corr} and the greatest E_{pit}-E_{corr} was related to A500 sample, confirming its higher tendency to passivation in the NaCl solution as compared to other samples, which indicates that the formation of new pits and also the propagation rate of pre-existing pits are slowed down [235].

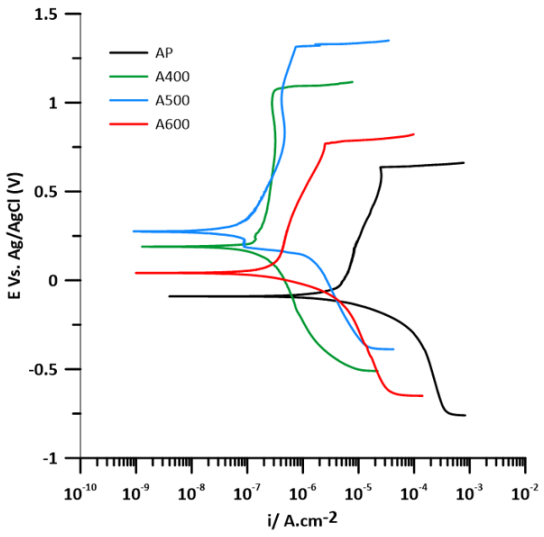

Figure 4.1.8 The PDP graphs of the AP, A400, A500, and A600 samples.

Table 4.1.3 Different electrochemical parameters detected from the PDP test for AP, A400, A500, and A600 samples.

Sample	E_{corr} ($V_{Ag/AgCl}$)	E_{pit} ($V_{Ag/AgCl}$)	I_{corr} ($\mu A\ cm^{-2}$)	I_{pit} ($\mu A\ cm^{-2}$)	$E_{pit-Ecorr}$ ($V_{Ag/AgCl}$)
AP	-0.091 ± 0.015	0.669 ± 0.025	2.441 ± 0.012	25.376 ± 0.194	0.760 ± 0.016
A400	0.188 ± 0.011	1.118 ± 0.022	0.088 ± 0.001	0.484 ± 0.110	0.930 ± 0.027
A500	0.277 ± 0.003	1.316 ± 0.010	0.041 ± 0.003	0.699 ± 0.045	1.039 ± 0.010
A600	0.056 ± 0.007	0.757 ± 0.024	0.192 ± 0.008	2.901 ± 0.191	0.701 ± 0.020

4.1.4.2.3 Electrochemical Impedance Spectroscopy (EIS)

EIS measurements were also conducted to further characterize integrity, protectiveness, and the progressive behavior of the oxide passive layers formed on the as-printed and heat-treated samples. Fig. 4.1.9 shows the Bode and Nyquist plots obtained from the EIS testing after exposure to aerated 3.5 wt.% NaCl solution at room temperature under OCP condition for 1 h, 3 days, and 5 days. Comparing the Bode and Nyquist plots at different time intervals reveals that longer times of immersion in the solution resulted in a noticeable reduction in the radius of the capacitive semi-arc (see Fig. 4.1.9b, d, and f), along with a relatively significant decrease of $|Z|$ at low and medium frequencies (see Fig. 4.1.9a, c, and e). These observations affirm that the passive layer of all samples provided inferior protection over time, which can be attributed to the continuous and intense dissolution of the oxide film in the solution and also its reduced electrochemical resistance as the immersion period increases [224]. As a numerical example, the $|Z|_{max}$ (at the lowest frequency) of the AP and A500 samples dropped form 222.34 and 1272.12 $K\Omega.cm^2$ to only 9.58 and 22.14 $K\Omega.cm^2$, respectively, as the immersion time increased from 1 h to 5 days.

Larger semi-circle radius in the Nyquist plots, and higher maximum absolute value of impedance ($|Z|_{max}$) of the heat-treated samples as compared to the as-printed sample shows an improvement in the electrochemical stability of the passive film as a result of the post-printing heat treatment. Additionally, the impedance module vs frequency plots of the heat-treated samples showed a higher linearity in comparison with the as-printed

sample confirming a more protective passive layer being formed on the heat-treated samples as compared to the as-printed sample. The heat-treated samples are also characterized by a higher constant phase angle (θ) over a wider range of frequency than that of the as-printed sample revealing that the post-printing heat treatment process drastically improved the corrosion resistance of the material [236]. In particular, the heat-treated samples after 3 days of immersion had a maximum constant phase angle of around 80° compared to the as-printed sample with a maximum constant phase angle of 67°.

The lower corrosion resistance of the as-printed sample can primarily be ascribed to the presence of delta ferrite phase, which can trigger the sensitization phenomena as this phase is enriched in chromium leaving the adjacent area with less than 13% of chromium facilitating the nucleation and growth of pits [173–175]. Additionally, the better corrosion performance of the heat-treated samples can be related to their lower residual stress, lower tetragonality of the martensitic matrix, and less dislocation density as a result of the aging process. It is worth noting that a detailed discussion on the effect of the microstructural features on the corrosion performance of different samples is presented in section 4.1.4.3.

In order to quantify the EIS measurements results, the obtained data were fitted and modeled applying the equivalent circuit (EC) depicted in Fig. 4.1.10, which is commonly suggested for stainless steels [237]. It should be noted that the fitted data from the modeling are presented by solid lines in the Bode and Nyquist plots shown in Fig. 4.1.9. To consider the potential nano/micro heterogeneities in the surface of the samples, such as impurities, intergranular porosities and roughness, and also to address the non-ideal capacitance response of the interface, constant phase elements (CPE) were utilized in this EC model whose impedance values (Z_{CPE}) can be calculated as follows [238]:

$$Z_{CPE} = [Q(i\omega)^{n}]^{-1} \tag{4.1.1}$$

where Q is the frequency-independent constant (CPE constant), i represents the imaginary unit ($i = \sqrt{-1}$), ω denotes the angular frequency, and n relates to the fractional exponent of the constant phase element.

The three resistors in the EC model correspond to the resistance of the solution (R_s), resistance of the passive layer (R_p), and charge transfer resistance (R_{ct}), while the two constant phase elements represent the passive film capacitance (CPE_p), and double layer capacitance (CPE_{dl}). Table 4.1.4 summarizes fitting parameters obtained from the employed equivalent circuit. It is notable that the values of n_1 and n_2 were all below 0.99 and the chi-square values are all less than 10^{-2}, showing a good harmony between the experimentally measured EIS data and the fitted values obtained from the modeling. According to Table 4.1.4, the values of charge transfer resistance are higher than passive layer resistance ($R_{ct} > R_p$) in A400 and A500 samples, while it is vice versa for the AP and A600 samples. The higher values of R_{ct} than R_p in the A400 and A500 samples indicates the formation of a protective surface layer with an ideal passive behavior [239]. On the other hand, the smaller values of R_{ct} than R_p in the case of AP and A600 samples suggests that these samples are more likely prone to localized corrosion attack. The localized attack in the AP sample can be correlated to the presence of sensitized regions adjacent to the residual delta ferrites, while the formation of carbides in the A600 sample can be responsible for its impaired corrosion properties. Comparing the R_{ct} of all samples reveals that A500 owns the highest value of charge transfer resistance, confirming its best passive performance against the localized corrosion [239]. On the other hand, the maximum value of (CPE_{dl}) is related to AP sample implying the formation of a more defective passive layer on this sample.

It is noticeable that as the immersion time increases, the values of R_{ct} and R_p decreases while CPE_p and CPE_{dl} increases, suggesting a continuous deterioration in the electrochemical stability of the passive layers at longer immersion time possibly due to progressive dissolution of surface oxide layer into the NaCl solution.

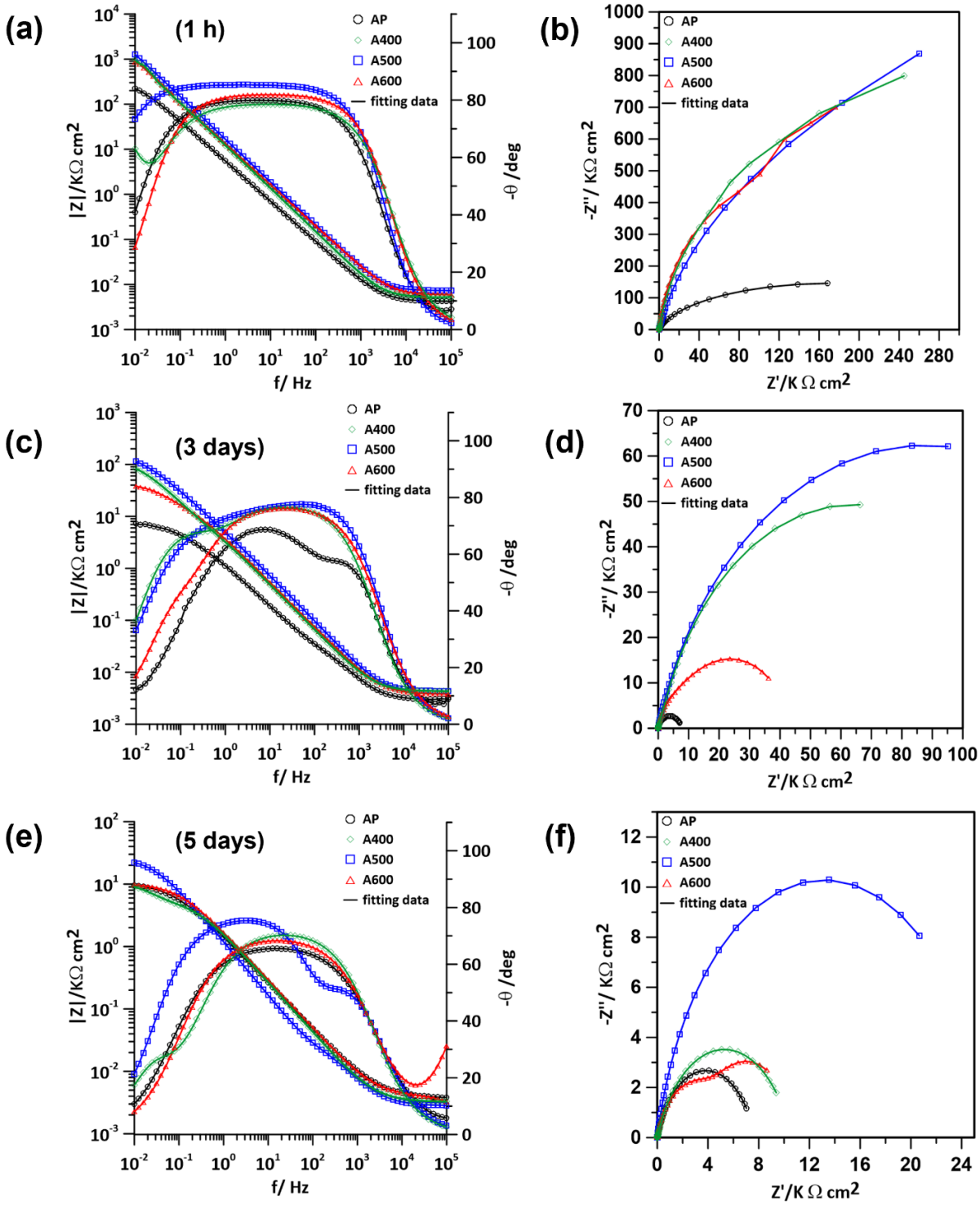

Figure 4.1.9 Bode and Nyquist spectra of the as-printed and heat-treated samples being immersed in aerated 3.5 wt.% NaCl solution at room temperature under OCP condition for (a and b): 1 h, (c and d): 3 days, and (e and f): 5 days.

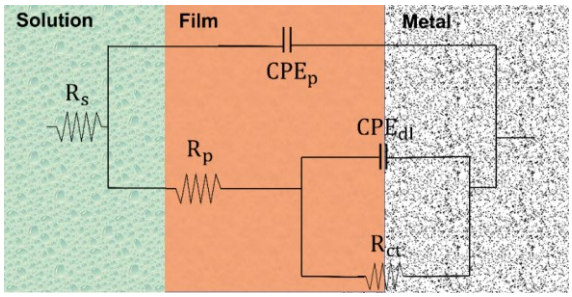

Figure 4.1.10 The equivalent circuit selected for modeling the experimental data obtained from the EIS measurements.

Table 4.1.4 The resultant fitted electrochemical parameters for EIS spectra modeling based on the selected equivalent electrical circuits.

Immersion Time	Sample	R_s ($\Omega^{-1}cm^{-2}s^n$)	CPE_n ($\Omega^{-1}cm^{-2}s^n$)	n_1	R_p (Ωcm^2)	CPE_{dl} ($\Omega^{-1}cm^{-2}s^n$)	n_2	R_{ct} (Ωcm^2)	$\sum \chi^2$
1 h	AP	2.94	7.88×10^{-8}	0.98	4.10×10^{6}	3.51×10^{-5}	0.89	1.45×10^{6}	3.98×10^{-4}
	A400	3.01	9.32×10^{-9}	0.88	8.31×10^{7}	$8.27\times10.^{7}$	0.98	9.40×10^{7}	1.64×10^{-5}
	A500	3.56	1.22×10^{-9}	0.96	9.91×10^{7}	3.32×10^{-7}	0.94	9.99×10^{7}	1.64×10^{-5}
	A600	3.22	2.31×10^{-8}	0.94	6.22×10^{7}	1.31×10^{-6}	0.92	2.40×10^{7}	7.39×10^{-3}
3 days	AP	2.95	9.54×10^{-4}	0.91	9.95×10^{2}	1.54×10^{-4}	0.73	7.69×10^{1}	1.03×10^{-3}
	A400	3.27	5.55×10^{-6}	0.87	1.31×10^{4}	2.86×10^{-6}	0.79	1.14×10^{5}	6.81×10^{-4}
	A500	2.96	1.02×10^{-7}	0.99	7.55×10^{5}	9.56×10^{-7}	0.74	1.77×10^{6}	1.76×10^{-5}
	A600	3.76	4.23×10^{-5}	0.86	2.03×10^{3}	1.19×10^{-5}	0.83	9.93×10^{2}	2.61×10^{-5}
5 days	AP	3.24	1.43×10^{-2}	0.80	7.85×10^{1}	9.40×10^{-2}	0.91	1.93×10^{1}	8.57×10^{-3}
	A400	2.95	2.14×10^{-3}	0.95	1.32×10^{2}	3.42×10^{-3}	0.74	2.11×10^{2}	5.51×10^{-3}
	A500	3.78	1.29×10^{-4}	0.81	6.88×10^{2}	4.62×10^{-4}	0.95	9.65×10^{2}	1.07×10^{-4}
	A600	3.02	7.82×10^{-3}	0.91	8.99×10^{1}	1.34×10^{-2}	0.78	4.02×10^{1}	7.33×10^{-5}

In order to have a better understanding from the corrosion behavior of the as-printed and heat-treated samples, the parallel plate expression [240,241], was employed to calculate the steady-state passive film thickness (L_{ss}) as follow:

$$L_{ss} = \frac{\varepsilon\varepsilon_0 A}{C_f} \tag{4.1.2}$$

where ε is the constant of dielectric for the passive layer (considered to be 15.6 for Cr_2O_3 [225,242], ε_0 is taken as 8.854×10^{-14} Fcm^{-1} which is the vacuum permittivity, A is the surface area of the sample being exposed corrosion, and C_f is the capacitance for the pure passive film, which can be calculated as follows [243]:

$$C_f = \frac{(Y_0 R_{ct})^{\frac{1}{n}}}{R_{ct}} \quad (4.1.3)$$

where Y_0 is the CPE constant (CPE_p in Table 4.1.4), R_{ct} is the charge transfer resistance at the interface between the matrix and passive film, and n is the exponent related to pure passive film capacitance (refer to n_1 in Table 4.1.4) [244–246]. The calculated L_{ss} values, summarized in Table 4.1.5, shows that the passive layer is in its thickest condition after 1 h of immersion for all samples while increasing the immersion time results in the reduction of passive layer thickness due to gradual dissolution, which is in good agreement with the previous results of EIS measurements. For example, the L_{ss} value of AP and A500 samples decreased from 9.34 and 39.12 nm for 1 h immersion to 1.46 and 11.25 nm for 5 days of immersion. More importantly, it is obvious that A500 sample had the highest values of passive layer thickness as compared to other samples at all immersion times, while AP sample has the thinnest passive film, which is consistent with the results of the other corrosion tests herein. As a numerical example, after 3 days of immersion, the passive layer thickness of the A500 sample was 21.25 nm as compared to the AP sample with only 5.46 nm of passive layer thickness.

Table 4.1.5 The values of the capacitance (C_f) and passive layer thickness (L_{ss}) calculated for AP, A400, A500, and A600 samples at immersion times of 1 h, 3 days, and 5 days.

Immersion Time	Sample	C_f (Fcm^{-2})	L_{ss} (nm)
1 h	AP	6.53×10^{-5}	9.34
	A400	7.64×10^{-6}	25.52
	A500	7.21×10^{-6}	39.12
	A600	9.46×10^{-6}	18.48
3 days	AP	1.12×10^{-4}	5.46
	A400	1.54×10^{-5}	12.33
	A500	1.24×10^{-5}	21.25
	A600	1.96×10^{-5}	10.21
5 days	AP	4.63×10^{-4}	1.46
	A400	5.34×10^{-5}	3.54
	A500	2.35×10^{-5}	11.25
	A600	9.69×10^{-5}	2.45

4.1.4.2.4 Mott-Schottcky test

It is well-known that the corrosion resistance of stainless steels mostly depends on the features of the protective film formed on their surfaces when being exposed to a corrosive environment [239]. These protective passive layers commonly contain point defects, which make them comparable with extrinsic semiconductors [247]. Herein, Mott–Schottky testing was employed to characterize the semiconducting behavior of the passive film formed on the surface of the as-printed and heat-treated samples dipped in 3.5 wt. % NaCl electrolyte at room temperature (see Fig. 4.1.11). According to Mott-Schottcky theory, the charge distribution at the interface of the semiconductor and electrolyte for n-type and p-type semiconductors can be measured using the following equations [239,248,249]:

$$\frac{1}{C^2} = \frac{2}{\varepsilon\varepsilon_0 e N_D}\left(E - E_{FB} - \frac{KT}{e}\right) \quad \text{for n-type semiconductors} \quad (4.1.4)$$

$$\frac{1}{C^2} = \frac{2}{\varepsilon\varepsilon_0 e N_A}\left(E - E_{FB} - \frac{KT}{e}\right) \quad \text{for p-type semiconductors} \quad (4.1.5)$$

where C is the capacitance of the working electrode, E represents the applied potential ($V_{Ag/AgCl}$), N_D is the donor density for n-type semiconductors (cm^3), N_A is the acceptor density for p-type semiconductors (cm^3), e is electron charge (1.6×10^{-19}C), ε represents the relative dielectric constant for the passive (oxide) film (ε =15.6 for stainless steel [250]), ε_0 is the vacuum permittivity (8.854×10^{-14} F cm^{-1}), k is Boltzmann's constant (8.16×10^{-5} eV/K), T is the absolute temperature, and E_{FB} relates to the flat band potential. It is notable that kT/e can be very insignificant, the value of E_{FB} can be calculated by extrapolation of the linear portion to $C^{-2} = 0$ [250], and the values of N_D and N_A can be determined using the slope of the linear section of the curves obtained from the MS tests [239,248]. The nature of the semiconductor (n or p type) can be determined according to the slope of the Mott-Schottky curve. A positive slope represents an n-type semiconductor, and a negative slope suggests a p-type semiconductor. The n-type semiconductors are primarily characterized by the presence of interstitials defects and

vacancies caused by oxygen, while the cation vacancies are the major defects in the case of p-type semiconductors [224,251].

Based on the theory of electron bands in solids, the relative number of electrons in conduction band and number of holes in valence band determine the type (n or p) of the semiconductors. In the case of the n-type semiconductors, such as MoO_3, TiO_2, and Fe_2O_3, the number of electrons in conduction band is higher than that of the holes in valence band. In contrast, a semiconductor can be identified as a p-type if the number of electrons in conduction band is lower than that of the holes in valence band, which is the case for some oxides, such as Cu_2O and Cr_2O_3 [239,252]. As the point defect model (PDM) suggests, the protective passive layer is characterized by a bilayer structure including a highly defective (metal vacancies as acceptor states) inner layer growing toward the substrate and an outer film with a hydroxide or oxide nature, which is formed as a result of hydrolysis of cations transported through the inner film [239]. It is commonly assumed that outer region of the passive layer on the Fe-Cr alloys predominantly comprised of Fe_2O_3, while the inner region essentially composed of Cr_2O_3 [253].

According to Fig. 4.1.11, the Mott-Schottky curves of all samples include both positive and negative slopes, which shows transitions from p-type to n-type nature over a range of different applied potentials separated by a plateau region, which is the flat bond potential (E_{FB}). Therefore, the passive film of all samples can be characterized by a p-n heterojunction. At lower potential ranges, the negative slope of the curve proves the presence of a p-type semiconductor that is assumed to be Cr_2O_3 [254]. However, the slope turns to positive at intermediate potential ranges, attributed to the existence of an n-type semiconductor, which is the characteristics of Fe_2O_3. It is notable that another transition to a p-type semiconductor occurred at higher potential ranges where no meaningful correlation between the semiconductor characteristics and donor/acceptor density can be assumed mainly because of unpredictability of the passive film at such high potential ranges [224,239].

The transition from p-type to n-type characteristic happened at the lowest flat band potential (E_{FB}= -602 $mV_{Ag/AgCl}$) for A500 sample followed by transition potentials of (E_{FB}) -531, -496, and -477 $mV_{Ag/AgCl}$ for A400, A600, and AP samples, respectively. This trend in flat band potentials validates the higher stability of the passive layer in A500 sample, and the lowest protectiveness of the passive film in the AP sample.

As reported in Table. 4.1.6, the acceptor density (N_A), donor density (N_D), and E_{FB} were calculated for all samples using equations 4.1.4 and 4.1.5, and the slop of the Mott-Schottky plots. As can be seen in Table 4.1.6, the passive layer of AP sample contains the highest density of defects (N_D= $94.35\times10^{17}cm^{-3}$, and N_A= $181.72\times10^{17}cm^{-3}$) as compared to other samples, while the passive film of A500 sample was characterized by the lowest density of defects (N_D=$6.87\times10^{17}cm^{-3}$, and N_A=$14.42\times10^{17}cm^{-3}$). It is notable that greater defect density increases the electrochemical reactivity between the chloride solution and the metal, resulting in the reduced stability of the passive film [239,248,251]. Moreover, donor density is an indicator of the adsorption affinity level of the chloride ions in the passive layer, which leads to nucleation and growth of pits in the protective film [255–257]. Accordingly, AP sample showed the highest affinity of Cl^- ions, while A500 sample represented the lowest tendency to the deteriorative reaction between oxygen vacancies/interstitial defects and chloride ions, which is in a good agreement with other electrochemical testing in this study.

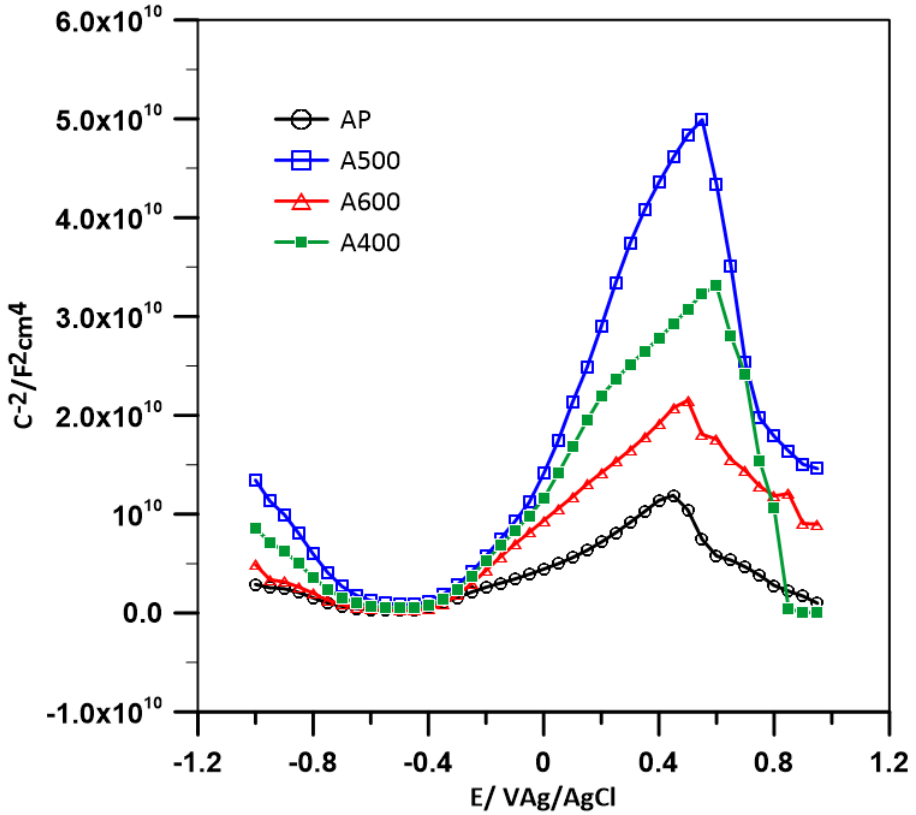

Figure 4.1.11 The Mott-Schottky graphs obtained from the passive layer formed on the surface of AP, A400, A500, and A600 samples in the aerated 3.5 wt.% NaCl solution.

Table 4.1.6 The values of acceptor density (NA), donor density (ND), and flat band potential (EFB) for AP, A400, A500, and A600 samples.

Sample	N_D (10^{17} cm^{-3})	NA (10^{17} cm^{-3})	E_{FB} ($mV_{Ag/AgCl}$)
AP	94.35	181.72	-477
A400	12.06	25.96	-531
A500	6.87	14.42	-602
A600	36.21	75.02	-496

4.1.4.3 Correlation between microstructure and corrosion response

It is generally challenging and intricated to correlate all the microstructural characteristics of an alloy to its corrosion response. Especially, it is true in the case of PH martensitic stainless whose phases are all in nano scale, which makes it difficult to conduct TEM

analysis after corrosion to investigate the corrosion onset point and comprehend the corrosion mechanism. The followings are the author's best attempt to correlate the microstructural features to the electrochemical response of the as-printed material and each heat treatment condition.

4.1.4.3.1 Effect of carbides and residual delta ferrites

Among all microstructural features, the effect of carbides on the corrosion behavior of stainless steels is the most well-established one. It has been frequently reported that the presence of Cr-enriched carbide in the microstructure of stainless steels render its adjacent area to be depleted in Cr to the values less than 13% which is not adequate to provide a stable passive protective layer on the surface [239]. From an electrochemical perspective, chromium carbides are characterized to be electrochemically nobler than the surrounding martensitic matrix, which could potentially results in a localized corrosion attack at the interface of carbide and matrix [258]. This potential transition from the carbide particles to the matrix triggers the formation of a micro-galvanic cell where carbide-matrix interface plays the anode's role and carbide particles behave as the local cathode [258]. This phenomenon is called sensitization, which results in instability of the passive layer and potentially a dramatic drop in the pitting potential of the material. The pits are usually concentrated locally around the Cr-enriched areas where is depleted in chromium. Based on the results of PDP tests (see Fig. 4.1.8), the lowest pitting potential is related to the as-printed sample (o.669 ± 0.025 $V_{Ag/AgCl}$) followed by 0.757 ± 0.024 $V_{Ag/AgCl}$, 1.118 ± 0.022 $V_{Ag/AgCl}$, 1.306 ± 0.010 $V_{Ag/AgCl}$ for A600, A400, and A500 samples, respectively. Obviously, the lower electrochemical response of A600 sample as compared to A400 and A500 samples can be attributed to the presence of carbides in A600 sample, which is the only sample containing $Cr_{23}C_6$. However, comparing the AP and A600 samples shows that the presence of $Cr_{23}C_6$ is not the only controlling factor in the corrosion performance of the alloy since the microstructure of AP sample is free of any carbides. Instead, AP sample contains of a high-volume fraction of residual delta ferrite, which most possibly is responsible for its poor corrosion performance. It is worth mentioning that residual delta ferrite was enriched in Cr as a ferrite stabilizing alloying element (see Fig. 4.1.1), which could act similar to chromium carbides and trigger the

sensitization phenomenon by leaving its adjacent area depleted in Cr resulting in localized corrosion attack [224][225]. Assuming the similar role of Cr-rich delta ferrites and chromium carbides, the lower pitting potential of AP sample as compared to A600 sample can be attributed to the size and volume fraction of these deteriorative constituents, which is much higher in the AP sample (compare Fig. 4.1.1 and Fig. 4.1.6 for details).

Fig. 4.1.12 depicts 3D-depth maps taken from the corroded surfaces after PDP test, which are representatives of the depth, size, distribution, and morphology of the pits formed on different samples. As can be seen with different magnifications in Fig. 4.1.12a_1 and a_2, the pits formed on the corroded surface of the as-printed sample are more uniaxial and groove-like with a maximum depth of 35.613 μm. These grooves were formed and stretched out along the lathy/vermicular delta ferrite phases being bulged as they were protected due to being enriched in chromium. It is well-known that chromium is considered as the most effective alloying element to development a perfect protective passive layer.

The morphology of the pits formed on all heat-treated samples are more spherical rather than elongated, which can be attributed to the absence of delta ferrite in the heat-treated samples (see Fig. 4.1.12b-d). A comparison between the corroded surfaces of the heat-treated samples reveals a much more sever corrosion attack in A600 sample being characterized by a higher density of pits with a deeper penetration, which can be correlated to the presence of Cr-enriched carbides formed during aging at 600 °C. To be more precise, the maximum pit depth in the A600 sample was 21.577 μm as compared to around 10 μm in the case of A400 and A500 samples.

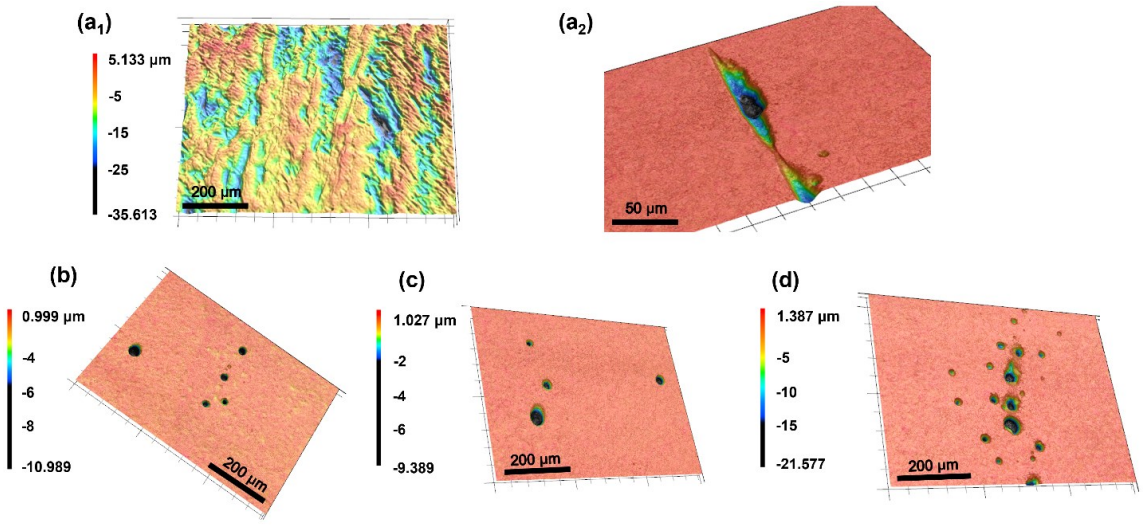

Figure 4.1.12 3D-depth profiles taken from the corroded surfaces after PDP test for (a1 and a2) AP, (b) A400, (c), A500 and (d) A600 samples.

It is notable that the results of other electrochemical analysis were consistent with the above discussion. To be more precise, the results of Mott-Schottcky tests (see Fig. 4.1.11 and Table 4.1.6) revealed that the lowest flat band potentials were related to AP and A600 samples revealing that their passive layers had the least protectiveness and the poorest electrochemical stability attributed to the sensitization phenomenon occurred as a consequence of delta ferrite (in AP) and chromium carbides (in A600). Additionally, the values of the acceptor density (N_A) and donor density (N_D) also confirm that A600 sample containing $Cr_{23}C_6$ had the most defective protective layer among the heat-treated samples, while the passive layer of AP sample with residual delta ferrite in its microstructure is the most defective layer among all samples (see Table 4.1.6 for the details).

Interestingly, the results of EIS tests were also in a good agreement with other electrochemical analysis. Based on the Nyquist plots, the smallest semi circles in all immersion times were corresponded to the AP sample followed by A600, A400, and A500 samples. Not only that, but also AP and A600 samples were characterized by the lowest values of $|Z|_{max}$ (at the lowest frequency) confirming their more unstable protective layer as compared to A400 and A500 samples. Comparing R_{ct} and R_p values

for each sample reveals that $R_{ct}/R_p>1$in the case of A400 and A500 samples indicating the formation of stable passive layer on these samples, while $R_{ct}/R_p<1$ in the case of AP and A600 samples confirming the occurrence of localized attack as a result of Cr-rich delta ferrite and carbides, respectively. Overall, based on the values obtained from the simulations, it can be deduced that the lowest effective capacitance (C_f) is related to the passive film formed on the A500 sample followed by A400, A600, and finally AP, which confirms a better corrosion performance and thicker passive film formed on the surface of A500 and A400 samples as compared to A600 and AP samples [259].

To sum up, the inferior corrosion performance of AP and A600 samples as compared to A400, and A500 samples can be correlated to the sensitization phenomenon occurred as a result of the presence of Cr-rich phases in the microstructure leading to localized corrosion attack and instability of the passive layer. However, it is not valid to compare the electrochemical behavior of A400 and A500 samples based on the mentioned justification as none of them contain any of Cr-rich delta ferrite and/or carbides. Therefore, the corrosion performance of A400 and A500 will be correlated to other microstructural features being discussed in the following sections.

4.1.4.3.2 Effect of dislocation density

Dislocation density can also affect the corrosion performance of materials. According to point defect model (PDM), nucleation of oxygen vacancies commonly occurs at the substrate-passive layer interface, which could potentially be the onset of pit formation, passive film breakdown, and finally localized corrosion attacks [260]. The presence of tangled dislocations can also contribute to the formation of oxygen vacancies and consequently adversely impact the stability of passive film, which can be quantified based on the following equation [261]:

$$M + T \rightarrow M + \frac{x}{2}V_o^{\cdot\cdot} + xe^{'} \tag{4.1.6}$$

where M represents the substrate (as-printed and heat-treated PH 13-8Mo MSS herein), T refers to the dislocations being produced at the interface of passive film-substrate, and $V_{O}^{\cdot\cdot}$ denotes to the oxygen vacancy, and $e^{'}$ represents the transferred electron. Accordingly, each mole of martensite-induced dislocation results in the nucleation of x/2 mole of oxygen vacancies at the passive oxide film at the surface of the substrate [262,263]. This can be correlated to the corrosion response of samples investigated in this study since the aging process directly affect the dislocation density and subsequently the stability of the passive film.

The dislocation density of the as-printed and heat-treated samples were calculated based on the XRD data shown in Fig. 4.1.13 using Williamson-Smallman equation [264]:

$$\delta = \frac{1}{D^2} \tag{4.1.7}$$

where, δ is the dislocation density and D is the crystallite size, which can be calculated using Scherrer's relation [265] as follows:

$$D = \frac{K\lambda}{\beta cos\ \theta} \tag{4.1.8}$$

where K is a dimensionless shape factor, with a value close to unity, λ is the X-ray wavelength, which is equal to 1.54056 Å for Cu-Kα radiation, β is full-width at half maximum (FWHM), and θ is the Bragg's angle.

The value of crystallite size (D) was calculated for all the detected BCC peaks, *i.e.* (110) at 44°, (200) at 64°, (211) at 82°, (220) at 98°, and the average value was used to calculate the dislocation density. Following the above calculation steps, the dislocation densities were found to be 9.87×10^{16}, 1.32×10^{15}, 3.12×10^{14}, and 2.89×10^{14} m^{-2} for the AP, A400, A500 and A600 samples, respectively. A noticeable change was observed in the dislocation density of the as-printed and heat-treated samples. The reduced dislocation density during the aging process can be ascribed to the rearrangement of dislocation, formation of sub-grain boundaries accompanying the reduction of the strain

energy during recovery process [266]. It is notable that dislocation densities of the heat-treated samples are close to each other especially for A500 and A600 samples, which means that the recovery process was almost completed at 500 °C. The results of dislocation density analysis by XRD were also supported by TEM analysis. As can be seen in Fig. 4.1.14a, the martensite laths in AP sample contains dense and tangled dislocations as compared to A500 samples with much lower dislocation density (see Fig. 4.1.14b), showing the formation of sub-grains by rearrangement of dislocations as a result of recovery. The results of the corrosion tests also support the above discussion regarding the effect of dislocation density on the corrosion behavior. To be more precise, the as-printed sample with much higher dislocation density showed a high degree of instability in its passive layer as compared to the heat-treated samples being recovered during the aging treatment. Comparing the heat-treated samples also proves that A500 sample with lower dislocation density (3.12×10^{14} m^{-2}) had a better electrochemical response than A400 sample with 1.32×10^{15} m^{-2} dislocation density. However, comparing A500 and A600 samples with almost equal dislocation densities (3.12×10^{14} and 2.89×10^{14} m^{-2}, respectively) reveals that another controlling factor (*i e.* presence of carbides in A600 sample) dictated the corrosion resistance of the samples.

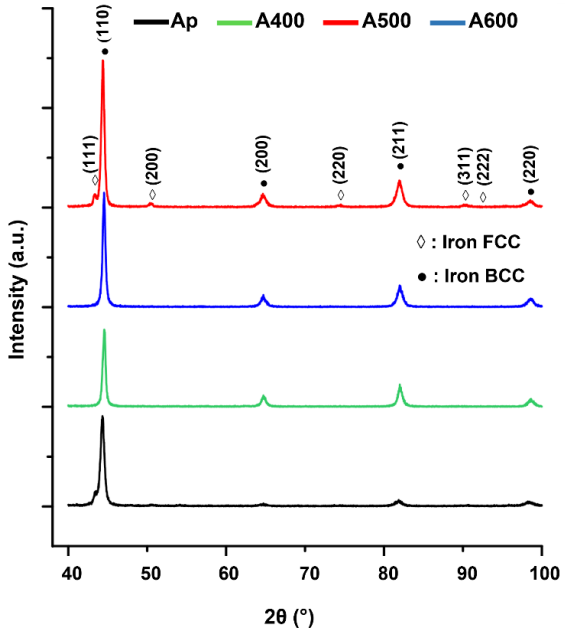

Figure 4.1.13 X-ray diffraction patterns of AP, A400, A500, and A600 samples.

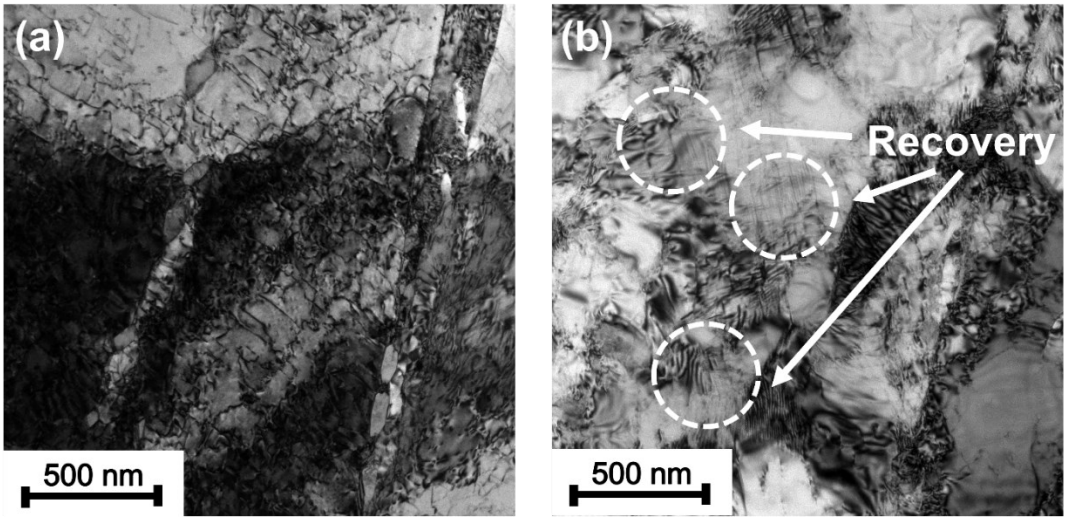

Figure 4.1.14 TEM bright field images showing (a) high density of tangled dislocations in AP sample, and (b) recovery and annihilation of dislocations in A500 sample.

4.1.4.3.3 Effect of martensite lath size and lath boundary orientation

The martensite lath size and lath boundary orientation are two paired factors affecting the formation of passive layer on the surface of martensitic stainless steels [267][224][268][269]. Lath boundaries with a higher diffusion coefficient are more favorable paths than inside the laths for diffusion of atoms [268]. It is well-established that the surface passive layer of stainless steels are developed by diffusion of chromium and formation of a dense chromium oxide layer on the surface of the material [268][269]. Obviously, a finer lath structure provides a higher density of lath boundaries with a high diffusion rate offering easy paths for chromium to reach to the surface and form the passive oxide layer [268]. In addition, it has been reported that the dissolution of iron will be increased by microstructural refinement [269], which causes a higher Cr/Fe content on the surface of the material resulting in the growth of a Cr-enriched oxide layer being denser and thicker than Fe-enriched oxide layer [269].

Another complementary factor to martensite lath size is the relative fraction of LAGBs and HAGBs since the stored energy in the grain boundaries (γ_{gb}) is highly dependent to the grain boundary misorientation angle (θ) according to the Read-Shockley equation [224,270]:

$$\gamma_{gb} = \frac{Ga\ \theta}{4\pi(1-\sigma)}(A - ln\theta) \quad (4.1.9)$$

where (γ_{gb}) is the grain boundary energy, G is the shear modulus, (θ) is the misorientation angle, σ is the Poisson ratio, A is a constant value nearly close to 0.23, and a is the Burgers vector. Accordingly, higher values of grain boundary misorientation angle (θ) results in increased grain boundary energy (γ_{gb}).

Although lath boundaries are considered as the fastest paths for diffusion of Cr to the surface for the formation of the passive layer, low angle boundaries having low interface energy could decelerate the diffusion process [248]. Thus, it can be inferred that a higher fraction of LAGBs can decrease the diffusivity of lath boundaries as low as bulk diffusivity resulting in a thinner and less dense passive layer.

The grain boundary misorientation maps, and lath size distributions of the as-printed sample along with samples aged at the lowest and highest temperatures (400 and 600 °C) are shown in Fig. 4.1.15. It has been reported that the grain boundary misorientation angle for martensite packets and blocks can be roughly estimated in the range of 48-62.8°, for primary austenite grain boundaries (PAGs) between 15-48°, and for martensitic laths below 5° [193,271]. It is also notable that the grain boundary misorientation angles between 5-15° can be possibly ascribed to any of the former boundary types [271]. Based on the previous studies [193,271], and also extensive processing the obtained EBSD data, the best fits for the grain boundaries misorientation angles in current study were found in three ranges, including low angle grain boundaries (LAGB) between 2-5° for martensite laths, medium angle grain boundaries (MAGB) between 15-50° for PAGs, and high angle grain boundaries (HAGB) between 50-62.8° for packets and blocks. According to the lath size distribution of the as-printed and heat-treated samples (Fig. 4.1.15 d-f), aging process led to an increase in the average martensite lath size from 1.75 μm for the AP sample to 2.95 μm, and 3.35 μm for the A400 and A600 samples, respectively. The increased martensite lath size can be attributed to the presence of larger PAGs in the heat-treated

samples [193], and also recrystallization, growth, and lath boundary migration during the aging process [272]. Interestingly, the higher fraction of MAGBs (in blue color) in the as-printed sample (24.5 %) as compared to 8.5 %, and 7 % for the A400, and A600 samples, respectively, also confirms the formation of coarser PAGs in the heat-treated samples (compare Fig. 4.1.15a, b, and c). It is notable that the coarser PAGs in the heat-treated samples can be attributed to their higher soaking time (1 h) at the single-phase austenite region (1050 °C) as compared to the PAGs of AP sample being formed as a results of direct rapid cooling following the solidification process. The results of lath size analysis were not always aligned with corrosion response of all different conditions. For example, although the as-printed sample has a lower martensite lath average size than the heat-treated samples, all different electrochemical measurements (PDP, Mott-Schottky, and EIS) approved that the heat-treated samples showed a better electrochemical response than the as-printed sample. This is not consistent with the above discussion on the effect of martensite lath size on the corrosion properties of martensitic stainless steels. This inconsistency can be justified by the presence of Cr-rich delta ferrite phases as a major role player in the AP sample.

However, comparing the corrosion tests results of the heat-treated samples reveals that A600 sample with the coarsest martensite lath size (3.35 μm) showed the lowest stability of the passive layer, which is in a good agreement with above justification about the effect of martensite lath size. Considering this contradiction, one may conclude that the influence of martensite lath size on the corrosion resistance of stainless steels is of less importance that other dictating factors such as delta ferrite.

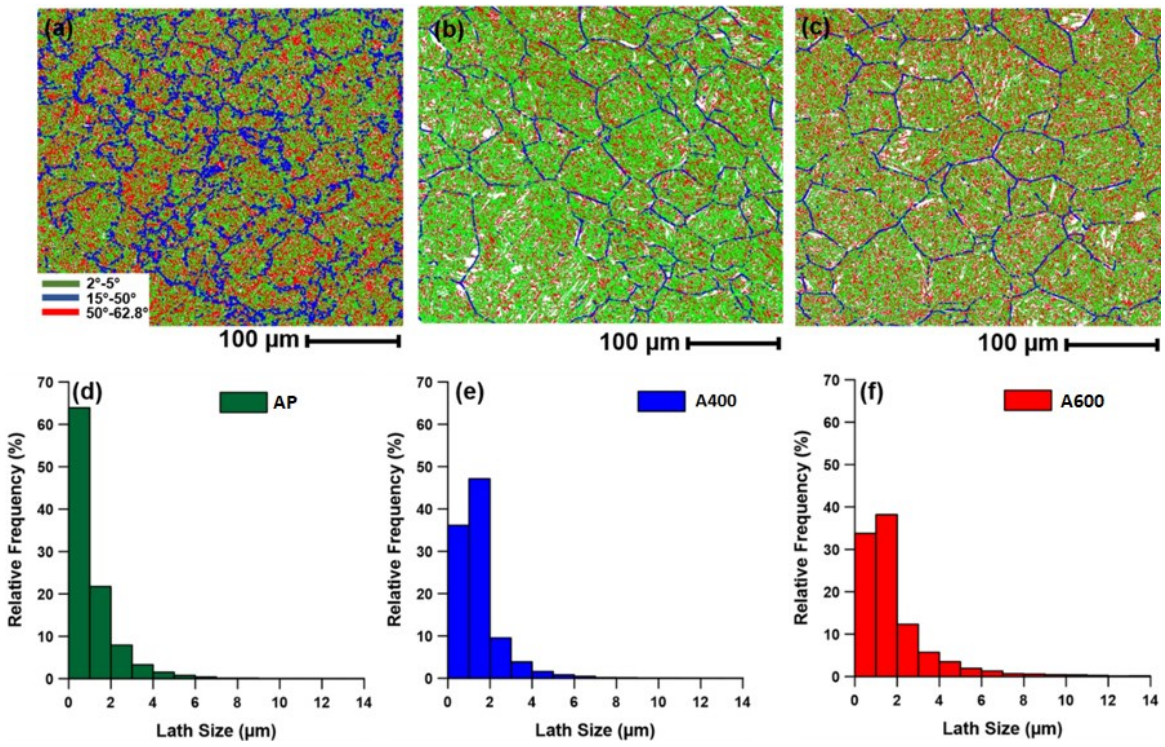

Figure 4.1.15 (a-c) Grain boundary misorientation maps, and (d-f) lath size distributions of the AP, A400, and A600 samples, respectively.

Analysis of the grain boundary maps (Fig. 4.1.15a-c) revealed that the fraction of HAGBs (in red color) for the as-printed sample (49.3%) was higher than that of A400, and A600 samples with 33.3% and 27.1% respectively. In addition, the fraction of the LAGBs (in green color) in the as-printed sample is approximately 26.2%, while it increases to 58.2% and 65.9% for A400, and A600 samples due to the formation of sub-grain boundaries during the aging process [266]. Interestingly, this is in agreement with the calculated dislocation density based on XRD results and TEM analysis (see Fig. 4.1.13 and 14), which showed the decreased dislocation density in the aged sample ascribed to the formation of sub-grain boundaries by rearrangement and alignment of dislocations. Similar to the lath size distribution, the results of lath boundary misorientation analysis were not always consistent with the results of electrochemical measurements. For instance, the heat-treated samples with higher fractions of LAGBs were supposed to show an impaired electrochemical response as compared to the as-printed samples, but it was not satisfied by the results of corrosion measurements. However, among the heat-treated samples, A400 with a lower fraction of LAGBs had a better corrosion resistance than

A600 with higher fraction of LAGBs, which is aligned with the mentioned discussion on the effect of lath boundary misorientation angle on the corrosion properties of stainless steels.

The authors' understanding from this controversially results is that the corrosion behavior of different conditions can be separately analyzed based on the lath size and misorientation angle only if all other microstructural features are the same in the studied samples. However, herein, the analyzed samples contain different phases such as carbides, delta ferrites, and austenite, which may play a more crucial role than lath size and misorientation angle in the corrosion performance of the alloy. For example, the effect of a high-volume fraction of Cr-enriched delta ferrite in the as-printed sample was much more dominant than that of its finer martensite lath size or lower fraction of LAGBs as compared to the heat-treated samples.

4.1.4.3.4 Effect of retained/reverted austenite

It is very difficult to separately criticize the exact effect of austenite on the corrosion performance in the current study as there is no two samples whose only microstructural difference were the presence/absence of austenite. As comprehensively explained in the microstructural characterizations section, the microstructure of AP and A600 samples contained retained and reverted austenite, while A400 and A500 samples were free of any FCC phase in their microstructure. It is generally believed that the formation of austenite is beneficiary to the pitting corrosion resistance of stainless steels due to the higher solubility of Ni, Mo, and especially Cr in FCC-Fe as compared to the martensitic matrix with a BCC structure [273]. In addition, it is believed that the presence of austenite at the periphery of Cr-enriched phases compensate the Cr-depletion in their adjacent area and consequently enhance the electrochemical stability of the material [273]. On the other hand, martensite to austenite transformation during the aging process stimulates excessive elastic energy in material as a result of shape and volume transitions from BCC to FCC crystal structures [274]. Accordingly, the phase boundary of martensite and austenite will be surrounded by a higher density of dislocation and point defects, which are potential favorable sites for electrochemical reactions [267]. High density of tangled

dislocations was observed adjacent to martensite-austenite phase boundaries in A600 sample in this study, which is shown in Fig. 4.1.16. Furthermore, the compositional variations from austenite to martensite could potentially results in self-potential differences leading to micro-galvanic coupling [267]. Additionally, referring to point-defect model (PDM), the presence of secondary phases in the microstructure could cause a micro-chemical discontinuity, which increases the vacancy and ion fluxes at the interface of substrate and passive film [234]. These vacancies facilitate the formation of micro-voids, which dramatically accelerate the breakdown of the passive layer [273]. The results of electrochemical analysis including PDP, Mott-Schottky, and EIS measurements are all in favor of the formation of a less protective and more defective passive layer on AP and A600 samples containing retained/reverted austenite as compared to A400 and A500 samples being free of austenite phase in their microstructure. It is worth mentioning that the insignificant amount of retained/reverted austenite cannot be considered as a major factor determining the corrosion behavior, but just one of the complementary factors contributing to the electrochemical response of the materials.

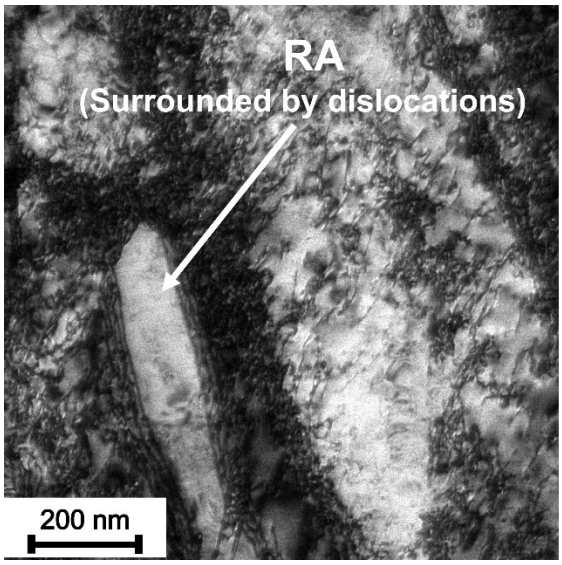

Figure 4.1.16 TEM image taken from A600 sample showing reverted austenite being surrounded by high density of tangled dislocation.

4.1.4.3.5 Schematic illustration of the correlation between microstructure and corrosion response

To sum up, microstructural features associated with the as-printed part and each heat treatment condition in addition to their contributions to the electrochemical interactions between the surface and the electrolyte are schematically illustrated in Fig 4.1.17.

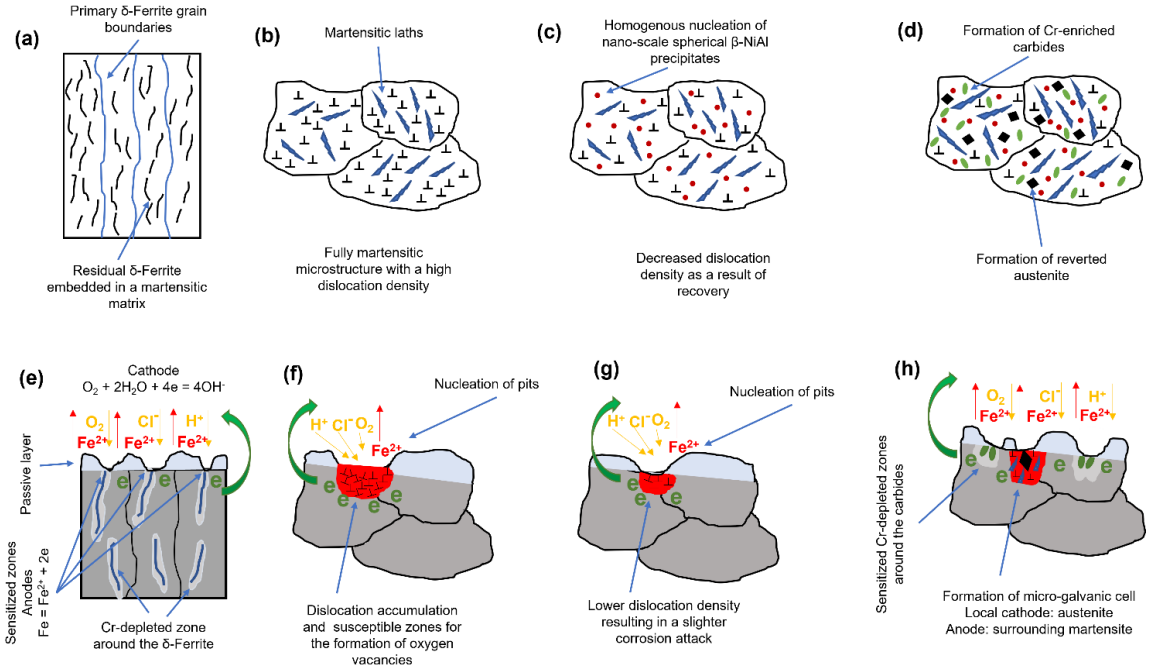

Figure 4.1.17 Schematic illustration indicating the microstructural features along with their contributions to the electrochemical interactions between the surface and the electrolyte for (a and e) AP, (b and f) A400, (c and g) A500, and (d and h) A600 samples.

4.1.5. CONCLUSIONS

In the current study, the effect of post-printing solution and aging treatments on the microstructure and corrosion properties of a wire arc additive manufactured PH 13-8Mo martensitic stainless steel were investigated and the following observations and conclusions were obtained:

The rapid cooling rate of the fabrication process and the high Cr content of the feedstock material (13%) resulted in the formation of undesired residual delta ferrite in microstructure of the as-printed part, which deteriorated the corrosion performance of the material due to the formation of Cr-depleted regions at the vicinity of the Cr-enriched delta ferrite phases. The solution treatment at low temperature (950 °C) was not sufficient to remove delta ferrite phases from the microstructure, while heating up to 1200 °C resulted in the re-formation delta ferrite phase at the primary austenite grain boundaries. On the other hand, solution treatment at intermediate temperature (1050 °C) led to the formation of a fully martensitic microstructure being the most desired condition for the further aging process. Aging process at 400 °C did not significantly alter the microstructure of the solution treated material except for martensite lath boundary migration and a decreased dislocation density as a result of recovery process. However, a considerable improvement in the electrochemical stability was observed as compared to the as-printed material, which could be attributed to the removal of the undesired delta ferrite phase during the post-printing heat treatment. Microstructural characterizations revealed the formation of nano-size coherent β-NiAl precipitates in the sample aged at 500 °C with a relatively better corrosion resistance as compared with the sample aged at 400 °C, which could mainly be attributed to the lower residual stress due to lower dislocation density as a result of higher degree of recovery occurred at 500 °C. Aging process at the highest temperature of 600 °C resulted in the formation of reverted austenite and also nucleation and growth of new secondary phase *i.e.* $M_{23}C_6$ carbides, which adversely affected the corrosion performance of the material due to the sensitization phenomena around the Cr-enriched carbides.

Overall it can be concluded that it is not advisable to employ the wire arc additively manufactured PH 13-8Mo martensitic stainless steels due to the presence of undesired delta ferrite in its microstructure, which could significantly deteriorate the electrochemical stability of the passive film in the service condition. Therefore, it is essential to implement post-printing heat treatment including solution treatment followed by aging process. For the best corrosion performance, it is highly recommended to consider the complete removal of undesired delta ferrite phases during the solution

treatment and also avoid aging at higher temperature, which could results in the formation of Cr-enriched carbides being detrimental to pitting resistance of stainless steels.

Acknowledgments

The authors gratefully acknowledge the support of Natural Sciences and Engineering Research Council of Canada (NSERC) [grant number RGPIN-2017-04368], Canada Research Chair program, Ocean Frontier Institute, and Dalhousie University for sponsoring this work.

4.2 On The Nucleation Site and Formation Sequence of Secondary Phases during Isothermal High-Temperature Aging of Wire Arc Additively Manufactured PH13-8Mo Stainless Steel

Alireza Vahedi Nemani[1], Mahya Ghaffari[1], Ali Nasiri[2]

1- Graduate Student, Dalhousie University, Halifax, Nova Scotia, Canada

2- Assistant Professor, Dalhousie University, Halifax, Nova Scotia, Canada

Status: Submitted to the Journal of Vacuum (IF= 3.627)

Authors' Contribution

Alireza Vahedi Nemani: Conceptualization, Investigation, Writing - original draft, Visualization.

Mahya Ghaffari: Methodology, Fabrication Process, Validation, Investigation, Review & Editing.

Ali Nasiri: Supervision, Writing - review & editing, Funding acquisition.

4.2.1. Abstract

For the first time, the nucleation site and the formation sequence of secondary phases during isothermal high-temperature (600 °C) aging process of a wire arc additively manufactured PH13-8Mo martensitic stainless steel were investigated herein. The microstructural characterizations revealed that the aging process starts with the nucleation of homogenously distributed spherical nano-sized β-NiAl phase within the martensite laths, followed by the formation of ellipsoidal $M_{23}C_6$ carbides, which promoted the formation of reverted austenite within the martensite laths and also along the lath boundaries at intermediate aging times. Lastly, new $M_{23}C_6$ carbides were formed within the reverted austenite at the final stage of the aging process.

4.2.2. Introduction

Precipitation-hardened (PH) 13-8Mo martensitic stainless steel (MSS) holds a broad range of engineering applications from die-cast molds to marine and aerospace industries owing to its great combination of strength, toughness, and corrosion resistance [275][276]. This alloy is essentially employed in the heat-treated (aged) condition as it can be strengthened through the precipitation of nano-sized highly coherent β-NiAl phases, boosting the hardness of the alloy to around 50 HRC [267][277]. Due to its great

strength and hardness, the fabrication of PH13-8Mo alloy through conventional subtractive manufacturing methods is quite challenging, validating the use of additive manufacturing (3D-printing) as a one-step fabrication method to produce a near-net-shape component [276][12]. However, it should be considered that a 3D-printed PH-MSS cannot be used in the as-printed condition since the post-printing heat treatment is crucial to elevate the mechanical properties of the alloy [267]. It is notable that PH13-8Mo alloy is mostly used in the over-aged condition due to the formation of reverted austenite at higher aging temperatures (usually above 600 °C), which significantly improves the toughness and resistance of the alloy to hydrogen embrittlement and stress corrosion cracking [222][223]. Therefore, focusing on the crucial topic of phase (trans)formation during aging, this research for the first time aims to investigate the sequence of microstructural evolution of a wire arc additive manufactured (WAAM) PH13-8Mo stainless steel part during an isothermal high-temperature (600 °C) aging process at different time intervals. It is notable that the effect of different secondary phases formed during the aging process on the mechanical and corrosion properties of the WAAM-PH13-8Mo part is the subject of the authors' future studies.

4.2.3. MATERIALS AND METHODS

A PH13-8Mo martensitic stainless steel thin-wall component was fabricated through wire arc additive manufacturing using an S-350 Power Wave Lincoln Electric GMAW machine with a torch mounted on a multi-axis Fanuc robotic arm. The nominal chemical composition of the feedstock wire and the optimum process parameters are reported in Tables 4.2.1 and 4.2.2, respectively. More details about the manufacturing process can be found in the authors' previous publication [276]. Post-printing heat treatment process was applied in two steps including solution treatment at the single-phase austenite stability region (1050 °C) for 1 h followed by high-temperature aging (600 °C) at different time intervals (20 min, 1 h, 2 h, 4 h). The as-printed and heat-treated samples underwent a comprehensive microstructural investigation implementing scanning and transmission electron microscopy techniques using an FEI MLA 650FEG SEM and a Talos 200X TEM.

Table 4.2.1 The nominal chemical composition of the PH 13-8Mo wire (wt. %).

Cr	Ni	Mo	Al	Mn	Si	C	S	N	Fe
12.25-13.25	7.5-8.5	2-2.5	0.9-1.35	0.1	0.1	0.05	0.01	0.01	Bal.

Table 4.2.2 The optimum process parameters used for wire arc additive manufacturing of PH 13-8Mo stainless steel.

Arc Current	Arc Voltage	Wire Feeding Speed	Scanning Rate	Shielding Gas	Argon Flow Rate
135 A	28 V	67 mm/s	4 mm/s	90% He, 7.5% Ar, and 2.5% O_2	20 L/min

4.2.4. RESULTS AND DISCUSSION

Fig. 4.2.1a-c depicts the SEM and TEM images along with the corresponding selected area electron diffraction (SAED) pattern taken from the as-printed sample. As shown in Fig. 4.2.1a, the microstructure of the as-printed sample dominantly consists of residual δ-ferrite embedded in a fine and low-carbon lath martensitic matrix. According to the TEM analysis results (Figs. 4.2.1b and 1c), retained austenite was also detected to be trapped between the martensite laths. A detailed discussion on the microstructure of the as-printed sample was reported in the author's previous publication [276]. However, applying the solution treatment led to the complete dissolution of residual δ-ferrite (see Fig. 4.2.1d) and entire elimination of retained austenite (see Fig. 4.2.1e and 1f) as a result of maintaining the sample for 1 h in the single-phase austenite region (1050 °C) followed by direct air-cooling to below the martensite finish temperature ($M_f \sim 30$ °C [276][226]) of the alloy.

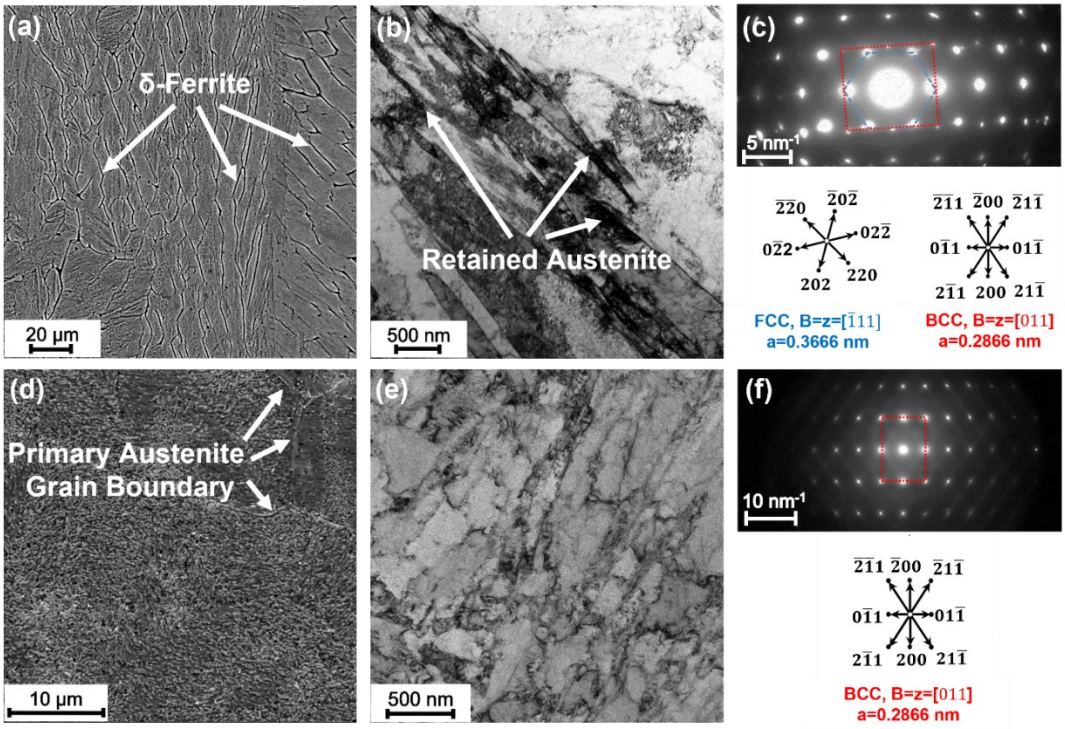

Figure 4.2.1 SEM and TEM images along with the corresponding SAED patterns taken from the (a-c) as-printed and (d-f) solution treated samples.

As a result of aging at 600 °C for 20 min, a noticeable number of round-shaped precipitates were formed with an approximate radius of 5-15 nm (Fig. 4.2.2a). These precipitates were not formed on a pre-exiting preferential site, such as high-energy lath boundaries as they were uniformly distributed within the martensite laths indicating a homogeneous nucleation process [52]. According to the SAED pattern shown in Fig. 4.2.2b, the precipitates were indexed as β-NiAl phase with a B2 (CsCl) crystal structure and a lattice parameter of 0.2887 nm [278][232]. The corresponding EDS elemental maps also confirm that the β-NiAl precipitates were enriched in Ni & Al, and depleted in Cr. It has been reported that the close lattice parameter of β-NiAl to the matrix (BCC-Fe, a=0.2866 nm) results in a highly coherent interface, retaining their coherency even until their size reaches to 150 nm [228][220].

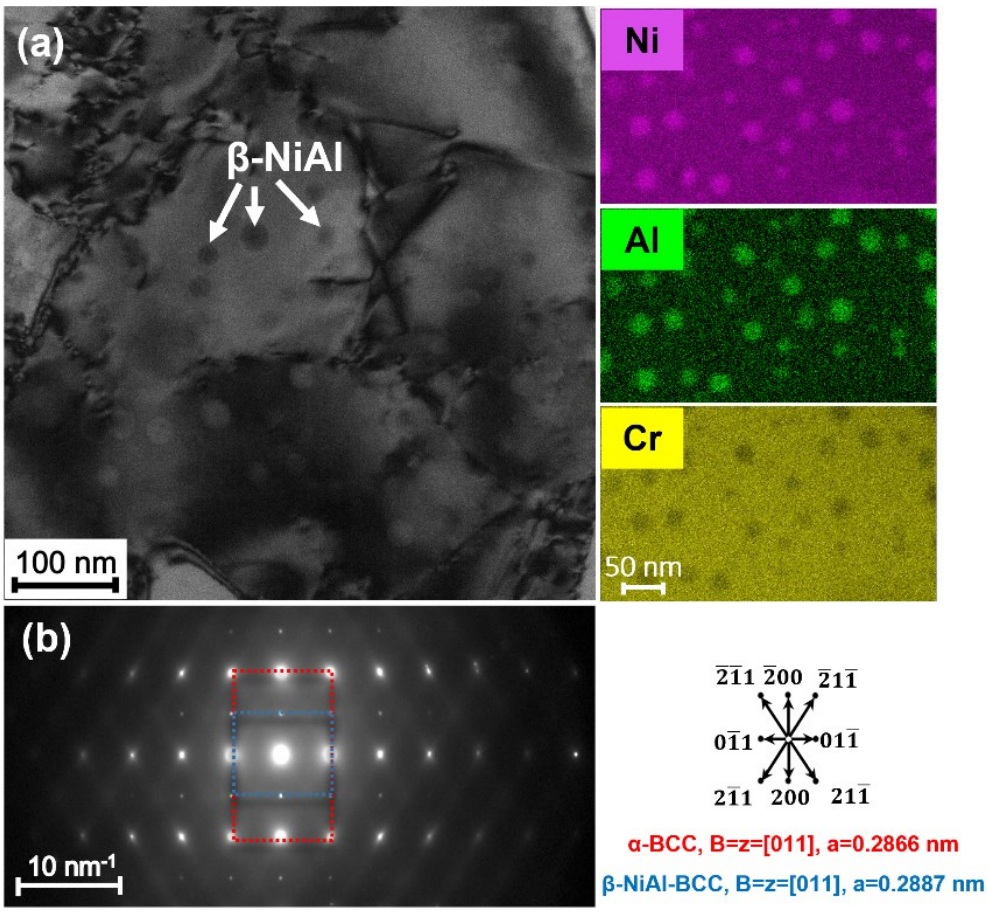

Figure 4.2.2 (a) A high-magnification bright field TEM image taken from the sample aged for 20 min along with its EDS elemental maps and (b) the corresponding SAED pattern.

As depicted in Fig. 4.2.3a, 1 h of aging process resulted in the formation of another secondary phase with an ellipsoidal morphology and a size range of 10-30 nm in the matrix. The derived SAED pattern (Fig. 4.2.3b) identified the detected secondary phases to be $M_{23}C_6$ with a FCC crystal structure and a lattice parameter of 1.0668 nm, which is in agreement with similar observations in the literature [52][217][233]. The EDS elemental maps taken from these secondary phases revealed that the carbides were highly enriched in Cr and depleted in Fe. It is notable that the presence of $M_{23}C_6$ matrix carbides with very restricted solubility for Ni leaves the surrounding area with an enriched Ni content, which subsequently promotes the nucleation of reverted austenite [233]. The

EDS elemental line scan taken from a carbide particle also confirms its Ni depletion, which was balanced by enrichment of Ni in its vicinity.

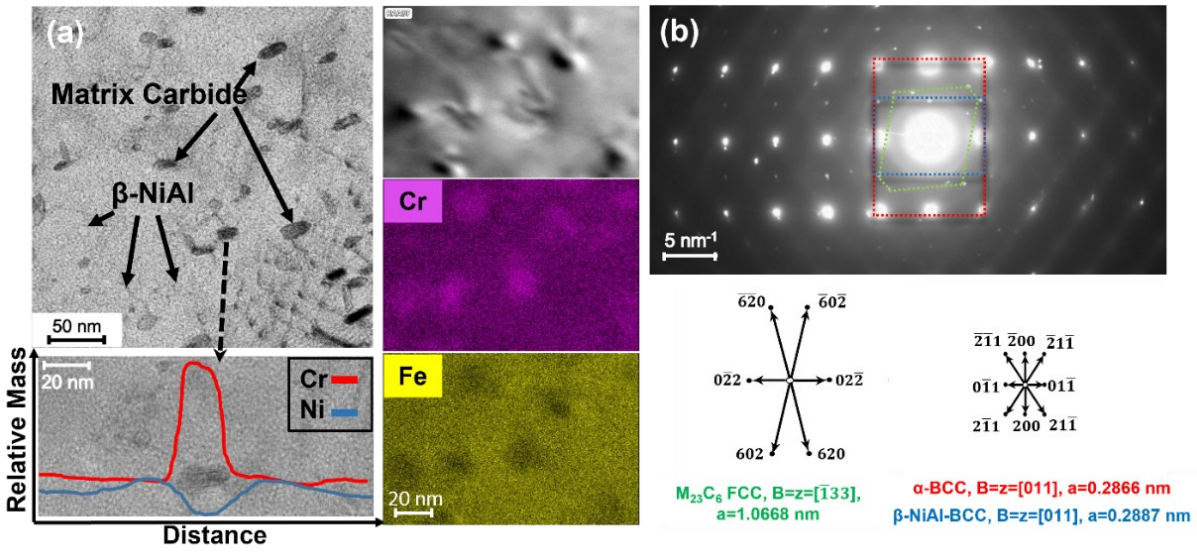

Figure 4.2.3 (a) High-magnification bright field TEM image taken from the sample aged for 1 h along with its EDS maps and line scan analysis results, and (b) the corresponding SAED pattern.

Interestingly, the high-magnification TEM image (Fig. 4.2.4a) taken from the sample aged for a longer time (2 h) showed the formation of the reverted austenite adjacent to the carbides, affirming the aforementioned hypothesis regarding the promoting effect of carbides on the formation of reverted austenite during the aging process. It is worth mentioning that the detected austenite phase cannot be characterized as retained austenite since the FCC phase was not detected in the solution treated and aged samples at shorter aging periods (20 min and 1 h). The low-magnification TEM images along with the SAED pattern (Fig. 4.2.4b-4d) revealed that the reverted austenite phases were appeared in elongated and blocky shapes, consistent with other researcher's observations [216][222][220][228]. According to the classification offered by Shiang and Wayman [279], the observed reverted austenite phases in this sample can be categorized as, *(i) lath-like austenite* formed on the martensite lath boundaries with an elongated morphology (Fig. 4.2.4b) and *(ii) matrix austenite* formed inside the martensite laths with a blocky morphology (Fig. 4.2.4c). It is well-known that the most preferential site for

nucleation of a secondary phase in solid state is lath/grain boundaries since they are energetically favorable sites with a relatively higher diffusion coefficient of solute atoms [233]. Meanwhile, the formation of matrix austenite inside the martensite laths can be attributed to the presence of tangled dislocations inside the martensite structure providing high-energy sites for nucleation of a new phase [280][216]. There is a controversy in the literature regarding the co-existence of β-NiAl and reverted austenite in the microstructure. On one side, the formation of reverted austenite is believed to be a diffusional transformation, controlled by the dissolution of precipitates (β-NiAl in this case) at higher aging temperatures providing austenite promoter elements (Ni in this case) [281][63]. On the other side, Schnitzer *et al*. [216] disregarded this theory as their thermodynamic and kinetic simulations confirmed that the formation of reverted austenite and β-NiAl precipitates is independent from each other and their simultaneous formation is thermodynamically possible. Sinha *et al*. [280] also suggested that micro-segregation of austenite stabilizing elements (Ni in this case) into high energy sites, such as dislocations and lattice defects, causes the formation of reverted austenite. Li *et al*. [282] also confirmed that the formation mechanism of reverted austenite during aging is related to micro-segregation of Ni as their energy-dispersive X-ray microanalysis showed that the Ni-content of reverted austenite was two times higher than the average Ni-content of the alloy. As illustrated in Fig. 4.2.4, the EDS line scan taken from the blocky reverted austenite detected in the current study also confirms the higher local concentration of Ni in the austenite phase. Considering the annihilation of dislocations as the aging process progresses, it can be assumed that the formation of matrix austenite is more plausible at the initial stages of the aging process when there are still sufficient high-energy sites (dislocations) in the matrix. With further advance in the aging process, the formation of matrix austenite declines, while the lath-like austenite formation at the lath boundaries is still active.

Interestingly, the reverted austenite does not transform back to martensite during the cooling cycle, which can be thermodynamically justified as follows. The stability of the austenite phase can be quantitatively analyzed by the critical driving force (ΔG) required

for the transformation of reverted austenite to martensite (α′) based on equation (4.2.1) [233][283]:

$$\Delta G = -\Delta G^{\gamma \rightarrow \alpha'} + E^{str} + \Upsilon \quad (4.2.1)$$

where $\Delta G^{\gamma \rightarrow \alpha'}$ is the chemical Gibbs free energy of the transformation, E^{str} is the elastic strain energy, and Υ is the interfacial energy generated by new martensite interfaces. The key point is the reduction in chemical Gibbs free energy of the transformation ($\Delta G^{\gamma \rightarrow \alpha'}$) by increasing the Ni-content of the austenite phase [233]. This simultaneously results in solution hardening of the austenite phase leading to increased interfacial energy (Υ) of the resultant martensite during the cooling process, hindering the transformation of reverted austenite to martensite. Therefore, it can be concluded that Ni-enrichment of the reverted austenite can be accounted for the stability of this phase during the subsequent cooling cycle. According to the TEM image taken from the sample aged at the longest time interval (4 h), new carbides were formed inside the reverted austenite phase (Fig. 4.2.4e), while the pre-existing matrix carbides were still stable. This observation shows that the presence of reverted austenite mutually promotes the formation of carbides. The nucleation of new carbide phases inside the reverted austenite can be attributed to the higher solid solubility of carbon in FCC structure as compared to the BCC structure of the matrix, making the reverted austenite a preferential site for carbide nucleation [216].

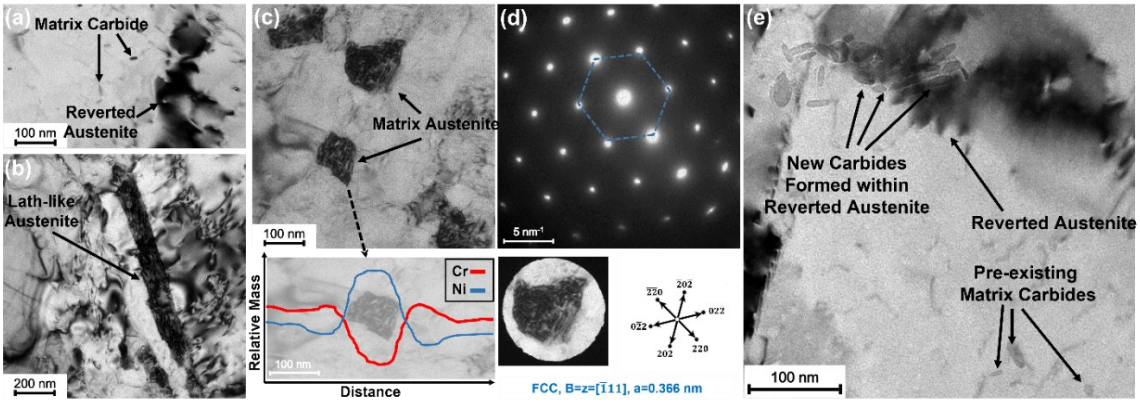

Figure 4.2.4 (a-d) Multi-scale TEM images along with the corresponding EDS line scan and SAED pattern taken from the sample aged for 2 h, and (e) high-magnification TEM image taken from the sample aged for 4 h.

To sum up, the sequence of secondary phase formation during the isothermal (600 °C) aging process of WAAM-PH13-8Mo at different aging times is schematically illustrated in Fig. 4.2.5.

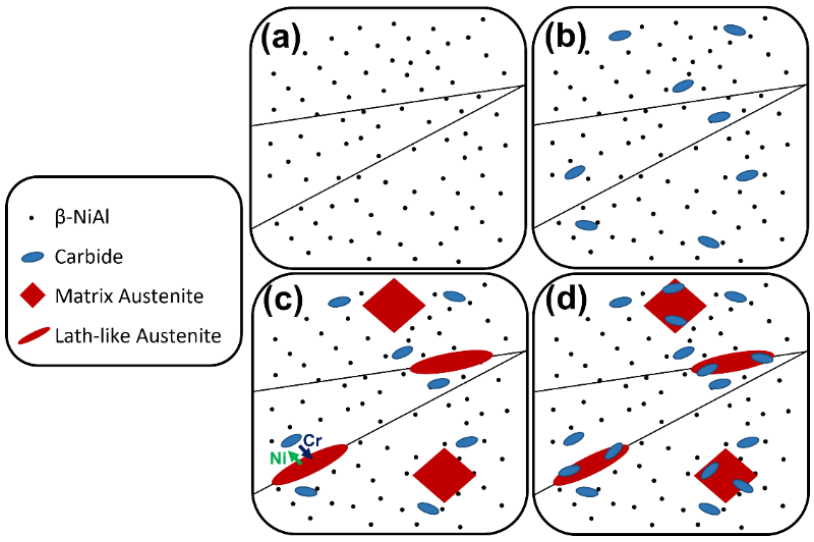

Figure 4.2.5 Schematic illustration of microstructural evolution during isothermal (600 °C) aging process of WAAM-PH13-8Mo alloy at different time intervals, i.e. (a) 20 min, (b) 1 h, (c) 2 h, and (d) 4 h.

4.2.5. CONCLUSIONS

In conclusion, the aging process of WAAM-PH13-8Mo initiates with the homogeneous nucleation of round-shaped nano-sized β-NiAl precipitates, followed by the formation of ellipsoidal $M_{23}C_6$ carbides in the martensitic matrix. Afterwards, the presence of carbides increases the relative weight percentage of Ni as an austenite stabilizer in the adjacent matrix, which facilitates the subsequent formation of reverted austenite. At the final stage of the aging process, the formed reverted austenite provides a preferential nucleation site for further formation of carbides dictated by the higher carbon content of the FCC austenite as compared to that in the BCC structure of the matrix.

Acknowledgments

The authors gratefully acknowledge the support of Natural Sciences and Engineering Research Council of Canada (NSERC) [grant number RGPIN-2017-04368], Canada Research Chair program, Ocean Frontier Institute, and Dalhousie University for sponsoring this work.

CHAPTER 5 CONCLUSION

This thesis aimed to investigate the beneficial influence of different post-printing heat treatment cycles on the microstructure, mechanical properties, and corrosion performance of three different ferrous alloys *i.e.,* low-carbon low-alloy steel (ER70S), martensitic stainless steel (ER420), and precipitation hardening martensitic stainless steel (PH 13-8Mo) which is presented in three main phases. A summary of the observations and conclusions obtained from each phase are presented below:

5.1 Summary and Conclusions of the First Phase

In the first phase of this research, the fabrication feasibility of a conventionally rolled low-carbon low-alloy shipbuilding steel plate (EH36) by wire arc additive manufacturing technology using ER70S feedstock wire was investigated. With the purpose of mechanical properties improvement, post-printing heat treatment cycles, including air-cooling and water-quenching from the intercritical austenitizing temperature (800 °C) were applied on the additively manufactured part to meet the mechanical properties requirements of the as-received conventionally rolled ship plate. Microstructural characterizations on the as-received rolled ship plate (EH36) revealed a banded ferritic-pearlitic structure aligned along the rolling direction. On the other hand, microstructure of the WAAM-fabricated part was characterized by a periodic variation along the building direction with three distinguishable regions in each deposited track, including a ferritic-pearlitic structure in the melt pool centers, acicular ferrite, bainite, and martensite - austenite phases in the narrow melt pool boundaries, and coarse polygonal ferrite grains in the heat affected zones. The microstructural transitions in the as-printed part were attributed to the sequential heating and cooling cycles and complex thermal history experienced by the material during the manufacturing process. Although the tensile strength of the conventionally and additively manufactured components were comparable, the heterogenous microstructure of the as-printed part resulted in anisotropic ductility in vertical and horizontal directions. Both post-printing heat treatment cycles (austenitizing followed by air-cooling and water-quenching) were found to be successful

in homogenizing the microstructure and minimizing the anisotropic ductility, while the obtained tensile strength varied based on the adopted cooling rate. To be more precise, the air-cooling heat treatment resulted in a coarse polygonal ferritic-pearlitic microstructure and consequently reduced the ultimate tensile strength from ~500 MPa for the as-printed sample to ~450 MPa in air-cooled condition. However, the higher cooling rate associated with water-quenching heat treatment improved the ultimate tensile strength to ~550 MPa as a result of the formation of tiny and sharp acicular ferrite at the grain boundaries of the polygonal ferrite grains plus a low volume fraction of intergranular lamellar pearlite. In conclusion, the fabrication feasibility of low-carbon low-alloy shipbuilding steel plate (EH36) by wire arc additive manufacturing technology using ER70S feedstock wire was approved provided that the post-printing austenitizing heat treatment followed by water-quenching is implemented to eliminate the anisotropic ductility and improve the tensile strength of the additively manufactured counterpart. It is worth mentioning that austenitizing at upper-critical temperature (900 °C) followed by water quenching increased the tensile strength of the component by around 20%, while this treatment was found to be inefficient in minimizing the anisotropic mechanical properties.

5.2 Summary and Conclusions of the Second Phase

In the second phase of this research, effects of post-printing heat treatment on the microstructure and mechanical properties of a wire arc additive manufactured 420 martensitic stainless steel part was investigated. Initial microstructure of the as-printed part being deposited with an interpass temperature of 25 °C was characterized by the formation of residual δ-ferrite patches distributed in the inter-dendritic regions of the martensitic matrix. The stabilization of δ-ferrite phase at room temperature was attributed to high Cr-content (13 wt.%) of the feedstock material as a ferrite stabilizing element and also the rapid cooling rate associated with the fabrication process which retarded the diffusional transformation of δ-ferrite to γ-austenite during the cooling process. It is worth mentioning that the implementation of interpass temperature of 200 °C being between martensite start and martensite finish temperatures of the alloy led to the in-situ quenching and partitioning heat treatment resulting in the formation of higher volume

fraction of retained austenite as compared to the sample deposited with an interpass temperature of 25 °C. Since δ-ferrite is considered as an undesired phase being detrimental to both corrosion and mechanical properties, austenitizing and tempering heat treatment at different temperatures were applied to the as-printed part to optimize the post-printing heat treatment parameters. Austenitizing temperature of 1150 °C was picked as the ideal cycle due to the complete elimination of undesirable phases, resulting in a fully martensitic microstructure with the maximum hardness of 670 ± 4 H V as compared to the as-printed part with a hardness value of 550 ± 12 H V. However, either lower or higher austenitizing temperatures led to the formation of adverse phases like carbides and δ-ferrite with a reduced hardness. Interestingly, the optimum austenitizing temperature (1150 °C) for the additively manufactured 420 martensitic stainless steel herein was found to be 100–150 °C higher than the common austenitizing temperature implemented for conventionally fabricated 420 martensitic stainless steel. This inconsistency was attributed to their different initial microstructure *i.e.* carbides phases dispersed in α-ferritic matrix for the conventionally fabricated 420 martensitic stainless steel in contrast to δ-ferrite phases embedded in a martensitic matrix for the additively manufactured 420 martensitic stainless steel. In order to decrease the brittleness of the as-quenched fully martensitic microstructure and improve the ductility, further tempering process was performed at different temperatures, including 200, 300, 400, 500, and 600 °C. Increasing the tempering temperature led to the variations in the size, morphology, and distribution of secondary phases from sub-micron needle-like chromium carbides at 300 °C to spherical shape at 400 °C, followed by their segregation along the primary austenite grain boundaries at 500 °C, and finally further carbides coarsening at 600 °C. Microhardness evaluations revealed the occurrence of secondary hardening during the post-printing tempering process at 400 °C with a maximum hardness of 550 ± 7 H V due to the formation of fine spherical Cr-enriched carbides with a homogeneous distribution in the martensitic matrix. However, tempering at higher temperatures (500 and 600 °C) reduced the microhardness value to 490 ± 7 H V and 300 ± 1 H V due to intergranular segregation and further coarsening of carbides. Uniaxial tensile testing results were also in agreement with the microhardness measurements and approved that the tempering process at 400 °C leads to the optimum combination of strength (1442 ± 5 MPa) and

ductility (11.8 ± 1%) as compared to the as-printed sample with the strength of 1151 ± 9 MPa and ductility of 9.9 ± 0.5%. Overall, it can be concluded that it is essential to implement post-printing heat treatment on WAAM-fabricated 420 martensitic stainless steel to remove undesired meta-stable phases (*i.e.,* δ-ferrite) and also achieve an optimal combination of strength and ductility.

5.3 Summary and Conclusion of the Third Phase

In the third phase of this research, microstructural features and corrosion performance of a wire arc additively manufactured PH 13-8Mo stainless steel part were compared before and after solution-aging treatments at different times and temperatures. The dominant microstructure of the as-printed part was a martensitic matrix containing lathy and vermicular residual Cr-enriched δ-ferrite phases which are detrimental to corrosion resistance due to the formation of Cr-depleted regions at their vicinity resulting in sensitization phenomena and localized corrosion attack. Solution treatment at 1050 °C was found to be effective in eliminating the undesired δ-ferrite, while subsequent aging resulted in recovery of martensite, annihilation of dislocations, and formation of secondary phases, such as β-NiAl precipitates, Cr-enriched carbides, and reverted austenite. In particular, aging treatment at 400 °C did not significantly affect the microstructure of the solution-treated material except for a partial shrinkage in the martensite laths due to the lath boundaries migration and a decreased dislocation density associated with the martensite recovery process. Aging treatment at 500 °C, however, led to the formation of nano-scale spherical β-NiAl precipitates within martensite laths characterized by a lower density of dislocation compared to the sample aged at 400 °C. The highest aging temperature (600 °C) resulted in the local nucleation and growth of reverted austenite and the formation of a new secondary phase, *i.e.,* $M_{23}C_6$ carbides with an ellipsoidal morphology. The formation sequence of the secondary phases at the highest studied aging temperature was investigated by isothermal aging in the over-aged condition (600 °C) at different time intervals and it was revealed that following the precipitation of β-NiAl phase, ellipsoidal $M_{23}C_6$ carbides start to precipitate, facilitating the subsequent formation of reverted austenite by increasing the relative weight percentage of Ni as an austenite stabilizer in the matrix. Afterwards, the formed reverted

austenite provides a preferential nucleation site for further formation of carbides dictated by the higher carbon content of the FCC austenite as compared to that in the BCC structure of the matrix.

The corrosion performance of the as-printed and heat-treated samples was investigated using different electrochemical measurements, which revealed a much better corrosion resistance in all heat-treated samples as compared to the as-printed part. The higher electrochemical stability of the heat-treated samples was attributed to the elimination of undesired residual Cr-enriched δ-ferrite patches, which provoked the sensitization phenomena and local corrosion attack in the as-printed sample. Among the different heat-treatment conditions, the sample aged at 500 °C was characterized by the highest corrosion resistance, while aging treatment at the highest temperature (600 °C) showed the lowest electrochemical stability. The superior corrosion performance of the sample aged at 500 °C compared to the sample aged at 400 °C was correlated to the lower residual stress due to a lower dislocation density as a result of higher degree of recovery occurred at 500 °C. On the other hand, the formation of Cr-enriched $M_{23}C_6$ carbides in the sample aged at 600 °C adversely affected the corrosion performance of the material due to the formation of micro-galvanic coupling between the Cr-enriched carbides and the depleted matrix. In conclusion, it is highly recommended to avoid employing as-printed PH 13-8Mo martensitic stainless steels for harsh environment applications due to its electrochemical instability dominated by the presence of Cr-enriched δ-ferrite phase. Moreover, the solution treatment should be performed in intermediate temperatures to ensure the complete elimination of pre-existing residual δ-ferrite and avoid the re-formation of δ-ferrite at elevated temperatures. The aging process at high temperatures (600 °C and above) should also be avoided to prevent the formation of detrimental Cr-enriched carbides.

5.4 Future Work

The thesis covered the effect of post-printing heat treatment on the additively manufactured ferrous alloys, *i.e.,* low-carbon low-alloy steel (ER70S), martensitic stainless steel (ER420), and precipitation hardening martensitic stainless steel (PH 13-8Mo). However, due to the limited time, it was not possible to investigate all different process variants and also cover all different materials characterization methods available in materials science and engineering research. Therefore, the author provides some recommendations and suggestions for future work on each phase of this thesis.

1- As the optimum process parameters for wire arc additive manufacturing of low-carbon low-alloy steel (ER70S) wall was obtained according to the recommendations provided by power source supplier in addition to trial and error based on the attained minimum splashing and the highest arc stability during deposition, it is highly recommended to study the effect of other process parameters on the interpass defects and microstructural features, especially the width of the HAZs and also the unstable phases in the melt pool boundaries. Since the main source of the anisotropic ductility was attributed to the microstructural heterogeneities and process induced defects, further optimization of the process parameters might also help with minimizing the anisotropic properties and eliminate the required post-printing heat treatment cycles.

2- As the post-printing tempering process of the additively manufactured ER420 martensitic stainless steel was accompanied by secondary hardening as a result of the formation of chromium carbides with different size, morphology, and distribution, it is highly recommended to characterize the type of carbides *i.e.,* $M_{23}C_6$, M_3C, M_7C_3, or M_2C by TEM analysis and the corresponding SAED patterns to better understand the effect of each type of carbides formed in different tempering temperature. In addition, as the type, size and distribution of carbides drastically affect the corrosion performance of stainless steels, it is important to study the effect of tempering process on the electrochemical response of the material. Moreover, although the effect of interpass temperature and retained austenite content on the corrosion performance of the material was investigated in another work as the co-author, it is important to also study the mechanical properties especially the toughness and

ductility of the as-printed part fabricated by different interpass temperatures and various retained austenite content.

3- As the wire arc additively manufactured PH 13-8Mo part was characterized by a strong columnar grain structure aligned along the building direction, it is highly recommended to study different possible methods to prevent the formation of such a textured structure in the as-printed condition. One of the recommended methods is to add nano-particles to the fusion zone which act as inoculant and grain refinement agents to avoid epitaxial grain growth from each deposited track to the subsequent layer. This topic is the subject of the upcoming research of the author's research group. Moreover, although the effect of post-printing aging process on the passive layer stability of the material was studied under simulated sea-water condition (naturally-aerated 3.5 wt.% NaCl solution), it is also important to investigate the stress corrosion cracking under harsh environments such as hydrogen or saturated H_2S solution.

BIBLIOGRAPHY

[1] J.Z. Li, M.R. Alkahari, N.A.B. Rosli, R. Hasan, M.N. Sudin, F.R. Ramli, Review of wire arc additive manufacturing for 3D metal printing, Int. J. Autom. Technol. 13 (2019) 346–353.

[2] M. Liberini, A. Astarita, G. Campatelli, A. Scippa, F. Montevecchi, G. Venturini, M. Durante, L. Boccarusso, F.M.C. Minutolo, A. Squillace, Selection of Optimal Process Parameters for Wire Arc Additive Manufacturing, Procedia CIRP. 62 (2017) 470–474. https://doi.org/10.1016/j.procir.2016.06.124.

[3] J. Xiong, G. Zhang, Adaptive control of deposited height in GMAW-based layer additive manufacturing, J. Mater. Process. Technol. 214 (2014) 962–968. https://doi.org/10.1016/j.jmatprotec.2013.11.014.

[4] A.C.M. Bekker, J.C. Verlinden, Life cycle assessment of wire + arc additive manufacturing compared to green sand casting and CNC milling in stainless steel DC Power Electrode wire Nozzle Shielding gas Arc Weld pool Workpiece Substrate, J. Clean. Prod. 177 (2018) 438–447. https://doi.org/10.1016/j.jclepro.2017.12.148.

[5] I. Gibson, D.W. Rosen, B. Stucker, M. Khorasani, Additive manufacturing technologies, Springer, 2021.

[6] J. Xiong, Z. Yin, W. Zhang, Closed-loop control of variable layer width for thin-walled parts in wire and arc additive manufacturing, J. Mater. Process. Technol. 233 (2016) 100–106. https://doi.org/10.1016/j.jmatprotec.2016.02.021.

[7] M. Ghaffari, A. Vahedi Nemani, M. Rafieazad, A. Nasiri, Effect of Solidification Defects and HAZ Softening on the Anisotropic Mechanical Properties of a Wire Arc Additive-Manufactured Low-Carbon Low-Alloy Steel Part, JOM. 71(11) (2019) 4215–4224. https://doi.org/10.1007/s11837-019-03773-5.

[8] M. Rafieazad, M. Ghaffari, A.V. Nemani, A. Nasiri, Microstructural evolution and mechanical properties of a low-carbon low-alloy steel produced by wire arc additive manufacturing, Int. J. Adv. Manuf. Technol. (2019) 1–14.

[9] H.A. Hegab, Design for additive manufacturing of composite materials and potential alloys: a review, Manuf. Rev. 3 (2016) 11.

[10] F. Bos, R. Wolfs, Z. Ahmed, T. Salet, Additive manufacturing of concrete in construction: potentials and challenges of 3D concrete printing, Virtual Phys. Prototyp. 11 (2016) 209–225.

[11] T.D. Ngo, A. Kashani, G. Imbalzano, K.T.Q. Nguyen, D. Hui, Additive manufacturing (3D printing): A review of materials, methods, applications and challenges, Compos. Part B Eng. (2018). https://doi.org/10.1016/j.compositesb.2018.02.012.

[12] A.V. Nemani, M. Ghaffari, S. Salahi, A. Nasiri, Effects of post-printing heat treatment on the microstructure and mechanical properties of a wire arc additive manufactured 420 martensitic stainless steel part, Mater. Sci. Eng. A. (2021) 141167.

[13] J.J. Lewandowski, M. Seifi, Metal Additive Manufacturing: A Review of Mechanical Properties, Annu. Rev. Mater. Res. 46 (2016) 151–186. https://doi.org/10.1146/annurev-matsci-070115-032024.

[14] B. Wu, Z. Pan, D. Ding, D. Cuiuri, H. Li, J. Xu, J. Norrish, A review of the wire arc additive manufacturing of metals: Properties, defects and quality improvement, J. Manuf. Process. 35 (2018) 127–139.

[15] J. Gunasekaran, P. Sevvel, I. John Solomon, Metallic materials fabrication by selective laser melting: A review, Mater. Today Proc. 37 (2021) 252–256. https://doi.org/https://doi.org/10.1016/j.matpr.2020.05.162.

[16] C. Xia, Z. Pan, J. Polden, H. Li, Y. Xu, S. Chen, Y. Zhang, A review on wire arc additive manufacturing: Monitoring, control and a framework of automated system, J. Manuf. Syst. 57 (2020) 31–45. https://doi.org/https://doi.org/10.1016/j.jmsy.2020.08.008.

[17] X. Chen, J. Li, X. Cheng, B. He, H. Wang, Z. Huang, Microstructure and mechanical properties of the austenitic stainless steel 316L fabricated by gas metal arc additive manufacturing, Mater. Sci. Eng. A. 703 (2017) 567–577. https://doi.org/https://doi.org/10.1016/j.msea.2017.05.024.

[18] D. Yang, C. He, G. Zhang, Forming characteristics of thin-wall steel parts by double electrode GMAW based additive manufacturing, J. Mater. Process. Technol. 227 (2016) 153–160. https://doi.org/10.1016/j.jmatprotec.2015.08.021.

[19] J. Xiong, Y. Li, R. Li, Z. Yin, Influences of process parameters on surface roughness of multi-layer single-pass thin-walled parts in GMAW-based additive manufacturing, J. Mater. Process. Technol. 252 (2018) 128–136. https://doi.org/10.1016/j.jmatprotec.2017.09.020.

[20] A.E. Wilson-Heid, Z. Wang, B. McCornac, A.M. Beese, Quantitative relationship between anisotropic strain to failure and grain morphology in additively manufactured Ti-6Al-4V, Mater. Sci. Eng. A. 706 (2017) 287–294. https://doi.org/10.1016/j.msea.2017.09.017.

[21] Z. Wang, T.A. Palmer, A.M. Beese, Effect of processing parameters on microstructure and tensile properties of austenitic stainless steel 304L made by directed energy deposition additive manufacturing, Acta Mater. 110 (2016) 226–235. https://doi.org/10.1016/j.actamat.2016.03.019.

[22] F. Wang, S. Williams, P. Colegrove, A.A. Antonysamy, Microstructure and Mechanical Properties of Wire and Arc Additive Manufactured Ti-6Al-4V, (n.d.). https://doi.org/10.1007/s11661-012-1444-6.

[23] C. V Haden, G. Zeng, F.M. Carter III, C. Ruhl, B.A. Krick, D.G. Harlow, Wire and arc additive manufactured steel: Tensile and wear properties, Addit. Manuf. 16 (2017) 115–123.

[24] N. Sridharan, M.W. Noakes, A. Nycz, L.J. Love, R.R. Dehoff, S.S. Babu, On the toughness scatter in low alloy C-Mn steel samples fabricated using wire arc additive manufacturing, Mater. Sci. Eng. A. 713 (2018) 18–27. https://doi.org/https://doi.org/10.1016/j.msea.2017.11.101.

[25] V.D. Fachinotti, A. Cardona, B. Baufeld, O. Van der Biest, Finite-element modelling of heat transfer in shaped metal deposition and experimental validation, Acta Mater. 60 (2012) 6621–6630. https://doi.org/https://doi.org/10.1016/j.actamat.2012.08.031.

[26] Y. Li, Y. Sun, Q. Han, G. Zhang, I. Horváth, Enhanced beads overlapping model for wire and arc additive manufacturing of multi-layer multi-bead metallic parts, J. Mater. Process. Technol. 252 (2018) 838–848. https://doi.org/10.1016/j.jmatprotec.2017.10.017.

[27] R. Hu, X. Chen, G. Yang, S. Gong, S. Pang, Metal transfer in wire feeding-based

electron beam 3D printing: Modes, dynamics, and transition criterion, Int. J. Heat Mass Transf. 126 (2018) 877–887.

[28] S. Gook, A. Gumenyuk, M. Rethmeier, Hybrid laser arc welding of X80 and X120 steel grade, Sci. Technol. Weld. Join. 19 (2014) 15–24.

[29] B.D. DeRuntz, Assessing the benefits of surface tension transfer welding to industry, J. Ind. Technol. 19 (2003) 55–62.

[30] A. Garcia-Colomo, D. Wood, F. Martina, S.W. Williams, A comparison framework to support the selection of the best additive manufacturing process for specific aerospace applications, Int. J. Rapid Manuf. 9 (2020) 194–211.

[31] C.R. Cunningham, J.M. Flynn, A. Shokrani, V. Dhokia, S.T. Newman, Invited review article : Strategies and processes for high quality wire arc additive manufacturing, Addit. Manuf. 22 (2018) 672–686. https://doi.org/10.1016/j.addma.2018.06.020.

[32] S. Das, D.L. Bourell, S.S. Babu, Metallic materials for 3D printing, MRS Bull. 41 (2016) 729–741.

[33] R.B. Dinwiddie, R.R. Dehoff, P.D. Lloyd, L.E. Lowe, J.B. Ulrich, Thermographic in-situ process monitoring of the electron-beam melting technology used in additive manufacturing, in: Thermosense Therm. Infrared Appl. XXXV, International Society for Optics and Photonics, 2013: p. 87050K.

[34] X. Xu, S. Ganguly, J. Ding, S. Guo, S. Williams, F. Martina, Microstructural evolution and mechanical properties of maraging steel produced by wire+arc additive manufacture process, Mater. Charact. (2017). https://doi.org/10.1016/j.matchar.2017.12.002.

[35] J. Ge, J. Lin, Y. Lei, H. Fu, Location-related thermal history, microstructure, and mechanical properties of arc additively manufactured 2Cr13 steel using cold metal transfer welding, Mater. Sci. Eng. A. 715 (2018) 144–153.

[36] Y. Sun, R.J. Hebert, M. Aindow, Effect of heat treatments on microstructural evolution of additively manufactured and wrought 17-4PH stainless steel, Mater. Des. 156 (2018) 429–440. https://doi.org/10.1016/j.matdes.2018.07.015.

[37] L. Thijs, M.L.M. Sistiaga, R. Wauthle, Q. Xie, J.-P. Kruth, J. Van Humbeeck, Strong morphological and crystallographic texture and resulting yield strength

anisotropy in selective laser melted tantalum, Acta Mater. 61 (2013) 4657–4668.

[38] A. Riemer, S. Leuders, M. Thöne, H.A. Richard, T. Tröster, T. Niendorf, On the fatigue crack growth behavior in 316L stainless steel manufactured by selective laser melting, Eng. Fract. Mech. 120 (2014) 15–25.

[39] T. Niendorf, S. Leuders, A. Riemer, H.A. Richard, T. Tröster, D. Schwarze, Highly anisotropic steel processed by selective laser melting, Metall. Mater. Trans. B. 44 (2013) 794–796.

[40] S. Gorsse, C. Hutchinson, M. Gouné, R. Banerjee, Additive manufacturing of metals: a brief review of the characteristic microstructures and properties of steels, Ti-6Al-4V and high-entropy alloys, Sci. Technol. Adv. Mater. 18 (2017) 584–610.

[41] L.N. Carter, C. Martin, P.J. Withers, M.M. Attallah, The influence of the laser scan strategy on grain structure and cracking behaviour in SLM powder-bed fabricated nickel superalloy, J. Alloys Compd. 615 (2014) 338–347. https://doi.org/https://doi.org/10.1016/j.jallcom.2014.06.172.

[42] J. Lunde, M. Kazemipour, S. Salahi, A. Nasiri, Microstructure and Mechanical Properties of AISI 420 Stainless Steel Produced by Wire Arc Additive Manufacturing, in: TMS 2020 149th Annu. Meet. Exhib. Suppl. Proc., Springer, 2020: pp. 413–424.

[43] M. Ghaffari, A.V. Nemani, A. Nasiri, Interfacial bonding between a wire arc additive manufactured 420 martensitic stainless steel part and its wrought base plate, Mater. Chem. Phys. (2020) 123199. https://doi.org/https://doi.org/10.1016/j.matchemphys.2020.123199.

[44] S.K. Bonagani, V. Bathula, V. Kain, Influence of tempering treatment on microstructure and pitting corrosion of 13 wt.% Cr martensitic stainless steel, Corros. Sci. 131 (2018) 340–354. https://doi.org/https://doi.org/10.1016/j.corsci.2017.12.012.

[45] Y.C. Lin, S.C. Chen, Effect of residual stress on thermal fatigue in a type 420 martensitic stainless steel weldment, J. Mater. Process. Technol. 138 (2003) 22–27. https://doi.org/https://doi.org/10.1016/S0924-0136(03)00043-8.

[46] P. Mayr, T.A. Palmer, J.W. Elmer, E.D. Specht, S.M. Allen, Formation of delta ferrite in 9 Wt pct Cr steel investigated by in-situ X-ray diffraction using

synchrotron radiation, Metall. Mater. Trans. A. 41 (2010) 2462–2465.

[47] A.E. Korneev, A.F. Gromov, A.M. Kiselev, Effect of δ-Ferrite on the Properties of Martensitic Steels, Met. Sci. Heat Treat. 55 (2013) 445–450.

[48] C. Pandey, M.M. Mahapatra, P. Kumar, J.G. Thakre, N. Saini, Role of evolving microstructure on the mechanical behaviour of P92 steel welded joint in as-welded and post weld heat treated state, J. Mater. Process. Technol. 263 (2019) 241–255.

[49] B.E. Carroll, T.A. Palmer, A.M. Beese, Anisotropic tensile behavior of Ti-6Al-4V components fabricated with directed energy deposition additive manufacturing, Acta Mater. 87 (2015) 309–320. https://doi.org/10.1016/j.actamat.2014.12.054.

[50] Q. Zhang, J. Chen, Z. Zhao, H. Tan, X. Lin, W. Huang, Microstructure and anisotropic tensile behavior of laser additive manufactured TC21 titanium alloy, Mater. Sci. Eng. A. 673 (2016) 204–212. https://doi.org/10.1016/j.msea.2016.07.040.

[51] T. LeBrun, T. Nakamoto, K. Horikawa, H. Kobayashi, Effect of retained austenite on subsequent thermal processing and resultant mechanical properties of selective laser melted 17–4 PH stainless steel, Mater. Des. 81 (2015) 44–53.

[52] D.H. Ping, M. Ohnuma, Y. Hirakawa, Y. Kadoya, K. Hono, Microstructural evolution in 13Cr-8Ni-2.5Mo-2Al martensitic precipitation-hardened stainless steel, Mater. Sci. Eng. A. 394 (2005) 285–295. https://doi.org/10.1016/j.msea.2004.12.002.

[53] P. Bajaj, A. Hariharan, A. Kini, P. Kürnsteiner, D. Raabe, E.A. Jägle, Steels in additive manufacturing: A review of their microstructure and properties, Mater. Sci. Eng. A. 772 (2020) 138633. https://doi.org/https://doi.org/10.1016/j.msea.2019.138633.

[54] Y. Sun, R.J. Hebert, M. Aindow, Effect of heat treatments on microstructural evolution of additively manufactured and wrought 17-4PH stainless steel, Mater. Des. 156 (2018) 429–440. https://doi.org/10.1016/j.matdes.2018.07.015.

[55] S. Cheruvathur, E.A. Lass, C.E. Campbell, Additive Manufacturing of 17-4 PH Stainless Steel: Post-processing Heat Treatment to Achieve Uniform Reproducible Microstructure, Jom. 68 (2016) 930–942. https://doi.org/10.1007/s11837-015-1754-4.

[56] F. Deirmina, N. Peghini, B. AlMangour, D. Grzesiak, M. Pellizzari, Heat treatment and properties of a hot work tool steel fabricated by additive manufacturing, Mater. Sci. Eng. A. 753 (2019) 109–121. https://doi.org/https://doi.org/10.1016/j.msea.2019.03.027.

[57] A. Hadadzadeh, A. Shahriari, B.S. Amirkhiz, J. Li, M. Mohammadi, Additive manufacturing of an Fe–Cr–Ni–Al maraging stainless steel: Microstructure evolution, heat treatment, and strengthening mechanisms, Mater. Sci. Eng. A. 787 (2020) 139470. https://doi.org/https://doi.org/10.1016/j.msea.2020.139470.

[58] K. Saeidi, X. Gao, F. Lofaj, L. Kvetková, Z.J. Shen, Transformation of austenite to duplex austenite-ferrite assembly in annealed stainless steel 316L consolidated by laser melting, J. Alloys Compd. 633 (2015) 463–469.

[59] T. Wang, Y. Zhang, Z. Wu, C. Shi, Microstructure and properties of die steel fabricated by WAAM using H13 wire, Vaccum. 149 (2018) 185–189. https://doi.org/10.1016/j.vacuum.2017.12.034.

[60] K. Li, M.A. Klecka, S. Chen, W. Xiong, Wire-arc additive manufacturing and post-heat treatment optimization on microstructure and mechanical properties of Grade 91 steel, Addit. Manuf. 37 (2021) 101734. https://doi.org/https://doi.org/10.1016/j.addma.2020.101734.

[61] B.K. Agrawal, Introduction to engineering materials, Tata McGraw-Hill Education, 1988.

[62] W. Jin, C. Zhang, S. Jin, Y. Tian, D. Wellmann, W. Liu, Wire Arc Additive Manufacturing of Stainless Steels: A Review, Appl. Sci. . 10 (2020). https://doi.org/10.3390/app10051563.

[63] C.N. Hsiao, C.S. Chiou, J.R. Yang, Aging reactions in a 17-4 PH stainless steel, Mater. Chem. Phys. 74 (2002) 134–142.

[64] A. Caballero, J. Ding, S. Ganguly, S. Williams, Wire + Arc Additive Manufacture of 17-4 PH stainless steel: Effect of different processing conditions on microstructure, hardness, and tensile strength, J. Mater. Process. Technol. 268 (2019) 54–62. https://doi.org/10.1016/j.jmatprotec.2019.01.007.

[65] A. Zielińska-Lipiec, A. Ziewiec, E. Tasak, Microstructure of Welded Joints of X5CrNiCuNb16-4 (17-4 PH) Martensitic Stainlees Steel After Heat Treatment,

Arch. Metall. Mater. (2014). https://doi.org/10.2478/amm-2014-0162.

[66] S.Y. Tarasov, A. V Filippov, N.N. Shamarin, S. V Fortuna, G.G. Maier, E.A. Kolubaev, Microstructural evolution and chemical corrosion of electron beam wire-feed additively manufactured AISI 304 stainless steel, J. Alloys Compd. 803 (2019) 364–370. https://doi.org/https://doi.org/10.1016/j.jallcom.2019.06.246.

[67] H. Li, L. Sun, L. Zhu, Y. Liu, Y. Li, Research on influential mechanism of HAZ impact toughness for shipbuilding steel with mg addition, Metals (Basel). 8 (2018) 584.

[68] P. Dong, C. Nie, X. Yang, S. Song, L. DeCan, A math-based design-for-produceability evaluation of titanium applications in ship hull structures, Trans-Soc Nav Arch. Mar. Eng. 120 (2013) 299–305.

[69] S.H. Wang, C.C. Chiang, S.L.I.I. Chan, Effect of initial microstructure on the creep behavior of TMCP EH36 and SM490C steels, Mater. Sci. Eng. A. 344 (2003) 288–295. https://doi.org/10.1016/S0921-5093(02)00425-2.

[70] T.M. Donizete Borba, W. Duarte Flores, L. de Oliveira Turani, R. Cardoso Junior, Assessment of the weldability of EH36 TMCP shipbuilding steel welded by high heat input submerged arc welding, Weld. Int. 31 (2017) 184–195.

[71] S.H. Wang, W.C. Luu, K.F. Ho, J.K. Wu, Hydrogen permeation in a submerged arc weldment of TMCP steel, Mater. Chem. Phys. 77 (2003) 447–454.

[72] J. Xiong, Y. Lei, H. Chen, G. Zhang, Fabrication of inclined thin-walled parts in multi-layer single-pass GMAW-based additive manufacturing with flat position deposition, J. Mater. Process. Technol. 240 (2017) 397–403. https://doi.org/10.1016/j.jmatprotec.2016.10.019.

[73] N. Shamsaei, A. Yadollahi, L. Bian, S.M. Thompson, An overview of Direct Laser Deposition for additive manufacturing; Part II: Mechanical behavior, process parameter optimization and control, Addit. Manuf. 8 (2015) 12–35. https://doi.org/10.1016/j.addma.2015.07.002.

[74] W.E. Frazier, Metal Additive Manufacturing: A Review, J. Mater. Eng. Perform. 23 (2014) 1917–1928. https://doi.org/10.1007/s11665-014-0958-z.

[75] E. Herderick, Additive manufacturing of metals: A review, Mater. Sci. Technol. (2011) 1413.

[76] S.W. Williams, F. Martina, A.C. Addison, J. Ding, G. Pardal, P. Colegrove, Wire + Arc Additive Manufacturing, Mater. Sci. Technol. 32 (2016) 641–647. https://doi.org/10.1179/1743284715Y.0000000073.

[77] W. Wu, S.B. Tor, C.K. Chua, K.F. Leong, A. Merchant, Investigation on processing of ASTM A131 Eh36 high tensile strength steel using selective laser melting, Virtual Phys. Prototyp. 10 (2015) 187–193.

[78] J. Wang, W.J. Wu, W. Jing, X. Tan, G.J. Bi, S.B. Tor, K.F. Leong, C.K. Chua, E. Liu, Improvement of densification and microstructure of ASTM A131 EH36 steel samples additively manufactured via selective laser melting with varying laser scanning speed and hatch spacing, Mater. Sci. Eng. A. 746 (2019) 300–313. https://doi.org/10.1016/j.msea.2019.01.019.

[79] D. Ding, Z. Pan, D. Cuiuri, H. Li, A multi-bead overlapping model for robotic wire and arc additive manufacturing (WAAM), Robot. Comput. Integr. Manuf. 31 (2015) 101–110. https://doi.org/10.1016/j.rcim.2014.08.008.

[80] X.D. Luo, Y.X. Zhu, H. Liu, M.Y. Li, Effect of Normalizing on Microstructure and Mechanical Properties of EH36 Alloy, in: Appl. Mech. Mater., Trans Tech Publ, 2014: pp. 110–113.

[81] F. Hayat, H. Uzun, Effect of heat treatment on microstructure, mechanical properties and fracture behaviour of ship and dual phase steels, J. Iron Steel Res. Int. 18 (2011) 65–72.

[82] X.D. Luo, H. Liu, Y.X. Zhu, C.Y. Zheng, Effect of Heat Treatment on Microstructure and Mechanical Properties of EH36 Alloy, in: Appl. Mech. Mater., Trans Tech Publ, 2014: pp. 177–180.

[83] M.A. Maleque, Y.M. Poon, H.H. Masjuki, The effect of intercritical heat treatment on the mechanical properties of AISI 3115 steel, J. Mater. Process. Technol. 153 (2004) 482–487.

[84] M.S. Rashid, Formable HSLA and dual-phase steels, in Proceedings of the Metallurgical Society of AIME, Michigan, USA. (1979).

[85] J. Luo, S.H.I. Wen, Q. Huang, L. Lin, Heat treatment of cold-rolled low-carbon Si-Mn dual phase steels, J. Iron Steel Res. Int. 17 (2010) 54–58.

[86] F. Ozturk, S. Toros, S. Kilic, Tensile and spring-back behavior of DP600 advanced

high strength steel at warm temperatures, J. Iron Steel Res. Int. 16 (2009) 41–46.

[87] A. Hüseyin, K.Z. Havva, K. Ceylan, Effect of intercritical annealing parameters on dual phase behavior of commercial low-alloyed steels, J. Iron Steel Res. Int. 17 (2010) 73–78.

[88] C. Roepke, S. Liu, S. Kelly, R. Martukanitz, Hybrid laser arc welding process evaluation on DH36 and EH36 steel, Weld. J. 89 (2010) 140s-150s.

[89] D. Mihailescu, M.C. Gheonea, E. Scutelnicu, O. Mircea, Evaluation of carbon monoxide and microparticles concentrations generated during MAG-C welding process, Teh. Vjesn. Gaz. 24 (2017) 591–598.

[90] B.D. Deruntz, Assessing the Benefits of Surface Tension Transfer Welding to Industry, J. Ind. Technol. 19 (2003) 2–8.

[91] A.W.S.A. 28/A5. 28M, Specification for Low Alloy Steel Electrodes and Rods for Gas Shielded Arc Welding, (2005).

[92] K.W. Andrews, Empirical formulae for the calculation of some transformation temperatures, J. Iron Steel Inst. (1965) 721–727.

[93] ASTM E8M-04, Standard Test Methods for Tension Testing of Metallic Materials [Metric], ASTM International, West Conshohocken, PA, 2008. https://doi.org/10.1520/E0008M-04.

[94] E.O. Hall, The Deformation and Ageing of Mild Steel: III Discussion of Results, Proc. Phys. Soc. Sect. B. 64 (1951) 747–753. https://doi.org/10.1088/0370-1301/64/9/303.

[95] Q. Wang, S. Zhang, C. Zhang, C. Wu, J. Wang, J. Chen, Z. Sun, Microstructure evolution and EBSD analysis of a graded steel fabricated by laser additive manufacturing, Vacuum. 141 (2017) 68–81.

[96] K. V Yang, Y. Shi, F. Palm, X. Wu, P. Rometsch, Columnar to equiaxed transition in Al-Mg(-Sc)-Zr alloys produced by selective laser melting, Scr. Mater. 145 (2018) 113–117. https://doi.org/https://doi.org/10.1016/j.scriptamat.2017.10.021.

[97] V.B. Biscuola, M.A. Martorano, Mechanical Blocking Mechanism for the Columnar to Equiaxed Transition, Metall. Mater. Trans. A. 39 (2008) 2885–2895. https://doi.org/10.1007/s11661-008-9643-x.

[98] R.K. Ray, J.J. Jonas, Transformation textures in steels, Int. Mater. Rev. 35 (1990)

1–36.

[99] N. Huda, A.R.H. Midawi, J. Gianetto, R. Lazor, A.P. Gerlich, Influence of martensite-austenite (MA) on impact toughness of X80 line pipe steels, Mater. Sci. Eng. A. 662 (2016) 481–491. https://doi.org/https://doi.org/10.1016/j.msea.2016.03.095.

[100] S. Moeinifar, A.H. Kokabi, H.R.M. Hosseini, Effect of tandem submerged arc welding process and parameters of Gleeble simulator thermal cycles on properties of the intercritically reheated heat affected zone, Mater. Des. 32 (2011) 869–876.

[101] F. Matsuda, K. IKEUCHI, Y. FUKADA, Y. HORII, H. OKADA, T. SHIWAKU, C. SHIGA, Review of mechanical and metallurgical investigations of MA constituent in welded joint in Japan, Trans. JWRI. 24 (1995) 1–24.

[102] P.A. Colegrove, H.E. Coules, J. Fairman, F. Martina, T. Kashoob, H. Mamash, L.D. Cozzolino, Journal of Materials Processing Technology Microstructure and residual stress improvement in wire and arc additively manufactured parts through high-pressure rolling, J. Mater. Process. Tech. 213 (2013) 1782–1791. https://doi.org/10.1016/j.jmatprotec.2013.04.012.

[103] P. Mohseni, Brittle and ductile fracture of X80 arctic steel, (2012).

[104] A. Lambert-Perlade, A.-F. Gourgues, J. Besson, T. Sturel, A. Pineau, Mechanisms and modeling of cleavage fracture in simulated heat-affected zone microstructures of a high-strength low alloy steel, Metall. Mater. Trans. A. 35 (2004) 1039–1053.

[105] E. Bayraktar, D. Kaplan, Mechanical and metallurgical investigation of martensite–austenite constituents in simulated welding conditions, J. Mater. Process. Technol. 153 (2004) 87–92.

[106] H.K.D.H. Bhadeshia, Local brittle zones and the role of Niobium, in: Mater. Sci. Forum, Trans Tech Publ, 2014: pp. 2129–2135.

[107] Y. Li, G. MJW, The effect of vanadium and niobium on the properties and microstructure of the intercritically reheated coarse grained heat affected zone in low carbon microalloyed steels, ISIJ Int. 41 (2001) 46–55.

[108] J. Zhang, W. Sun, H. Sun, Mechanical properties and microstructure of X120 grade high strength pipeline steel, J. Iron Steel Res. Int. 17 (2010) 63–67.

[109] Y. Tian, Q. Li, Z. Wang, G. Wang, Effects of ultra fast cooling on microstructure

and mechanical properties of pipeline steels, J. Mater. Eng. Perform. 24 (2015) 3307–3314.

[110] S. Moeinifar, Influence of Thermal Simulated and Real Tandem Submerged Arc Welding Process on the Microstructure and Mechanical Properties of the Coarse Grained Heat Affected Zone, in: Appl. Mech. Mater., Trans Tech Publ, 2012: pp. 3191–3198.

[111] F. MATSUDA, L.I. ZHONGLIN, P. Bernasovsky, K. Ishihara, H. Okada, An investigation on the behaviour of the ma constituent in simulated haz of hsla steels, Weld. Res. Abroad. 39 (1993) 24–30.

[112] B.C. Kim, S. Lee, N.J. Kim, D.Y. Lee, Microstructure and local brittle zone phenomena in high-strength low-alloy steel welds, Metall. Trans. A. 22 (1991) 139–149. https://doi.org/10.1007/BF03350956.

[113] D.P. Farichild, N. V Bangaru, J.Y. Koo, P.L. Harrison, A. Ozekcin, A study concerning intercritical HAZ microstructure and toughness in HSLA steels, Weld. J. 70 (1991) 321-s.

[114] A. Lambert, A. Lambert, J. Drillet, A.F. Gourgues, T. Sturel, A. Pineau, Microstructure of martensite–austenite constituents in heat affected zones of high strength low alloy steel welds in relation to toughness properties, Sci. Technol. Weld. Join. 5 (2000) 168–173. https://doi.org/10.1179/136217100101538164.

[115] N.-R. V Bangaru, A.K. Sachdev, Influence of cooling rate on the microstructure and retained austenite in an intercritically annealed vanadium containing HSLA steel, Metall. Trans. A. 13 (1982) 1899–1906.

[116] I. Hrivnak, F. Matsuda, Z. Li, K. IKEUCHI, H. OKADA, Investigation of metallography and behavior of MA constituent in Weld HAZ of HSLA steels (Materials, Metallurgy & Weldability), Trans. JWRI. 21 (1992) 241–250.

[117] C. Natividad, R. García, V.H. López, L.A. Falcón, M. Salazar, Mechanical and Metallurgical Properties of Grade X70 Steel Linepipe Produced by Non-conventional Heat Treatment, in: Charact. Met. Alloy., Springer, 2017: pp. 3–11.

[118] X. Yang, M. Salem, E.J. Palmiere, The effect of processing conditions and cooling rate on the microstructure and properties of API X-70 and API X-100 steels, Mater. Manuf. Process. 25 (2010) 48–53.

https://doi.org/10.1080/10426910903202567.

[119] I. Madariaga, I. Gutierrez, H. Bhadeshia, Acicular ferrite morphologies in a medium-carbon microalloyed steel, Metall. Mater. Trans. A. 32 (2001) 2187–2197.

[120] K.-S. Ro, Improvement on the sulfide stress corrosion cracking properties of hot rolled line-pipe steels, in: Corros. 2000, NACE International, 2000.

[121] B.T. Lu, J.L. Luo, Relationship between yield strength and near-neutral pH stress corrosion cracking resistance of pipeline steels—an effect of microstructure, Corrosion. 62 (2006) 129–140.

[122] G. A.-F., H.M. Flower, T.C. Lindley, Electron backscattering diffraction study of acicular ferrite, bainite, and martensite steel microstructures, Mater. Sci. Technol. 16 (2000) 26–40.

[123] M. Diaz-Fuentes, A. Iza-Mendia, I. Gutierrez, Analysis of different acicular ferrite microstructures in low-carbon steels by electron backscattered diffraction. Study of their toughness behavior, Metall. Mater. Trans. A. 34 (2003) 2505–2516.

[124] P. Mohseni, J.K. Solberg, M. Karlsen, O.M. Akselsen, E. Østby, Cleavage fracture initiation at M–A constituents in intercritically coarse-grained heat-affected zone of a HSLA steel, Metall. Mater. Trans. A. 45 (2014) 384–394.

[125] C.L. Davis, J.E. King, Cleavage initiation in the intercritically reheated coarse-grained heat-affected zone: Part I. Fractographic evidence, Metall. Mater. Trans. A. 25 (1994) 563–573. https://doi.org/10.1007/BF02651598.

[126] X. Zhang, H. Gao, A study of impact toughness of intercritically reheated coarse-grain heat effected zone of two type X80 grade pipeline steel, Trans. JWRI. (2012) 101–104.

[127] L. Lan, C. Qiu, D. Zhao, X. Gao, L. Du, Analysis of martensite–austenite constituent and its effect on toughness in submerged arc welded joint of low carbon bainitic steel, J. Mater. Sci. 47 (2012) 4732–4742.

[128] C.R. Cunningham, J.M. Flynn, A. Shokrani, V. Dhokia, S.T. Newman, Invited review article : Strategies and processes for high quality wire arc additive manufacturing, Addit. Manuf. 22 (2018) 672–686. https://doi.org/10.1016/j.addma.2018.06.020.

[129] G. Posch, K. Chladil, H. Chladil, Material properties of CMT—metal additive manufactured duplex stainless steel blade-like geometries, Weld. World. 61 (2017) 873–882.

[130] Y. Zhou, L. Zhang, X. Wang, Z. Chen, P.F. Yuan, Exploration of computational design and robotic fabrication with wire-arc additive manufacturing techniques, Intell. Inf. - Proc. 24th Int. Conf. Comput. Archit. Des. Res. Asia, CAADRIA 2019. 1 (2019) 143–152.

[131] A. Vahedi Nemani, M. Ghaffari, A. Nasiri, Comparison of microstructural characteristics and mechanical properties of shipbuilding steel plates fabricated by conventional rolling versus wire arc additive manufacturing, Addit. Manuf. 32 (2020) 101086. https://doi.org/10.1016/j.addma.2020.101086.

[132] S.W. Williams, F. Martina, A.C. Addison, J. Ding, G. Pardal, P. Colegrove, Wire + Arc additive manufacturing, Mater. Sci. Technol. (United Kingdom). 32 (2016) 641–647. https://doi.org/10.1179/1743284715Y.0000000073.

[133] Z. Wang, A.D. Stoica, D. Ma, A.M. Beese, Diffraction and single-crystal elastic constants of Inconel 625 at room and elevated temperatures determined by neutron diffraction, Mater. Sci. Eng. A. 674 (2016) 406–412.

[134] A.M. Beese, B.E. Carroll, Review of mechanical properties of Ti-6Al-4V made by laser-based additive manufacturing using powder feedstock, Jom. 68 (2016) 724–734.

[135] N. Sridharan, M.W. Noakes, A. Nycz, L.J. Love, R.R. Dehoff, S.S. Babu, On the toughness scatter in low alloy C-Mn steel samples fabricated using wire arc additive manufacturing, Mater. Sci. Eng. A. 713 (2018) 18–27. https://doi.org/10.1016/j.msea.2017.11.101.

[136] C. V Haden, G. Zeng, F.M. Carter, C. Ruhl, B.A. Krick, D.G. Harlow, Wire and arc additive manufactured steel: Tensile and wear properties, Addit. Manuf. 16 (2017) 115–123. https://doi.org/https://doi.org/10.1016/j.addma.2017.05.010.

[137] M. Ghaffari, A. Vahedi Nemani, M. Rafieazad, A. Nasiri, Effect of Solidification Defects and HAZ Softening on the Anisotropic Mechanical Properties of a Wire Arc Additive-Manufactured Low-Carbon Low-Alloy Steel Part, JOM. 71(11) (2019) 4215–4224. https://doi.org/10.1007/s11837-019-03773-5.

[138] A. Lopez, R. Bacelar, I. Pires, T.G. Santos, J.P. Sousa, L. Quintino, Non-destructive testing application of radiography and ultrasound for wire and arc additive manufacturing, Addit. Manuf. 21 (2018) 298–306. https://doi.org/https://doi.org/10.1016/j.addma.2018.03.020.

[139] B.A. Szost, S. Terzi, F. Martina, D. Boisselier, A. Prytuliak, T. Pirling, M. Hofmann, D.J. Jarvis, A comparative study of additive manufacturing techniques: Residual stress and microstructural analysis of CLAD and WAAM printed Ti-6Al-4V components, Mater. Des. 89 (2016) 559–567. https://doi.org/10.1016/j.matdes.2015.09.115.

[140] X. Xu, S. Ganguly, J. Ding, S. Guo, S. Williams, F. Martina, Microstructural evolution and mechanical properties of maraging steel produced by wire+ arc additive manufacture process, Mater. Charact. 143 (2018) 152–162.

[141] K. V. Yang, P. Rometsch, C.H.J. Davies, A. Huang, X. Wu, Effect of heat treatment on the microstructure and anisotropy in mechanical properties of A357 alloy produced by selective laser melting, Mater. Des. 154 (2018) 275–290. https://doi.org/10.1016/j.matdes.2018.05.026.

[142] B.D. DeRuntz, Assessing the benefits of surface tension transfer® welding to industry, J. Ind. Technol. 19 (2003) 1–8.

[143] A.O. Benscoter, B.L. Bramfitt, Metallography and microstructures of low-carbon and coated steels, Metallogr. Microstruct. 9 (2004) 588–607.

[144] A. International, Standard test methods for tension testing of metallic materials, ASTM international, 2016.

[145] A.S. Haselhuhn, B. Wijnen, G.C. Anzalone, P.G. Sanders, J.M. Pearce, In situ formation of substrate release mechanisms for gas metal arc weld metal 3-D printing, J. Mater. Process. Technol. 226 (2015) 50–59. https://doi.org/10.1016/j.jmatprotec.2015.06.038.

[146] H.K. Lee, K.S. Kim, C.M. Kim, Fracture resistance of a steel weld joint under fatigue loading, Eng. Fract. Mech. 66 (2000) 403–419. https://doi.org/10.1016/S0013-7944(00)00017-5.

[147] Y.M. Kim, H. Lee, N.J. Kim, Transformation behavior and microstructural characteristics of acicular ferrite in linepipe steels, Mater. Sci. Eng. A. 478 (2008)

361–370. https://doi.org/10.1016/j.msea.2007.06.035.

[148] B. Hwang, Y.M. Kim, S. Lee, N.J. Kim, S.S. Ahn, Correlation of microstructure and fracture properties of API X70 pipeline steels, Metall. Mater. Trans. A. 36 (2005) 725–739. https://doi.org/10.1007/s11661-005-0188-y.

[149] T. Mohandas, G. Madhusudan Reddy, B. Satish Kumar, Heat-affected zone softening in high-strength low-alloy steels, J. Mater. Process. Technol. 88 (1999) 284–294. https://doi.org/10.1016/S0924-0136(98)00404-X.

[150] X. Shi, S. Ma, C. Liu, Q. Wu, J. Lu, Y. Liu, W. Shi, Selective laser melting-wire arc additive manufacturing hybrid fabrication of Ti-6Al-4V alloy: Microstructure and mechanical properties, Mater. Sci. Eng. A. 684 (2017) 196–204. https://doi.org/10.1016/j.msea.2016.12.065.

[151] B. Shassere, A. Nycz, M.W. Noakes, C. Masuo, N. Sridharan, Correlation of Microstructure and Mechanical Properties of Metal Big Area Additive Manufacturing, Appl. Sci. 9 (2019) 787.

[152] N. Huda, A.R.H. Midawi, J. Gianetto, R. Lazor, A.P. Gerlich, Influence of martensite-austenite (MA) on impact toughness of X80 line pipe steels, Mater. Sci. Eng. A. 662 (2016) 481–491. https://doi.org/10.1016/j.msea.2016.03.095.

[153] R. Lacalle, J.A. Álvarez, D. Ferreño, J. Portilla, E. Ruiz, B. Arroyo, F. Gutiérrez-Solana, Influence of the flame straightening process on microstructural, mechanical and fracture properties of S235 JR, S460 ML and S690 QL structural steels, Exp. Mech. 53 (2013) 893–909.

[154] M. Kowal, M. Szala, Diagnosis of the microstructural and mechanical properties of over century-old steel railway bridge components, Eng. Fail. Anal. 110 (2020) 104447.

[155] S. Bordbar, M. Alizadeh, S.H. Hashemi, Effects of microstructure alteration on corrosion behavior of welded joint in API X70 pipeline steel, Mater. Des. 45 (2013) 597–604. https://doi.org/10.1016/j.matdes.2012.09.051.

[156] Z. Wang, A.M. Beese, Effect of chemistry on martensitic phase transformation kinetics and resulting properties of additively manufactured stainless steel, Acta Mater. 131 (2017) 410–422. https://doi.org/10.1016/j.actamat.2017.04.022.

[157] B.E. Carroll, A. Palmer, A.M. Beese, Anisotropic tensile behavior of Ti – 6Al –

4V components fabricated with directed energy deposition additive manufacturing, Acta Mater. 87 (2015) 309–320. https://doi.org/10.1016/j.actamat.2014.12.054.

[158] Q. Zhang, J. Chen, Z. Zhao, H. Tan, X. Lin, W. Huang, Microstructure and anisotropic tensile behavior of laser additive manufactured TC21 titanium alloy, Mater. Sci. Eng. A. 673 (2016) 204–212. https://doi.org/10.1016/j.msea.2016.07.040.

[159] H. Luo, Q. Yu, C. Dong, G. Sha, Z. Liu, J. Liang, L. Wang, G. Han, X. Li, Influence of the aging time on the microstructure and electrochemical behaviour of a 15-5PH ultra-high strength stainless steel, Corros. Sci. 139 (2018) 185–196. https://doi.org/https://doi.org/10.1016/j.corsci.2018.04.032.

[160] A.N. Isfahany, H. Saghafian, G. Borhani, The effect of heat treatment on mechanical properties and corrosion behavior of AISI420 martensitic stainless steel, J. Alloys Compd. 509 (2011) 3931–3936.

[161] J. Ge, J. Lin, H. Fu, Y. Lei, R. Xiao, A spatial periodicity of microstructural evolution and anti-indentation properties of wire-arc additive manufacturing 2Cr13 thin-wall part, Mater. Des. 160 (2018) 218–228.

[162] C. Köse, R. Kaçar, The effect of preheat & post weld heat treatment on the laser weldability of AISI 420 martensitic stainless steel, Mater. Des. 64 (2014) 221–226.

[163] T. DebRoy, H.L. Wei, J.S. Zuback, T. Mukherjee, J.W. Elmer, J.O. Milewski, A.M. Beese, A. Wilson-Heid, A. De, W. Zhang, Additive manufacturing of metallic components–process, structure and properties, Prog. Mater. Sci. 92 (2018) 112–224.

[164] S.W. Williams, F. Martina, A.C. Addison, J. Ding, G. Pardal, P. Colegrove, Wire+ arc additive manufacturing, Mater. Sci. Technol. 32 (2016) 641–647.

[165] C. Dharmendra, A. Hadadzadeh, B.S. Amirkhiz, G.D.J. Ram, M. Mohammadi, Microstructural evolution and mechanical behavior of nickel aluminum bronze Cu-9Al-4Fe-4Ni-1Mn fabricated through wire-arc additive manufacturing, Addit. Manuf. 30 (2019) 100872.

[166] J.F. Wang, Q.J. Sun, H. Wang, J.P. Liu, J.C. Feng, Effect of location on microstructure and mechanical properties of additive layer manufactured Inconel 625 using gas tungsten arc welding, Mater. Sci. Eng. A. 676 (2016) 395–405.

https://doi.org/https://doi.org/10.1016/j.msea.2016.09.015.

[167] E. Brandl, B. Baufeld, C. Leyens, R. Gault, Additive manufactured Ti-6Al-4V using welding wire: comparison of laser and arc beam deposition and evaluation with respect to aerospace material specifications, Phys. Procedia. 5 (2010) 595–606. https://doi.org/https://doi.org/10.1016/j.phpro.2010.08.087.

[168] J. Bai, H.L. Ding, J.L. Gu, X.S. Wang, H. Qiu, Porosity evolution in additively manufactured aluminium alloy during high temperature exposure, in: IOP Conf. Ser. Mater. Sci. Eng., IOP Publishing, 2017: p. 12045.

[169] A. Vahedi Nemani, M. Ghaffari, A. Nasiri, On the Post-Printing Heat Treatment of a Wire Arc Additively Manufactured ER70S Part, Materials (Basel). 13 (2020) 2795.

[170] M. Kazemipour, J.H. Lunde, S. Salahi, A. Nasiri, On the Microstructure and Corrosion Behavior of Wire Arc Additively Manufactured AISI 420 Stainless Steel, in: TMS 2020 149th Annu. Meet. Exhib. Suppl. Proc., Springer, 2020: pp. 435–448.

[171] J. Ge, J. Lin, H. Fu, Y. Lei, R. Xiao, Tailoring microstructural features of wire arc additive manufacturing 2Cr13 part via varying inter-layer dwelling time, Mater. Lett. 232 (2018) 11–13.

[172] P. Wang, S.P. Lu, N.M. Xiao, D.Z. Li, Y.Y. Li, Effect of delta ferrite on impact properties of low carbon 13Cr–4Ni martensitic stainless steel, Mater. Sci. Eng. A. 527 (2010) 3210–3216.

[173] B.T. Lu, Z.K. Chen, J.L. Luo, B.M. Patchett, Z.H. Xu, Pitting and stress corrosion cracking behavior in welded austenitic stainless steel, Electrochim. Acta. 50 (2005) 1391–1403. https://doi.org/https://doi.org/10.1016/j.electacta.2004.08.036.

[174] M.G. Pujar, R.K. Dayal, T.P.S. Gill, S.N. Malhotra, Role of delta-ferrite in the dissolution of passive films on the austenitic stainless-steel weld metals, J. Mater. Sci. Lett. 18 (1999) 823–826.

[175] S. Kožuh, M. Gojić, L. Vrsalović, B. Ivković, Corrosion failure and microstructure analysis of AISI 316L stainless steels for ship pipeline before and after welding, Kov. Mater. 51 (2013) 53–61.

[176] L.D. Barlow, M. Du Toit, Effect of austenitizing heat treatment on the

microstructure and hardness of martensitic stainless steel AISI 420, J. Mater. Eng. Perform. 21 (2012) 1327–1336.

[177] S.K. Bonagani, B. Vishwanadh, S. Tenneti, N.N. Kumar, V. Kain, Influence of tempering treatments on mechanical properties and hydrogen embrittlement of 13 wt% Cr martensitic stainless steel, Int. J. Press. Vessel. Pip. 176 (2019) 103969.

[178] S.K. Bonagani, V. Bathula, V. Kain, Influence of tempering treatment on microstructure and pitting corrosion of 13 wt.% Cr martensitic stainless steel, Corros. Sci. (2018). https://doi.org/10.1016/j.corsci.2017.12.012.

[179] ASTM E8/E8M-13a, Standard test methods for tension testing of metallic materials, ASTM International, West Conshohocken, PA, 2013. 10.1520/E0008_E0008M-13A.

[180] J.C. Lippold, D.J. Kotecki, Welding metallurgy and weldability of stainless steels, Weld. Metall. Weldability Stainl. Steels. (2005) 60–68.

[181] H. Fujii, H. Matsunaga, Y. Murakami, Effect of δ ferrite on fatigue strength of SUS630 stainless steel, Zair. Soc. Mater. Sci. Japan. 51 (2002) 215–220.

[182] C. Pandey, M.M. Mahapatra, P. Kumar, N. Saini, Comparative study of autogenous tungsten inert gas welding and tungsten arc welding with filler wire for dissimilar P91 and P92 steel weld joint, Mater. Sci. Eng. A. 712 (2018) 720–737. https://doi.org/https://doi.org/10.1016/j.msea.2017.12.039.

[183] J. Dossett, G.E. Totten, Introduction to Steel Heat Treatment, Steel Heat Treat. Fundam. Process. 4 (2013) 3–25.

[184] A.F. Candelaria, C.E. Pinedo, Influence of the heat treatment on the corrosion resistance of the martensitic stainless steel type AISI 420, J. Mater. Sci. Lett. 22 (2003) 1151–1153.

[185] X. Tao, J. Gu, L. Han, Characterization of precipitates in X12CrMoWVNbN10-1-1 steel during heat treatment, J. Nucl. Mater. 452 (2014) 557–564. https://doi.org/https://doi.org/10.1016/j.jnucmat.2014.06.018.

[186] B. Sunil Kumar, V. Kain, B. Vishwanadh, Effect of Tempering Treatments on Microstructure and Intergranular Corrosion of 13 wt% Cr Martensitic Stainless Steel, Corrosion. 73 (2017) 362–378.

[187] J. Dossett, G.E. Totten, Heat Treating of Martensitic Stainless Steels, ASM Int. 4D

(2014) 382–396. https://doi.org/https://doi.org/10.31399/asm.hb.v04d.a0005985.

[188] S.Y. Lu, K.F. Yao, Y.B. Chen, M.H. Wang, X. Liu, X. Ge, The effect of tempering temperature on the microstructure and electrochemical properties of a 13 wt.% Cr-type martensitic stainless steel, Electrochim. Acta. 165 (2015) 45–55.

[189] S.Y. Lu, K.F. Yao, Y.B. Chen, M.H. Wang, X.Y. Ge, Influence of heat treatment on the microstructure and corrosion resistance of 13 wt pct Cr-type martensitic stainless steel, Metall. Mater. Trans. A. 46 (2015) 6090–6102.

[190] T. Tsuchiyama, J. Tobata, T. Tao, N. Nakada, S. Takaki, Quenching and partitioning treatment of a low-carbon martensitic stainless steel, Mater. Sci. Eng. A. 532 (2012) 585–592. https://doi.org/https://doi.org/10.1016/j.msea.2011.10.125.

[191] P. Krakhmalev, I. Yadroitsava, G. Fredriksson, I. Yadroitsev, In situ heat treatment in selective laser melted martensitic AISI 420 stainless steels, Mater. Des. 87 (2015) 380–385.

[192] H. Kitahara, R. Ueji, N. Tsuji, Y. Minamino, Crystallographic features of lath martensite in low-carbon steel, Acta Mater. 54 (2006) 1279–1288.

[193] J. Hidalgo, M.J. Santofimia, Effect of prior austenite grain size refinement by thermal cycling on the microstructural features of as-quenched lath martensite, Metall. Mater. Trans. A. 47 (2016) 5288–5301.

[194] T. Ohmura, A.M. Minor, E.A. Stach, J.W. Morris, Dislocation–grain boundary interactions in martensitic steel observed through in situ nanoindentation in a transmission electron microscope, J. Mater. Res. 19 (2004) 3626–3632.

[195] J.C. Lippold, D.J. Kotecki, Welding metallurgy and weldability of stainless steels, Weld. Metall. Weldability Stainl. Steels, by John C. Lippold, Damian J. Kotecki, Pp. 376. ISBN 0-471-47379-0. Wiley-VCH, March 2005. (2005) 376.

[196] M.A. Rehan, A. Medvedeva, L.-E. Svensson, L. Karlsson, Retained austenite transformation during heat treatment of a 5 Wt Pct Cr cold work tool steel, Metall. Mater. Trans. A. 48 (2017) 5233–5243.

[197] O. Kazum, M.B. Kannan, H. Beladi, I. Timokhina, P. Hodgson, S. Khoddam, Selective dissolution of retained austenite in nanostructured bainitic steels, Adv. Eng. Mater. 16 (2014) 442–444.

[198] C. Pandey, M.M. Mahapatra, P. Kumar, N. Saini, Dissimilar joining of CSEF

steels using autogenous tungsten-inert gas welding and gas tungsten arc welding and their effect on δ-ferrite evolution and mechanical properties, J. Manuf. Process. 31 (2018) 247–259. https://doi.org/https://doi.org/10.1016/j.jmapro.2017.11.020.

[199] I. Calliari, M. Zanesco, M. Dabalà, K. Brunelli, E. Ramous, Investigation of microstructure and properties of a Ni–Mo martensitic stainless steel, Mater. Des. 29 (2008) 246–250. https://doi.org/https://doi.org/10.1016/j.matdes.2006.11.020.

[200] G.V.P. Gaunkar, A.M. Huntz, P. Lacombe, Role of carbon in embrittlement phenomena of tempered martensitic 12Cr-0.15% C steel, Met. Sci. 14 (1980) 241–252.

[201] S.S.M. Tavares, L.F. Noris, J.M. Pardal, M.R. da Silva, Temper embrittlement of supermartensitic stainless steel and non-destructive inspection by magnetic Barkhausen noise, Eng. Fail. Anal. 100 (2019) 322–328.

[202] G. Chakraborty, C.R. Das, S.K. Albert, A.K. Bhaduri, V. Thomas Paul, G. Panneerselvam, A. Dasgupta, Study on tempering behaviour of AISI 410 stainless steel, Mater. Charact. 100 (2015) 81–87. https://doi.org/https://doi.org/10.1016/j.matchar.2014.12.015.

[203] E. De Moor, S. Lacroix, A.J. Clarke, J. Penning, J.G. Speer, Effect of Retained Austenite Stabilized via Quench and Partitioning on the Strain Hardening of Martensitic Steels, Metall. Mater. Trans. A. 39 (2008) 2586. https://doi.org/10.1007/s11661-008-9609-z.

[204] S.-Y. Lu, K.-F. Yao, Y.-B. Chen, M.-H. Wang, N. Chen, X.-Y. Ge, Effect of quenching and partitioning on the microstructure evolution and electrochemical properties of a martensitic stainless steel, Corros. Sci. 103 (2016) 95–104.

[205] M. Kimura, Y. Miyata, T. Toyooka, Y. Kitahaba, Effect of retained austenite on corrosion performance for modified 13% Cr steel pipe, Corrosion. 57 (2001) 433–439.

[206] H. Hill, S. Huth, S. Weber, W. Theisen, Corrosion properties of a plastic mould steel with special focus on the processing route, Mater. Corros. 62 (2011) 436–443.

[207] A.F. Candelaria, C.E. Pinedo, Influence of the heat treatment on the corrosion

resistance of the martensitic stainless steel type AISI 420, J. Mater. Sci. Lett. 22 (2003) 1151–1153.

[208] L. Yuan, D. Ponge, J. Wittig, P. Choi, J.A. Jiménez, D. Raabe, Nanoscale austenite reversion through partitioning, segregation and kinetic freezing: Example of a ductile 2 GPa Fe–Cr–C steel, Acta Mater. 60 (2012) 2790–2804.

[209] D. V Edmonds, K. He, F.C. Rizzo, B.C. De Cooman, D.K. Matlock, J.G. Speer, Quenching and partitioning martensite—A novel steel heat treatment, Mater. Sci. Eng. A. 438 (2006) 25–34.

[210] C. Guo, R. Hu, F. Chen, Microstructure and performances for 15-5 PH stainless steel fabricated through the wire-arc additive manufacturing technology, Mater. Technol. (2020) 1–12.

[211] M. Rafieazad, A.V. Nemani, M. Ghaffari, A. Nasiri, On Microstructure and Mechanical Properties of a Low-Carbon Low-Alloy Steel Block Fabricated by Wire Arc Additive Manufacturing, J. Mater. Eng. Perform. (2021) 1–9.

[212] T.A. Rodrigues, V. Duarte, R.M. Miranda, T.G. Santos, J.P. Oliveira, Current status and perspectives on wire and arc additive manufacturing (WAAM), Materials (Basel). 12 (2019). https://doi.org/10.3390/ma12071121.

[213] A. Vahedi Nemani, M. Ghaffari, A. Nasiri, Comparison of microstructural characteristics and mechanical properties of shipbuilding steel plates fabricated by conventional rolling versus wire arc additive manufacturing, Addit. Manuf. 32 (2020). https://doi.org/10.1016/j.addma.2020.101086.

[214] M. Ghaffari, A. Vahedi Nemani, A. Nasiri, Interfacial bonding between a wire arc additive manufactured 420 martensitic stainless steel part and its wrought base plate, Mater. Chem. Phys. 251 (2020). https://doi.org/10.1016/j.matchemphys.2020.123199.

[215] M. Ghaffari, A.V. Nemani, A. Nasiri, Microstructure and mechanical behaviour of PH 13-8Mo martensitic stainless steel fabricated by wire arc additive manufacturing, Addit. Manuf. (2021) 102374. https://doi.org/10.1016/j.addma.2021.102374.

[216] R. Schnitzer, R. Radis, M. Nöhrer, M. Schober, R. Hochfellner, S. Zinner, E. Povoden-Karadeniz, E. Kozeschnik, H. Leitner, Reverted austenite in PH 13-8 Mo

maraging steels, Mater. Chem. Phys. 122 (2010) 138–145.

[217] J.H. Shin, J. Jeong, J.W. Lee, Microstructural evolution and the variation of tensile behavior after aging heat treatment of precipitation hardened martensitic steel, Mater. Charact. 99 (2015) 230–237. https://doi.org/10.1016/j.matchar.2014.11.024.

[218] R. Schnitzer, G.A. Zickler, E. Lach, H. Clemens, S. Zinner, T. Lippmann, H. Leitner, Influence of reverted austenite on static and dynamic mechanical properties of a PH 13-8 Mo maraging steel, Mater. Sci. Eng. A. 527 (2010) 2065–2070. https://doi.org/10.1016/j.msea.2009.11.046.

[219] C. V. Robino, M.J. Cieslak, P.W. Hochanadel, G.R. Edwards, Heat treatment of investment cast PH 13-8 Mo stainless steel: Part II. Isothermal aging kinetics, Metall. Mater. Trans. A. 25 (1994) 697–704. https://doi.org/10.1007/BF02665446.

[220] P.W. Hochanadel, G.R. Edwards, C. V Robino, M.J. Cieslak, Heat treatment of investment cast PH 13-8 Mo stainless steel: Part I. Mechanical properties and microstructure, Metall. Mater. Trans. A. 25 (1994) 789–798.

[221] X. Li, J. Zhang, E. Akiyama, Q. Li, Y. Wang, Effect of heat treatment on hydrogen-assisted fracture behavior of PH13-8Mo steel, Corros. Sci. 128 (2017) 198–212. https://doi.org/10.1016/j.corsci.2017.09.018.

[222] X. Li, J. Zhang, J. Chen, S. Shen, G. Yang, T. Wang, X. Song, Effect of aging treatment on hydrogen embrittlement of PH 13-8 Mo martensite stainless steel, Mater. Sci. Eng. A. 651 (2016) 474–485. https://doi.org/10.1016/j.msea.2015.09.116.

[223] L.W. Tsay, H.H. Chen, M.F. Chiang, C. Chen, The influence of aging treatments on sulfide stress corrosion cracking of PH 13-8 Mo steel welds, Corros. Sci. 49 (2007) 2461–2473. https://doi.org/10.1016/j.corsci.2006.12.006.

[224] S. Salahi, A.V. Nemani, M. Ghaffari, J. Lunde, A. Nasiri, On Microstructure, Crystallographic Orientation, and Corrosion Properties of Wire Arc Additive Manufactured 420 Martensitic Stainless Steel: Effect of the Inter-layer Temperature, Addit. Manuf. (2021) 102157.

[225] S. Salahi, M. Ghaffari, A.V. Nemani, A. Nasiri, Effects of Secondary-Phase Formation on the Electrochemical Performance of a Wire Arc Additive

Manufactured 420 Martensitic Stainless Steel under Different Heat Treatment Conditions, J. Mater. Eng. Perform. (2021) 1–12.

[226] J.A. Brooks, W.M. Garrison, Weld microstructure development and properties of precipitation-strengthened martensitic stainless steels, Weld. J. (Miami, Fla). 78 (1999) 280–291.

[227] M.J. Cieslak, Hot-Cracking Mechanism in Co//2 Laser Beam Welds of Dissimilar Metals Involving Ph Martensitic Stainless Steels., Weld. J. (Miami, Fla). 66 (1987) 57–60.

[228] V. Seetharaman, M. Sundararaman, R. Krishnan, Precipitation hardening in a PH 13-8 Mo stainless steel, Mater. Sci. Eng. 47 (1981) 1–11.

[229] S. Li, I.J. Beyerlein, M.A.M. Bourke, Texture formation during equal channel angular extrusion of fcc and bcc materials: comparison with simple shear, Mater. Sci. Eng. A. 394 (2005) 66–77.

[230] D. Raabe, K. Luecke, Rolling and annealing textures of bcc metals, Mater. Sci. Forum. (1994). https://doi.org/10.4028/www.scientific.net/msf.157-162.597.

[231] S. Suwas, R. Kumar Ray, Crystallographic texture og materials, Springer, London, 2014.

[232] H. Leitner, R. Schnitzer, M. Schober, S. Zinner, Precipitate modification in PH13-8 Mo type maraging steel, Acta Mater. 59 (2011) 5012–5022. https://doi.org/10.1016/j.actamat.2011.04.053.

[233] Y.Y. Song, X.Y. Li, L.J. Rong, D.H. Ping, F.X. Yin, Y.Y. Li, Formation of the reversed austenite during intercritical tempering in a Fe-13%Cr-4%Ni-Mo martensitic stainless steel, Mater. Lett. 64 (2010) 1411–1414. https://doi.org/10.1016/j.matlet.2010.03.021.

[234] G.S. Frankel, Pitting corrosion of metals: a review of the critical factors, J. Electrochem. Soc. 145 (1998) 2186.

[235] E. McCafferty, Introduction to corrosion science, Springer Science & Business Media, 2010.

[236] S.-Y. Lu, K.-F. Yao, Y.-B. Chen, M.-H. Wang, X. Liu, X. Ge, The effect of tempering temperature on the microstructure and electrochemical properties of a 13wt.% Cr-type martensitic stainless steel, Electrochim. Acta. 165 (2015) 45–55.

https://doi.org/https://doi.org/10.1016/j.electacta.2015.02.038.

[237] M. Serdar, L.V. Žulj, D. Bjegović, Long-term corrosion behaviour of stainless reinforcing steel in mortar exposed to chloride environment, Corros. Sci. 69 (2013) 149–157. https://doi.org/https://doi.org/10.1016/j.corsci.2012.11.035.

[238] S. Salahi, M. Kazemipour, A. Nasiri, Effect of Uniaxial Tension-Induced Plastic Strain on the Microstructure and Corrosion Behavior of 13Cr Martensitic Stainless Steel, CORROSION. (2020).

[239] S. Salahi, M. Kazemipour, A. Nasiri, Effects of microstructural evolution on the corrosion properties of AISI 420 martensitic stainless steel during cold rolling process, Mater. Chem. Phys. 258 (2021). https://doi.org/10.1016/j.matchemphys.2020.123916.

[240] D. Kong, A. Xu, C. Dong, F. Mao, K. Xiao, X. Li, D.D. Macdonald, Electrochemical investigation and ab initio computation of passive film properties on copper in anaerobic sulphide solutions, Corros. Sci. (2017). https://doi.org/10.1016/j.corsci.2016.12.010.

[241] E. Sikora, D.D. Macdonald, Defining the passive state, Solid State Ionics. (1997). https://doi.org/10.1016/s0167-2738(96)00505-x.

[242] A. Fattah-Alhosseini, M.A. Golozar, A. Saatchi, K. Raeissi, Effect of solution concentration on semiconducting properties of passive films formed on austenitic stainless steels, Corros. Sci. 52 (2010) 205–209.

[243] B. Hirschorn, M.E. Orazem, B. Tribollet, V. Vivier, I. Frateur, M. Musiani, Constant-phase-element behavior caused by resistivity distributions in films: I. Theory, J. Electrochem. Soc. 157 (2010) C452.

[244] I. Nicic, D.D. Macdonald, The passivity of Type 316L stainless steel in borate buffer solution, J. Nucl. Mater. (2008). https://doi.org/10.1016/j.jnucmat.2008.06.014.

[245] Z. Feng, X. Cheng, C. Dong, L. Xu, X. Li, Passivity of 316L stainless steel in borate buffer solution studied by Mott–Schottky analysis, atomic absorption spectrometry and X-ray photoelectron spectroscopy, Corros. Sci. 52 (2010) 3646–3653.

[246] D. Kong, X. Ni, C. Dong, X. Lei, L. Zhang, C. Man, J. Yao, X. Cheng, X. Li, Bio-

functional and anti-corrosive 3D printing 316L stainless steel fabricated by selective laser melting, Mater. Des. (2018). https://doi.org/10.1016/j.matdes.2018.04.058.

[247] R.M. Fernández-Domene, E. Blasco-Tamarit, D.M. García-García, J. García-Antón, Effect of alloying elements on the electronic properties of thin passive films formed on carbon steel, ferritic and austenitic stainless steels in a highly concentrated LiBr solution, Thin Solid Films. 558 (2014) 252–258. https://doi.org/https://doi.org/10.1016/j.tsf.2014.03.042.

[248] H. Luo, X. Wang, C. Dong, K. Xiao, X. Li, Effect of cold deformation on the corrosion behaviour of UNS S31803 duplex stainless steel in simulated concrete pore solution, Corros. Sci. 124 (2017) 178–192.

[249] M.J. Carmezim, A.M. Simoes, M.F. Montemor, M.D.C. Belo, Capacitance behaviour of passive films on ferritic and austenitic stainless steel, Corros. Sci. 47 (2005) 581–591.

[250] Y.X. Qiao, Y.G. Zheng, W. Ke, P.C. Okafor, Electrochemical behaviour of high nitrogen stainless steel in acidic solutions, Corros. Sci. 51 (2009) 979–986. https://doi.org/https://doi.org/10.1016/j.corsci.2009.02.026.

[251] L. V Taveira, M.F. Montemor, M.D.C. Belo, M.G. Ferreira, L.F.P. Dick, Influence of incorporated Mo and Nb on the Mott–Schottky behaviour of anodic films formed on AISI 304L, Corros. Sci. 52 (2010) 2813–2818.

[252] S.R. Morrison, Electrochemistry at semiconductor and oxidized metal electrodes, (1980).

[253] S. Ningshen, U. Kamachi Mudali, V.K. Mittal, H.S. Khatak, Semiconducting and passive film properties of nitrogen-containing type 316LN stainless steels, Corros. Sci. 49 (2007) 481–496. https://doi.org/https://doi.org/10.1016/j.corsci.2006.05.041.

[254] H. Tsuchiya, S. Fujimoto, O. Chihara, T. Shibata, Semiconductive behavior of passive films formed on pure Cr and Fe–Cr alloys in sulfuric acid solution, Electrochim. Acta. 47 (2002) 4357–4366. https://doi.org/https://doi.org/10.1016/S0013-4686(02)00508-X.

[255] J. Amri, T. Souier, B. Malki, B. Baroux, Effect of the final annealing of cold rolled

stainless steels sheets on the electronic properties and pit nucleation resistance of passive films, Corros. Sci. 50 (2008) 431–435.

[256] D.D. Macdonald, The point defect model for the passive state, J. Electrochem. Soc. 139 (1992) 3434–3449.

[257] N. Chandra, D.K. Singh, M. Sharma, R.K. Upadhyay, S.S. Amritphale, S.K. Sanghi, Synthesis and characterization of nano-sized zirconia powder synthesized by single emulsion-assisted direct precipitation, J. Colloid Interface Sci. 342 (2010) 327–332.

[258] K.H. Anantha, C. Ornek, S. Ejnermark, A. Medvedeva, J. Sj, Correlative Microstructure Analysis and In Situ Corrosion Study of AISI 420 Martensitic Stainless Steel for Plastic Molding, 164 (2017) 85–93. https://doi.org/10.1149/2.0531704jes.

[259] A. Lasia, Electrochemical impedance spectroscopy and its applications, in: Mod. Asp. Electrochem., Springer, 2002: pp. 143–248.

[260] D.D. Macdonald, A. Sun, An electrochemical impedance spectroscopic study of the passive state on Alloy-22, Electrochim. Acta. 51 (2006) 1767–1779.

[261] J.-B. Lee, S.-I. Yoon, Effect of nitrogen alloying on the semiconducting properties of passive films and metastable pitting susceptibility of 316L and 316LN stainless steels, Mater. Chem. Phys. 122 (2010) 194–199.

[262] T. Yamamoto, K. Fushimi, S. Miura, H. Konno, Influence of substrate dislocation on passivation of pure iron in pH 8.4 borate buffer solution, J. Electrochem. Soc. 157 (2010) C231.

[263] A. Nazarov, D. Thierry, Application of Volta potential mapping to determine metal surface defects, Electrochim. Acta. 52 (2007) 7689–7696.

[264] G.K. Williamson, R.E. Smallman, III. Dislocation densities in some annealed and cold-worked metals from measurements on the X-ray debye-scherrer spectrum, Philos. Mag. 1 (1956) 34–46.

[265] A.L. Patterson, The Scherrer formula for X-ray particle size determination, Phys. Rev. 56 (1939) 978.

[266] J. Pešička, R. Kužel, A. Dronhofer, G. Eggeler, The evolution of dislocation density during heat treatment and creep of tempered martensite ferritic steels, Acta

Mater. 51 (2003) 4847–4862.

[267] A. Shahriari, M. Ghaffari, L. Khaksar, A. Nasiri, A. Hadadzadeh, B.S. Amirkhiz, M. Mohammadi, Corrosion resistance of 13wt.% Cr martensitic stainless steels: Additively manufactured CX versus wrought Ni-containing AISI 420, Corros. Sci. 184 (2021) 109362.

[268] L. Jinlong, L. Hongyun, Comparison of corrosion properties of passive films formed on phase reversion induced nano/ultrafine-grained 321 stainless steel, Appl. Surf. Sci. 280 (2013) 124–131. https://doi.org/https://doi.org/10.1016/j.apsusc.2013.04.108.

[269] G.T. Burstein, P.I. Marshall, The coupled kinetics of film growth and dissolution of stainless steel repassivating in acid solutions, Corros. Sci. 24 (1984) 449–462. https://doi.org/https://doi.org/10.1016/0010-938X(84)90070-2.

[270] W.T. Read, W. Shockley, Dislocation models of crystal grain boundaries, Phys. Rev. 78 (1950) 275.

[271] J. Gyhlesten Back, G. Engberg, Investigation of parent austenite grains from martensite structure using EBSD in a wear resistant steel, Materials (Basel). 10 (2017) 453.

[272] A.S. Murthy, Role of alloy additions on strengthening in 17-4 PH stainless steel, Missouri University of Science and Technology, 2012.

[273] X. Lei, Y. Feng, J. Zhang, A. Fu, C. Yin, D.D. Macdonald, Impact of Reversed Austenite on the Pitting Corrosion Behavior of Super 13Cr Martensitic Stainless Steel, Electrochim. Acta. 191 (2016) 640–650. https://doi.org/https://doi.org/10.1016/j.electacta.2016.01.094.

[274] J.W. Christian, The theory of transformations in metals and alloys, Newnes, 2002.

[275] A. Shahriari, L. Khaksar, A. Nasiri, A. Hadadzadeh, B.S. Amirkhiz, M. Mohammadi, Microstructure and corrosion behavior of a novel additively manufactured maraging stainless steel, Electrochim. Acta. 339 (2020) 135925. https://doi.org/10.1016/j.electacta.2020.135925.

[276] M. Ghaffari, A.V. Nemani, A. Nasiri, Microstructure and mechanical behaviour of PH 13-8Mo martensitic stainless steel fabricated by wire arc additive manufacturing, Addit. Manuf. (2021) 102374.

[277] M. Sanjari, A. Hadadzadeh, H. Pirgazi, A. Shahriari, B.S. Amirkhiz, L.A.I. Kestens, M. Mohammadi, Selective laser melted stainless steel CX: Role of built orientation on microstructure and micro-mechanical properties, Mater. Sci. Eng. A. 786 (2020) 139365.

[278] J.W. Edington, K.C.T. Russell, Practical electron microscopy in materials science, in: Macmillan International Higher Education, 1977: pp. 95–104.

[279] L.T. Shiang, C.M. Wayman, Maraging behavior of an Fe-19.5 Ni-5Mn alloy II: Evolution of reverse-transformed austenite during overaging, Metallography. 21 (1988) 425–451.

[280] P.P. Sinha, D. Sivakumar, N.S. Babu, K.T. Tharian, A. Natarajan, Austenite reversion in 18 Ni Co-free maraging steel, Steel Res. 66 (1995) 490–494.

[281] S. Höring, D. Abou-Ras, N. Wanderka, H. Leitner, H. Clemens, J. Banhart, Characterization of reverted austenite during prolonged ageing of maraging steel CORRAX, Steel Res. Int. 80 (2009) 84–88.

[282] X. Li, Z. Yin, Reverted austenite during aging in 18Ni(350) maraging steel, Mater. Lett. 24 (1995) 239–242. https://doi.org/https://doi.org/10.1016/0167-577X(95)00109-3.

[283] G.B. Olson, M. Azrin, E.S. Wright, Innovations in ultrahigh-strength steel technology, in: US Army Laboratory Command, Materials Technology Laboratory, 1987: pp. 549–564.

APPENDIX A Copyright Permission

Alireza Vahedi Nemani

From: Permissions Helpdesk <permissionshelpdesk@elsevier.com>
Sent: Sunday, April 3, 2022 1:14 PM
To: Alireza Vahedi Nemani
Subject: Re: Copyright Permission Letter for PhD thesis [220328-024045]

Dear Alireza Vahedi Nemani,

We hereby grant you permission to reprint the material below at no charge in your thesis subject to the following conditions:

RE:

1. **Effect of interpass temperature on the formation of retained austenite in a wire arc additive manufactured ER420 martensitic stainless steel, Alireza Vahedi Nemani, Mahya Ghaffari, Salar Salahi, Jonas Lunde, Ali Nasiri, Journal of Materials Chemistry and Physics, 124555, 2021.**
2. **Effects of post-printing heat treatment on the microstructure and mechanical properties of a wire arc additive manufactured 420 martensitic stainless steel part, Alireza Vahedi Nemani, Mahya Ghaffari, Salar Salahi, Ali Nasiri, Materials Science and Engineering: A, 141167, 2021.**
3. **Comparison of microstructural characteristics and mechanical properties of shipbuilding steel plates fabricated by conventional rolling versus wire arc additive manufacturing, Alireza Vahedi Nemani, Mahya Ghaffari, Ali Nasiri, Journal of Additive Manufacturing, 101086, 2020.**

1. If any part of the material to be used (for example, figures) has appeared in our publication with credit or acknowledgement to another source, permission must also be sought from that source. If such permission is not obtained then that material may not be included in your publication/copies.

2. Suitable acknowledgment to the source must be made, either as a footnote or in a reference list at the end of your publication, as follows:

"This article was published in Publication title, Vol number, Author(s), Title of article, Page Nos, Copyright Elsevier (or appropriate Society name) (Year)."

3. Your thesis may be submitted to your institution in either print or electronic form.

4. Reproduction of this material is confined to the purpose for which permission is hereby given.

5. This permission is granted for non-exclusive world English rights only. For other languages please reapply separately for each one required. Permission excludes use in an electronic form other than submission. Should you have a specific electronic project in mind please reapply for permission.

6. As long as the article is embedded in your thesis, you can post/share your thesis in the University repository.

7. Should your thesis be published commercially, please reapply for permission.

Kind regards,

Roopa Lingayath
Senior Copyrights Coordinator
ELSEVIER | HCM - Health Content Management

Visit Elsevier Permissions